SIMPLIFIED PREDICTIVE MODELS FOR CO_2 SEQUESTRATION PERFORMANCE ASSESSMENT

RESEARCH TOPICAL REPORT ON TASK #2 SIMPLIFIED PHYSICS BASED MODELS

Reporting Period: July 1, 2014 through September 30, 2014

Principal Investigator: Dr. Srikanta Mishra
mishras@battelle.org 614-424-5712
Principal Authors: Priya Ravi Ganesh and Srikanta Mishra

Date Report Issued: October 2014

U.S. Department of Energy National Energy Technology Laboratory
DOE Award No. DE-FE0009051, Task #2

Submitting Organization:

Battelle Memorial Institute
505 King Avenue
Columbus, OH 43201
DUNS Number: 00 790 1598

Abstract

We present a simplified-physics based approach, where only the most important physical processes are modeled, to develop and validate simplified predictive models of CO_2 sequestration in deep saline formation. The system of interest is a single vertical well injecting supercritical CO_2 into a 2-D layered reservoir-caprock system with variable layer permeabilities. We use a set of well-designed full-physics compositional simulations to understand key processes and parameters affecting pressure propagation and buoyant plume migration. Based on these simulations, we have developed correlations for dimensionless injectivity as a function of the slope of fractional-flow curve, variance of layer permeability values, and the nature of vertical permeability arrangement. The same variables, along with a modified gravity number, can be used to develop a correlation for the total storage efficiency within the CO_2 plume footprint. Similar correlations are also developed to predict the average pressure within the injection reservoir, and the pressure buildup within the caprock.

Table of Contents

List of Appendices

List of Figures

Page

List of Tables

Page

Executive Summary

The objective of this research project is to develop and validate a portfolio of simplified modeling approaches for CO_2 sequestration in deep saline formations – based on simplified physics, statistical learning, and/or mathematical approximations – for predicting: (a) injection well and formation pressure buildup, (b) lateral and vertical CO_2 plume migration, and (c) brine displacement to overlying formations and the far-field. Such computationally-efficient alternatives to conventional numerical simulators can be valuable assets during preliminary CO_2 injection project screening, serve as a key element of probabilistic system assessment modeling tools, and assist regulators in quickly evaluating geological storage projects. The project team includes Battelle and Stanford University. Support for the project is provided by U.S. DOE National Energy Technology Laboratory and the Ohio Development Service Agency Office of Coal Development (ODSA).

Over the last decade, the development and demonstration of geologic sequestration technologies to mitigate greenhouse gas emissions has been an area of active research. Geologic sequestration of CO_2 in deep saline formations has been recognized for its immense potential for long-term storage of captured CO_2. To ensure safe and effective deployment of this technology, it is crucial for us to understand the nature of pressure and plume propagation as injected CO_2 displaces the native reservoir fluids. Detailed numerical simulation of such processes generally requires extensive reservoir characterization data and computational burden. In this context, validated simplified models can be valuable as they have minimal data and computational requirements in comparison. Simplified models that are based on the most relevant physical processes and validated against full-physics simulators are thus being sought after as efficient and useful alternatives for rapid screening and evaluation of CO_2 sequestration projects.

This topical results presents results from Task2 of the research project. Our research objective is to develop and validate simplified physics based models for CO_2 sequestration in deep saline formations based on insights from a set of well-designed full-physics compositional simulations of this system. The study involves an extensive parameter space covering different reservoir and cap rock properties. We investigate the sensitivity of system behavior for high and low variants from a reference case for various reservoir and caprock properties and systematically seek to quantify their effect on each performance metric.

Our computational model consists of a single vertical well radially injecting supercritical CO_2 in the middle of a 2-D layered reservoir overlain by a caprock. We add relevant buoyancy and heterogeneity effects to the system considerations in the simplified 1-D 3-region model of Oruganti and Mishra (2013) and Burton et al. (2008). Simulations are run for an injection period of 30 years to observe CO_2 displacement characteristics in a closed system – as would be the case in a network of injection wells. The independent variables of interest are thickness and porosity of reservoir and caprock, reservoir permeability heterogeneity, permeability and capillary pressure of the caprock, and CO_2 injection rate. Reservoir heterogeneity is varied by controlling the permeability of the reservoir, permeability anisotropy ratio (ratio of vertical to horizontal permeability) in the reservoir, spatial arrangement of the heterogeneous reservoir permeability layers, and relative permeability curves for the reservoir.

The maximum plume extent at the end of CO_2 injection is affected by the efficiency of the two-phase (CO_2-brine) displacement process – this total storage efficiency, E_S, being a product of: (a) volumetric sweep efficiency i.e. fraction of total pore volume contacted by CO_2, and (b) displacement efficiency within the pore volume contacted by CO_2. We establish a relationship for maximum plume extent at the end of injection as a function of the amount of CO_2 injected and the storavitity (porosity-thickness product) of the reservoir, for a given total storage efficiency. The most important terms in the simplified model for total storage efficiency involve the relative permeability model followed by the reservoir heterogeneity.

CO_2 injectivity, which is the ratio of amount of CO_2 injected to the corresponding pressure buildup, is a critical performance metric to determine operational constraints of pressure buildup or injection rate for allowable injected volume of CO_2 or operating pressure constraints respectively. We consistently observe from the sensitivity analyses that our system response to CO_2 injection is such that the pressure at the injection well quickly jumps to a quasi-steady value and remains relatively stable thereafter during the early transient period before boundary effects come into play. This pressure jump can be converted into a dimensionless pressure buildup, P_D, which includes the effects of reservoir permeability-thickness, CO_2 injection rate and brine viscosity, and helps us effectively capture the injectivity index of the well

The pressure buildup at the mid-point of the reservoir is observed to be affected primarily by the permeability-thickness product of the reservoir, the CO_2 injection rate, and the relative permeability model for the reservoir. When expressed in terms of the dimensionless variable P_D, we determine the dimensionless pressure buildup at the CO_2 injector well to be a function of the slope of the fractional flow curve (df_g/dS_g) and the Dykstra-Parson's coefficient (V_{DP}). Thus, using a steady-state version of Darcy's law and dominant parameter groups identified from the sensitivity analysis exercise with full-physics compositional simulations, we develop a multivariate linear regression model to determine P_D, and hence, the injectivity index. This predictive model is successfully validated to check for robustness of fit.

We also evaluate the average pressure behavior in the reservoir for a given amount of CO_2 injected into closed and semi-closed saline formations. For closed reservoirs, the effectiveness of two-phase flow in a given reservoir depends on an '*f*' factor (which is a function of the relative permeability) and is correlated to the square of the ratio of the reservoir radius to the plume radius at the end of injection. For semi-closed formations when an overlying caprock is present, this '*f*' factor is modified to account for the relative storage capacity of the rock i.e. ratio of reservoir storavitity to the total system storativity.

Finally, the effect of the overlying cap rock properties – mainly thickness and permeability, were investigated for their effect on the pressure buildup in the system. The ratio of the pressure buildup in the cap rock to that in a given reservoir at the end of injection was determined to be a function of the ratios of the thickness and permeability of cap rock and the reservoir.

Thus, using the basic physical processes involved, these simplified physics models can be used to reasonably predict the plume extent in the reservoir and pressure propagation in both the reservoir and the cap rock resulting from the injection of a given amount of CO_2.

1 Introduction

1.1 Background

CO_2 injection into the sub-surface is emerging as a viable technology for reducing anthropogenic CO_2 emissions into the atmosphere (Benson and Cook, 2005). Deep saline formations provide a particularly attractive target for this purpose, with potential storage capacity in such systems in North America estimated to be of the order of 3400 billion tons of CO_2, or the equivalent of emissions from hundreds of years (DOE/NETL, 2010). Over the last decade, the development and demonstration of geologic sequestration technologies to mitigate greenhouse gas emissions has been a field of active study. The U.S. Department of Energy's (DOE's) Carbon Storage Program has provided the primary impetus for R&D activities in the U.S. to develop and advance technologies that will significantly improve the efficacy of the geologic carbon storage technology, reduce the cost of implementation, and be ready for widespread commercial deployment between 2020 and 2030.

When large amounts of CO_2 are sequestered underground, excess pressure buildup in the storage formations and cap rock is an associated risk in terms of endangering integrity of underground formation and wellbores, along with the risk of potential plume movement beyond the injected domain. Multiple technologies related to the evaluation of capacity and injectivity, monitoring of CO_2 plume movement, and risk assessment are needed to ensure safe and effective deployment of geologic storage. One key technology in this regard is the simulation of CO_2 injection and migration over very large areas and over long periods of time. Detailed numerical models of CO_2 geological storage are, however, data and computation intensive. In this context, validated simplified analytical or semi-analytical modeling tools can be valuable assets in preliminary CO_2 injection project screening and implementation phases. Such tools have minimal data and computational requirements compared to detailed-physics numerical simulators. Simplified models are therefore being sought after as alternatives for rapid feasibility and risk assessment of CO_2 sequestration projects.

The primary motivation for this research is to provide simplified modeling tools that will enable rapid feasibility and risk assessment of CO_2 sequestration projects in deep saline formations. These tools will: (a) provide project developers with quick and simple tools to screen sites and estimate monitoring needs, (b) provide regulators with tools to evaluate geological storage projects quickly without running full-scale detailed numerical simulations, (c) enable integrated

system risk assessments to be carried out with robust, yet simple to implement, reservoir performance models, and (d) allow modelers to efficiently analyze the impact of variable CO_2 injection rates on plume migration and trapping for optimal well placement and rate allocation.

1.2 Objective and Scope

Our research objective is to develop and validate simplified physics based models for CO_2 sequestration in deep saline formations for predicting: (a) CO_2 plume migration, and (b) pressure buildup in the injection well and the formation. Here, simplified physics refers to a modeling paradigm where only the most relevant processes and parameters are used in the modeling, based on insights derived from full physics simulations and/or first principles. We seek to specifically attempt the quantification of the following performance metrics in a 2D stratified aquifer- cap rock system: (a) outer extent of CO_2-brine interface, (b) average brine saturation in the two-phase region, (c) volumetric sweep efficiency, and (d) pressure increase at the injection well. Metrics (a) – (c) are related to the degree of brine displacement while (d) relates to pressure propagation in the system of interest.

1.3 Research Motivation

Simplified models are extremely useful for rapid integrated system performance assessment of CO_2 sequestration projects. Current simplified analytical and semi-analytical models of CO_2 geological storage generally do not account for realistic field conditions. For example, the Nordbotten and Celia (2005) sharp-interface model does not honor the dynamics of two-phase flow behind the CO_2-brine interface, while the semi-analytical three region model by Oruganti and Mishra (2012) is applicable only for confined systems (i.e., formations with impermeable overlying and underlying layers). We address the need for more relevant simplified two-phase models by considering semi-confined reservoir-caprock systems with vertical layering to include formation heterogeneity and finite lateral extent.

1.4 Research Approach

Our approach is based on using data from numerical experiments to develop insights into the relationship between the performance metrics of interest and fundamental reservoir/ cap rock properties. Detailed compositional simulations of CO_2 injection into a saline aquifer system are carried out using CMG-GEM® for a broad range of reservoir and cap rock properties.

We consider three different approaches for analyzing the computer simulation results. The first approach uses inspectional analysis to determine dimensionless groups for correlating the data.

The second approach uses an approach similar to that used by Mollaei (2011) in developing a forecasting tool for isothermal EOR and waterflooding, i.e., we use statistical data fitting techniques based on the computer simulation results to establish a relationship between the model output and underlying physical quantities. The third approach (discussed in Appendix II) uses the sharp interface model, modified to account for a flowing two-phase region behind the CO_2-brine interface. We also use the data from numerical experiments to investigate how the pressure difference between a confined system and a semi-confined system can be correlated to such parameters as the storativity ratio– with modifications as needed to account for changes in two-phase effective permeability in the near-wellbore region.

1.5 Organization of the Report

Section 2 gives a compiled review of relevant past work for simplified models of CO_2 sequestration in saline formations. Section 3 details the simulation elements and workflow. Sections 4 and 5 describe the development and validation of our plume migration model and pressure propagation models. Section 6 summarizes our conclusions and some recommendations for future work. Appendix I consists of a compilation of result plots from the reference relative permeability model simulations and data tables for the sake of completeness. Appendix II discusses our modified sharp interface model.

2 Literature Review

Geologic carbon sequestration has been studied as an effective measure to reduce anthropogenic CO_2 emissions for over two decades. CO_2 storage in aquifers or deep saline formations is particularly attractive due to their widespread availability in many sedimentary basins around the world and their large potential storage capacity (IPCC, 2005). Saline formations in North America have a likely storage capacity of the order of 3400 billion tons of CO_2 or the equivalent of hundreds of years of CO_2 emissions (DOE/NETL, 2010).

Ensuring storage integrity requires an understanding of the nature of plume and pressure propagation as the injected CO_2 displaces the native reservoir fluids. An idea of the storage capacity and injectivity is critical in screening and evaluation of the performance of saline aquifer targets for CO_2 sequestration. Numerical simulations are commonly used to evaluate storage capacity and pressure buildup during CO_2 injection (Kumar et al., 2005; Birkholzer et al., 2008; Doughty et al., 2008; Zhou et al., 2010; Pruess et al., 2003). However, comprehensive numerical simulations require extensive characterization and computational effort to evaluate the physically complex multi-phase and multi-component flow effects. Hence, researchers have been seeking (semi)analytical solutions to represent plume migration and pressure buildup during CO_2 injection into saline formations based on the most relevant subsurface processes. The Buckley-Leverett theory (Lake, 1989) indicates that the radial distance travelled by the brine-displacement shock front in a radial system increases as the square root of the time of injection. Kumar and Bryant (2008) have worked on simplified analytical models for the CO_2 plume velocity to predict the maximum lateral distance that the CO_2 plume travels form the injector in the dipping direction of the reservoir. They successfully compare estimates from their simplified models, which are parameterized using the gravity number, to ultimately determine the sequestration efficiency of CO_2 in a confined aquifer compartment. On the other hand, Ghanbarnezhad (2012) presented the Method of Characteristics (MOC) solution of the CO_2 mass conservation equation considering two-phase two-component flow in a 1D homogeneous aquifer in presence of compressibility but no mutual solubility. This solution explained how fast a compressible CO_2 plume would travel along the aquifer's length. He concludes that the velocity of the saturation waves depend on the combination of saturation, fractional flow terms and the slope of the fractional flow curve if the rock compressibility is negligible compared to that of CO_2.

Simplified models for CO_2 plume tracking and aquifer overpressure prediction generally build on the work of Woods and Comer (1962) for obtaining saturation and pressure distributions in a

radial gas-storage aquifer. The Woods-Comer model consists of: (1) a growing gas bubble, where two-phase flow occurs, and (2) the surrounding aquifer, with unsteady-state single-phase flow. They proposed a rapid semi-analytic computational scheme to solve for pressure and saturation as a function of time. Among the earliest efforts to develop a semi-analytical model for the problem of CO_2 injection in deep saline aquifers was by Saripalli and McGrail (2001). They used the Buckley-Leverett frontal advance theory to develop equations describing the growth and spread of CO_2 for radial injection of supercritical CO_2 into aquifers. They treated CO_2 as an immiscible phase, considered dissolution of CO_2 but did not explicitly discuss the issue of pressure buildup within the reservoir or at the injection well. Since injectivity clearly constrains storage capacity, a critical aspect of the design and selection of CO_2 storage systems is the assessment of the pressure buildup associated with the injected volume of CO_2. Birkholzer et al. (2008) demonstrate that considerable pressure buildup occurs in the storage formation more than 100 km away from the injection zone while the actual brine migration distance is much smaller. Alternative approaches to evaluate pressure propagation in the system under consideration are the application of numerical reservoir simulators (Zhou, 2010) and (semi) analytical approaches that have also been worked upon by many as discussed below.

Nordbotten *et al.* (2005) developed an elegant, but idealized, solution for space-time evolution of the CO_2 plume based on arguments of energy minimization. This solution reduces to a simple radial form of the Buckley-Leverett solution under viscous-dominated conditions with linear relative permeabilities. In their work, they show that there are two different time scales, proportional to $\sqrt{t}$, associated with the problem of supercritical CO_2 injection into a deep saline formation. The first corresponds to the diffusive transient pressure pulse propagation, and the second corresponds to the advective movement of the CO_2 front. CO_2 and brine are assumed to be separated by a sharp interface, with the vertical location of the interface being a function of both time and radial distance from the injection well. Mathias *et al*. (2009) built upon the Nordbotten *et al.* (2005) model to prescribe a solution for the pressure distribution in the saline injection formation of infinite lateral extent. A similarity solution was derived using the method of matched asymptotic expansions by solving the two coupled ordinary differential equations for continuity and Darcy's law. Mathias et al. (2011) extended their earlier pressure buildup equations to account for partial miscibility of CO_2 with brine and additionally account for volume change on mixing. However, gravity considerations are excluded from this analysis which breaks down for (thick) reservoirs where gravity segregation effects are exaggerated.

Benson (2003) developed an approximate analytical solution for pressure buildup at CO_2 injection wells based on the assumptions of Buckley-Leverett type displacement, vertical

equilibrium, a homogeneous aquifer, slightly compressible fluid and negligible capillary pressure. The solution consists of two components – (1) steady-state pressure buildup behind the CO_2 front and (2) transient pressure buildup outside of the front. Benson's model can be used for both open and closed systems but does not take into account the possibility of brine dry-out and the creation of a dry CO_2-filled region immediately near the wellbore because of mutual solubility effects.

A major improvement over the Benson (2003) two-region model was presented by Noh *et al.* (2007) where they modified Buckley-Leverett theory to account for mutual solubility of CO_2 and brine. Their analytical approach to characterize the semi-miscible displacement of water by CO_2 conceptualized that two distinct fronts develop when CO_2 is injected (i.e., the drying front and the Buckley-Leverett front) separating the storage formation into three regions – the single-phase CO_2 region or the drying front (documented by Ozah et al., 2005), the two-phase region comprising both brine and CO_2 or the Buckley-Leverett region, and the single-phase brine region. Figure 2-1 shows a conceptualization of the CO_2 saturation profile and pressure profile for this three-region model. Note also that both models are valid only for a simple 1D radial flow problem (i.e., confined aquifer).

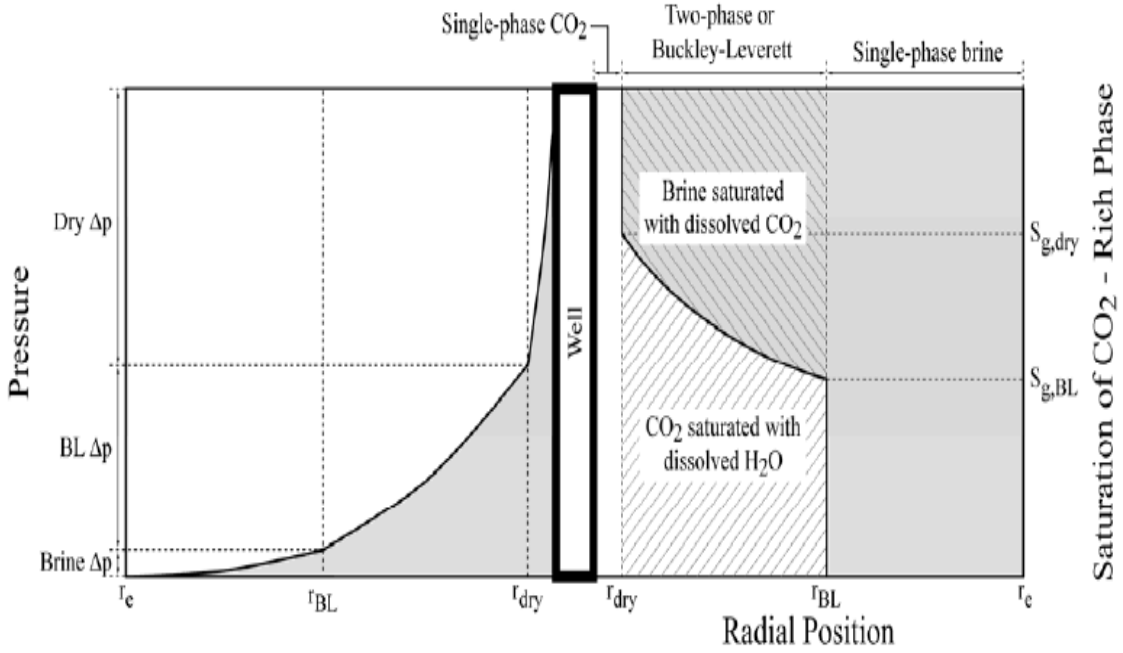

Figure 2-1. Schematic of the three-region model.

Following Noh *et al.* (2007), Figure 2-2 shows how the velocities of the drying front (the trailing shock) and the Buckley-Leverett front (leading shock), as well as the shock saturations, can be

determined from tangents drawn to the fractional flow curve. A simple material balance then yields the radial location of the shock fronts. Other points on the saturation profile can be readily obtained via the Welge construction method (Lake, 1989).

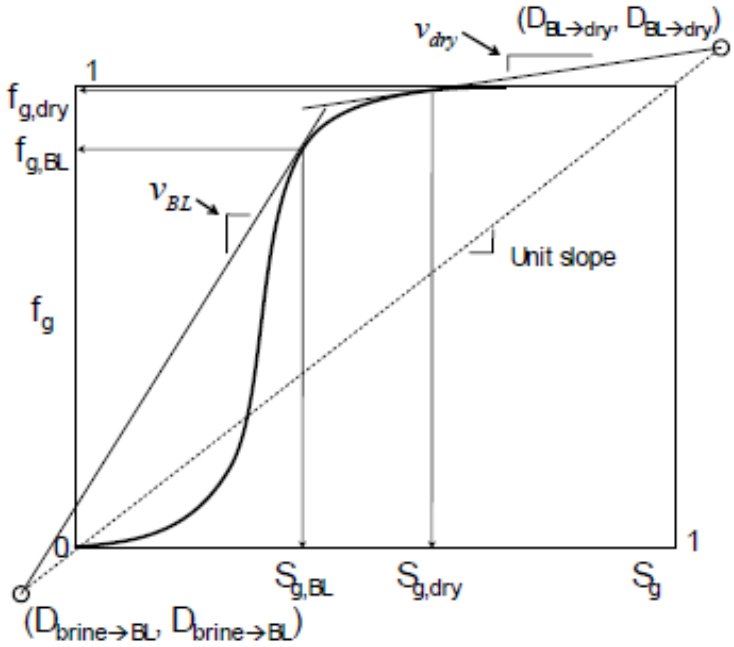

Figure 2-2. Calculation of shock velocities and saturations.

Burton *et al.* (2008) developed the pressure solution for this three-region model by assuming quasi-steady conditions within each region, with single-phase gas and brine mobilities in the two outer regions and an effective mobility (based on the average brine saturation) in the two-phase region used in conjunction with Darcy's law.

Recent semi-analytical models are moving closer to studying more realistic systems. Oruganti and Mishra (2012) proposed a new approach for computing the effective mobility in the two-phase region based on the recognition that the inverse of the mobility varies linearly with distance in the two-phase region. They performed a comprehensive evaluation of the Noh *et al.* (2007) and Burton *et al.* (2008) solutions by benchmarking them to detailed STOMP-CO_2 simulations. They found that in general, the Noh *et al.* (2007) solution for saturation produced reasonable results (Figure 2-3a), but the Burton *et al.* (2008) solution for pressure evolution underpredicted the pressure buildup. Their approach for computing the effective mobility in the two-phase region produced much better agreement with STOMP-CO_2 results (Figure 2-3b).

(a)

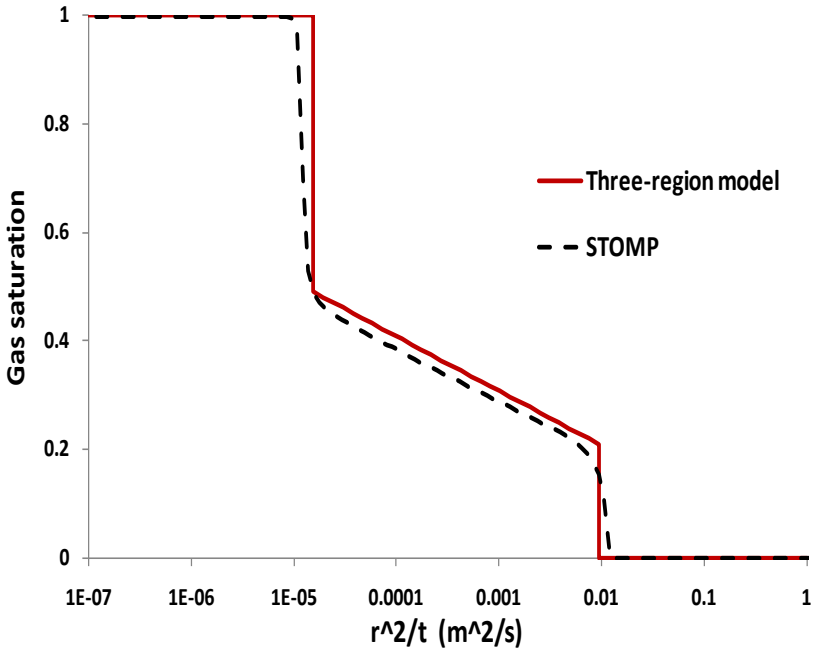

(b)

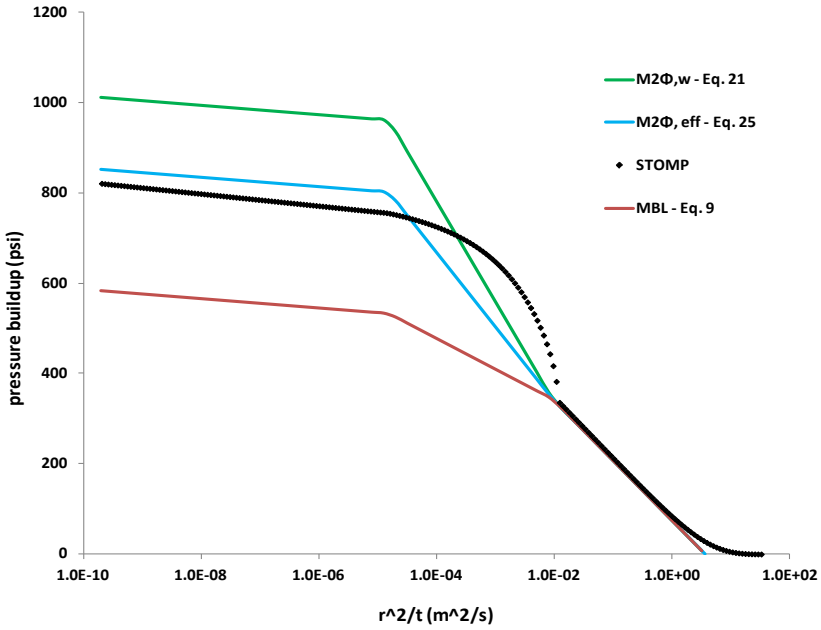

Figure 2-3. Comparison of (a) saturation solutions and (b) pressure solutions.
From Burton et al., 2008, (red line) and Oruganti and Mishra, 2012 (aqua line in b).

While previous mentioned models only considered unbounded systems, Zhou *et al.* (2008) came up with a simple method for quick prediction of the pressure buildup over a given injection period and storage capacity for CO_2 injection in closed and semi-closed saline formations. They define the storage efficiency factor as the volumetric fraction of stored CO_2 per unit initial pore volume of the formation. However their method makes several simplifying assumptions for an

idealized two-dimensional radial formation-seal system (homogeneous reservoir bounded by identical upper and lower homogeneous seals; no dissolution of CO_2, constant compressibility values, uniform pressure buildup) which reasonably match numerical simulation results.

Azizi and Cinar (2013) present analytical models using modified Buckley-Leverett theory to estimate the bottomhole pressure of a vertical CO_2 injection well in a radial, homogeneous, horizontal saline formation. Their work investigates the effect of various formation outer boundary conditions – infinite-acting, closed and constant pressure boundaries, while neglecting the effects of gravity. Considerations including relative permeability, compressibility and solubility help in improved modeling of the bottomhole pressure through the injection period, compared to Mathias *et al.* (2009 and 2011) which underestimate pressures (compared to numerical simulations).

Based on the discussion of previous work presented we can make the following remarks about research needs:

- Impact of reservoir heterogeneity: Heterogeneity impacts the movement and distribution of CO_2 plume in the system (Hovorka *et al.*, 2004).
- Impact of gravity: In practice, CO_2 and brine segregate because of difference between their densities, reservoir anisotropy and reservoir thickness.
- Impact of two-phase flow conditions: Single-phase flow models neglect two-phase flow regime near the injection site and these cannot be used to address the problem of storage integrity.

Keeping these issues in mind, this research seeks to develop simplified physics based approaches to model plume migration and pressure propagation for the problem of CO_2 sequestration in saline formations. Furthermore, the physical system underpinning the modeling will include a more realistic treatment of target injection horizons, viz.: (a) vertical layering and permeability / porosity variations in the reservoir, and (b) semi-confined conditions in the overlying formation.

3 Simulation Elements and Workflow

3.1 Model Inputs

3.1.1 Basic Model

The basic model is that of a single-well injecting supercritical CO_2 into a bounded 2D radial-cylindrical aquifer initially filled with brine. The model domain consists of a porous and permeable heterogeneous reservoir, overlain by a low-permeability cap rock. The top of the cap rock, the bottom of the reservoir and the lateral boundary are all assumed to be no-flow boundaries. The following simulation elements are considered for our system:

- A semi-confining system similar to the Mt Simon sandstone (reservoir) – Eau Claire shale (cap rock) configuration
- Reservoir and cap rock thickness (and variants) similar to that used for the Arches project (Sminchak *et al.*, 2012)
- Reservoir permeability, as well as porosity, (and variants) similar to that used for the Arches project (Sminchak *et al.*, 2012)
- Cap rock permeability and air entry pressure from the Illinois basin project (Zhou *et al.*, 2010)
- Permeability variation and anisotropy ratio assumed over a realistic range
- Injection rates to be varied
- Relative permeability models based on Saadatpoor (2009) and related literature to set variants.

Our model adds vertical heterogeneity considerations in the reservoir along with an overlying cap rock compared to the three-region model (Burton *et al.*, 2008). Compared to the Zhou *et al.* (2010) study, we model two- phase flow conditions and reservoir heterogeneity. Figure 3-1 illustrates the system of interest highlighting the layering and gridding implemented.

The system is divided into 20 vertical layers with 10 layers each for the reservoir and the cap rock. The cap rock is homogeneous while the reservoir rock has heterogeneity incorporated. The example shown in Figure 3-1 has permeability layering with increasing permeability from bottom to the top of the reservoir.

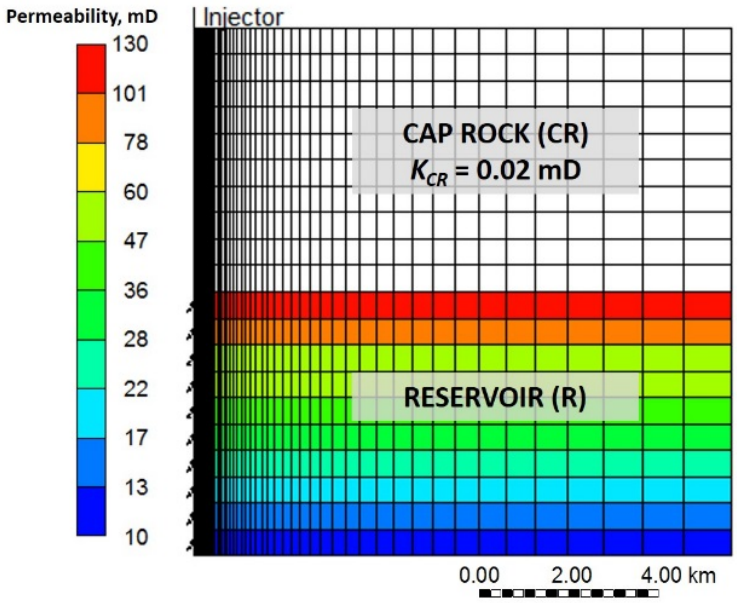

Figure 3-1. Model geometry and gridding for the system of interest.

The system is divided into 20 vertical layers; 10 each for the cap rock and the reservoir. Geometric grid spacing provides higher resolution closer to the injector.

3.1.2 Model Parameterization

A well-defined matrix of full-physics simulations is executed as part of the sensitivity analysis exercise to better understand the dynamics of CO_2-brine displacement. Key model parameters are defined below for a reference case, as well as for "high" and "low" variants. These values are also summarized in the subsection on Simulation Scenarios (see Table 3-1).

3.1.2.1 Thickness

Figure 3-2 shows the relative thickness of the potential reservoir (Mt. Simon) and cap rock (Eau Claire) formations at multiple locations within the ~700 km × 700 km study area for regional CO_2 storage in the Arches province (Sminchak *et al.*, 2012). Based on the thickness ranges observed at these locations, the reference thickness for the reservoir, h_R, is taken to be 150 m, with a low value of 50 m and a high value of 250 m. Similarly, the reference thickness for the cap rock, h_{CR}, is taken to be 150 m, with a low value of 100 m and a high value of 200 m.

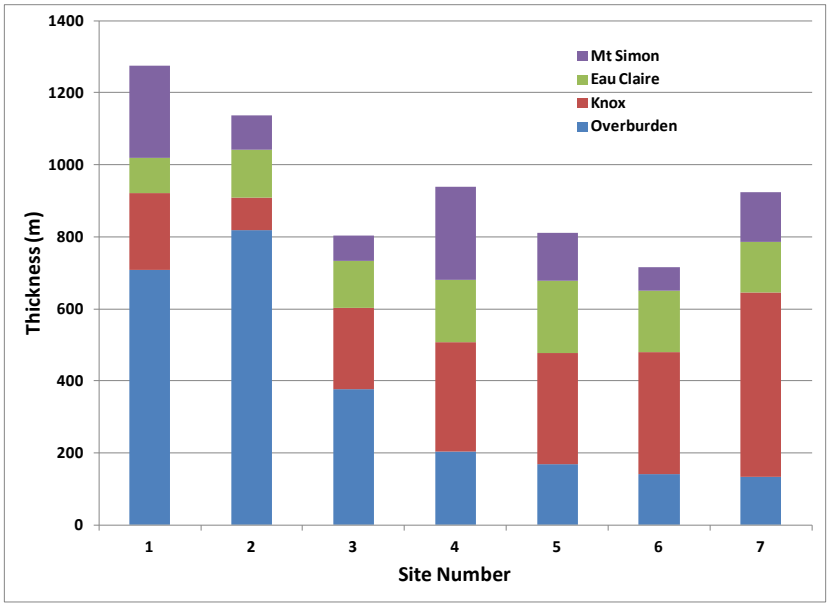

Figure 3-2. Relative thickness of reservoir and cap rock formations from the ARCHES province study.

3.1.2.2 Permeability

A 10-layer representation is selected to characterize permeability variations within the reservoir (k_R). Following Mishra (1987), the Dykstra-Parson's coefficient (V_{DP}) is used as the measure of permeability variation, with a reference value of 0.55 and a geometric mean permeability of 35 mD and a thickness-averaged value of 46 mD. For the low variant, V_{DP} is taken to be 0.35 with a geometric mean permeability of 12 mD and a thickness-averaged value of 12 mD. For the high variant, V_{DP} is taken to be 0.75 with a geometric mean permeability of 106 mD and a thickness-averaged value of 220 mD. The log-normal permeability distributions corresponding to these three variants, calculated using the procedure outlined by Willhite (1982), are shown in Figure 3-3. The individual layer permeability values (in mD) are as follows:

(a) reference case = {130, 80, 60, 48, 38, 32, 26, 21, 15, 10}

(b) low variant = {23, 18, 15, 14, 12, 11, 10, 9, 7, 6}

(c) high variant = {990, 420, 258, 174, 123, 87, 60, 54, 24, 12}.

For the cap rock, the reference permeability (k_{CR}) value is taken to 0.02 mD, with the low and high variants being 0.002 mD and 0.2 mD, respectively. Unlike the reservoir, the cap rock is considered to be homogeneous. Ranges of average permeability values considered for the reservoir and cap rock are consistent with the ranges observed from field data (Sminchak *et al.*, 2012).

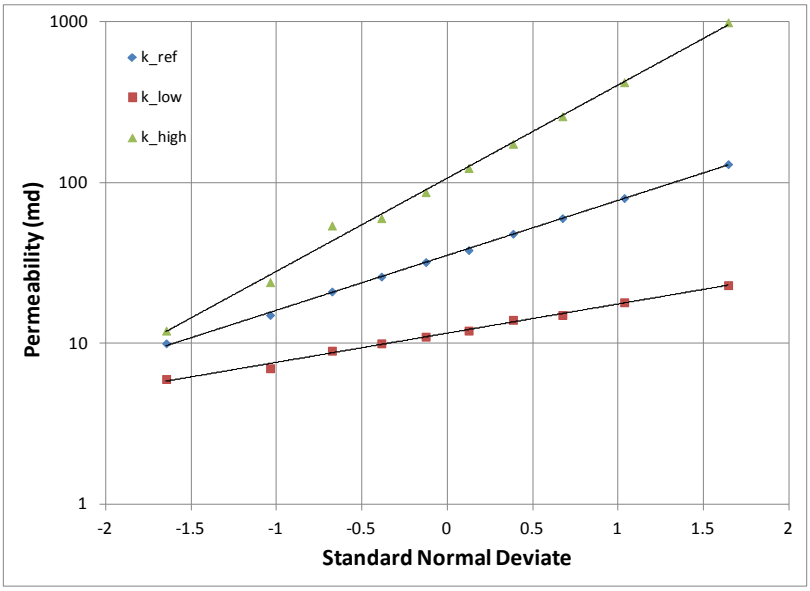

Figure 3-3. Permeability distributions considered for the reservoir.

3.1.2.3 Porosity

For the reservoir porosity (ϕ_R), the reference value is taken to 12 percent, with the low and high variants being 8 percent and 18 percent, respectively. For the cap rock porosity (ϕ_{CR}), the reference is taken to 7 percent, with the low and high variants being 5 percent and 10 percent, respectively. Unlike permeability, porosity variations are not considered in the system. Ranges of average porosity values considered for the reservoir and cap rock are consistent with the ranges observed from field data (Sminchak *et al.*, 2012).

3.1.2.4 Injection rate and system size

The injection rate and system size selected here represent fields capable of handling a range of injection volumes over a 30-year period. The reference case corresponds to a well injecting at 0.83 MMT/yr (total 25 MMT) in the middle of a 6x6 well network covering a 60-km radius area, i.e., with a per-well storage radius of 10 km. The other two variants are: (a) a well injecting at 0.33 MMT/yr (total 10 MMT) in the middle of a 5x5 well network covering a 25-km radius area, i.e., with a per-well storage radius of 5 km, and (b) a well injecting at 1.33 MMT/yr (total 40 MMT) in the middle of a 7x7 well network covering a 49-km radius area, i.e., with a per-well storage radius of 7 km.

Our considerations are comparable to the 5 MMt CO_2 per year (for 50 years) per site in 20 sites with an average site spacing of 30 km considered in Zhou *et al.* (2010). Yamamoto *et al.* (2009) simulated large-scale pressure buildup and brine migration for a storage scenario of 10 MMt CO_2 per year at 10 injection sites in the Tokyo Bay using a model domain of 60 km by 70 km. The Illinois Basin- Decatur Project has been operating at an annual injection rate of 0.36 MMt CO_2 injected into the Mt. Simon sandstone for three years.

3.1.2.5 Capillary pressure model

The reference capillary curves for the reservoir and cap rock are based on mercury injection experiments carried out on representative core samples from the Mt Simon (MS) and Eau Claire (EC) formations (Weatherford, 2011). These curves, converted for an equivalent gas-water system, are shown in Figure 3-4.

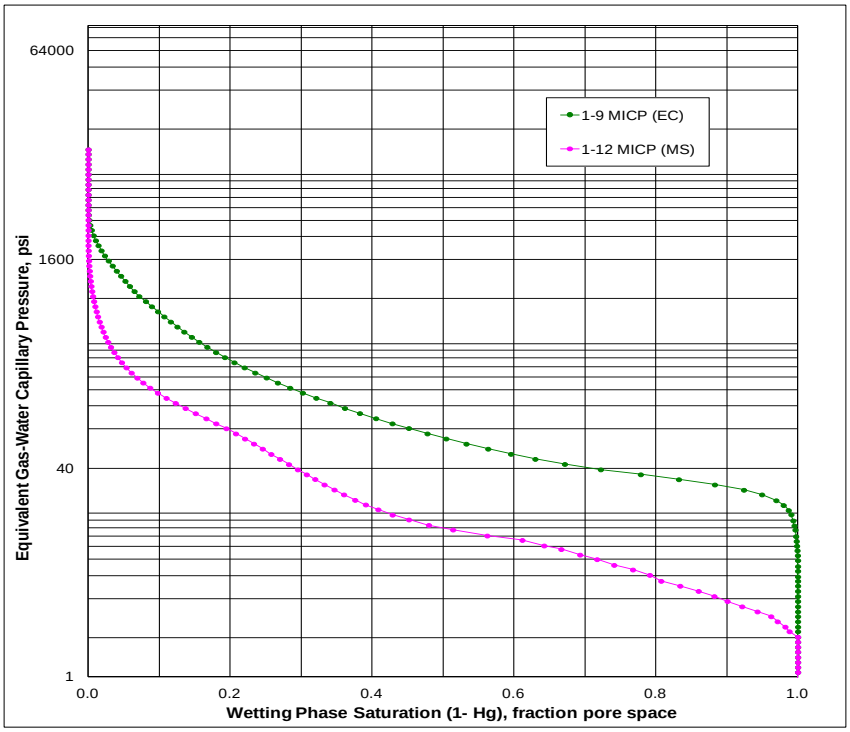

Figure 3-4. Reference capillary pressure curves.

The permeability and porosity values for these samples are 4.2 mD and 10 percent, respectively, for the Mt Simon sample, and 0.25 mD and 8.7 percent, respectively, for the Eau Claire sample. The capillary pressure curves are scaled based on the permeability and porosity assigned to the reference case using Leverett J-scaling (Leverett, 1941):

$$J(S_w) = \frac{p_c(S_w)\sqrt{\frac{k}{\phi}}}{\gamma\cos\theta} \quad (3\text{-}1)$$

where S_w is the water saturation, p_c is the capillary pressure, k is the permeability, ϕ is the porosity, γ is the surface tension and θ is the contact angle.

For the two variants around the reference case, the capillary pressure values for the caprock are increased by a factor of 3 and decreased by a factor of 3 from that used in the reference case. The capillary pressure curve for the reservoir is kept unchanged.

3.1.2.6 Relative permeability model

Relative permeability curves for the reservoir are taken from Saadatpoor (2009), and are assumed to be the same for the caprock. These curves are shown in Figure 3-5.

As far as variations from the reference case, the gas relative permeability curve for the reservoir is assumed to be linear for one of the variants (case A), whereas the other variant (case B) lies somewhere in between. The three separate models provide a range of permeability characteristics for the reservoir model.

3.1.2.7 Anisotropy ratio

The ratio of vertical to horizontal permeability, or the permeability anisotropy ratio, is assumed to be 0.1 for the reference case, and 0.01 and 1.0 for the two variants.

3.1.2.8 Permeability layering

For the reference case, permeability layering within the reservoir is taken to be random. For the two variants, the spatial arrangement of permeability layers is taken to be either monotonically increasing from the bottom, or monotonically increasing from the top. As mentioned earlier, the cap rock is treated as a homogeneous rock body for all cases.

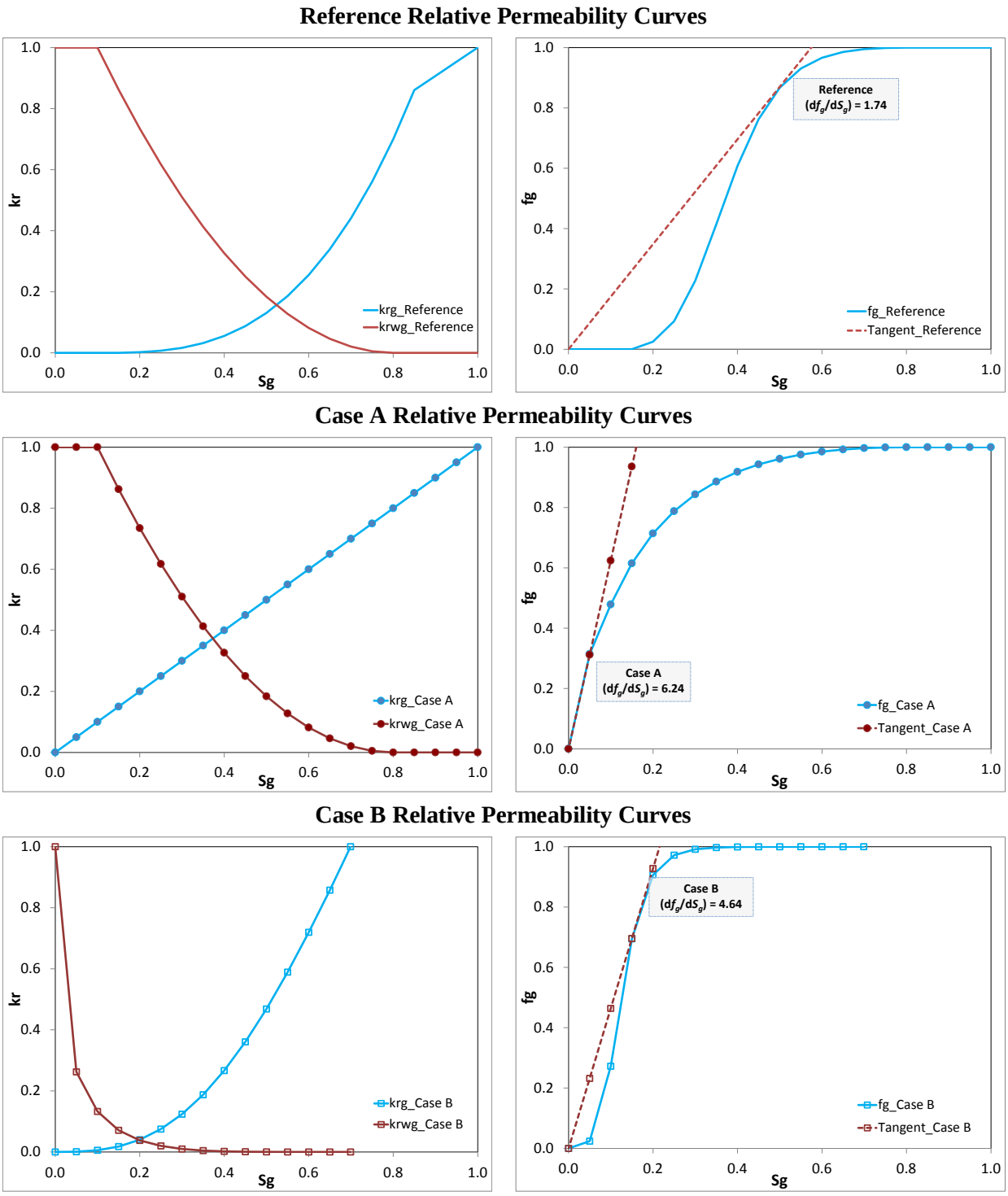

Figure 3-5. Relative permeability model variations considered with different gas-water relative permeability curves.

The figures on the right for each relative permeability model give the slope of the tangent to their respective gas fractional flow curves.

3.1.3 Simulation Scenarios

Table 3-1 includes 10 independent variables. A set of one-off simulations are carried out to develop a library of results from which insights related to the development of simplified-physics based model will be extracted. For each of these simulations, all other independent variables are kept fixed at their reference values. The reference case simulation is identified as Run0. Run1a and Run1b refer to simulations where only the thickness of the reservoir is modified with the low and high variant values (as shown in Table 3-1), and so on. This simulation matrix is run with the three different relative permeability models. Thus, a total of (1 + (10 × 2) × 3 =) 63 simulations covers all one-off parameter variations.

Table 3-1. Summary of test cases explored with parameter values for the reference case and the two variants

				Value			
	Parameter	**Description**	**Units**	**Reference**	**Low**	**High**	**Comments**
1	h_R	Thickness of reservoir	m	150	50	250	
2	h_{CR}	Thickness of caprock	m	150	100	200	
3	$k_{avg,R}$	Average horizontal permeability of reservoir	mD	46	12	220	
	V_{DP}	Dykstra-Parson's coefficient	–	0.55	0.35	0.75	Correlated with $k_{avg,R}$
4	$k_{avg,CR}$	Average horizontal permeability of caprock	mD	0.02	0.002	0.2	
5	k_V/k_H	Anisotropy ratio	–	0.1	0.01	1	
6	Q	CO_2 Injection rate	MMT /yr	0.83	0.33	1.33	
	L	Outer radius of reservoir	km	10	5	7	Correlated with q
7	ϕ_R	Porosity of reservoir	–	0.12	0.08	0.18	
8	ϕ_{CR}	Porosity of caprock	–	0.07	0.05	0.1	
9	$P_{C,CR}$	Capillary pressure model of caprock	–	reference	decrease P_c by 3×	increase P_c by 3×	
10	I_k	Indicator for permeability layering	–	Random	Increasing from top	Increasing from bottom	

3.2 Model Outputs as Performance Metrics

Our choice of output metrics is based on a macroscopic description of subsurface dynamics during CO_2 injection (as opposed to grid-block by grid-block variations in state variables). To this end, the radial extent of CO_2 plume migration and reservoir injectivity help understand CO_2-

brine displacement and pressure propagation in the system, respectively. An attempt has also been made to account for the effect of cap rock on pressure propagation. These metrics serve as performance indicators of CO_2-brine dynamics in any given injection reservoir setting for the purposes of simplified-physics based modeling.

3.2.1 Plume Migration

The CO_2 plume moves further away from the injection well into the reservoir with increasing amount of CO_2 injected. The path followed by CO_2 while displacing the native brine is controlled by mainly the effects of buoyancy (gravity), mobility contrast between the CO_2 and brine and reservoir heterogeneity. Supercritical CO_2, being less dense than brine, generally tends to rise upward while displacing the brine counter-currently. Figure 3-6 shows a system schematic of the plume.

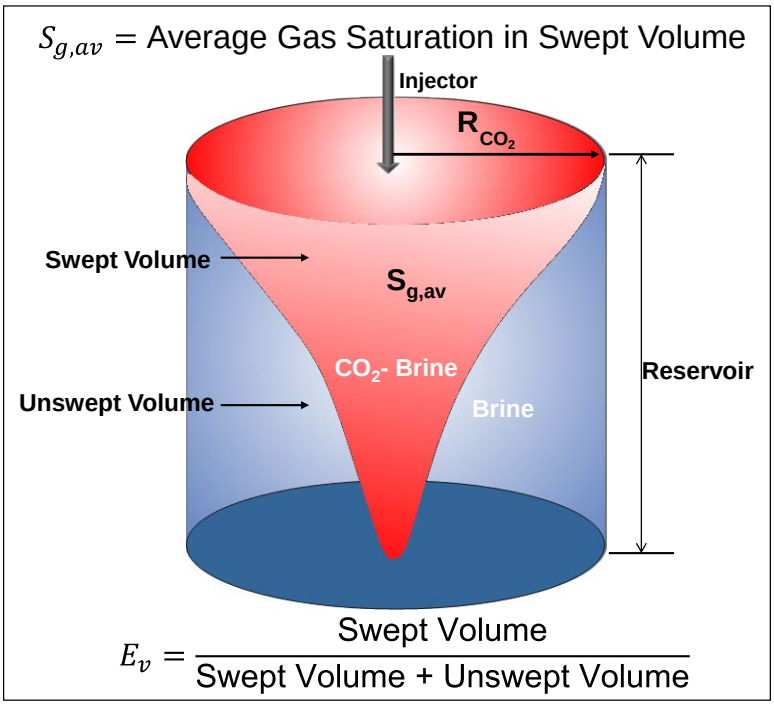

Figure 3-6. System schematic showing graphical definitions of plume extent, volumetric sweep and displacement efficiency for CO_2- brine displacement.

The efficiency of the CO_2-brine displacement process reflects the ability to effectively sequester CO_2 in that reservoir (E_s). It is a product of two factors: (a) volumetric sweep efficiency reflecting the fraction of the total pore volume contacted by CO_2, and (b) displacement efficiency within the pore volume contacted by CO_2. The volumetric sweep efficiency, E_v, is calculated

from the ratio of the actual pore volume contacted by CO_2 to the pore volume corresponding to the maximum extent of the CO_2 saturation front. As the initial gas saturation in the aquifer is zero, the average CO_2 saturation behind the front, $S_{g,av}$, gives the displacement efficiency. The lesser the total storage efficiency, the farther the plume extent would be from the injection well. Figure 3-7 illustrates the typical behavior of the total storage efficiency with time.

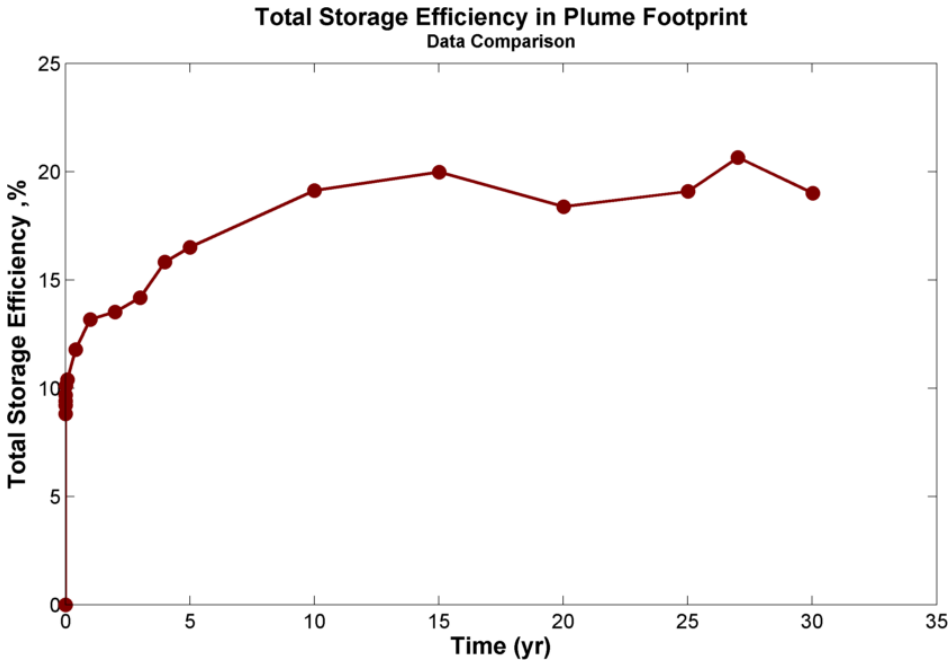

Figure 3-7. Sample plot showing E_s as a function of time.

The maximum radial extent of the CO_2 plume at the end of injection, R, can be expressed as:

$$R^2 = \frac{Q}{\pi \phi_R h_R S_{g,av} E_v} = \frac{Q}{\pi \phi_R h_R E_s} \tag{3-2}$$

where Q is the cumulative volume of CO_2 injected, ϕ_R is porosity, h_R is reservoir thickness, $S_{g,av}$ is the average gas saturation in the two-phase region behind the CO_2-brine front, and E_v is the volumetric sweep efficiency, i.e., the fractional volume contacted by CO_2.

Knowing E_s would thus enable a quick estimation of the maximum spatial extent of the CO_2 plume using equation 3-2.

3.2.2 Reservoir Injectivity

Reservoir injectivity is a critical operational constraint defined as the ratio of the injection rate to the corresponding pressure differential (buildup) in the reservoir. The injectivity is related to the

amount of CO_2 injected and the permeability-thickness of the reservoir. We consistently observe an initial pressure jump (shown in Figure 3-8) when CO_2 begins displacing brine in the reservoir. This initial pressure jump is followed by a transient period of quasi-steady injection well pressure. Once the pressure front reaches the system boundary, any further CO_2 injection causes pressure buildup in the reservoir as expected.

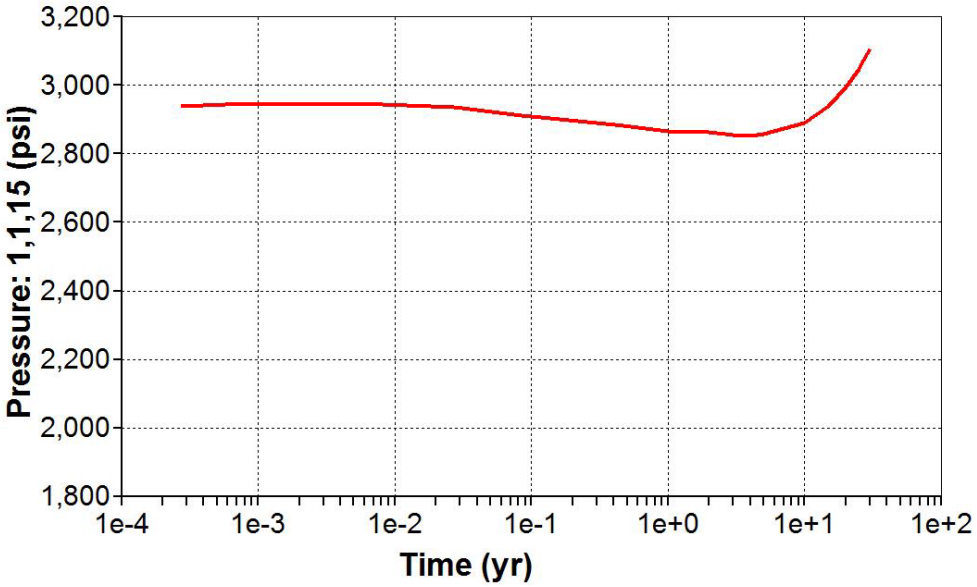

Figure 3-8. Sample pressure values at the injection well as a function of time to illustrate the initial pressure jump.

The initial pressure jump is followed by a period of quasi-steady pressure before boundary effects come into play.

The observed pressure jump can be converted into a dimensionless quantity, P_D, as follows:

$$P_D = \frac{2\pi k_r h}{q\mu_w}\Delta P_{jump} \tag{3-3}$$

where k_R is reservoir permeability, h_R is reservoir thickness, q is volumetric injection rate, μ_w is brine viscosity, and ΔP_{jump} is the minimum observed value of the pressure jump.

Knowing P_D would enable a quick estimation of the injectivity index ($q/\Delta P_{jump}$) of the well using equation 3-3.

3.2.3 Pressure Propagation

Once the boundary effects are felt, the system tends to behave like a closed tank – whereupon the average pressure buildup in the reservoir can be related to the reservoir pore volume and total

compressibility. Figure 3-9 illustrates the typical behavior of the average reservoir pressure (a) and ratio of pressure buildup in the caprock to that in the reservoir (b) with time.

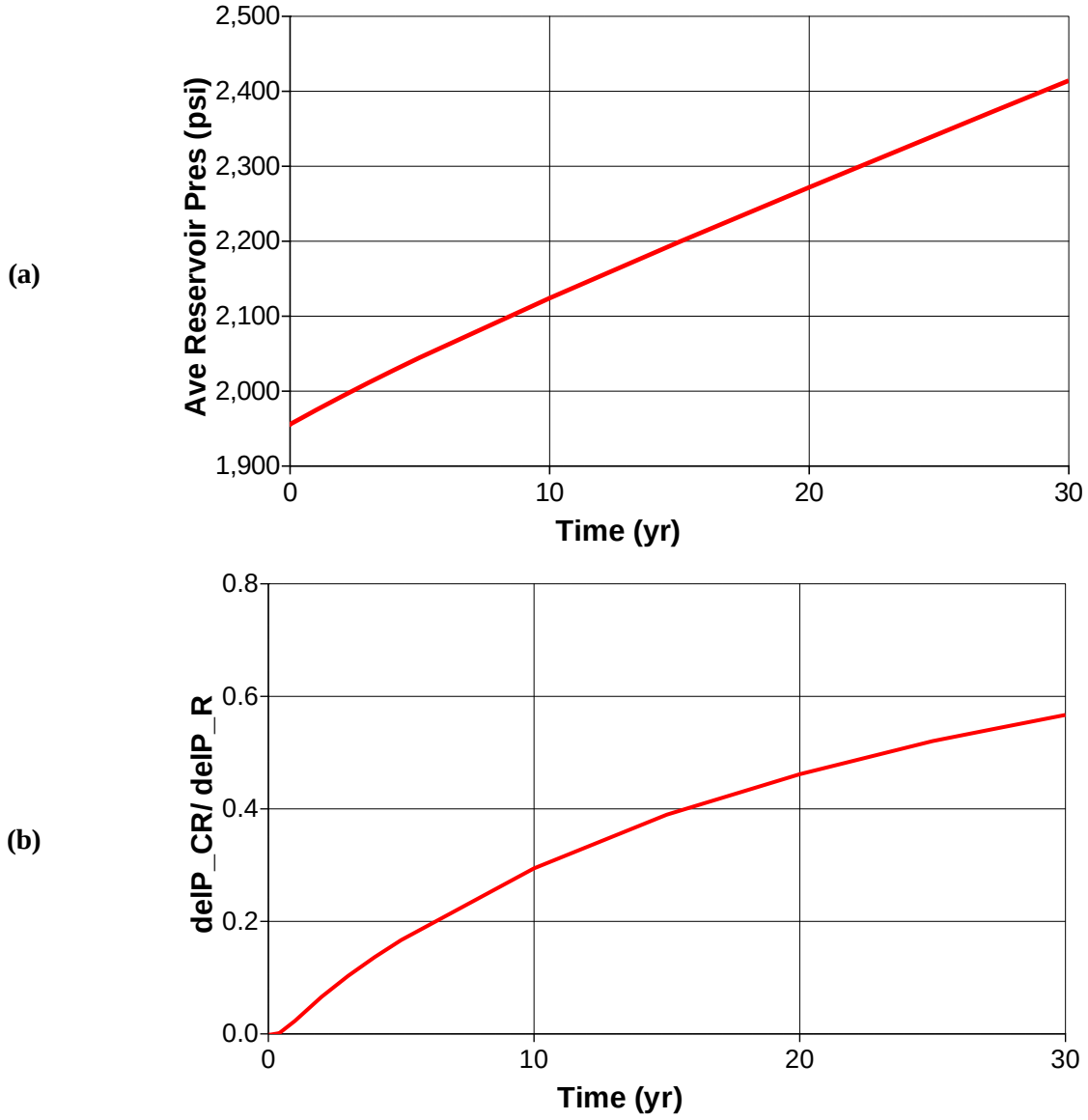

Figure 3-9. Sample pressure profiles to illustrate pressure response to CO_2 injection in the (a) reservoir and (b) the overlying cap rock formation as a ratio of the pressure buildup in the cap rock to that in the reservoir.

We find that any attenuation of pressure from the linear relationship between reservoir pressure buildup and amount of CO_2 injected (i.e., deviation from closed tank behavior) because of the presence of a cap rock (which potentially helps "bleed off" reservoir pressure increase) can be described using a correction term related to the relative thickness of the cap rock in the stratigraphic column. We use the ratio of pressure buildup in the cap rock to the pressure buildup

in the reservoir at the end of injection as the performance metric to determine the effect of the cap rock on pressure propagation in the system.

3.3 Simulator Description

The simulations are executed in the numerical simulator GEM® developed by the Computer Modeling Group (CMG). GEM or Generalized Equation of state Model is a robust, multidimensional and fully compositional reservoir simulator that is widely used as one of the standard simulators to model the flow of three-phase, multicomponent fluids in the industry. GEM utilizes the Peng Robinson or the Soave Redlich Kwong equations of state to predict phase equilibrium compositions and oil and gas phase densities. GEM supports various schemes for computing related properties such as oil and gas viscosities.

Table 3-2. Summary table for fluid properties used in this work

Parameter	Value
Binary interaction co-efficient with respect to H2O (*BIN) for	
CO2	-0.075
H2O	0
Co-efficients used for Pedersen correlation (*VISCOEFF)	
1	0
2	0
3	0.1
4	0.2
5	-1

We use the tuned Peng Robinson equation of state for CO_2 dissolution modeling and model brine as the "oil" phase. Kumar *et al.* (2005) tuned the Peng-Robinson equation of state using experimental data for density and solubility over a wide range of pressures, temperatures and salinities related to aquifer conditions. The corresponding states correlation given in Pedersen *et al.* (1984) was used to calculate the hydrocarbon phase viscosities in GEM that were cross-checked with the NIST database values.

3.4 Analysis Methodology

Our analysis approach is based on a combination of first-principles approach and inspectional analysis from detailed numerical experiments.

- Well-defined compositional simulations of CO_2 injection into a semi-confined saline aquifer system are carried out for a broad range of reservoir and cap rock properties.
- Data from this sensitivity analysis exercise is used to develop insights into the relationship between the performance metrics of interest and fundamental reservoir/ cap rock properties.

- Statistical data fitting techniques are used to establish P_D and E_s as a function of the underlying independent variable groups identified from the sensitivity analysis exercise.
- These predictive relationships are tested using results from other simulations that are not part of the "training set" used for building the regression models.

4 Plume Migration Model

This section gives a detailed description of the workflow involved in developing and validating a simplified physics model to predict plume extent at the end of injection. The predictive model for E_S includes the effect of all the independent variables considered in the sensitivity analysis for robustness. We exclude the sensitivity for capillary entry pressure of the cap rock which has a negligible observed effect on any performance metric due to the scale of the problem setup. We include two more sensitivity cases of the spatial arrangement of the various permeability layers in low and high permeability reservoirs apart from the reference permeability reservoir case. The total number of data points/ simulation cases considered is 60.

4.1 Selection of Dependent Variables

The plume extent is related to the amount of CO_2 injected and the efficiency of CO_2-brine displacement process. We determine the plume extent from the predicted total storage efficiency, E_S, given all other system parameters as explained in Subsection 3.2 (equation 3-2).

To predict the plume extent at the end of the CO_2 injection period, we need the corresponding value of total storage efficiency. The average gas saturation ($S_{g,\,av}$), sweep efficiency (E_v) and hence the total storage efficiency (E_S) are recorded through time during CO_2 injection into the aquifer for all simulation cases. A sample of this time-varying behavior is shown in Figure 4-1.

The average CO_2 saturation behind the CO2-brine interface is the displacement efficiency, and therefore a function of the relative permeability relationship. As such, it does not change with time, as verified by this figure. The sweep efficiency is a function of the size of the system contacted by the injected CO_2. Figure 4-1 shows how the sweep efficiency increases with increasing amount of CO_2 injected into the reservoir until a certain time after which is remains pretty steady. This point in time could be related to when the pressure front reaches the boundary of the system.

(a)

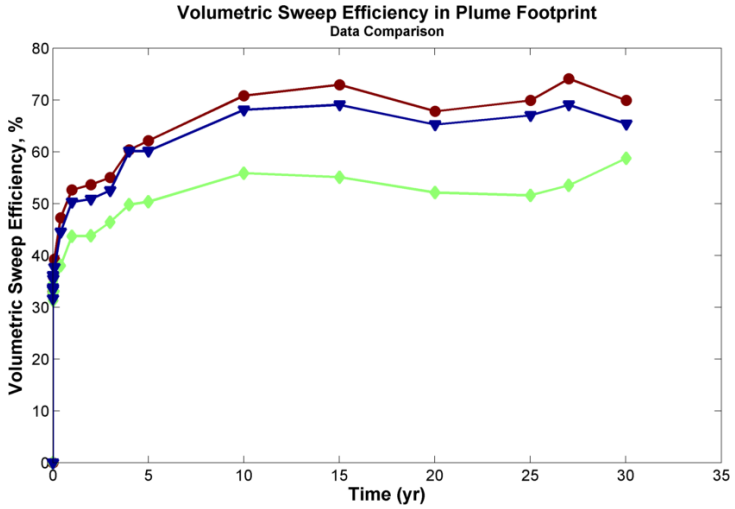

(b)

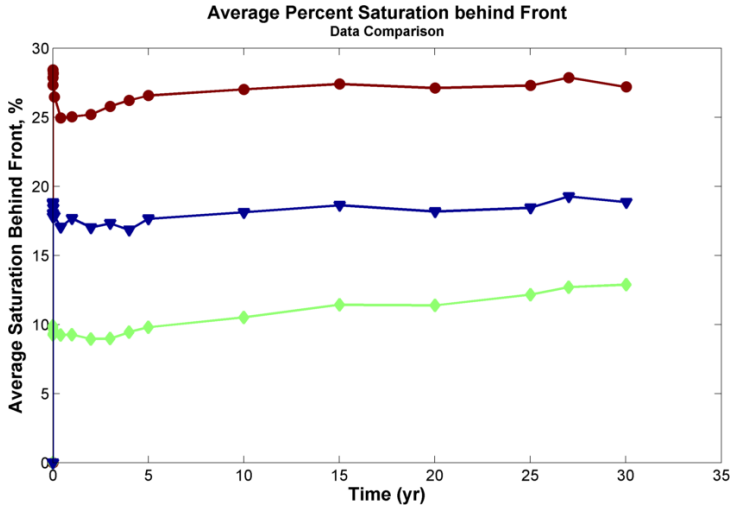

(c)

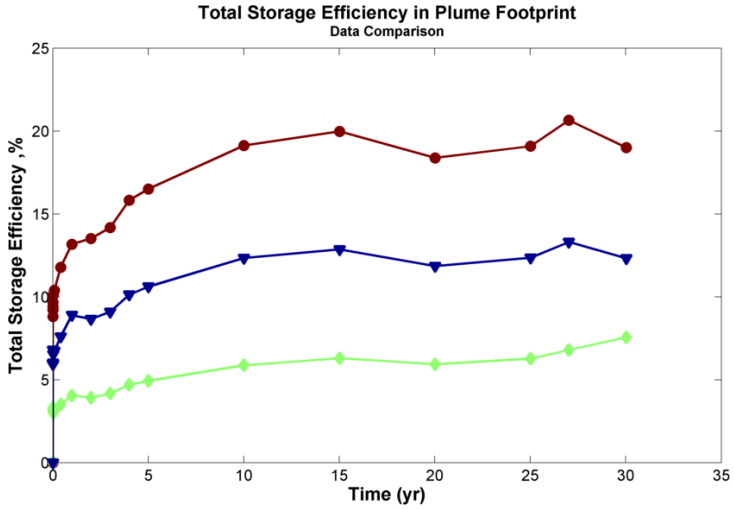

Figure 4-1. Values for (a) E_V, (b) Sg,av, and (c) E_S as a function of time.

Red curve is the reference 0 case; the green and the blue curves are the relative permeability cases A and B, respectively.

4.2 Identifying Independent Variable Groups

Total storage efficiency has been characterized as a function of the following variable groups derived from first principles and the sensitivity analysis exercise:

- Gravity number is a ratio of gravity and viscous effects. We define the dimensionless gravity number while accounting for the reservoir permeability anisotropy as

$$N_g = \frac{(\Delta\rho g h_R) k_R h_R (\frac{h_R}{L})}{q\mu_g \left(\frac{k_V}{k_H}\right)} \tag{4-1}$$

  The definition for gravity number in surveyed literature varies from source to source (Novakovic, 2002). However the fundamental behavior of this number remains the same through all definitions as to when the gravity effects are more pronounced compared to the viscous flow effects (such as in thicker reservoirs) and vice-versa.

- The heterogeneity of the reservoir, in terms of its spatial variation in permeability, is characterized by the Dykstra-Parsons coefficient (Dykstra and Parsons, 1950). It is defined as

$$\mathrm{V_{DP}} = \frac{(\mathrm{k_{50}} - \mathrm{k_{84.1}})}{\mathrm{k_{50}}} \tag{4-2}$$

  where k_{50} is median reservoir permeability and $k_{84.1}$ is reservoir permeability one standard deviation away from the median.

  The Dykstra-Parsons coefficient ranges from 0 to 1 with V_{DP} being null for homogeneous reservoirs and closer to one for extremely heterogeneous ones. The average or mean reservoir permeability is expected to be a known reservoir parameter with a reasonable degree of confidence.

- The heterogeneity of the reservoir can also be characterized in terms of the Lorenz coefficient which is related to the Dykstra-Parsons coefficient. It is defined as *(Lake, 1989):*

$$\mathrm{L_C} = 2\left\{\int_0^1 \mathrm{F_n dC_n} - \frac{1}{2}\right\} \tag{4-3}$$

  where F_n = cumulative flow capacity = $\frac{\sum_{i=1}^{n} k_{Ri} h_{Ri}}{\sum_{i=1}^{N} k_{Ri} h_{Ri}}$

  C_n = cumulative storage capacity = $\frac{\sum_{i=1}^{n} \phi_{Ri} h_{Ri}}{\sum_{i=1}^{N} \phi_{Ri} h_{Ri}}$

  The Lorenz coefficient also ranges from 0 to 1 with L_C being null for homogeneous reservoirs and closer to one for extremely heterogeneous ones. We calculate the Lorenz coefficient by honoring the permeability layering from the bottom-most to the top-most layer of the reservoir.

- Relative permeability model characterized by the slope of the tangent to fractional flow curve, df_g/dS_g. This parameter is related to the speed of propagation of the two-phase front through the reservoir. The slope of the tangent to the fractional flow curve, generally tested using core data, is one of the hardest inputs to obtain for a given reservoir.

Figure 4-2 shows E_S plotted as a function of all four independent variables defined above. As in waterflooding, we see the dependence of the total efficiency on relative permeability. We observe higher df_g/dS_g values tend to have lesser scatter. The effect of reservoir heterogeneity is captured from the dependency of E_s on both the Dykstra-Parsons coefficient and the Lorenz coefficient. Buoyant CO_2 displacing brine is also affected by gravity segregation which is shown from Figure 4-2(c).

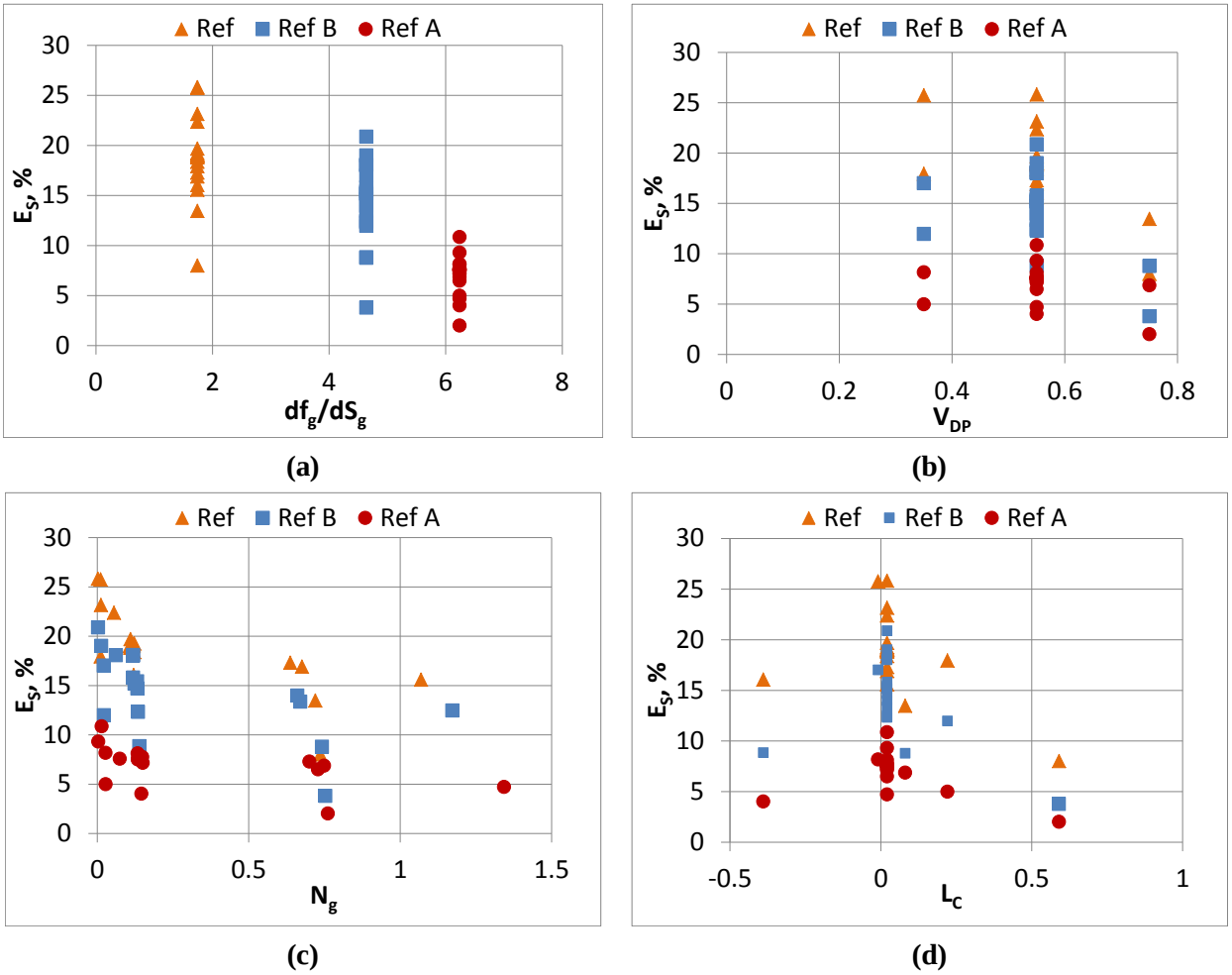

Figure 4-2. Scatter plot matrix of E_S values as a function of all four independent variables: (a) df_g/dS_g, (b) V_{DP}, (c) N_g, and (d) L_C.

4.3 Predictive Model Formulation and Validation

4.3.1 Predictive Model Formulation

The total storage efficiency was determined as a function of the four independent variables identified. A multivariate regression model was obtained for the total storage efficiency (in percentage) given by equation 4-4 below.

$$E_S = 32.7 + 0.522\frac{df_g}{dS_g} - 15.03L_C - 25.8V_{DP} - 12.6N_g + 4.45\frac{df_g}{dS_g}V_{DP} + 51.8L_CN_g - 0.693\left(\frac{df_g}{dS_g}\right)^2 - 53.5(L_C)^2 + 6.35(N_g)^2 \quad (4\text{-}4)$$

4.3.2 Predictive Model Validation

Figure 4-3 shows the agreement between simulated and predicted values of E_S using our model.

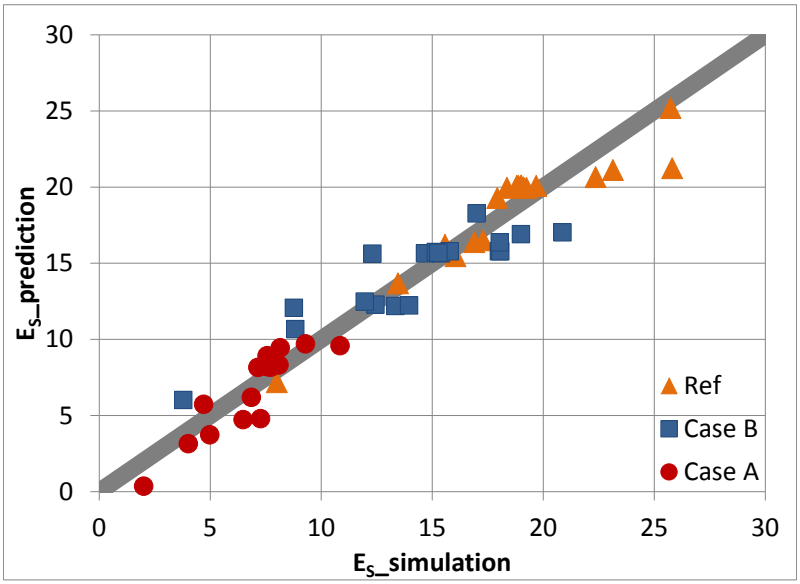

Figure 4-3. Comparison plot of regression model predictions and simulator output values for E_S.

The co-efficient of determination, $R^2 = 0.93$.

We identify variable importance by calculating the R^2-loss and ranking the variables in decreasing order of R^2-loss from the above-described full model for E_s. The R^2-loss for each parameter is calculated by subtracting the R^2 obtained from the full model from the R^2 obtained when that parameter is excluded from the regression. Table 4-1 gives the R^2-loss due to each independent variable.

Table 4-1. R^2-loss due to each independent variable.

	Parameter	R^2- loss
1	df_g/dS_g	0.701
2	L_c	0.058
3	V_{DP}	0.013
4	N_g	0.054

This data set helps analyze the relative importance of each of the independent variables on the total storage efficiency.

4.4 Predicting CO_2 Plume Extent at the End of Injection

The predicted total storage efficiency from equation 4-4 can be used to calculate the CO_2 plume extent for a given amount of CO_2 injected into the reservoir. Figure 4-4 compares the predicted CO_2 plume extents (using predicted E_s in equation 3-2) for our simulations with the plume extents resulting from the respective simulations.

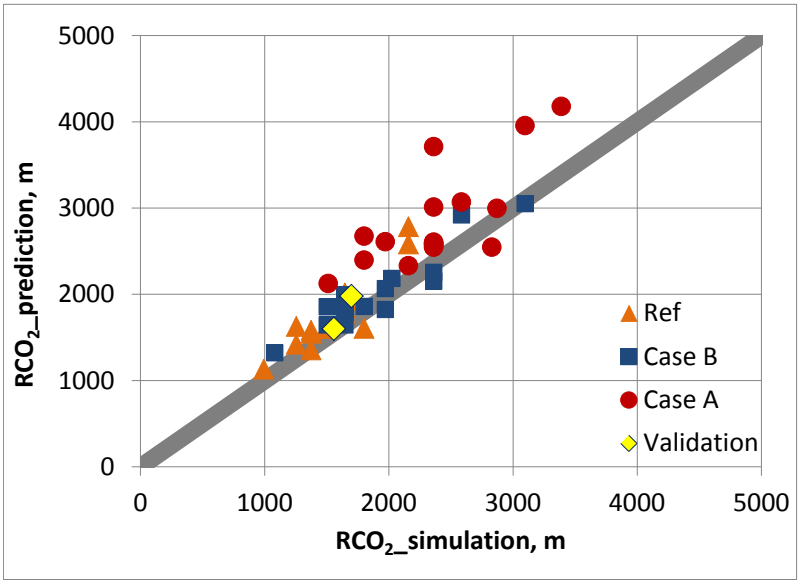

Figure 4-4. Comparison plot for predicted plume radii and plume radii determined from corresponding simulation runs.

Blind validation cases are shown using the red diamond symbols.

The simplified predictive model obtained for total storage efficiency and hence plume radius, is also validated for its robustness with two 'blind' simulation cases that were not part of the regression analysis. Tables 4-2 and 4-3 give the input parameter values and a comparison of the outputs from the simplified model and the simulator respectively.

We find that the plume radius predicted by our model for the first validation case is 1601 m compared to the simulation result of 1557 m. For the second validation case, the plume radius predicted by our model is 1980 m compared to the simulation result of 1670 m. Thus, our simplified model (equation 4-1) can be used to reasonably predict the total storage efficiency and hence determine the ultimate plume extent at the end of CO_2 injection from equation 3-2.

Table 4-2. Table of input values for the blind prediction cases.

	Parameter	Description	Units	Blind Validation No.	
				# 1	# 2
1	h_R	Thickness of reservoir	m	107.7	148.8
2	h_{CR}	Thickness of caprock	m	158.1	112.2
3	$k_{avg,R}$	Average horizontal permeability of reservoir	mD	18.46	58.25
	V_{DP}	Dykstra-Parson's coefficient	–	0.4119	0.5828
4	$k_{avg,CR}$	Average horizontal permeability of caprock	mD	0.0165	0.0156
5	k_V/k_H	Anisotropy ratio	–	0.0472	0.2482
6	q	CO_2 Injection rate	MMT/yr	1.33	1.33
	L	Outer radius of reservoir	m	7500	7500
7	ϕ_R	Porosity of reservoir	–	0.1304	0.1451
8	ϕ_{CR}	Porosity of caprock	–	0.0697	0.0795
9	I_k	Indicator for permeability layering	–	Increasing from bottom	Increasing from bottom
10		Relative permeability model		Reference	Reference

Table 4-3. Comparison of output values for the blind prediction case using the simulator and simplified predictive model.

	Parameter	Description	Units	Model Prediction		Simulator Result	
				Case 1	Case 2	Case 1	Case 2
1	E_S	Total storage efficiency	%	23.9	16.6	22.5	18.9
2	R_{CO2}	Plume radius at end of CO_2 injection	m	1601	1980	1557	1670

Thus, our simplified model (equation 4-1) can be used to predict the maximum plume extent with reasonable confidence at the end of a given amount of CO_2 injected into the reservoir.

4.5 Summary

In order to use the predictive model for plume extent we need to determine the input sources for each of the independent variables involved. Hence we establish a relationship for maximum plume extent at the end of injection as a function of the amount of CO_2 injected and the

storativity (porosity-thickness product) of the reservoir, for a given total storage efficiency. The most important terms in the simplified model for total storage efficiency involve the relative permeability model followed by the reservoir heterogeneity. Of the four independent variables, the porosity, thickness (from logs) and permeability are assumed to be known for any given reservoir. Dykstra-Parsons coefficient can be calculated with the knowledge of the permeability distribution in the reservoir obtained from well logs. Typical values of the Dykstra-Parsons coefficient found in literature lie between 0.5 and 0.7. The Lorenz coefficient is related to V_{DP} and can be obtained from knowledge of the spatial arrangement of permeability in the vertical layers. The slope of the tangent to the fractional flow curve is one of the hardest inputs to obtain for a given reservoir. In the absence of core data to test with, we encourage the user to use a lower and upper bound for the df_g/dS_g values from our study. This would yield an expected range of values for the injectivity.

5 Pressure Propagation Models

This section gives a detailed description of the workflow involved in developing and validating simplified physics models to predict injection well and formation pressure buildup. The predictive models include the effect of all the independent variables considered in the sensitivity analysis for robustness. We exclude the sensitivity for capillary entry pressure of the cap rock which has a negligible observed effect on any performance metric due to the scale of the problem setup. We include two more sensitivity cases of the spatial arrangement of the various permeability layers in low and high permeability reservoirs apart from the reference permeability reservoir case. The total number of data points/ simulation cases considered is 60.

5.1 Dimensionless Injectivity Evaluation

Injectivity, the ratio of the amount of fluid injected to the corresponding pressure change in the reservoir, is a critical metric of system performance for any injection operation. We determine a simplified physics model for minimum dimensionless pressure buildup at the injection well as a function of key reservoir and fluid properties. This model is then used to predict the injectivity (using equation 3-3) in similar layered aquifer systems, given their respective system parameters.

Equation 3-3 can be re-written for injectivity as:

$$J = \frac{q}{\Delta P_{jump}} = \frac{2\pi k_r h}{P_D \mu_w} \tag{3-3}$$

We describe the process of formulating and validating the predictive model for CO_2 injectivity below.

5.1.1 Selection of Independent Variables

As noted in Section 3, we observe from all sensitivity analysis simulations that there is always an initial pressure jump followed by a transient period of quasi-steady injection well pressure which is necessary to allow CO_2 to begin displacing brine in the vicinity of the wellbore. Once the pressure front reaches the lateral boundary of our system, further CO_2 injection causes pressure buildup in the reservoir as expected. Figure 5-1 shows the typical pressure at the injection well with time, illustrating the initial pressure jump observed.

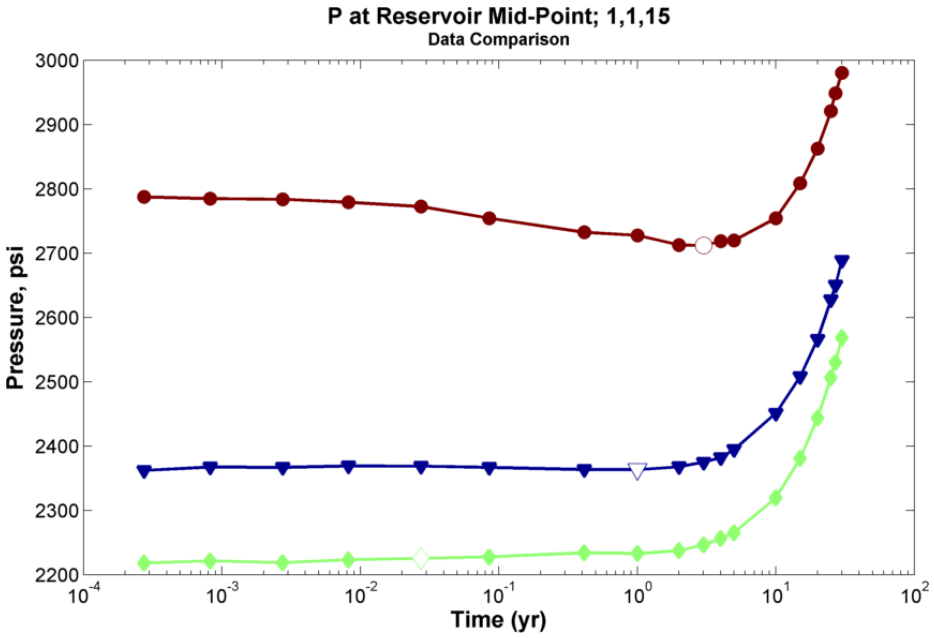

Figure 5-1. Pressure values at the injection well as a function of time.

Red curve is the reference 0 case while the green and blue curves are the relative permeability cases A and B, respectively. The initial pressure jump observed at the well is followed by a transient period of fairly constant pressure before boundary effects come into play.

The pressure jump at the well can be converted into a dimensionless quantity (P_D) using equation 3-3. Knowing P_D would enable a quick estimation of the injectivity index of the well (i.e., injection rate for a given pressure differential or vice-versa). We start with the initial observed pressure jump after 0.3 days of injection and compare it to the minimum pressure buildup at the well. Figure 5-2 shows the minimum value of P_D compared to the 0.3 day P_D value.

For most cases, we find that these two values agree well with each other as the pressure is steady at the injector after the jump at 0.3 days (Figure 5-1) until the pressure front reaches the boundary of the system. The minimum value of pressure buildup is used in further analysis to provide a conservative value of the injectivity.

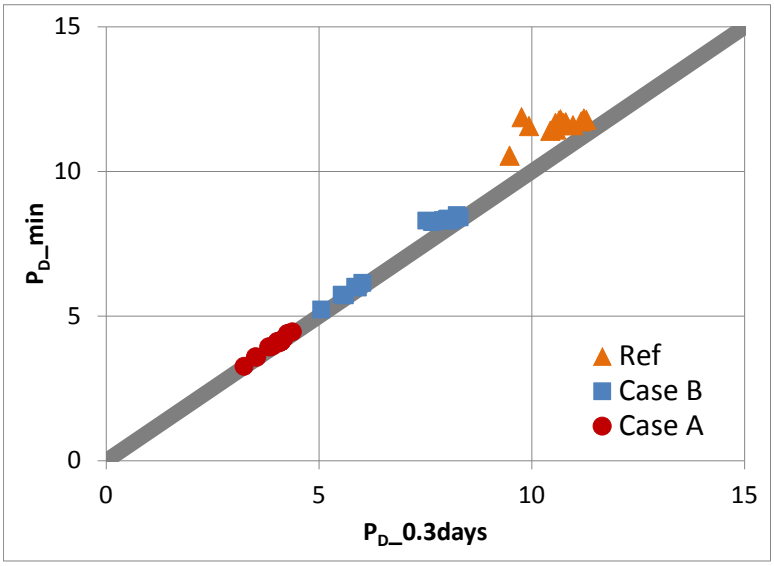

Figure 5-2. Comparison of minimum P_D values and the corresponding 0.3 day P_D values.

5.1.2 Identifying Key Independent Variable Groups

Independent variables such as thickness, porosity, permeability of the reservoir and caprock, spatial arrangement of the vertical permeability layers in the reservoir, permeability anisotropy (ratio of vertical to horizontal permeability) in the reservoir and the CO_2 injection rate have been varied to study sensitivity to pressure buildup (ΔP_{jump}) at the injection well. The total number of data points/ simulation cases considered is 60. Figure 5-3 is a simple spider chart representation of the result of this sensitivity analysis. The reference case is represented by 0 value on the X-axis while the low and high cases for each independent variable are indicated by -1 and +1 respectively on the X-axis. The change in the pressure buildup for each case is plotted on the Y-axis. Hence, the pressure buildup at the injector is the most sensitive to the variables that give the highest slopes in this figure.

The pressure jump for all relative permeability models is impacted most by the injection rate and the permeability-thickness product of the reservoir. The dimensionless P_D value hence calculated has been characterized as a function of the following variable groups derived from the sensitivity analysis exercise (as with the analysis for total storage efficiency in Section 4):

- Relative permeability model characterized by the slope of the tangent to fractional flow curve, df_g/dS_g
- Dykstra-Parson's co-efficient, V_{DP}.

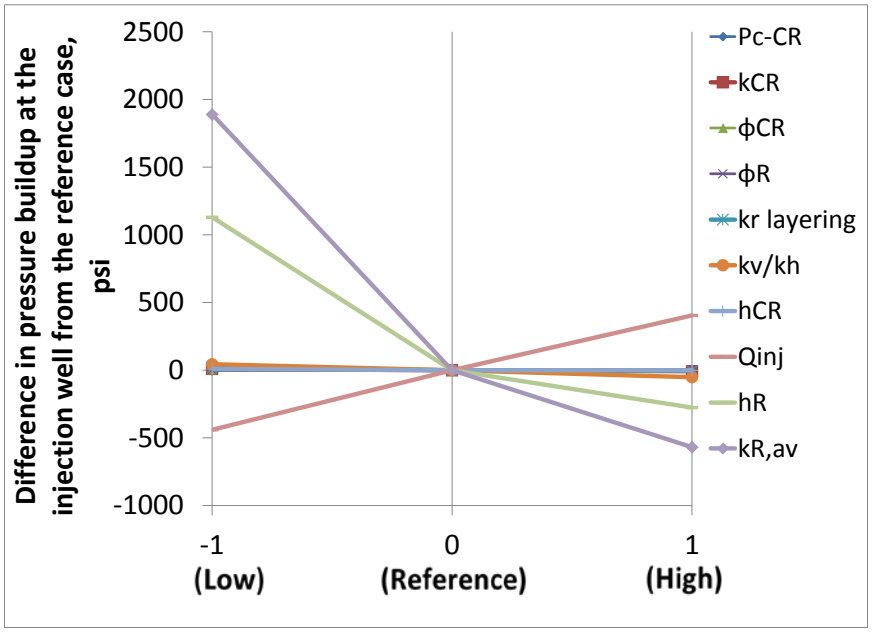

Figure 5-3. Spider chart showing sensitivity of minimum pressure buildup at the injector to various rock properties for the reference relative permeability model.

The reference case is indicated by 0 while the low and high cases for each independent variable are indicated by -1 and +1 respectively on the X-axis. Dominant variables give the highest slopes in this representation.

Figure 5-4 shows a scatter plot matrix of the dimensionless pressure jump, P_D, versus the slope of the fractional flow curve, df_g/dS_g and the Dykstra-Parsons coefficient. Scatter in the data in the figure shows the interrelationship of P_D with df_g/dS_g and V_{DP}.

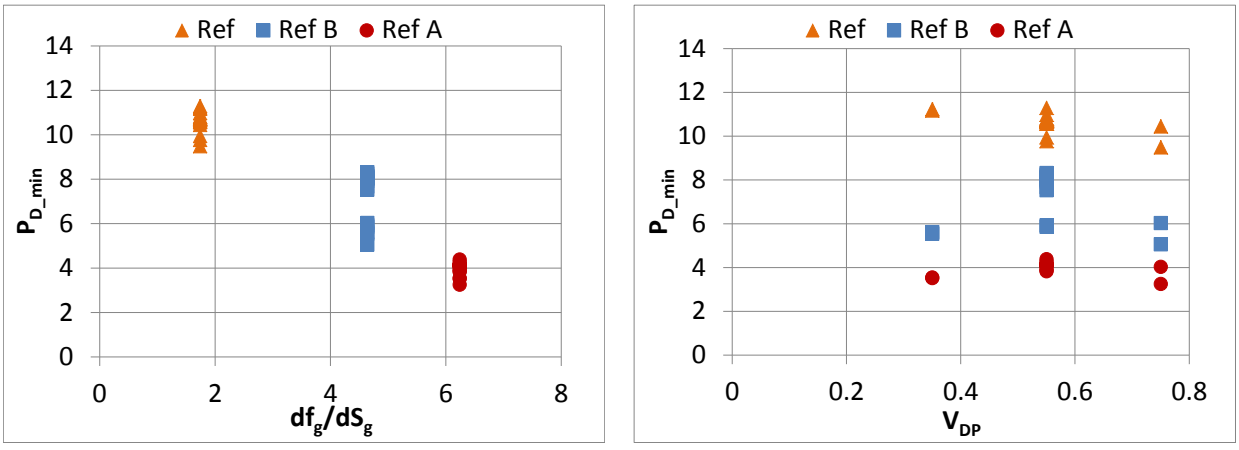

Figure 5-4. Scatter plot matrix of P_D values for varying df_g/dS_g and V_{DP}.

The scatter in data shows that P_D values are interrelated between the two independent variables.

5.1.3 Predicting Dimensionless Pressure Buildup

5.1.3.1 Predictive model formulation

A multivariate regression model was obtained for the dimensionless pressure buildup similar to that for E_S described in Section 4. Equation 5-1 gives the simplified model for dimensionless pressure buildup obtained.

$$P_D = 10.3 + 0.59\frac{df_g}{dS_g} + 3.41V_{DP} + 1.23(\frac{df_g}{dS_g})V_{DP} - 0.342\left(\frac{df_g}{dS_g}\right)^2 - 8.89{V_{DP}}^2 \qquad (5\text{-}1)$$

5.1.3.2 Predictive model validation

Results of the successful comparison between simulated and predicted values of P_D using our model (equation 5-1) are shown in Figure 5-5.

This model compares well with the simulated pressure buildup values but with a few random outliers in relative permeability model case B.

We identify variable importance by calculating the R^2-loss and ranking the variables in decreasing order of R^2-loss from the above- described full model for P_D. Table 5-1 gives the R^2-loss due to each independent variable.

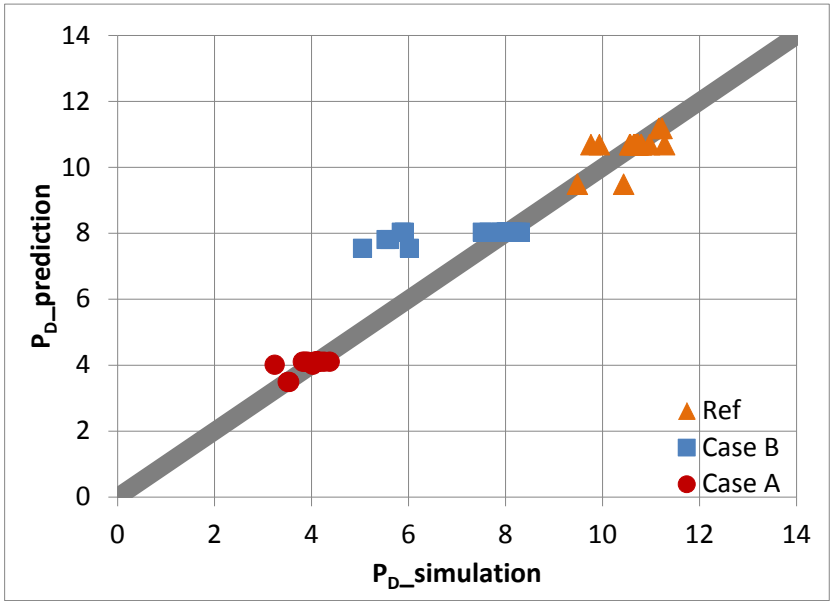

Figure 5-5. Comparison plot between regression model predictions and simulator output values for P_D.

The co-efficient of determination, R^2 = 0.93.

Table 5-1. R^2-loss due to each independent variable.

	Parameter	R^2- loss
1	df_g/dS_g	0.91
2	V_{DP}	0.015

This data set helps analyze the relative importance of each of the independent variables on the dimensionless pressure buildup.

5.1.4 Predicting Reservoir Injectivity

Injectivity index ($q/\Delta P_{jump}$) of the well is calculated from the dimensionless pressure buildup using equation 3-3. Figure 5-6 compares the predicted injectivities from our model with the injectivities calculated from our simulation dataset. The equivalence between the model predictions and the simulations for injectivity thus demonstrates our model performance.

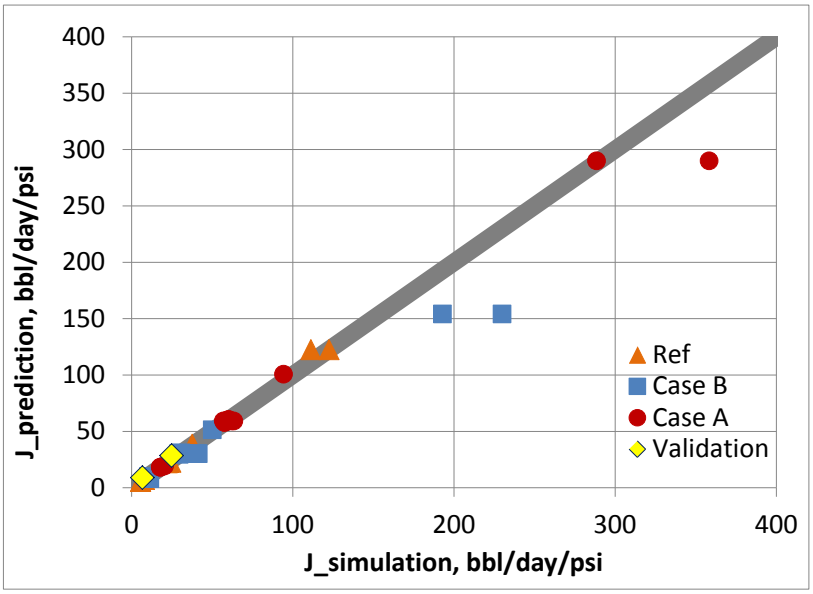

Figure 5-6. Comparison plot showing the equivalence between regression model predictions and simulator output values for injectivity, i.e. ($Q/\Delta P$).

Blind validation cases are shown using the red diamond symbols.

The simplified predictive model obtained for dimensionless pressure buildup and hence for CO_2 injectivity, is also validated successfully for its robustness with the earlier two 'blind' simulation cases (parameter values not part of the regression analysis). We find that the injectivity predicted by our model for the first validation case is 8.9 bbl/day/psi compared to the simulation result of

6.7 bbl/day/psi. For the second validation case, the injectivity predicted by our model is 28.5 bbl/day/psi compared to the simulation result of 24.8 bbl/day/psi. Thus, our simplified model (equation 5-1) can be used to reliably predict the CO_2 injectivity and hence determine the CO_2 injection rate for a given target pressure differential or alternatively, the pressure differential resulting from injecting CO_2 at a target rate.

5.1.5 Comparison with Field Data

Here we describe the analysis of data from Battelle's CO_2 sequestration field demonstration projects as a practical application of our predictive model. We have field data for injectivity and reservoir properties (such as permeability and formation thickness) for four different injection tests: (1) injection into the Copper Ridge dolomite formation at the AEP Mountaineer site, (2) injection into the Rose Run sandstone formation at the AEP Mountaineer site, (3) injection into the Bass Island dolomite formation at the Michigan Basin site, and (4) injection into the Mount Simon sandstone at the East Bend site. Figure 5-7 compares field data with our simulation dataset, plotted as the permeability thickness against the injectivity index, J=q/ΔP. The trends of the field data are in general agreement with the simulated data, approximately along a line of J ~$(0.1k_Rh_R)$ for the field data. The scatter in the data around this trend can be attributed to relative permeability and heterogeneity, as described next.

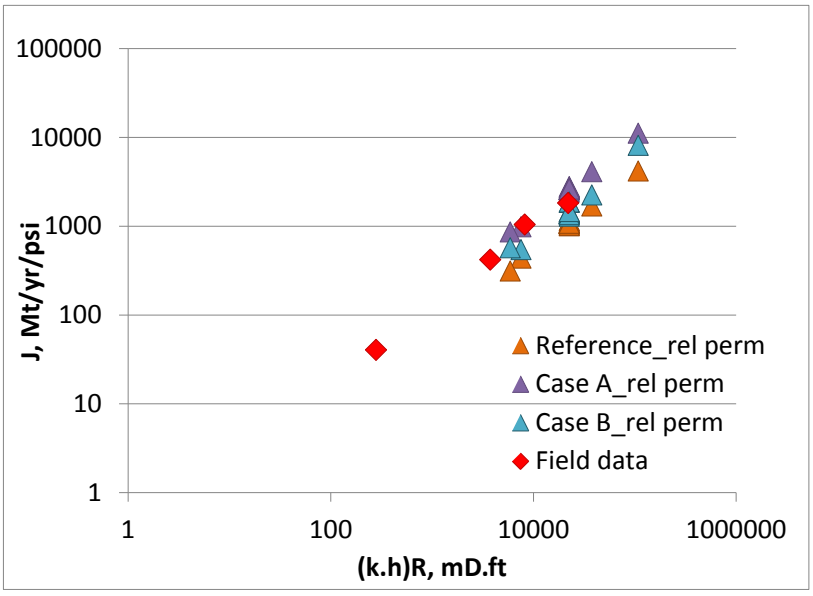

Figure 5-7. Plot illustrating the correspondence between field data and the simulation dataset.

The injectivity is plotted against permeability-thickness product of the reservoir on a log-log scale. Field injectivity values are seen to vary as $(0.1k_Rh_R)$.

Using this field data in comparison with our simulation dataset, we establish uncertain system parameters such as the relative permeability model. Assuming a V_{DP} of 0.55 for the each of the field sites, we can calculate the df_g/dS_g from equation (5-1). Table 5-2 gives the calculated df_g/dS_g values for the four field sites. This process helps us deduce system properties and hence reduce their uncertainty for use in any further reservoir analysis during characterization or optimization of the reservoir under consideration.

Table 5-2. Deduction of relative permeability models for reservoirs using our predictive model for dimensionless pressure buildup.

	Field Site	P_D	V_{DP} (assumption)	Calculated df_g/dS_g
1	Copper Ridge, AEP Mountaineer	8.56	0.55	4.33
2	Rose Run, AEP Mountaineer	4.84	0.55	5.98
3	East Bend, Mt Simon sandstone	3.37	0.55	6.47
4	MI Basin, Bass Island dolomite	3.08	0.55	6.56

Hence we establish a robust relationship for injectivity as a function of the permeability-thickness product of the reservoir, brine viscosity, slope of the tangent to the gas fractional flow curve and the Dykstra-Parsons coefficient. Of these independent variables, the permeability and thickness are assumed to be known for any given reservoir. Brine viscosity can be calculated using reservoir salinity, pressure and temperature data. Dykstra-Parsons coefficient can be calculated with the knowledge of the permeability distribution in the reservoir obtained from well logs. Typical values of the Dykstra-Parsons coefficient found in literature lie between 0.5 and 0.7. The slope of the tangent to the fractional flow curve is one of the hardest inputs to obtain for a given reservoir. In the absence of core data to test with, we encourage the user to use a lower and upper bound for the df_g/dS_g values from our study. This would yield an expected range of values for the injectivity.

5.2 Average Pressure Evaluation

5.2.1 Average Pressure Buildup in Closed Systems

For single phase flow in closed systems, the dimensionless form of the radial diffusivity equation simplifies to

$$P_D = 2\pi t_{DA} \tag{5-2}$$

where dimensionless pressure (P_D) is given in SI units by

$$P_D = \frac{kh(\bar{P}-P_i)}{q\mathrm{B}\mu} \tag{5-3}$$

and dimensionless time (t_{DA}) based on the drainage area, A, is given in SI units by

$$t_{DA} = \frac{kt}{\emptyset\mu c_t \mathrm{A}} \tag{5-4}$$

We calculate and plot the P_D versus t_{DA} data for all three relative permeability model cases in closed reservoirs. Figure 5-8 gives a comparison of the same for all three cases with respect to equation 5-2.

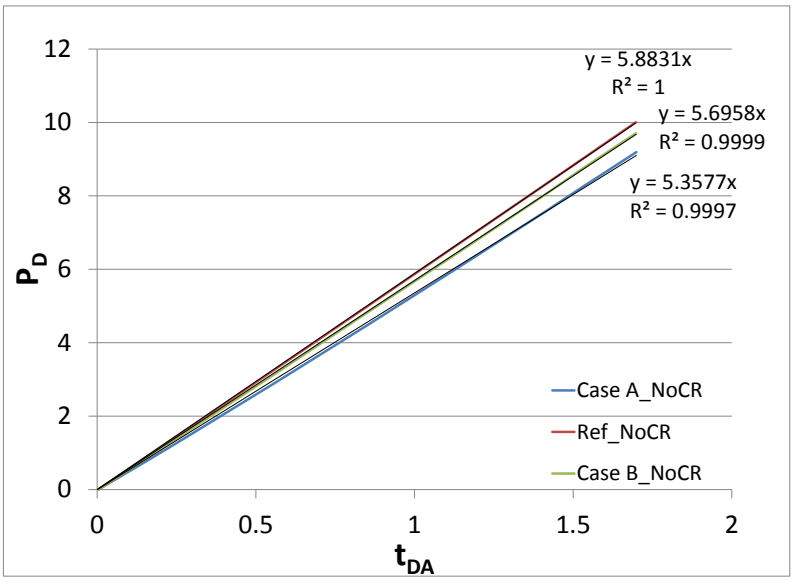

Figure 5-8. P_D versus t_{DA} for each of the three relative permeability models.

The deviation in the slope from (2π) in the above plot for our simulations is attributed to the effects of two-phase flow and the relative permeability models. This slope factor that quantifies the deviation from (2π) is denoted by '*f*' for each case. Table 5-3 lists the '*f*' for each of the three relative permeability models.

Table 5-3. Summary of *f* values for closed reservoir cases with each of the three relative permeability models.

	Relative Permeability Model	Slope of Tangent to Gas Fractional Flow Curve	Slope Value in P_D versus t_{DA} Plot	'f' Value
1	Reference	1.74	5.8831	0.9363
2	Case A	6.24	5.3577	0.8527
3	Case B	4.64	5.6958	0.9065

We attempt to quantitatively characterize this slope factor in the next subsection.

5.2.2 Characterizing 'f' in Closed Systems

As defined earlier, the deviation in slope from (2π) in the plot of P_D versus t_{DA} for closed systems is denoted by the slope factor '*f*'. Hence equation 5-2 can be re-written for our purposes as

$$P_D = f.2\pi t_{DA} \tag{5-5}$$

We characterize '*f*' as a function of the effectiveness of two-phase flow in the reservoir. This is dependent on the relative permeability model as well as the two-phase displacement dynamics itself. A proxy for the effectiveness of this displacement is the plume extent in each case. Hence we determine '*f*' to be directly related to the ratio of the reservoir boundary to the plume extent. Table 5-4 gives the values used in the correlation.

Table 5-4. Values for closed reservoir cases used in the '*f*' factor correlation for each of the three relative permeability models.

	Relative Permeability Model	Slope of Tangent to Gas Fractional Flow Curve	'f' Value	R_{CO2}, m
1	Reference	1.74	0.9363	1374.3
2	Case A	6.24	0.8527	1972.2
3	Case B	4.64	0.9065	1504.2

The '*f*' value for each relative permeability model is correlated to the square of the ratio of the reservoir radius to the plume radius at the end of injection. The reservoir radius is 10 km for all three cases. Figure 5-9 depicts this relationship at the end of 30 years of CO_2 injection in closed reservoirs.

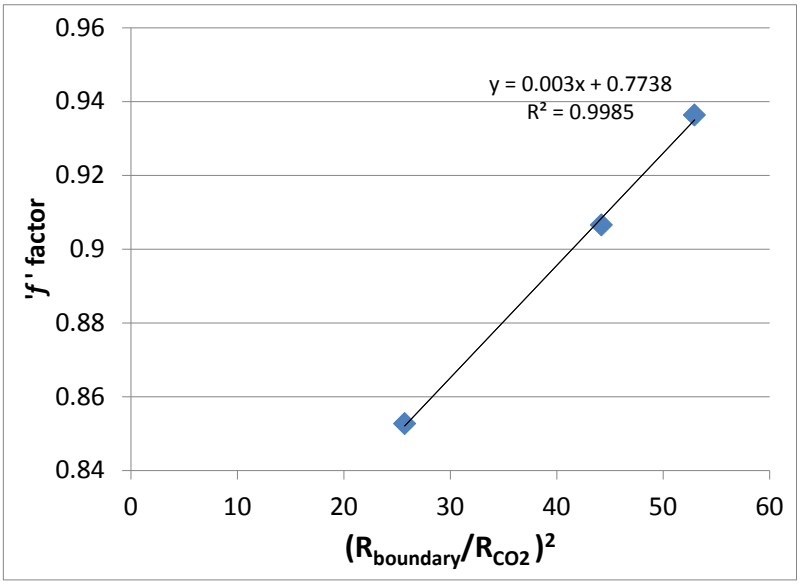

Figure 5-9. The '*f*' factor for closed reservoirs is correlated to the square of the ratio of the reservoir radius to the plume radius at the end of injection.

This factor accounts for the effectiveness of two-phase flow in the reservoir.

We thus find the slope factor to be

$$f = 0.003\left(\frac{R_{boundary}}{R_{CO2}}\right)^2 + 0.774 \tag{5-6}$$

The next step in this analysis is to determine the effect of reservoir and cap rock properties on '*f*'' in semi-confined systems.

5.2.3 Effect of 'f' on Varying Reservoir and Cap Rock Properties

This analysis determines the effect of different reservoir and cap rock properties on '*f*''. For semi-confined systems equation 5-5 becomes

$$P_D = f_{SC}.f.2\pi t_{DA} \tag{5-7}$$

We expect that 'f_{SC}' changes with varying storage capacity of the rock for each relative permeability model. All the simulation cases for all three relative permeability models have been analyzed to study the effect of rock properties on the slope factor. The 'f_{SC}' factor is thus found to be directly correlated with the ratio of the porosity-thickness of the reservoir to the total porosity-thickness of the system, i.e.

$$f_{SC} = \frac{\emptyset_R h_R}{\emptyset_R h_R + \emptyset_{CR} h_{CR}} \tag{5-8}$$

We summarize the results for each relative permeability model in Figure 5-10.

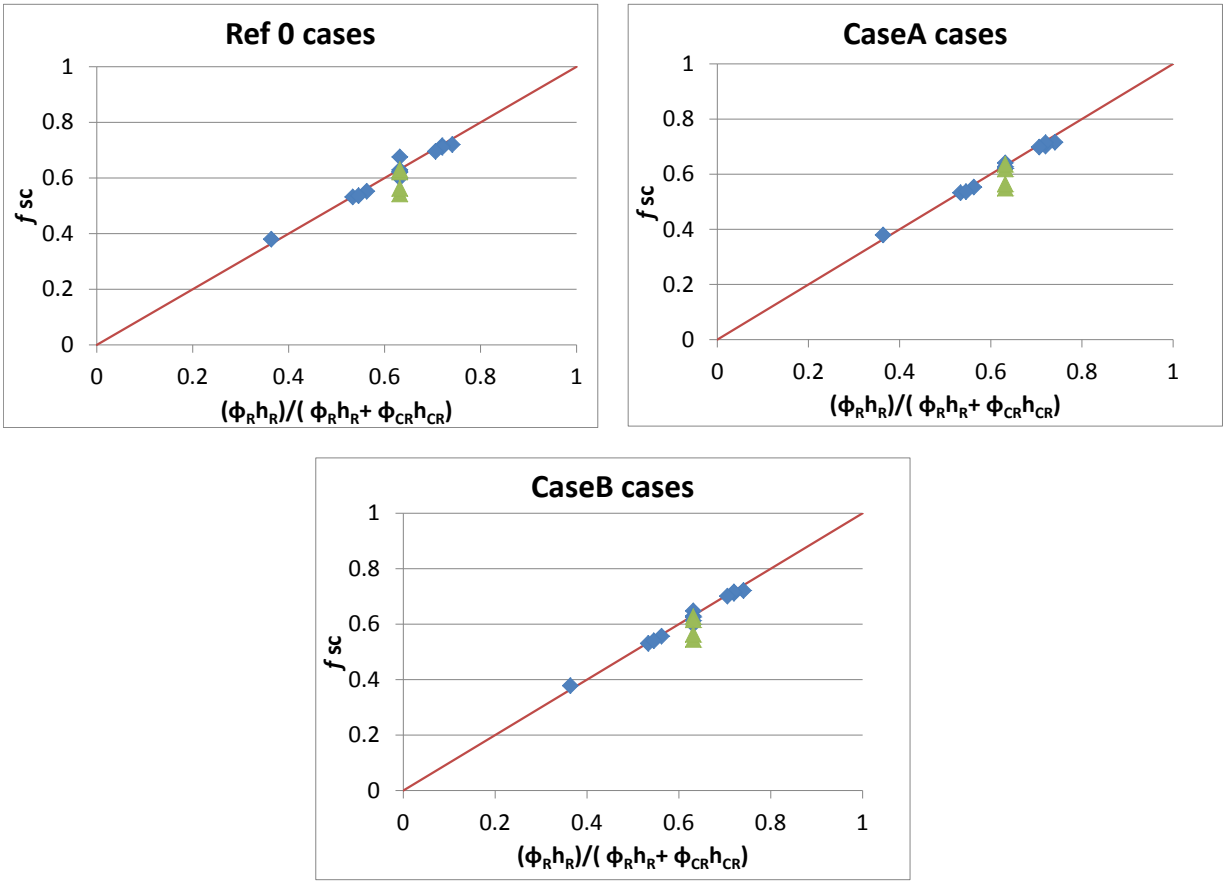

Figure 5-10. Plot illustrating equivalence of f_{SC} and ratio of porosity-thickness of the reservoir to the total porosity-thickness of the system (cap rock + reservoir) for all three relative permeability models.

5.3 Effect of Cap Rock on Pressure Buildup

We analyze pressure behavior in the cap rock (vs. pressure behavior of the reservoir) using a combination of dimensionless groups and regression analysis as with performance metrics like the total storage efficiency and injectivity. We consider a scenario where the overlying cap rock can potentially help dissipate part of the pressure buildup due to CO_2 injection into the reservoir and evaluate the effect of its thickness and permeability on pressure response in the system.

5.3.1 Selection of Independent Variables

Our system is set up such that the cap rock helps dissipate part of the pressure buildup due to CO_2 injection in the reservoir. We vary the permeability and thickness of the cap rock both of

which play a major role in its effectiveness as a "seal" for storage integrity within its underlying reservoir.

We use a constant cap rock permeability of 0.02 mD and vary its thickness from the reference case with 150 m thick cap rock overlying our reservoir rock to study the effect of the cap rock on the pressure buildup in the cap rock and reservoir at the end of injection. The three cap rock thickness variants from our reference case, for the same reservoir properties, were:

- No cap rock
- Thinner cap rock: 100 m thick
- Thicker cap rock: 200 m thick

Similarly, for the same underlying reservoir, the cap rock thickness is held constant at 150 m while we vary the cap rock permeability to study the effect of the cap rock on the pressure buildup in the cap rock and reservoir at the end of injection. The two cap rock permeability variants from our reference case with 0.02 mD cap rock, for the same reservoir properties, were:

- Low permeability cap rock = 0.002 mD
- High permeability cap rock = 0.2 mD

Hence we obtain 6 data points including the reference case for each of the three relative permeability models giving a total of 18 data points for this analysis.

For the same 150 m thick reservoir, we observe the effect of the overlying cap rock thickness and permeability on the pressure buildup in the system during CO_2 injection into the reservoir. We quantify this effect using the ratio of the pressure buildup in the cap rock to the reservoir. Figure 5-11 illustrates the typical time-varying behavior of this pressure buildup ratio during 30 years of CO_2 injection.

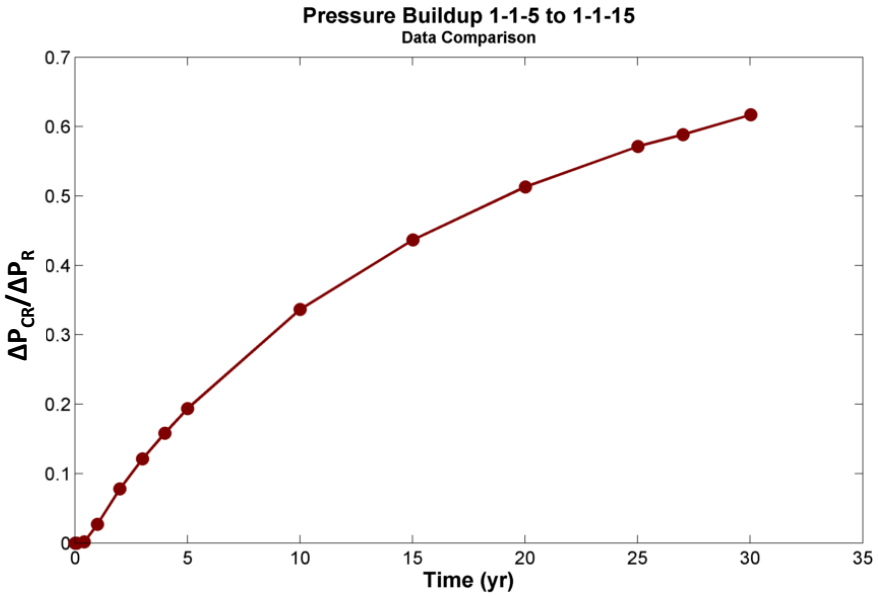

Figure 5-11. Plot of the ratio of pressure buildup in the cap rock to that in the reservoir as a function of time for the reference relative permeability case.

5.3.2 Predicting Ratio of Pressure Buildup in Cap Rock and Reservoir

5.3.2.1 Predictive model formulation

The ratio of pressure increase in cap rock and reservoir at the end of CO_2 injection can be expressed as a function of the ratios of the thickness and permeability of cap rock and the reservoir by simple multi-variate regression analysis as:

$$\frac{\Delta P_{CR}}{\Delta P_R} = 0.1 + 1.02\frac{h_{CR}}{h_R} + 0.028\left(\frac{h_{CR}}{h_R}\right)\left(\frac{df_g}{dS_g}\right) + 1657\left(\frac{k_{CR}}{k_R}\right)\left(\frac{h_{CR}}{h_R}\right) - 1.109\left(\frac{h_{CR}}{h_R}\right)^2 - 3.48\times 10^5\left(\frac{k_{CR}}{k_R}\right)^2 \quad (5\text{-}9)$$

5.3.2.2 Predictive model validation

Figure 5-12 shows the comparison between the above defined predictive model and simulation output for the ratio of the pressure increase in cap rock to that in the reservoir at the end of 30 years of injection.

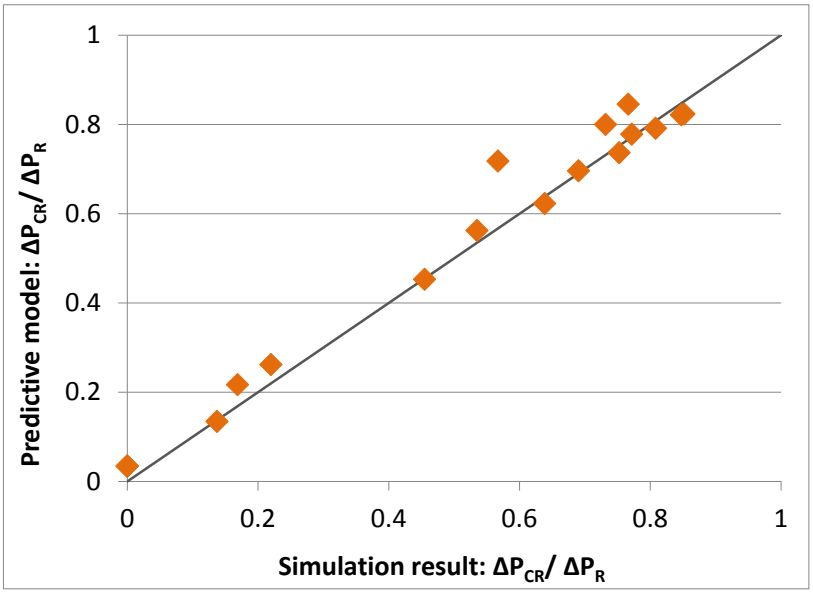

Figure 5-12. Comparison plot of regression model predictions and simulator output values for ratio of pressure increase in the cap rock to that in the reservoir.

The co-efficient of determination, $R^2 = 0.98$.

5.4 Summary

5.4.1 CO_2 Injectivity Model

We determine the dimensionless pressure buildup at the CO_2 injector well to be a function of df_g/dS_g and V_{DP}. CO_2 injectivity, which is the ratio of amount of CO_2 injected to the corresponding pressure buildup, is inversely proportional to the dimensionless pressure buildup. CO_2 injectivity can be calculated from the simplified model for P_D using equation 3-3. This performance metric is critical to determine operational constraints of pressure buildup or injection rate for allowable injected volume of CO_2 or operating pressure constraints respectively.

5.4.2 Average Pressure Buildup Evaluation

We evaluate the average pressure behavior in the reservoir for a given amount of CO_2 injected. We determine that the effectiveness of two-phase flow in a given reservoir depends on an '*f*' factor. For closed reservoirs, this '*f*' factor (which is a function of the relative permeability) is correlated to the square of the ratio of the reservoir radius to the plume radius at the end of injection. When an overlying cap rock is present, this '*f*' factor is modified to account for the relative storage capacity of the rock, i.e. ratio of reservoir storativity to the total system storativity.

5.4.3 Pressure Buildup Ratio Dependence on Cap Rock Properties

We also evaluate the effect of the overlying cap rock properties – mainly thickness and permeability, on the pressure buildup in the system. The ratio of the pressure buildup in the cap rock to that in a given reservoir at the end of injection was determined as a function of the cap rock properties. This pressure buildup ratio was expressed as a function of the ratios of the thickness and permeability of cap rock and the reservoir by a simple multi-variate regression model.

Thus, our simplified models provide us with a reasonable understanding of the effect of different system properties on pressure propagation. Using the basic physical processes involved, these models can be used to reasonably predict the pressure propagation in both the reservoir and the cap rock resulting from injecting a given amount of CO_2.

6 Conclusions

Validated simplified modeling tools can be valuable assets for rapid feasibility and risk assessment in preliminary CO_2 injection project screening and implementation phases. These tools will: (a) provide project developers with quick and simple tools to screen sites and estimate monitoring needs, (b) provide regulators with tools to evaluate geological storage projects quickly without running full-scale detailed numerical simulations, (c) enable integrated system risk assessments to be carried out with robust, yet simple to implement, reservoir performance models, and (d) allow modelers to efficiently analyze the impact of variable CO_2 injection rates on plume migration and trapping for optimal well placement and rate allocation.

Our research objective is to develop and validate simplified physics based models for CO_2 sequestration in deep saline formations. The study involved an extensive parameter space covering different reservoir and cap rock properties. We successfully develop and validate simplified physics models for the following performance metrics in a 2D stratified aquifer-cap rock system specifically: (a) outer extent of CO_2-brine interface from the total storage efficiency, (b) CO_2 injectivity from pressure buildup at the injection well, (c) average reservoir pressure buildup, and (d) pressure increase in the reservoir and the cap rock.

Thus, our simplified models provide us with a reasonable understanding of the effect of different system properties on pressure and saturation (plume) propagation. Using the basic physical processes involved, these models can be used to quantitatively predict the performance metrics of interest in both the reservoir and the cap rock resulting from injecting a given amount of CO_2.

7 Acknowledgments

This work was supported by U.S. Department of Energy National Energy Technology Laboratory award DE-FE0009051 and Ohio Development Services Agency grant D-13-02. We thank our colleagues Dr. Samin Raziperchikolaee and Dr. Rodney Osborne for their technical review of our report.

8 References

Azizi, E., and Cinar, Y., 2013. Approximate Analytical Solutions for CO_2 Injectivity Into Saline Formation. Paper SPE-165575 published at SPE J. Reservoir Evaluation & Engineering, May 2013.

Benson, S. M., 2003. Pressure buildup at CO_2 injection wells, Second Annual Conference on Carbon Sequestration, Alexandria, VA, May 5–8.

Benson, S. and Cook, P., 2005. Underground geological storage, Carbon Dioxide Capture and Storage, 431 pp., Chapter 5.

Birkholzer, J., Zhoue, Q., and Tsang, C., 2008. Large-scale impact of CO_2 storage in deep saline aquifers: A sensitivity study on pressure response in stratified systems. Int. J. Greenhouse Gas Control 3, 181–194.

Buckley, S. E., and Leverett, M. C., 1942. Mechanism of Fluid Displacement in Sands. Trans., AIME 146, 107–116.

Burton, M., Kumar, N., and Bryant, S., 2008. Time-Dependent Injectivity during CO_2 Storage in Aquifers. Paper SPE-11937 presented at the 2008 SPE/DOE Improved Oil Recovery Symposium, Tulsa, Oklahoma, 19–23 April.

Dykstra, H., and Parsons, R. L., 1950. The prediction of oil recovery by waterflooding. Secondary Recovery of Oil in the United States, 2nd Edition, 160–174, Washington D.C: API.

Doughty, C., Freifeld, B. M., and Trautz, R.C., 2008. Site Characterization for CO_2 Geologic Storage and vice versa: The Frio Brine Pilot, Texas, USA as a Case Study. Environmental Geology 54 (8), 1635–1656.

DOE/NETL, 2010. Carbon Sequestration Atlas III of the United States and Canada.

Ghanbarnezhad, R., 2012. A Graphical Solution to Model the Flow of Compressible CO_2 in Aquifers. Paper SPE-151679, presented at the Carbon Management Technology Conference, Orlando, Florida, 7–9 Feb.

Hovorka, S., Doughty, C., Benson, S., Pruess, K., and Knox, P., 2004. The impact of geological heterogeneity on CO_2 storage in brine formations: a case study from the Texas Gulf Coast. Special Publications, Geological Society London v. 233, 147–163.

IPCC, 2005. Special Report on Carbon Dioxide Capture and Storage. Cambridge University Press.

Kumar, A., Ozah, R., Noh, M., Pope, G. A., Bryant, S., Sepehrnoori, K., and Lake L.W., 2005. Reservoir simulation of CO_2 Storage in Deep Saline Aquifer. SPEJ 10 (3), 336-348. SPE-89343-PA. DOI: 10.2118/89343-PA.

Kumar, N., Bryant, S., and Nicot, J., 2008. Simplified Models for Plume Dynamics: Simulation Studies for Geological CO_2 Storage Certification Framework. Presented at 6th Annual Conference on Carbon Capture and Sequestration- DOE/NETL.

Leverett, M., 1941. Capillary behavior in porous solids. Transactions of the AIME (142): 159–172.

Lake, L.W., 1989. Enhanced Oil Recovery.Englewood Cliffs, New Jersey: Prentice Hall.

Mishra, S., 1987. On the Use of Pressure and Tracer Test Data for Reservoir Description, PhD dissertation, Stanford University, Stanford, CA.

Mathias, S., Hardisty, P., Trudell, M., and Zimmerman, R., 2008. Approximate Solutions for Pressure Buildup During CO_2 Injection in Brine Aquifers. Transport in Porous Media, no. 2. pp. 265–284.

Mathias, S., Gluyas, J., González Martínez de Miguel, G., and Hosseini, S., 2011. Role of partial miscibility on pressure buildup due to constant rate injection of CO_2 into closed and open brine aquifers. Water Resour. Res., 47, W12525.

Mollaei, A., 2011. Forecasting of Isothermal Enhanced Oil Recovery and Waterflood Processes, PhD Dissertation, The University of Texas at Austin, Austin, TX.

Noh, M., Lake, L., Bryant, S., and Araque-Martinez, A., 2007. Implications of Coupling Fractional Flow and Geochemistry for CO_2 Injection in Aquifers. SPE Res. Evaluation and Eng., 10(04), 406–414.

Nordbotten, J. M., and Celia, M. A., 2005. Similarity Solutions for Fluid Injection into Confined Aquifers. J. Fluid Mech. 561, 307–327.

Nordbotten, J. M., Celia, M. A., and Bachu, S., 2005, Injection and storage of CO_2 in deep saline aquifers: analytical solution for CO2 plume evolution during injection, Transport in Porous Media, DOI: 10.1007/s11242-004-0670-9.

Novakovic, D., 2002. Numerical Reservoir Characterization Using Dimensionless Scale Numbers with Application in Upscaling. PhD thesis, Louisiana State University, Aug 2002.

Oruganti, Y., and Mishra, S., 2012. An Improved Simplified Analytical Model for CO_2 Plume Movement and Pressure Buildup in Deep Saline Formations. Int. J. Greenhouse Gas Control 14, 49–59.

Ozah, R. C., Lakshminarasimhan, S., Pope, G. A., Sepehrnoori, K., and Bryant, S. L., 2005. Numerical Simulation of the Storage of Pure CO_2 and CO_2-H_2S Gas Mixtures in Deep Saline Aquifers. SPE Annual Technical Conference and Exhibition. Society of Petroleum Engineers, January 2005.

Pedersen, K. S., Fredenslund, A., Christensen, P. L., and Thomassen, P., 1984. Viscosity of Crude Oils, J. Chem. Eng. Sci. 39(6), 1011–1016.

Pruess, K., Xu, T., Apps, J., and Garcia, J., 2003. Numerical Modeling of Aquifer Disposal of CO_2. SPEJ, 49-60 (SPE 83695).

Saadatpoor, E., Bryant, S., and Sepehrnoori, K., 2009. Effect of Capillary Heterogeneity on Buoyant Plumes: A New Local Trapping Mechanism. Paper GHGT-9. Published in Energy Procedia 1, 3299–3306.

Saripalli, P., and McGrail, P., 2002. Semi-Analytical Approaches to Modeling Deep Well Injection of CO_2 for Geological Sequestration. Energy Conversion and Management, 43(2), 185–198.

Sminchak, J., Majors, S., Mishra, S., and Oruganti, Y., 2012. Infrastructure Analysis for Geologic CO_2 Storage Applications in the Arches Province of the Midwest United States. Carbon Management Technology Conference, January 2012.

Weatherford, 2011. Summary of Mercury Injection Test Results for Arches Simulation, Laboratory report, Weatherford Laboratories, Houston, TX.

Woods, E. G., and Comer, A. G., 1962. Saturation Distribution and Injection Pressure for a Radial Gas-Storage Reservoir. Journal of Petroleum Technology 14.12: 1–389.

Yamamoto, H., Zhang, K., Karasaki, K., Marui, A., Uehara, H., and Nishikawa, N., 2009. Numerical Investigation Concerning the Impact of CO_2 Geologic Storage on Regional Groundwater Flow. Int. J. Greenhouse Gas Control 3 (5), 586–599.

Zhou, Q., Birkholzer, J., Mehnert, E., Lin, Y., and Zhang, K., 2010. Modeling Basin and Plume-Scale Processes of CO_2 Storage for Full-Scale Deployment. Paper LBNL-2788E, Lawrence Berkeley National Laboratory, Berkeley, California.

Zhou, Q., Birkholzer, J., Tsang, C., and Rutqvist, J., 2008. A Method for Quick Assessment of CO_2 Storage Capacity in Closed and Semi-Closed Saline Formations. Int. J. Greenhouse Gas Control 2, 626–639.

APPENDIX I:

COMPILATION OF FIGURES AND DATA TABLES

Figures:

REFERENCE RELATIVE PERMEABILITY CASE:
Parameter 1 Comparison
R Thickness

	0.5 Slope Linear Fit x Value, psi (y =x*time^0.5)	
	Pressure Front	CO2Front
LOW R Thickness = 50m	13662.93	534.45
REF R Thickness = 150m	16554.65	359.68
HIGH R Thickness = 250m	11770.04	280.5

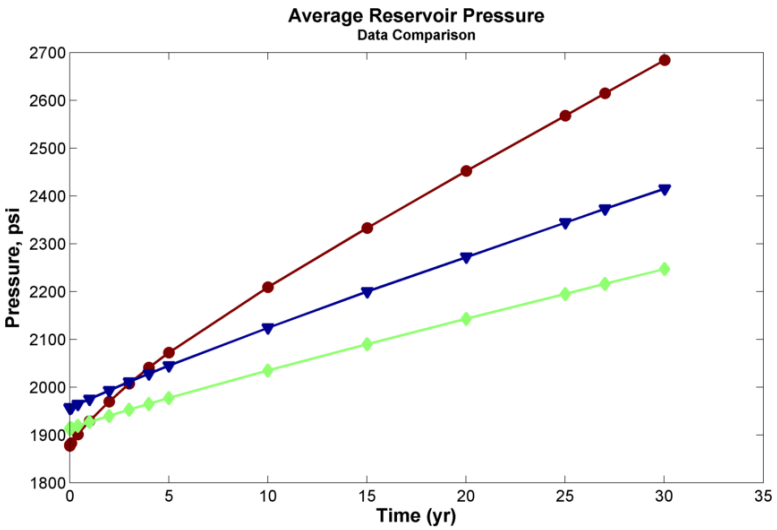

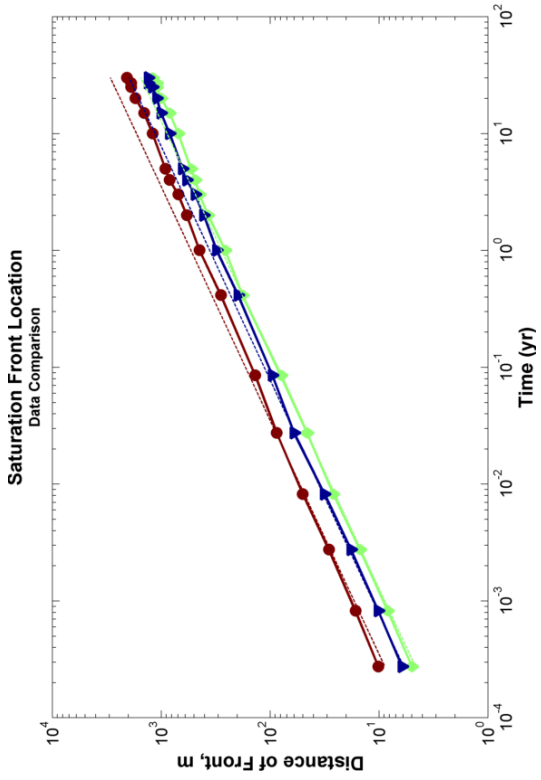
Saturation Front Location
Data Comparison
Distance of Front, m
Time (yr)

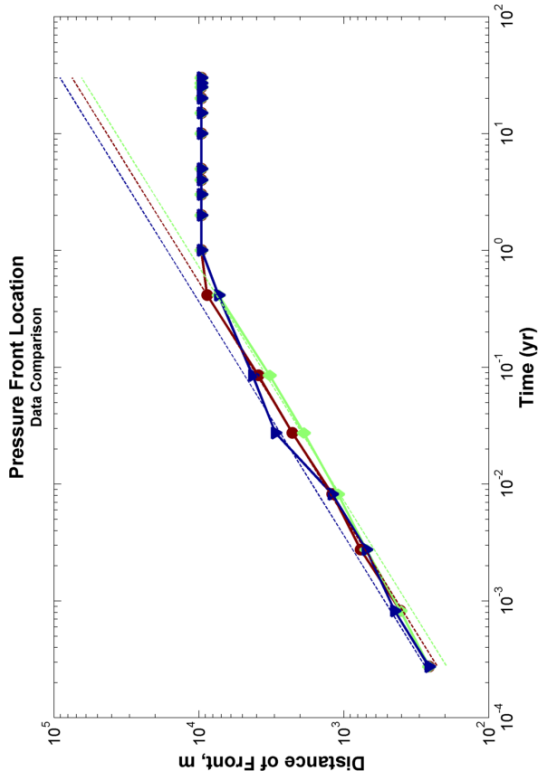
Pressure Front Location
Data Comparison
Distance of Front, m
Time (yr)

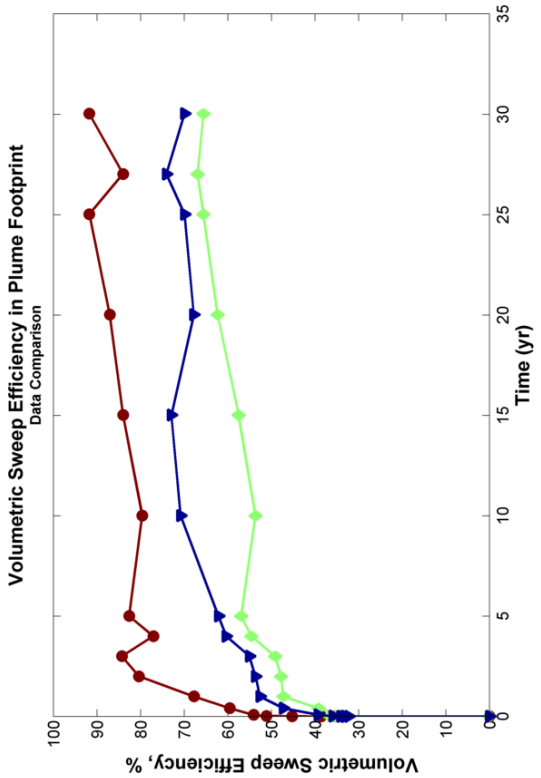
Volumetric Sweep Efficiency in Plume Footprint
Data Comparison
Volumetric Sweep Efficiency, %
Time (yr)

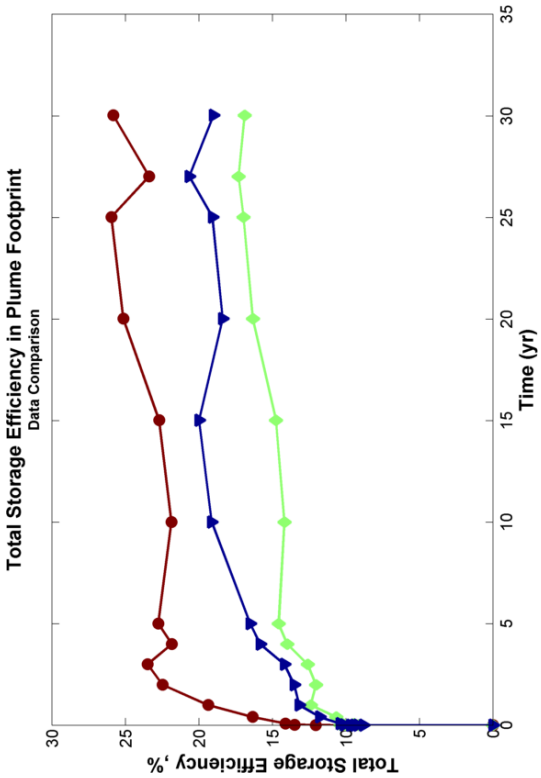
Total Storage Efficiency in Plume Footprint
Data Comparison
Total Storage Efficiency ,%
Time (yr)

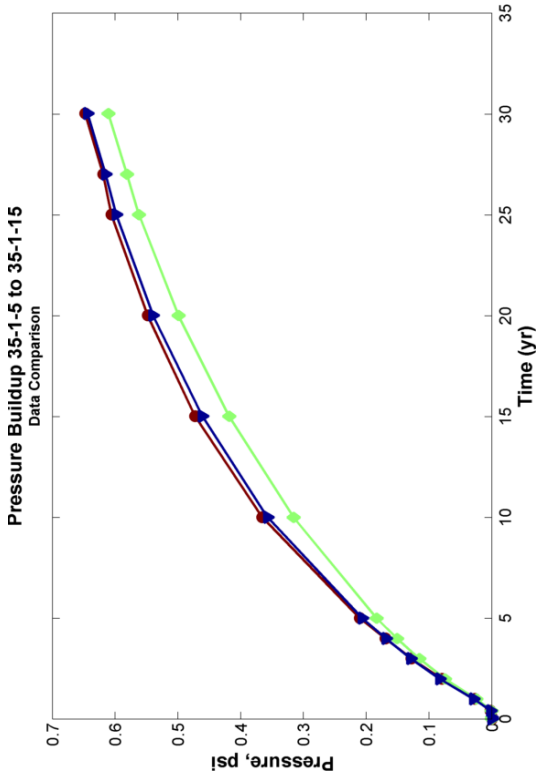
Pressure Buildup 35-1-5 to 35-1-15
Data Comparison
Pressure, psi
Time (yr)

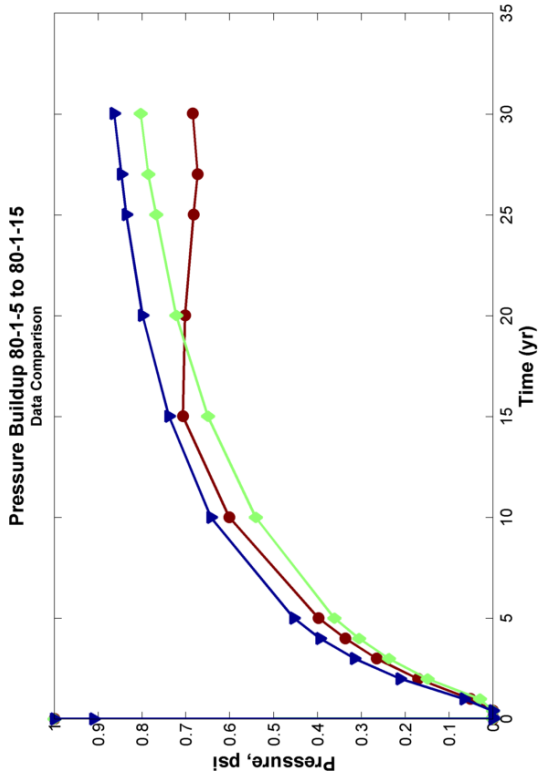
Pressure Buildup 80-1-5 to 80-1-15
Data Comparison
Pressure, psi
Time (yr)

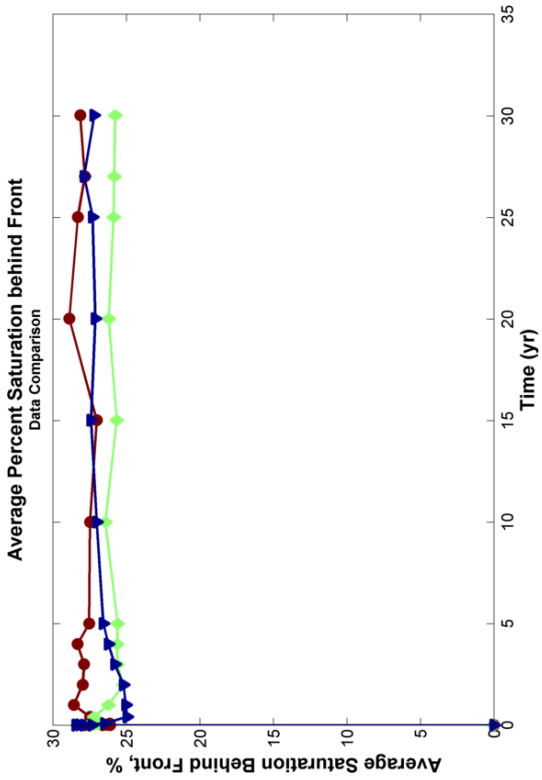
Average Percent Saturation behind Front
Data Comparison
Average Saturation Behind Front, %
Time (yr)

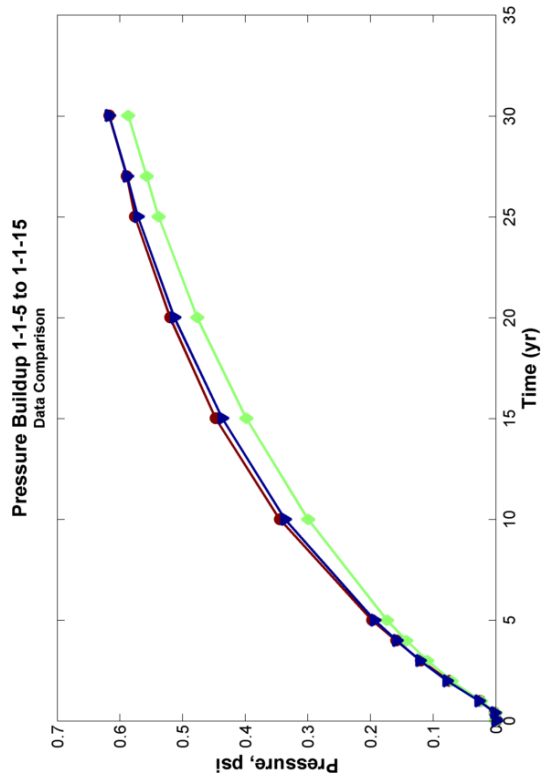
Pressure Buildup 1-1-5 to 1-1-15
Data Comparison
Pressure, psi
Time (yr)

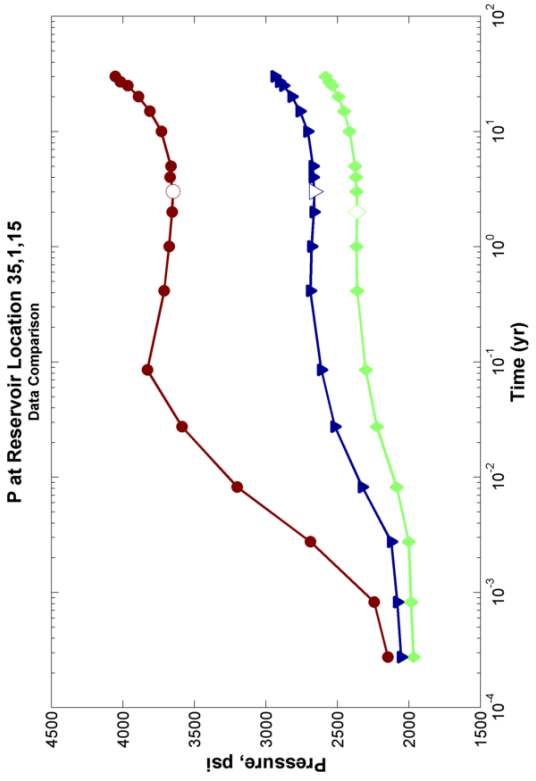
P at Reservoir Location 35,1,15
Data Comparison
Pressure, psi
Time (yr)

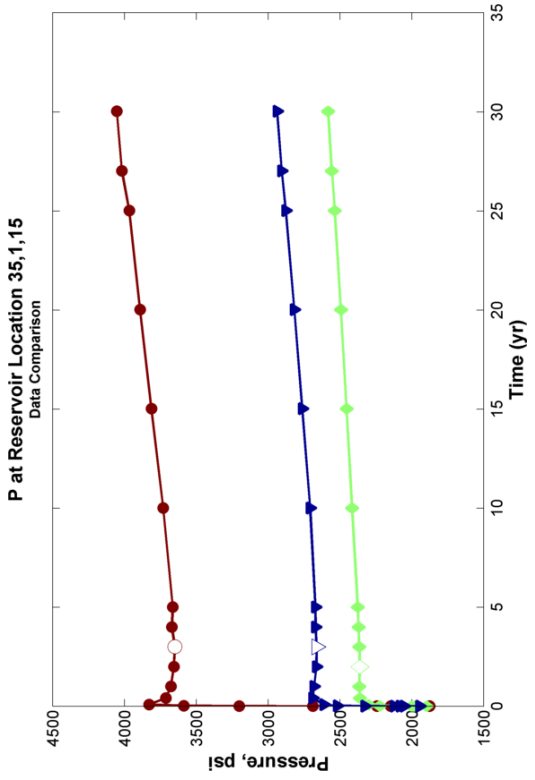
P at Reservoir Location 35,1,15
Data Comparison
Pressure, psi
Time (yr)

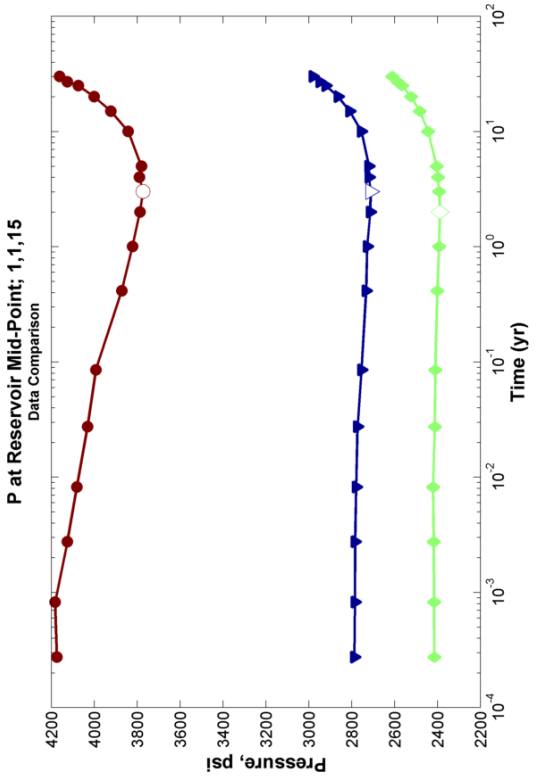
P at Reservoir Mid-Point; 1,1,15
Data Comparison
Pressure, psi
Time (yr)

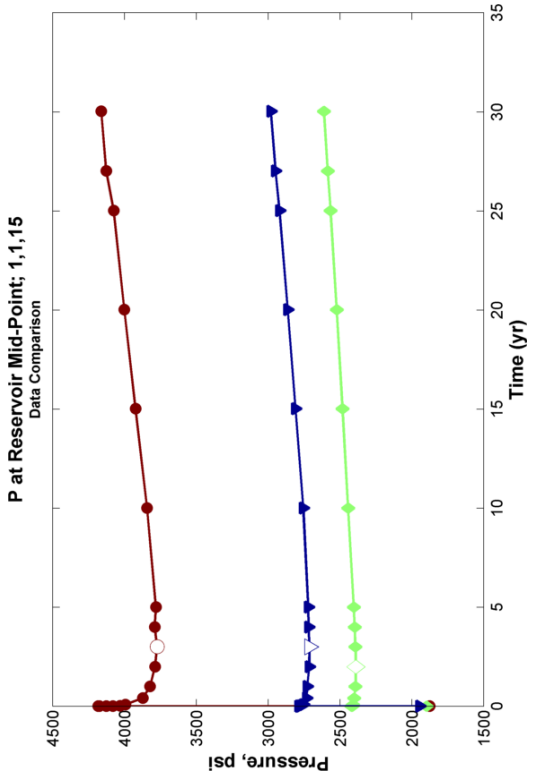
P at Reservoir Mid-Point; 1,1,15
Data Comparison
Pressure, psi
Time (yr)

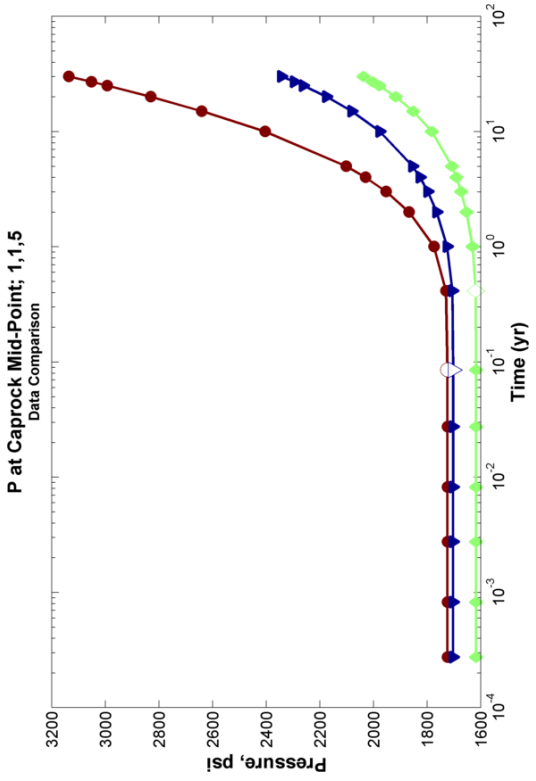
P at Caprock Mid-Point; 1,1,5
Data Comparison
Pressure, psi
Time (yr)

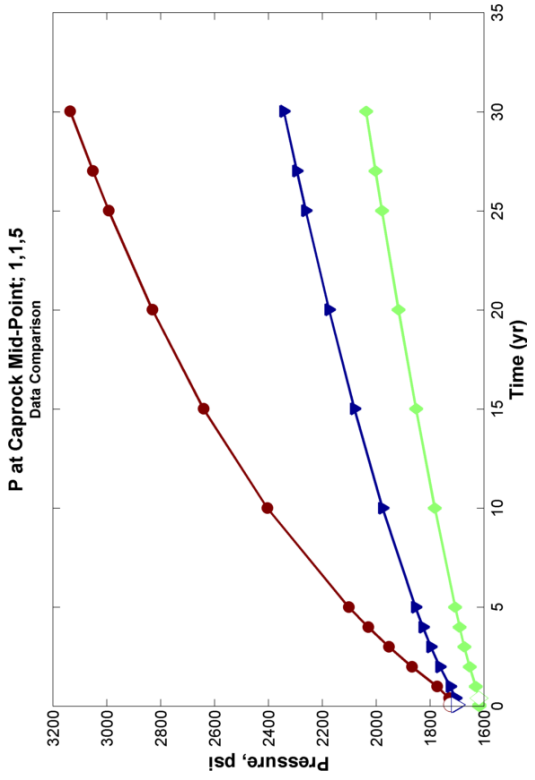
P at Caprock Mid-Point; 1,1,5
Data Comparison
Pressure, psi
Time (yr)

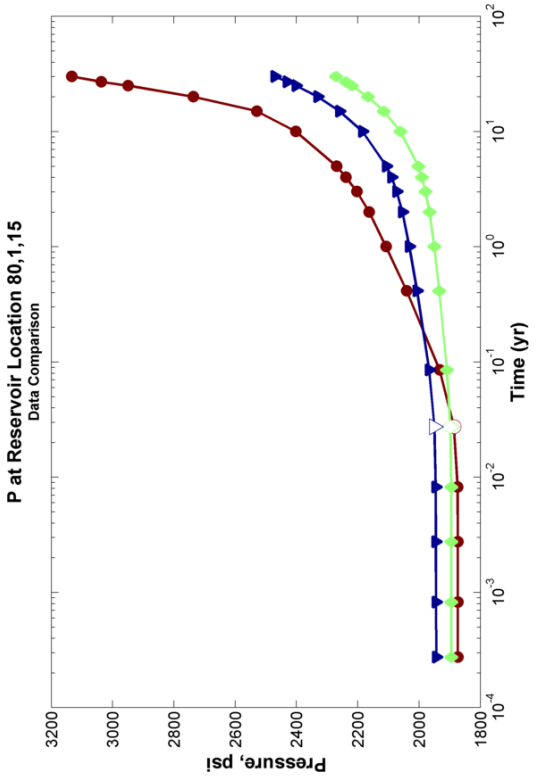
P at Reservoir Location 80,1,15
Data Comparison
Pressure, psi
Time (yr)

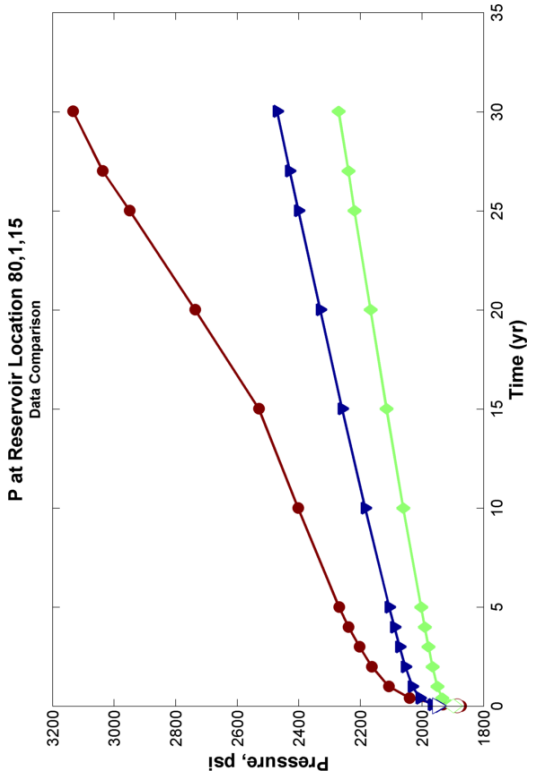
P at Reservoir Location 80,1,15
Data Comparison
Pressure, psi
Time (yr)

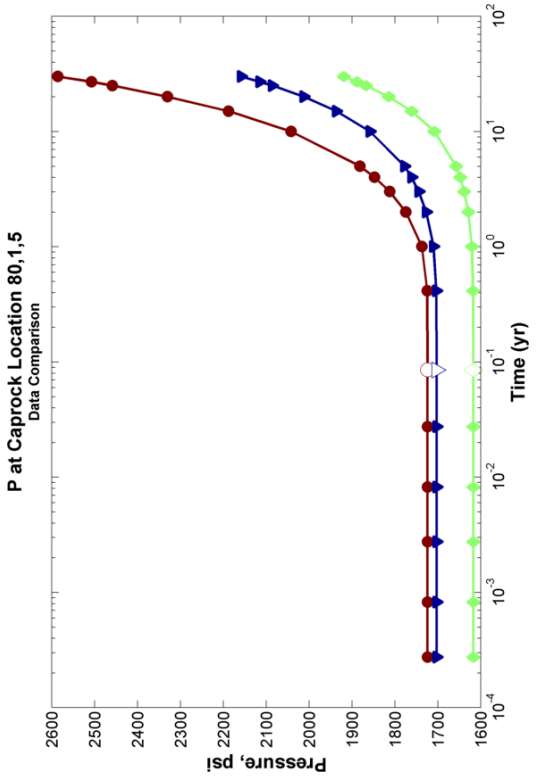
P at Caprock Location 80,1,5
Data Comparison
Pressure, psi
Time (yr)

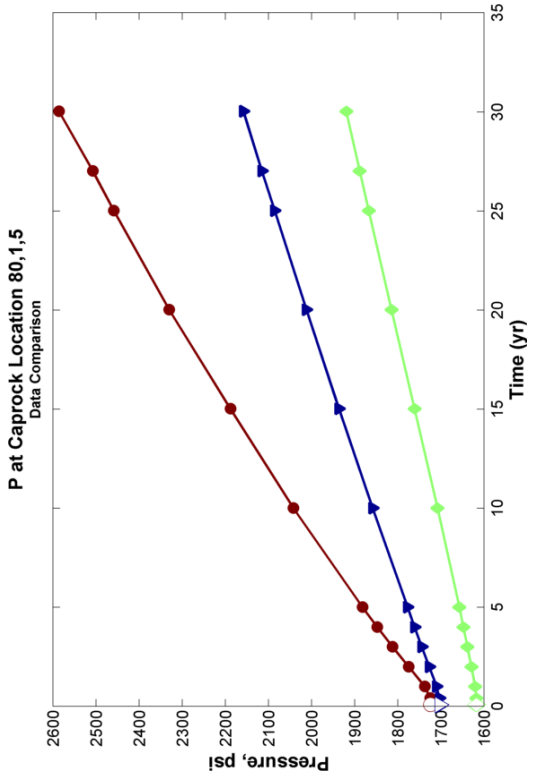
P at Caprock Location 80,1,5
Data Comparison
Pressure, psi
Time (yr)

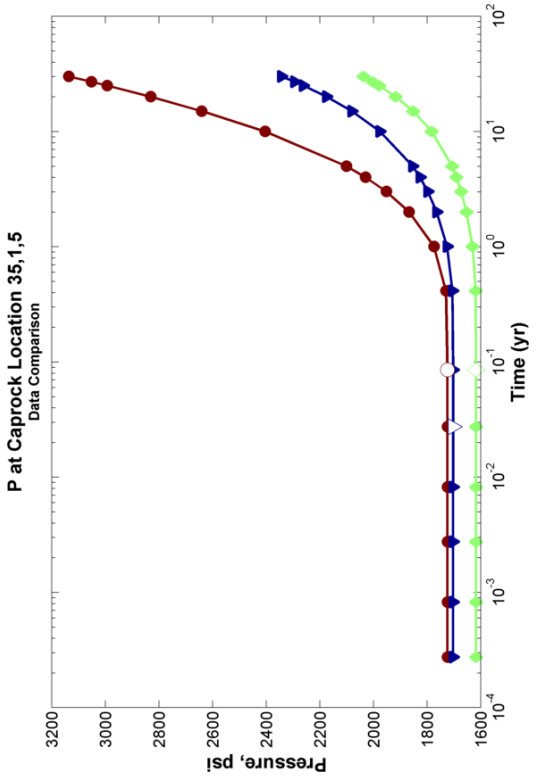
P at Caprock Location 35,1,5
Data Comparison
Pressure, psi
Time (yr)

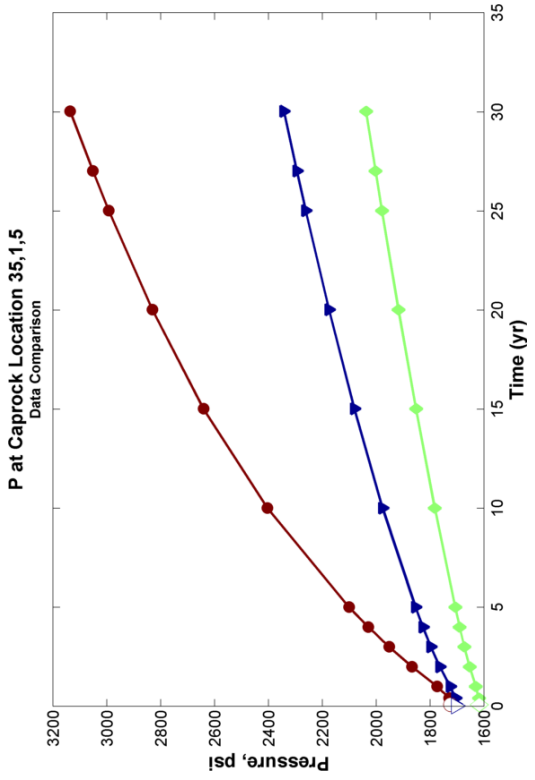
P at Caprock Location 35,1,5
Data Comparison
Pressure, psi
Time (yr)

REFERENCE RELATIVE PERMEABILITY CASE:
Parameter 2 Comparison
CR Thickness

	0.5 Slope Linear Fit x Value, psi (y =x*time^0.5)	
	Pressure Front	CO2Front
LOW CR Thickness = 100m	12794.74	359.68
REF CR Thickness = 150m	16554.65	359.68
HIGH CR Thickness = 200m	12528.39	359.68

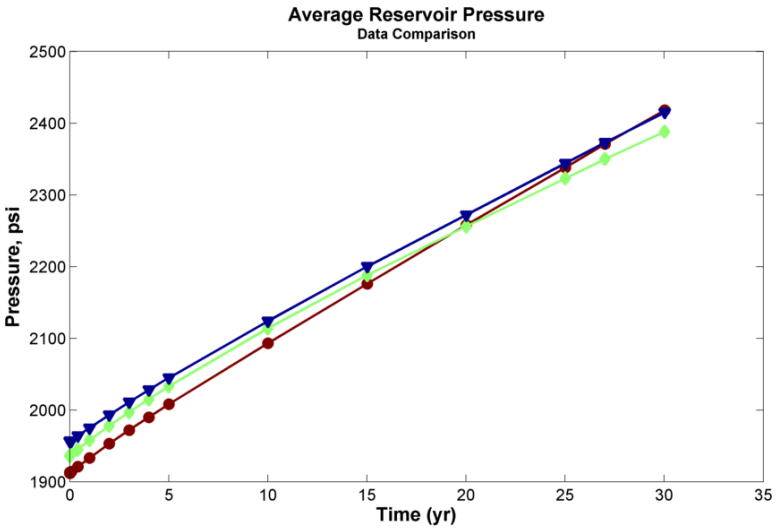

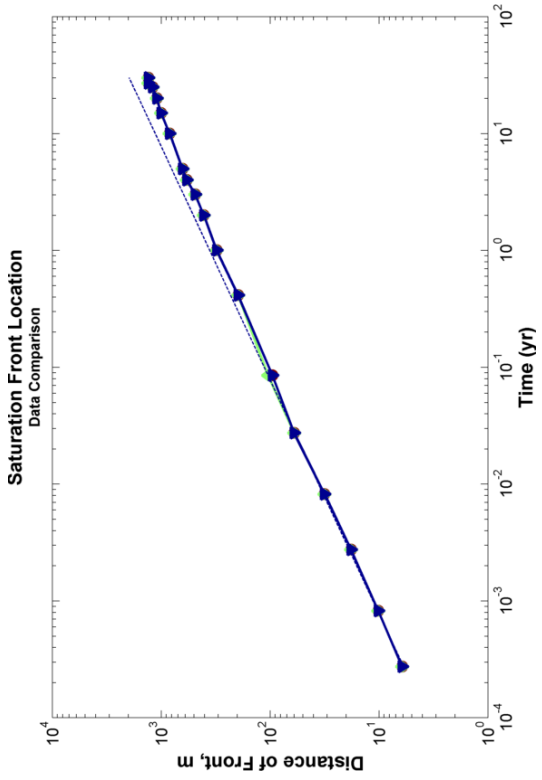
Saturation Front Location
Data Comparison
Distance of Front, m
Time (yr)

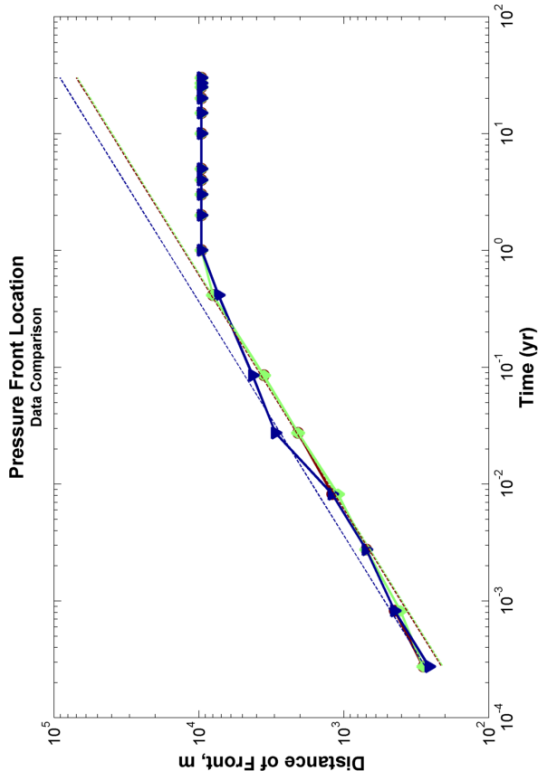
Pressure Front Location
Data Comparison
Distance of Front, m
Time (yr)

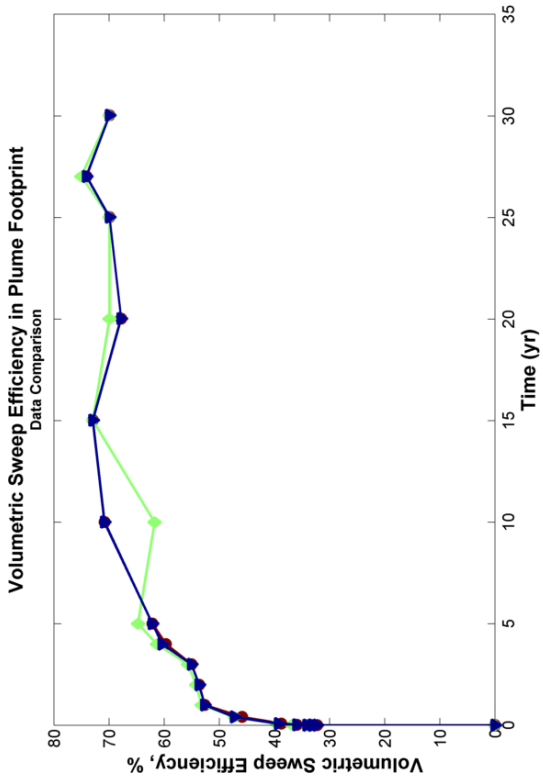
Volumetric Sweep Efficiency in Plume Footprint
Data Comparison
Volumetric Sweep Efficiency, %
Time (yr)

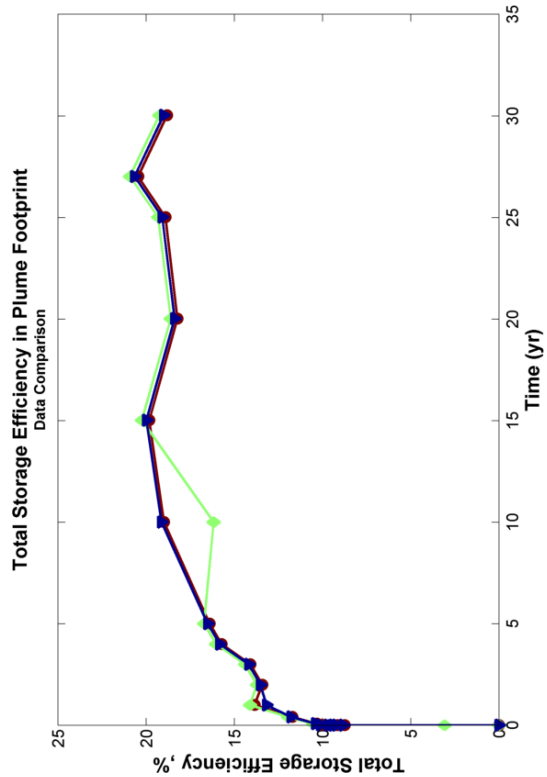
Total Storage Efficiency in Plume Footprint
Data Comparison
Total Storage Efficiency ,%
Time (yr)

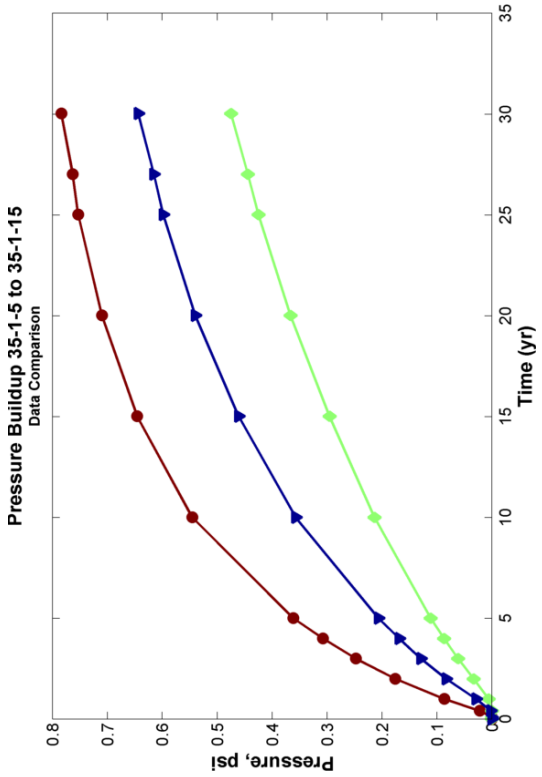
Pressure Buildup 35-1-5 to 35-1-15
Data Comparison
Pressure, psi
Time (yr)

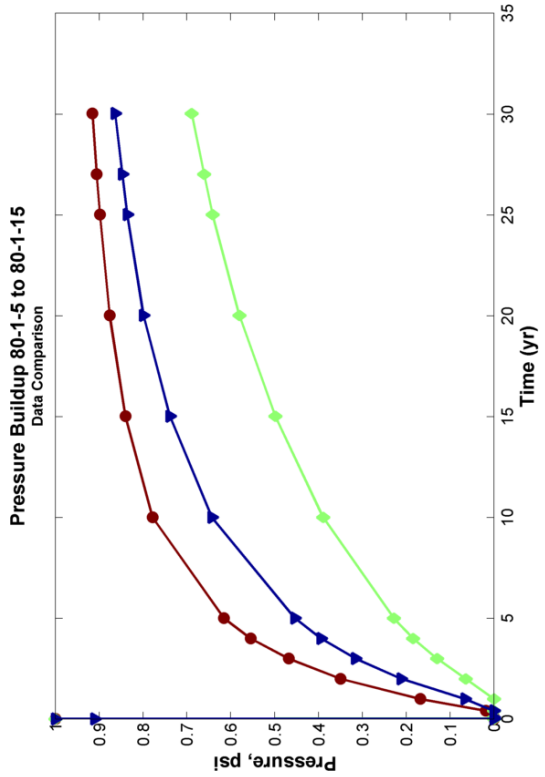
Pressure Buildup 80-1-5 to 80-1-15
Data Comparison
Pressure, psi
Time (yr)

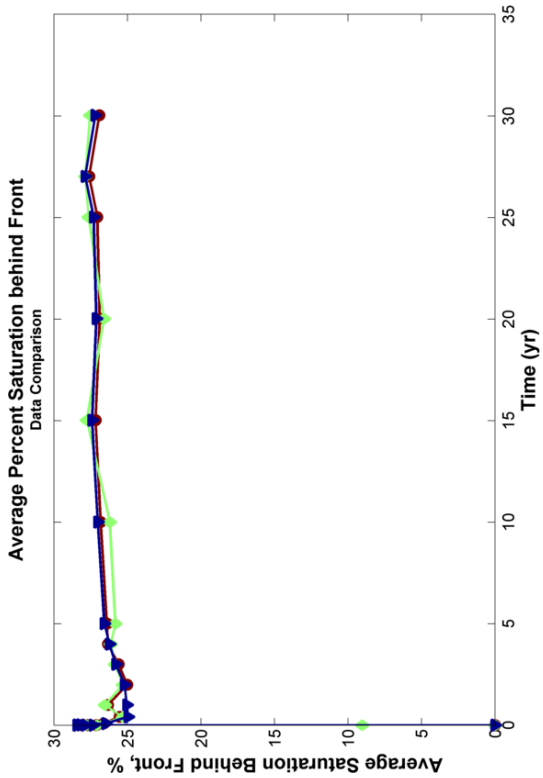
Average Percent Saturation behind Front
Data Comparison
Average Saturation Behind Front, %
Time (yr)

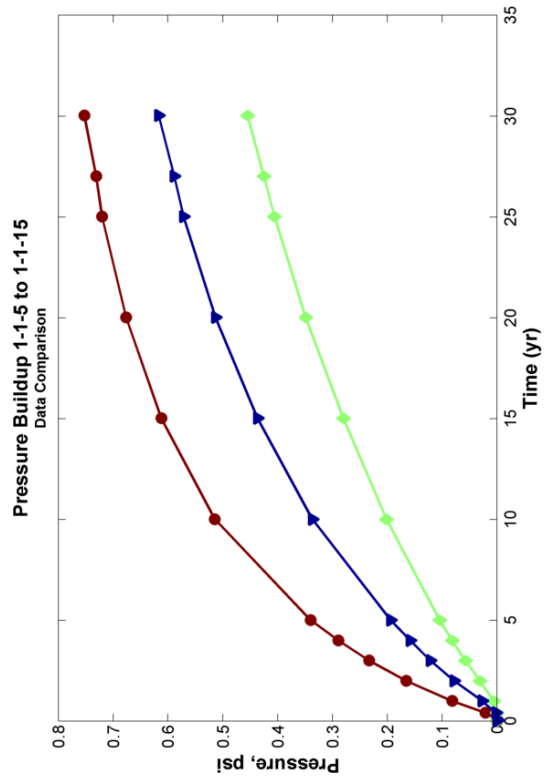
Pressure Buildup 1-1-5 to 1-1-15
Data Comparison
Pressure, psi
Time (yr)

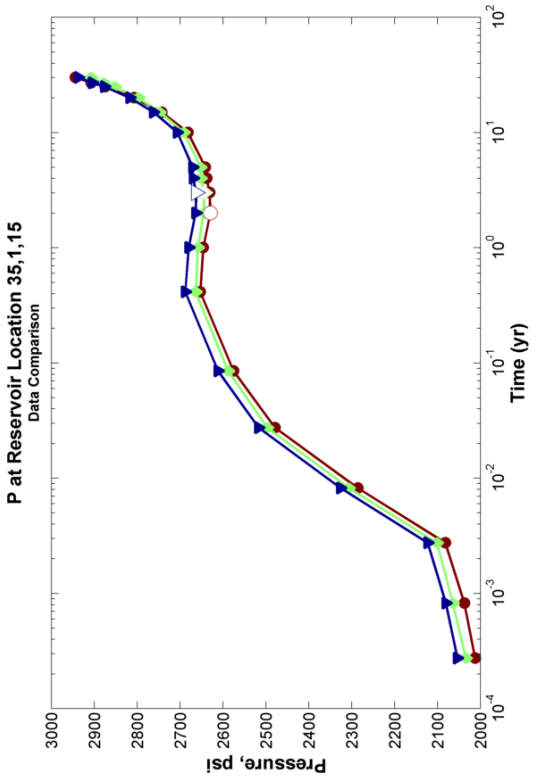
P at Reservoir Location 35,1,15
Data Comparison
Pressure, psi
Time (yr)

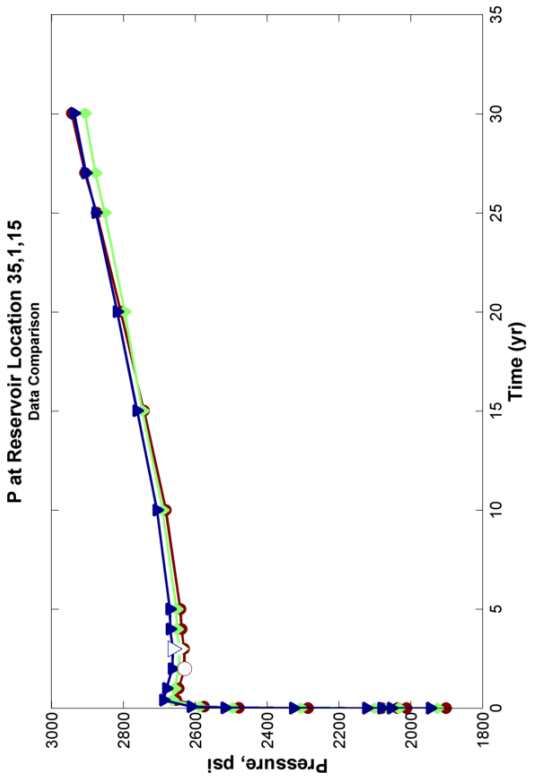
P at Reservoir Location 35,1,15
Data Comparison
Pressure, psi
Time (yr)

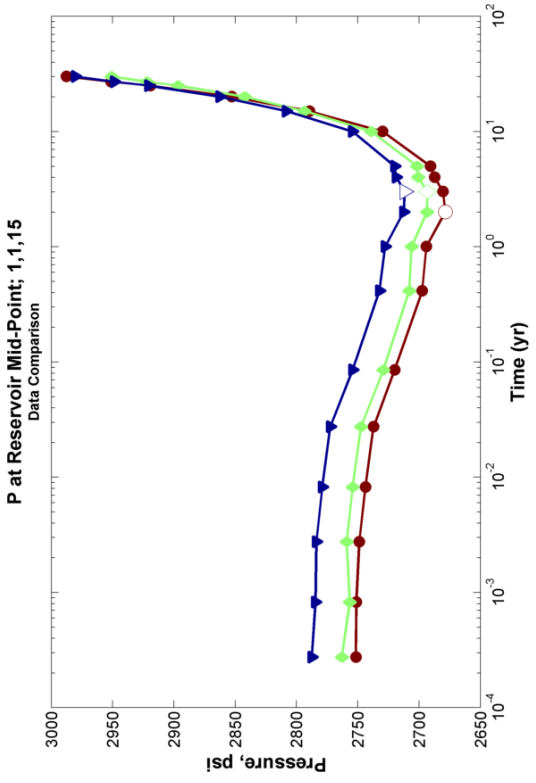
P at Reservoir Mid-Point; 1,1,15
Data Comparison
Pressure, psi
Time (yr)

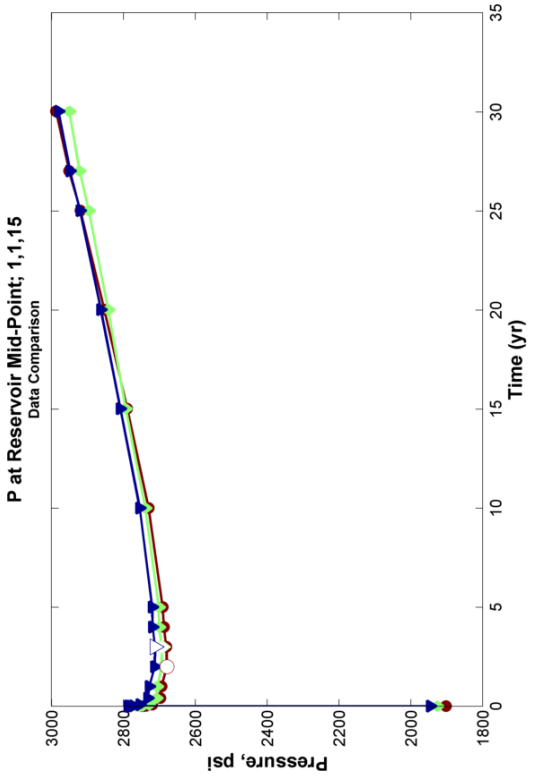
P at Reservoir Mid-Point; 1,1,15
Data Comparison
Pressure, psi
Time (yr)

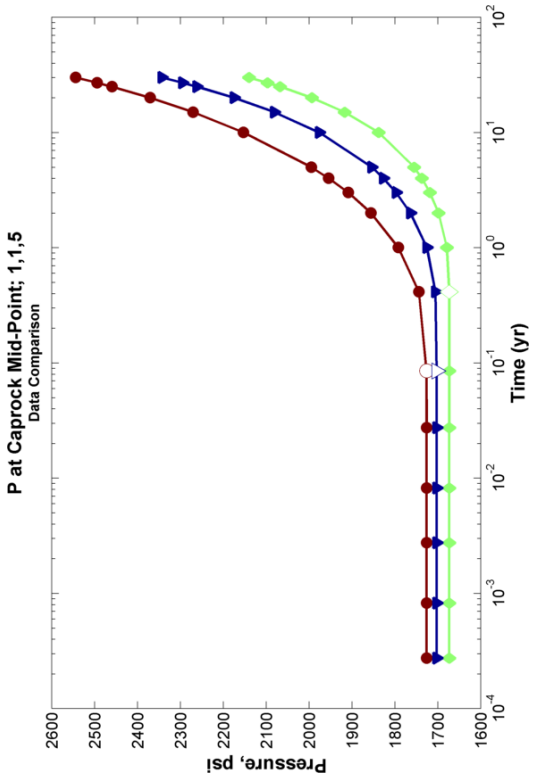
P at Caprock Mid-Point; 1,1,5
Data Comparison
Pressure, psi
Time (yr)

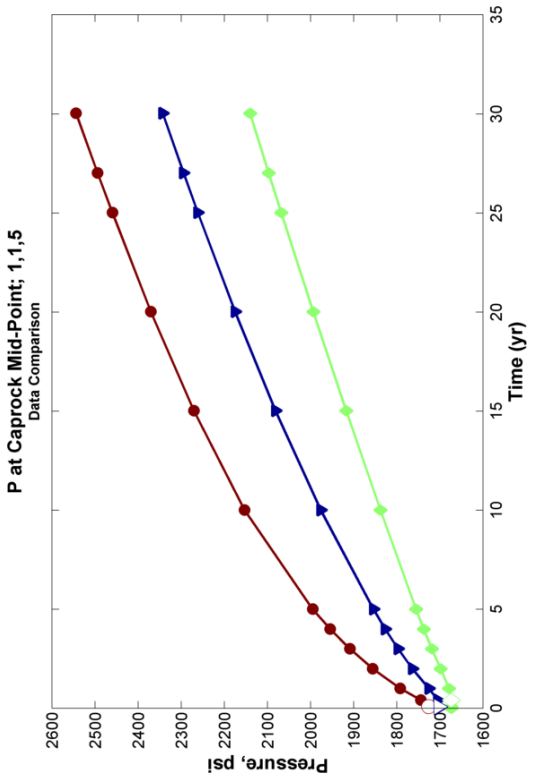
P at Caprock Mid-Point; 1,1,5
Data Comparison
Pressure, psi
Time (yr)

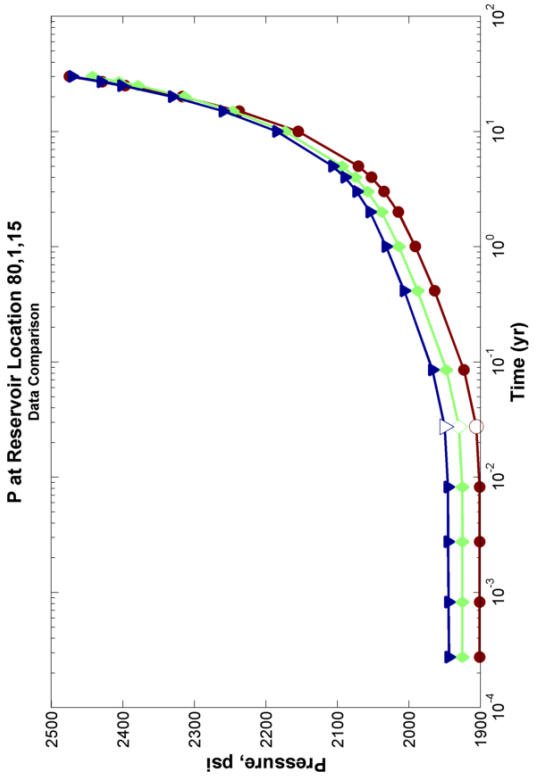
P at Reservoir Location 80,1,15
Data Comparison
Pressure, psi
Time (yr)

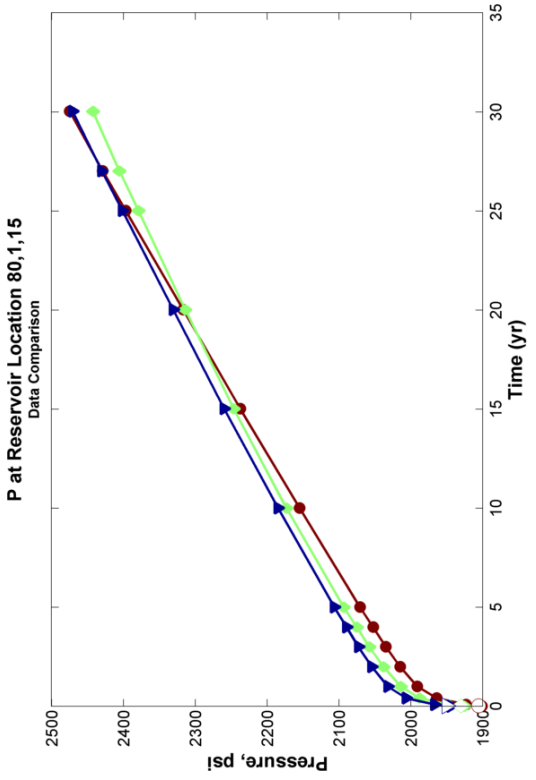
P at Reservoir Location 80,1,15
Data Comparison
Pressure, psi
Time (yr)

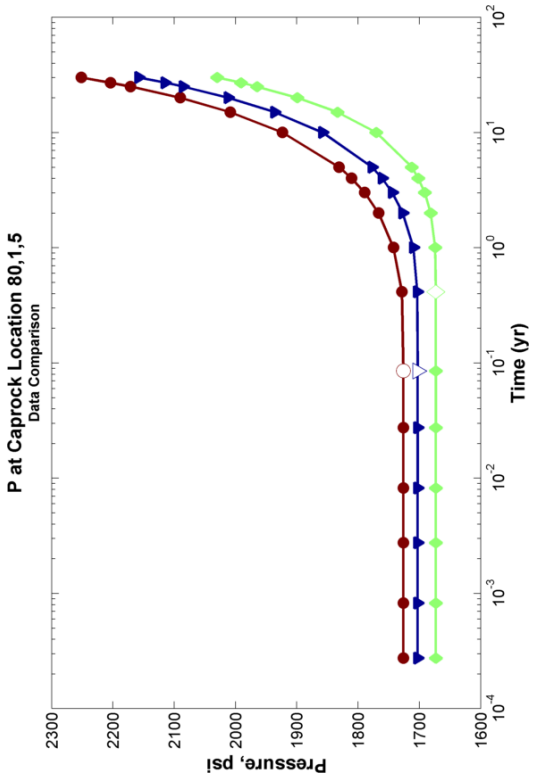
P at Caprock Location 80,1,5
Data Comparison
Pressure, psi
Time (yr)

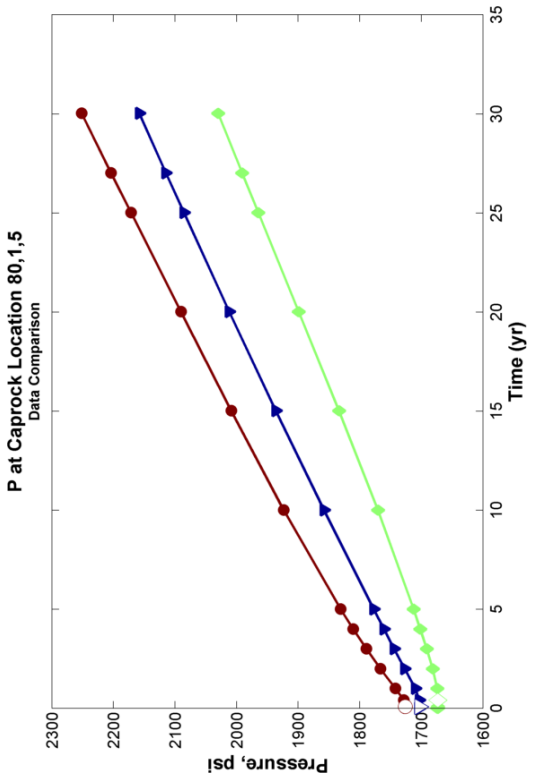
P at Caprock Location 80,1,5
Data Comparison
Pressure, psi
Time (yr)

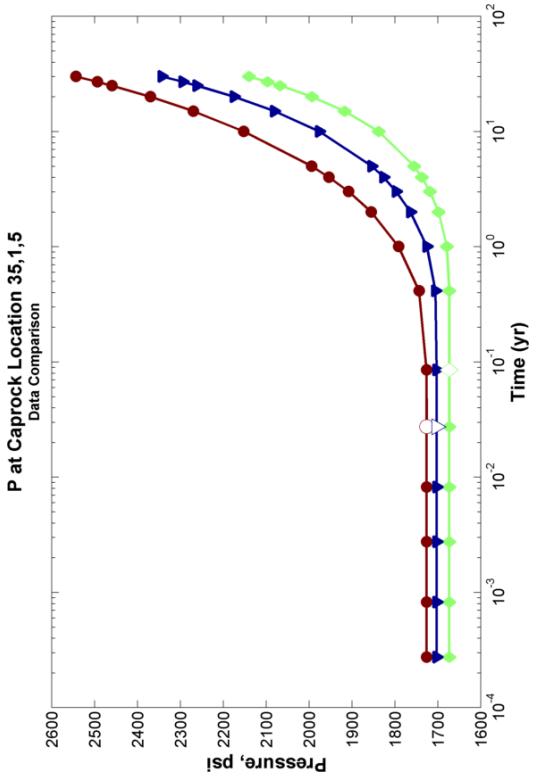
P at Caprock Location 35,1,5
Data Comparison
Pressure, psi
Time (yr)

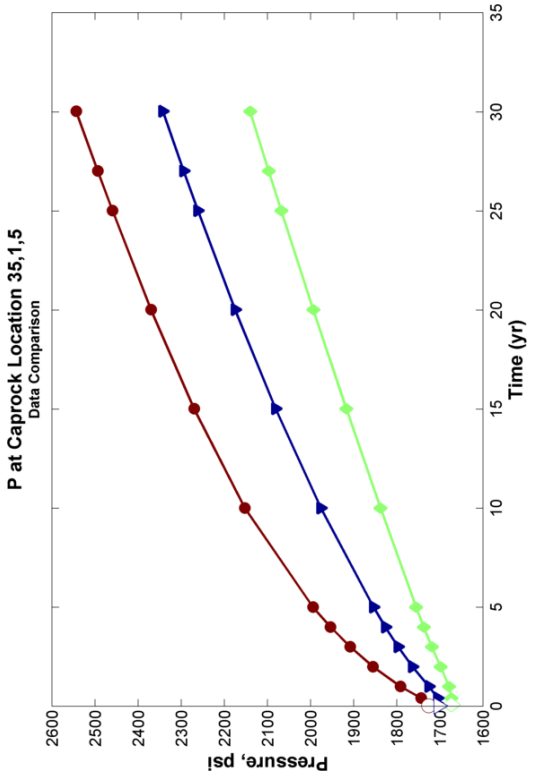
P at Caprock Location 35,1,5
Data Comparison
Pressure, psi
Time (yr)

REFERENCE RELATIVE PERMEABILITY CASE:
Parameter 3 Comparison
kR Arrangement/Layering

	0.5 Slope Linear Fit x Value, psi (y =x*time^0.5)	
	Pressure Front	CO2Front
Increasing kR from Top	12356.25	175.82
Ref - Random kR Arrangement	16554.65	359.68
Increasing kR from Bottom	12466.79	193.13

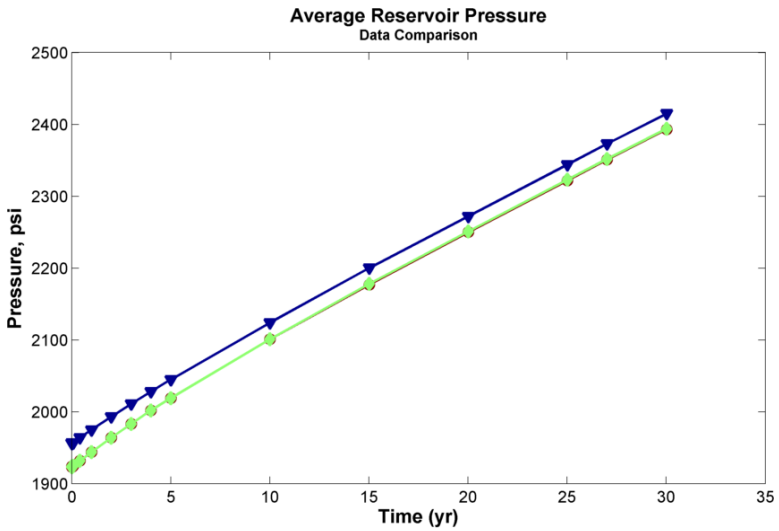

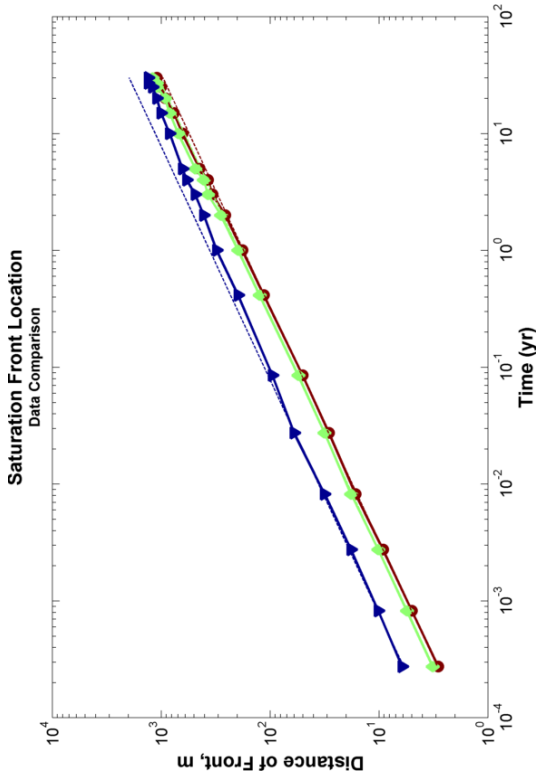
Saturation Front Location
Data Comparison
Distance of Front, m
Time (yr)

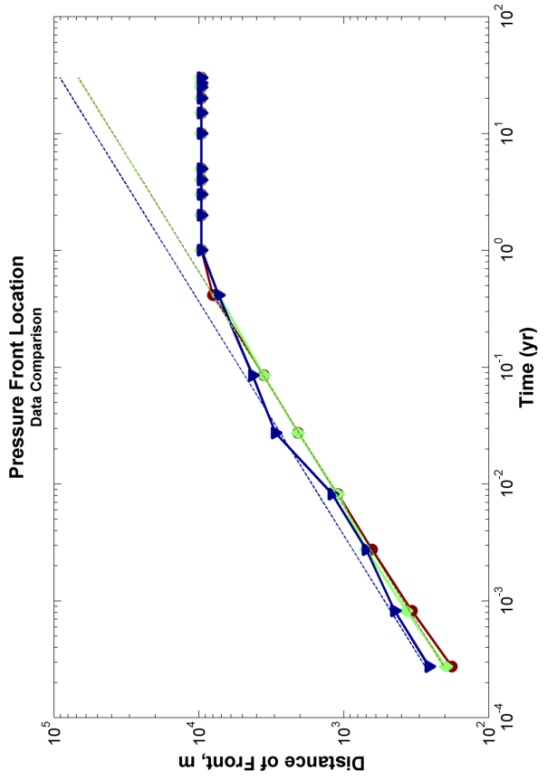
Pressure Front Location
Data Comparison
Distance of Front, m
Time (yr)

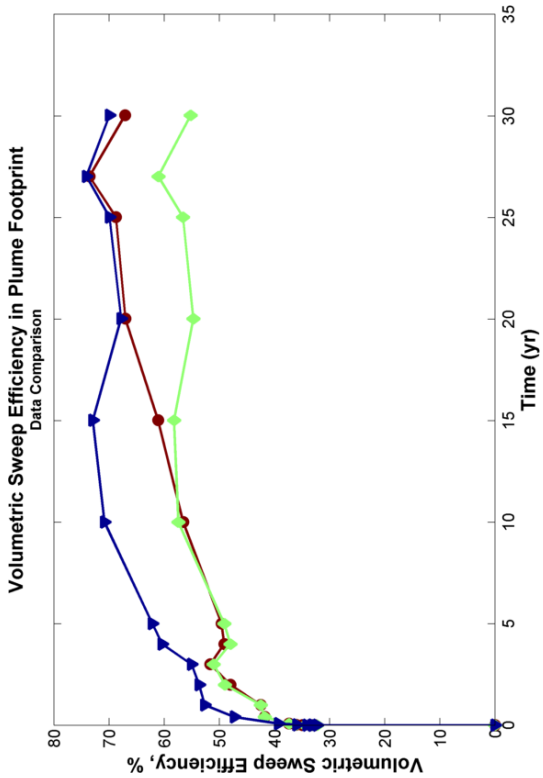
Volumetric Sweep Efficiency in Plume Footprint
Data Comparison
Volumetric Sweep Efficiency, %
Time (yr)

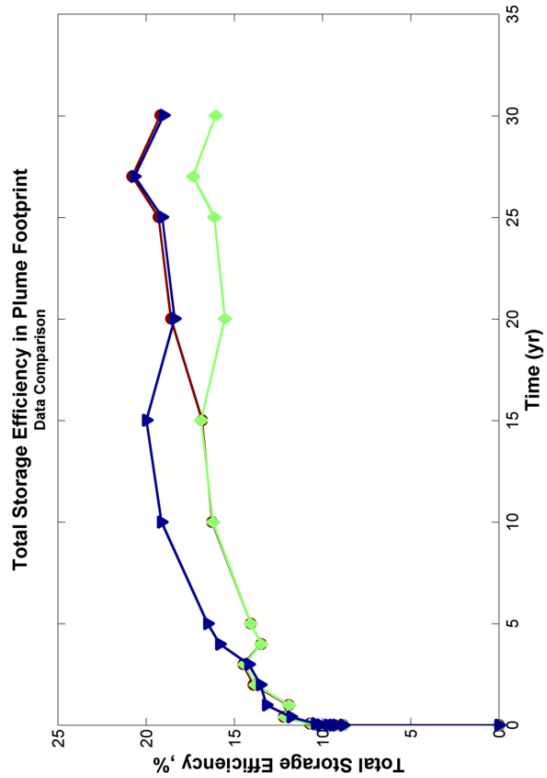
Total Storage Efficiency in Plume Footprint
Data Comparison
Total Storage Efficiency ,%
Time (yr)

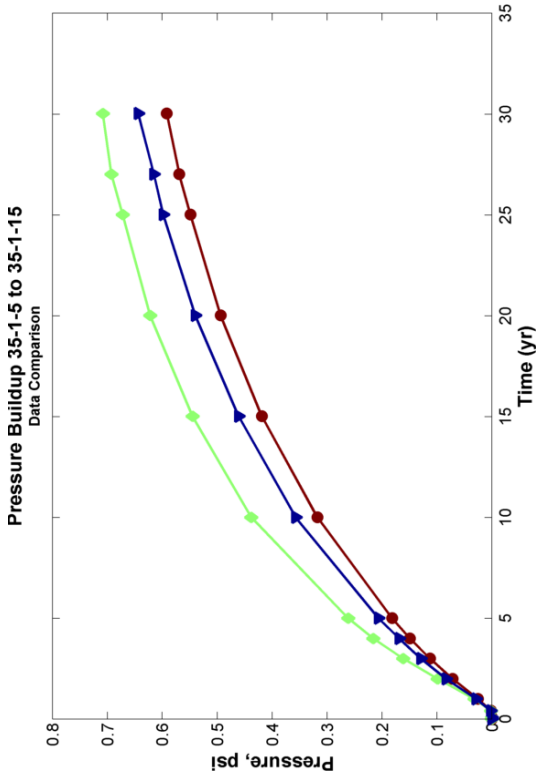
Pressure Buildup 35-1-5 to 35-1-15
Data Comparison
Pressure, psi
Time (yr)

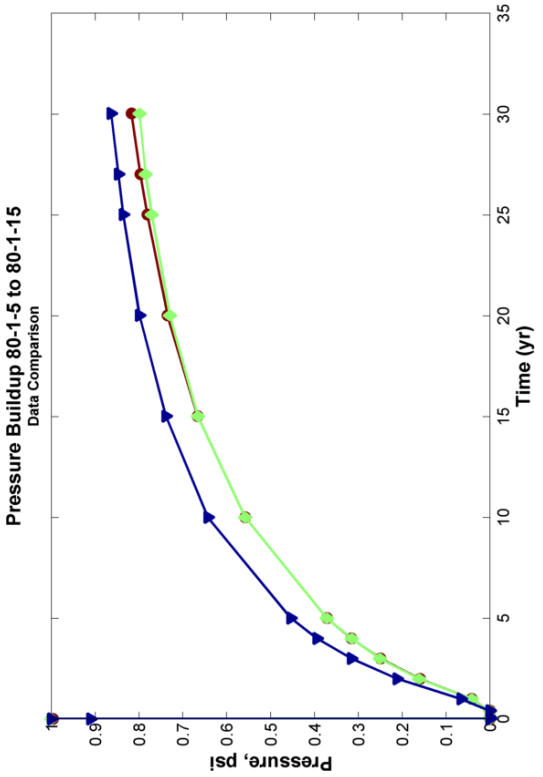
Pressure Buildup 80-1-5 to 80-1-15
Data Comparison
Pressure, psi
Time (yr)

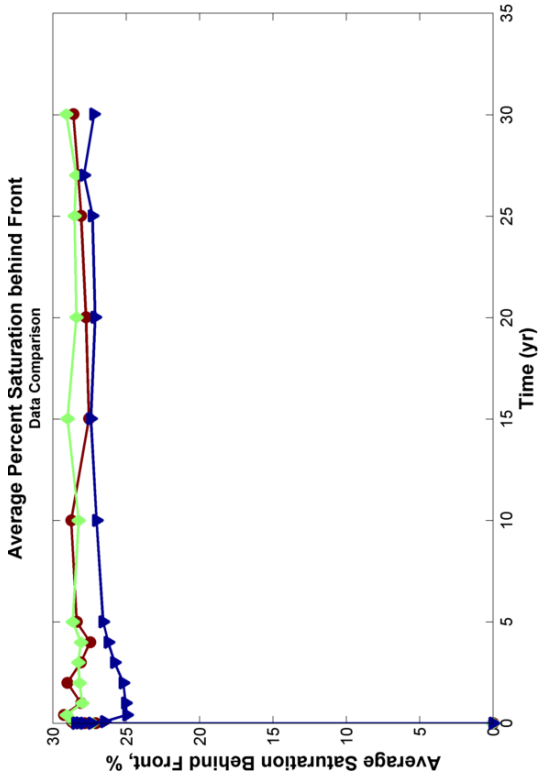
Average Percent Saturation behind Front
Data Comparison
Average Saturation Behind Front, %
Time (yr)

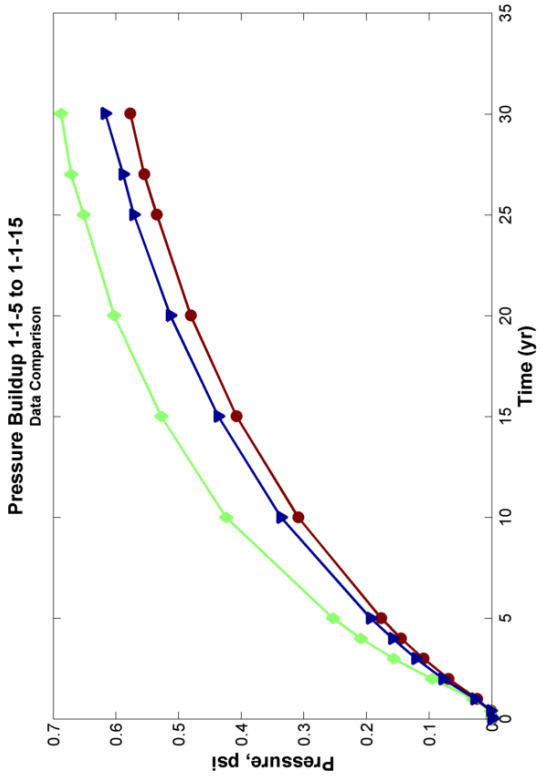
Pressure Buildup 1-1-5 to 1-1-15
Data Comparison
Pressure, psi
Time (yr)

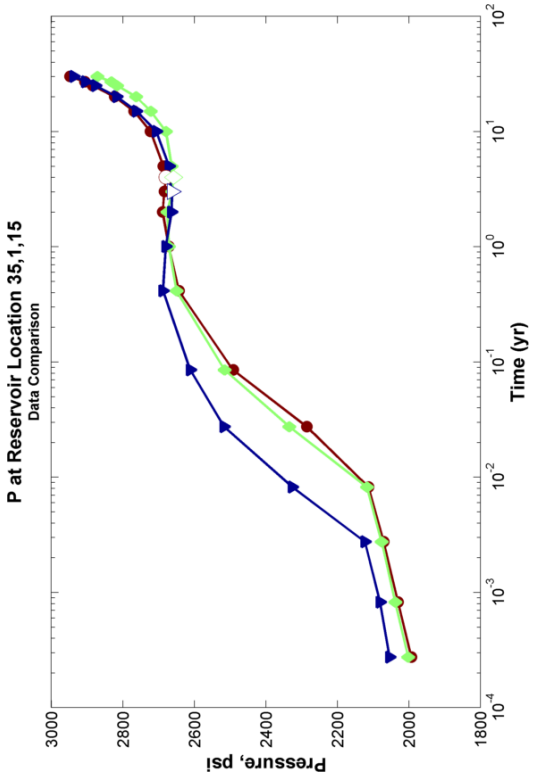
P at Reservoir Location 35,1,15
Data Comparison
Pressure, psi
Time (yr)

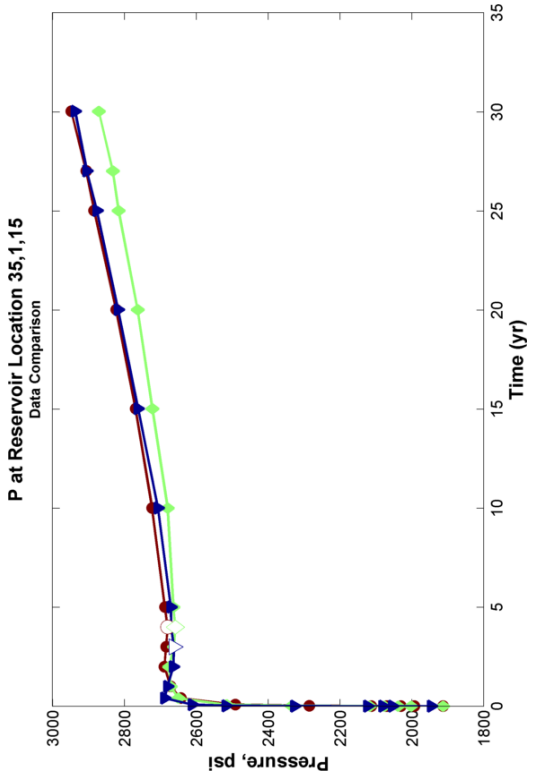
P at Reservoir Location 35,1,15
Data Comparison
Pressure, psi
Time (yr)

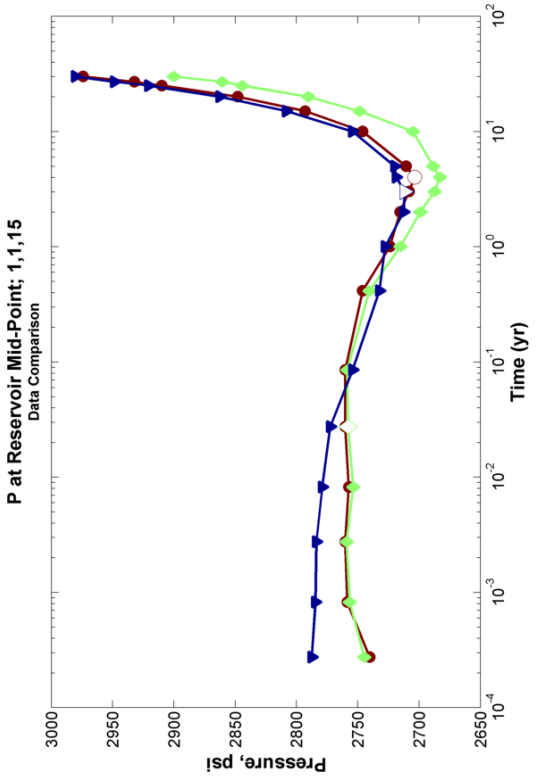
P at Reservoir Mid-Point; 1,1,15
Data Comparison
Pressure, psi
Time (yr)

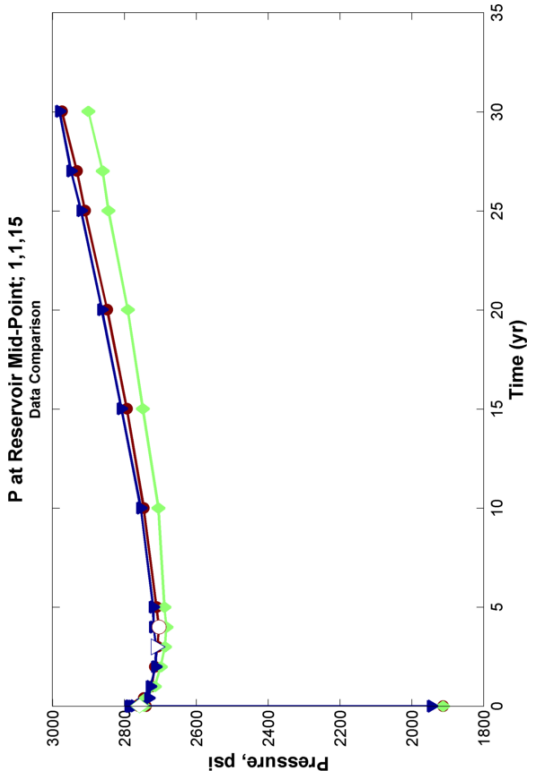
P at Reservoir Mid-Point; 1,1,15
Data Comparison
Pressure, psi
Time (yr)

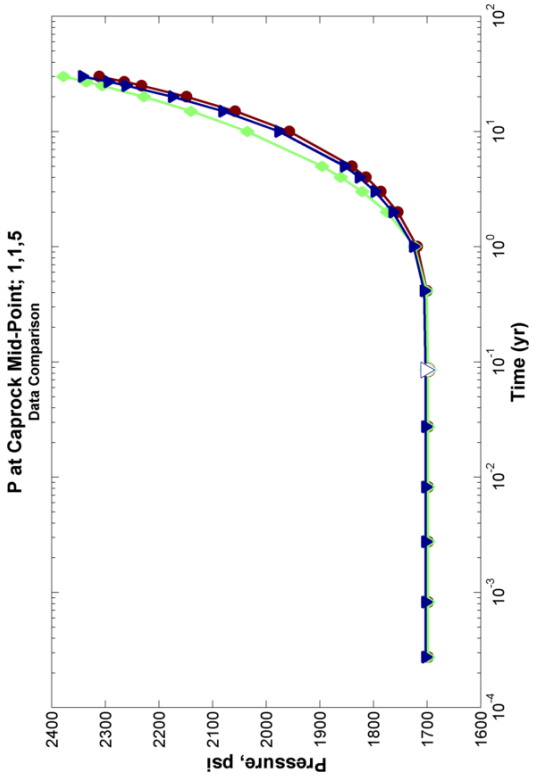
P at Caprock Mid-Point; 1,1,5
Data Comparison
Pressure, psi
Time (yr)

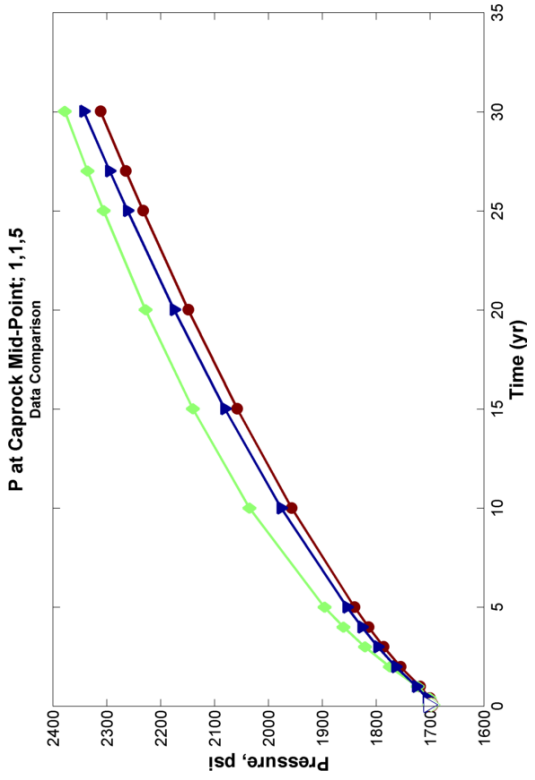
P at Caprock Mid-Point; 1,1,5
Data Comparison
Pressure, psi
Time (yr)

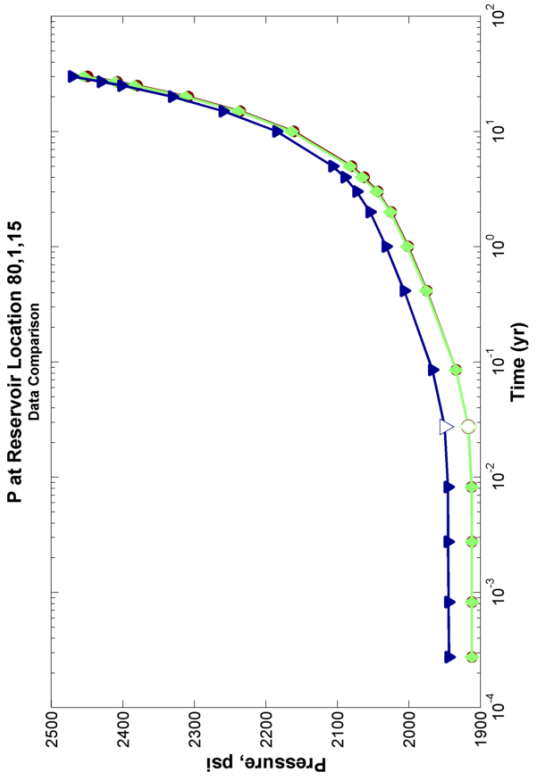
P at Reservoir Location 80,1,15
Data Comparison
Pressure, psi
Time (yr)

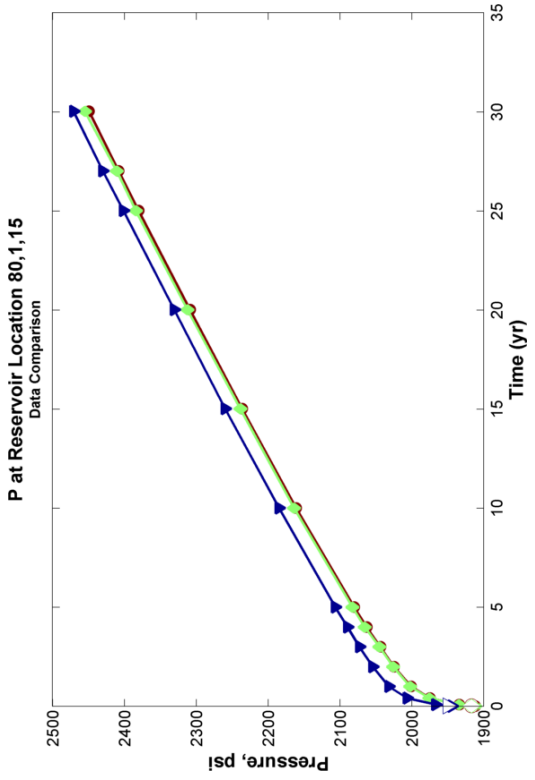
P at Reservoir Location 80,1,15
Data Comparison
Pressure, psi
Time (yr)

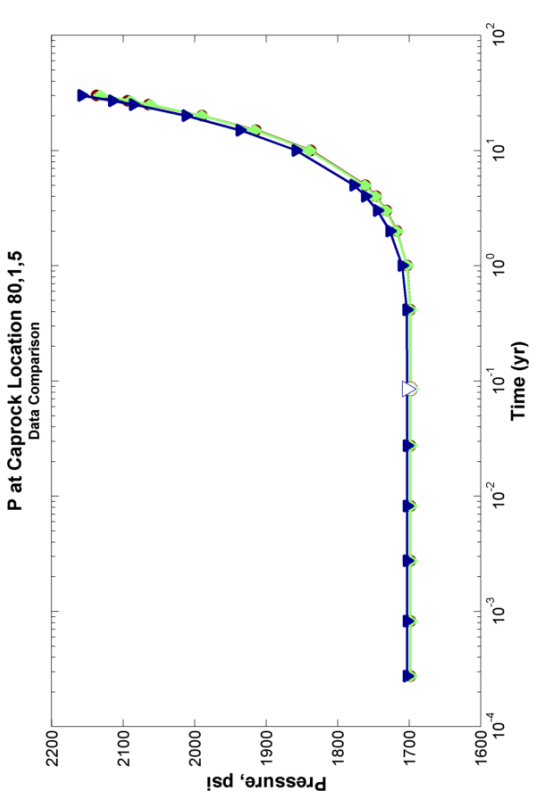
P at Caprock Location 80,1,5
Data Comparison
Pressure, psi
Time (yr)

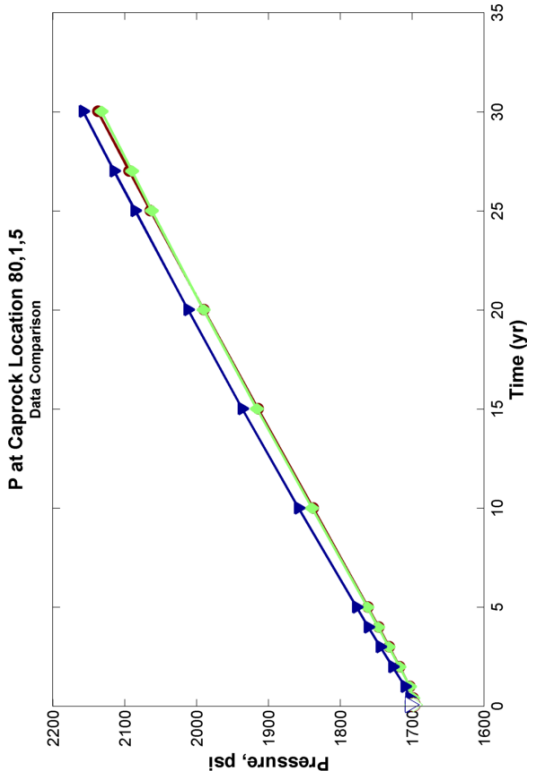
P at Caprock Location 80,1,5
Data Comparison
Pressure, psi
Time (yr)

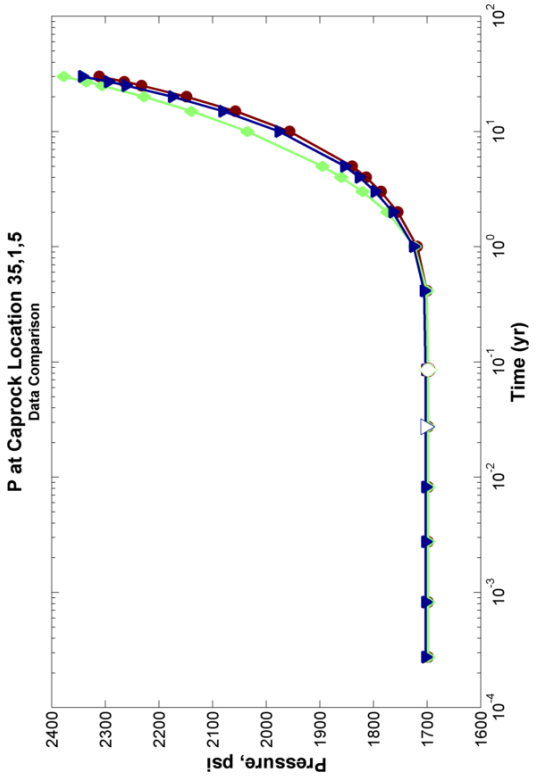
P at Caprock Location 35,1,5
Data Comparison
Pressure, psi
Time (yr)

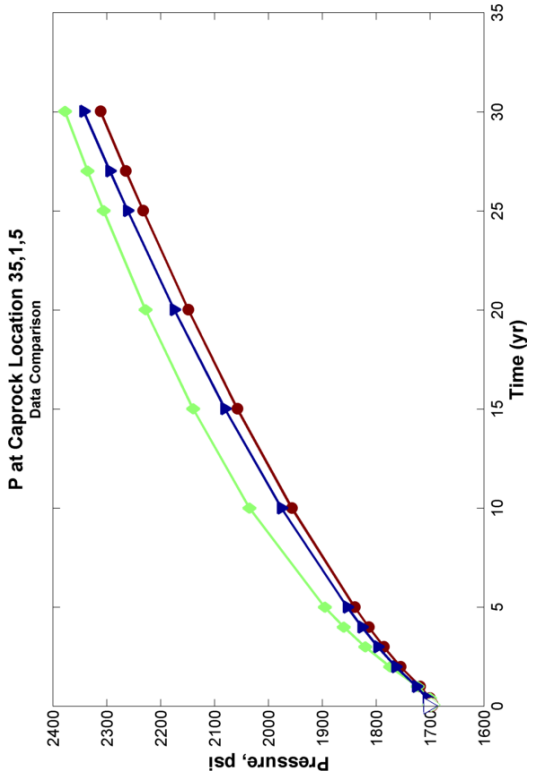
P at Caprock Location 35,1,5
Data Comparison
Pressure, psi
Time (yr)

REFERENCE RELATIVE PERMEABILITY CASE:
Parameter 4 Comparison
Mean Reservoir Permeability

	0.5 Slope Linear Fit x Value, psi (y =x*time^0.5)	
	Pressure Front	CO2Front
LOW Mean Reservoir Permability = 12 mD	7331.81	272.5
REF Mean Reservoir Permability = 46 mD	16554.65	359.68
HIGH Mean Reservoir Permability = 220 mD	19335.19	444.58

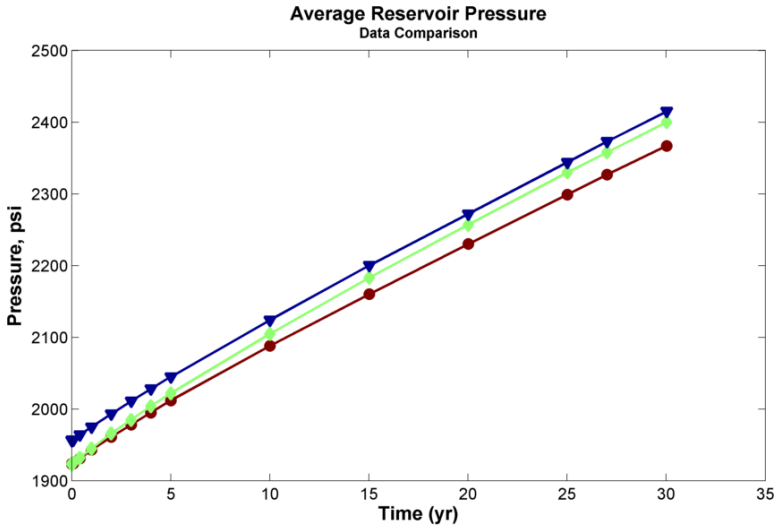

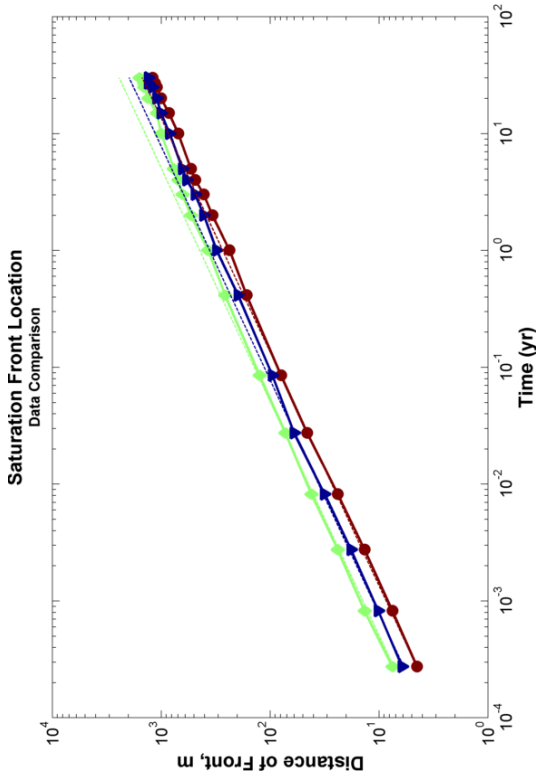
Saturation Front Location
Data Comparison
Distance of Front, m
Time (yr)

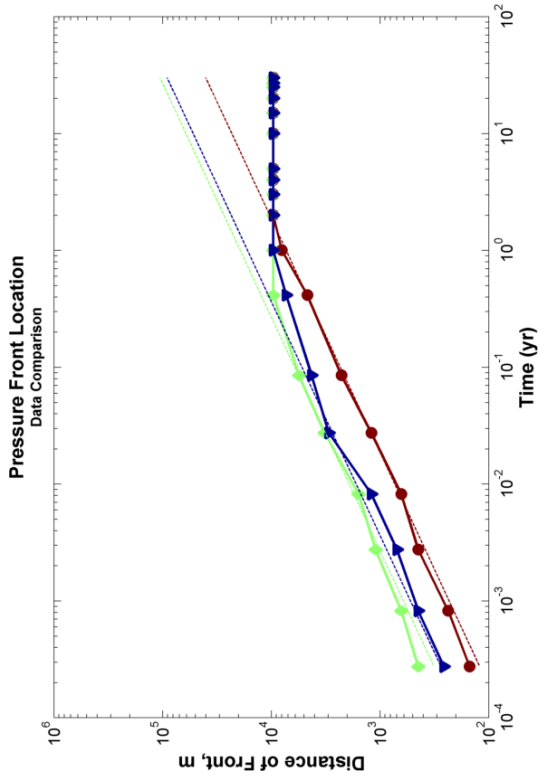
Pressure Front Location
Data Comparison
Distance of Front, m
Time (yr)

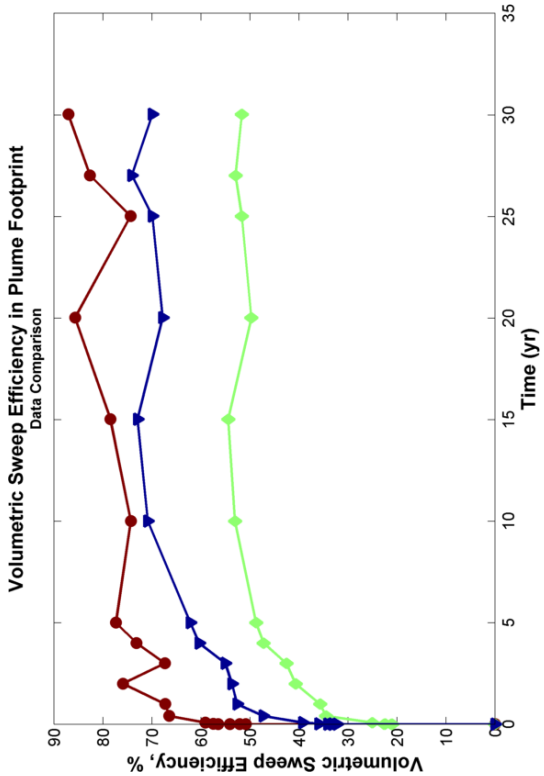
Volumetric Sweep Efficiency in Plume Footprint
Data Comparison
Volumetric Sweep Efficiency, %
Time (yr)

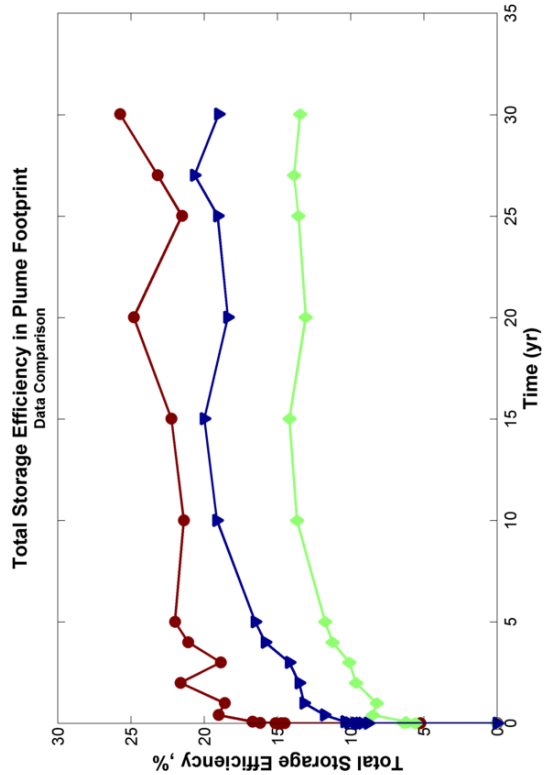
Total Storage Efficiency in Plume Footprint
Data Comparison
Total Storage Efficiency ,%
Time (yr)

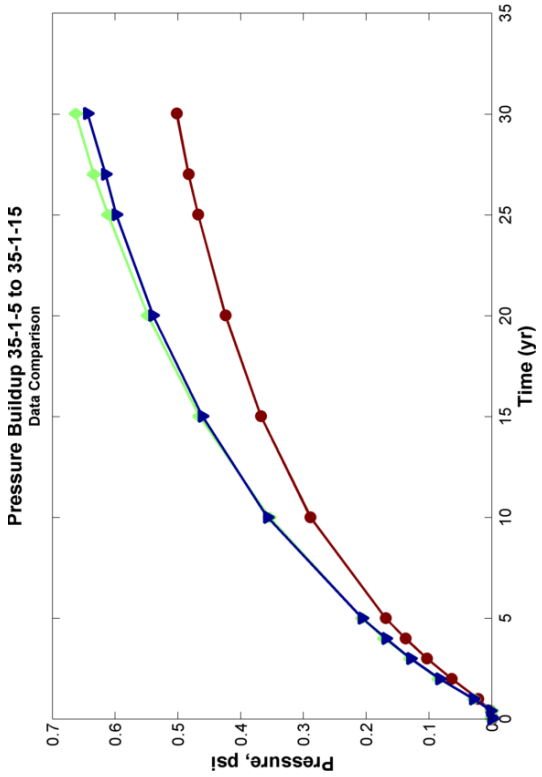
Pressure Buildup 35-1-5 to 35-1-15
Data Comparison
Pressure, psi
Time (yr)

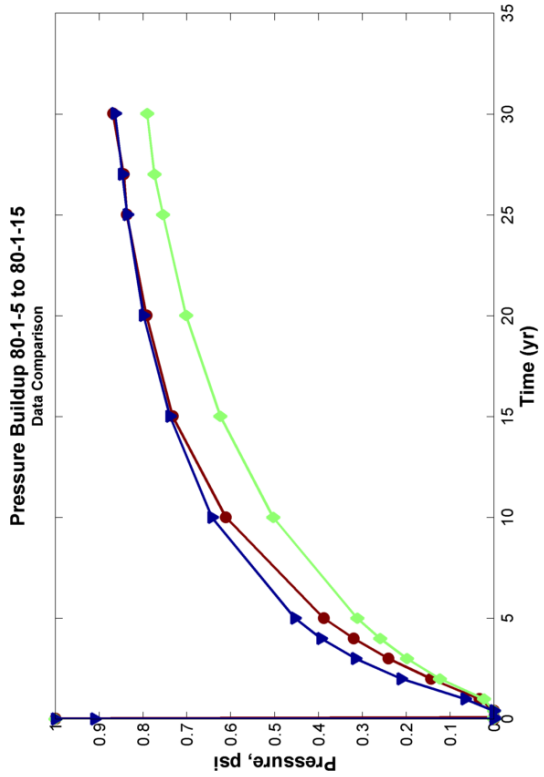
Pressure Buildup 80-1-5 to 80-1-15
Data Comparison
Pressure, psi
Time (yr)

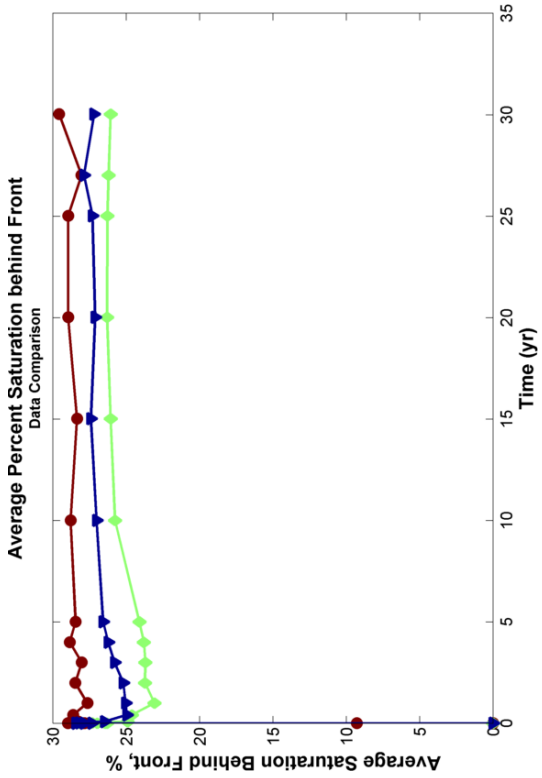
Average Percent Saturation behind Front
Data Comparison
Average Saturation Behind Front, %
Time (yr)

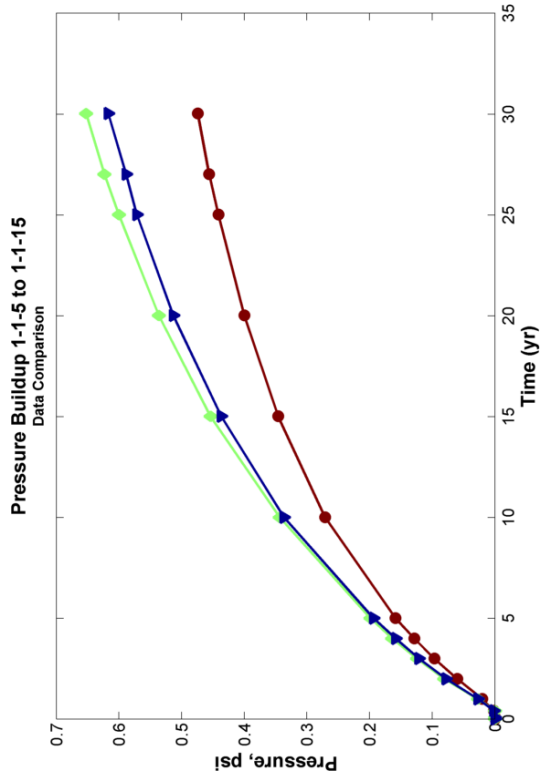
Pressure Buildup 1-1-5 to 1-1-15
Data Comparison
Pressure, psi
Time (yr)

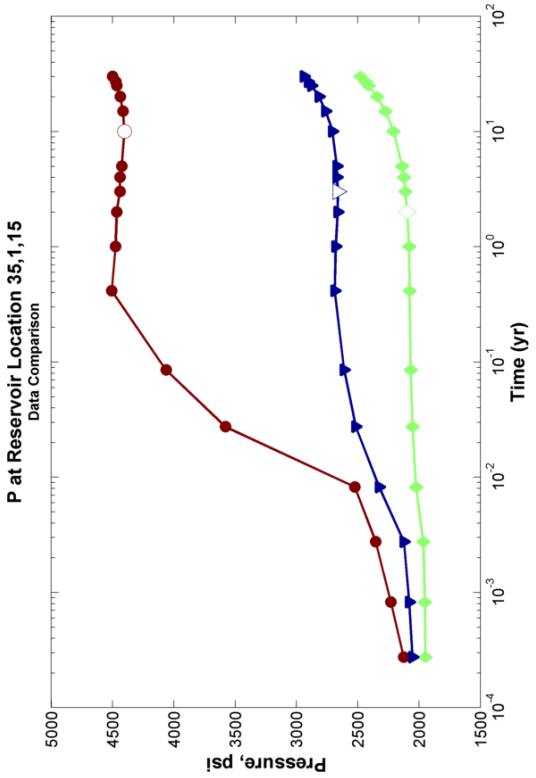
P at Reservoir Location 35,1,15
Data Comparison
Pressure, psi
Time (yr)

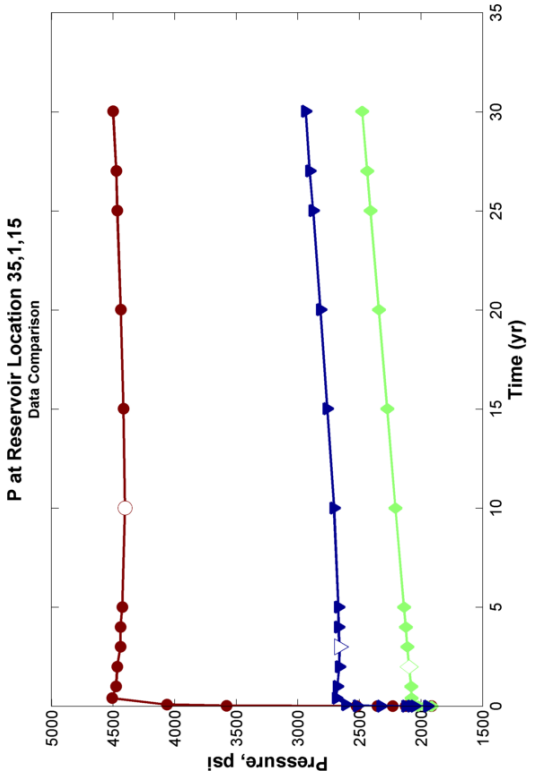
P at Reservoir Location 35,1,15
Data Comparison
Pressure, psi
Time (yr)

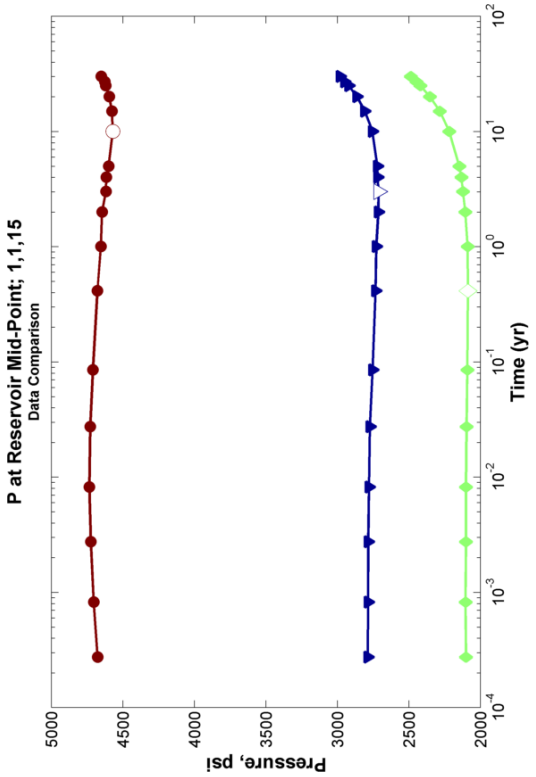
P at Reservoir Mid-Point; 1,1,15
Data Comparison
Pressure, psi
Time (yr)

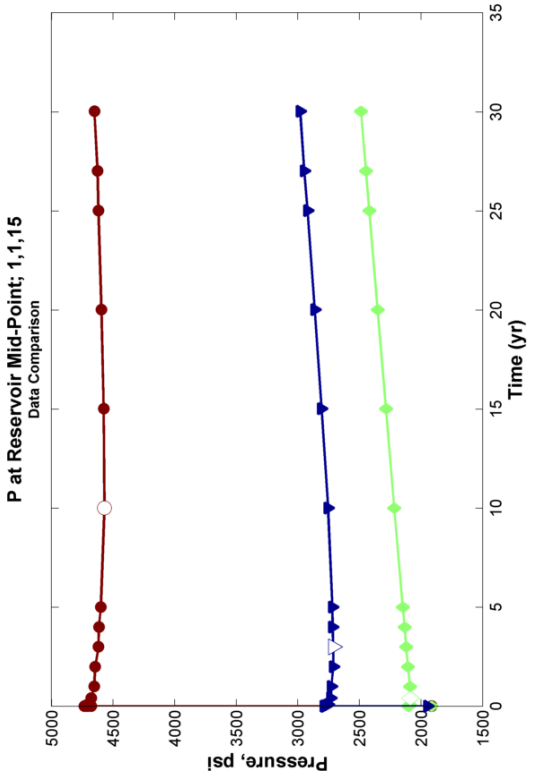
P at Reservoir Mid-Point; 1,1,15
Data Comparison
Pressure, psi
Time (yr)

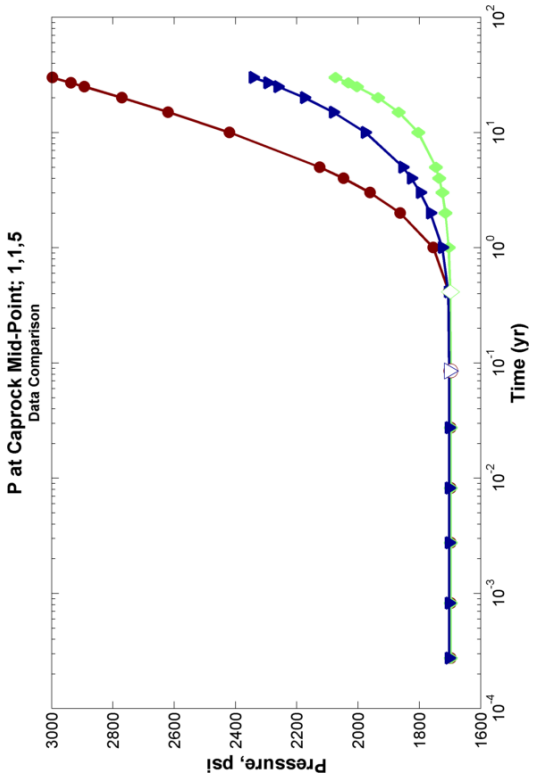
P at Caprock Mid-Point; 1,1,5
Data Comparison
Pressure, psi
Time (yr)

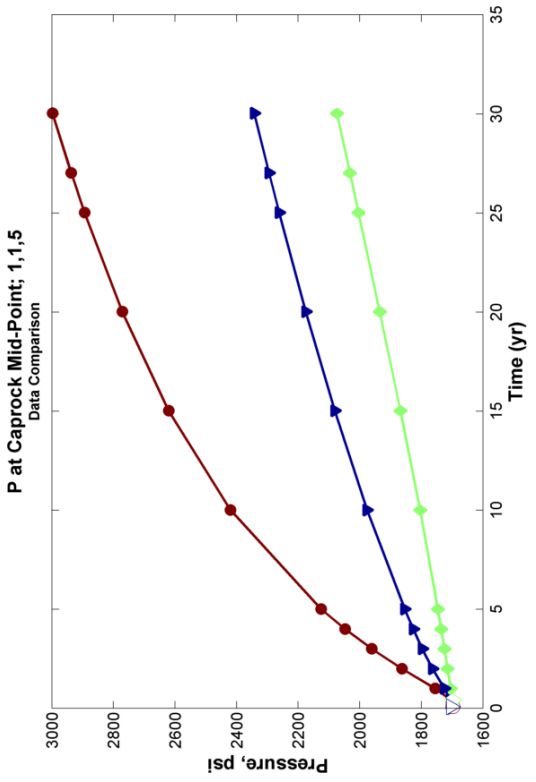
P at Caprock Mid-Point; 1,1,5
Data Comparison
Pressure, psi
Time (yr)

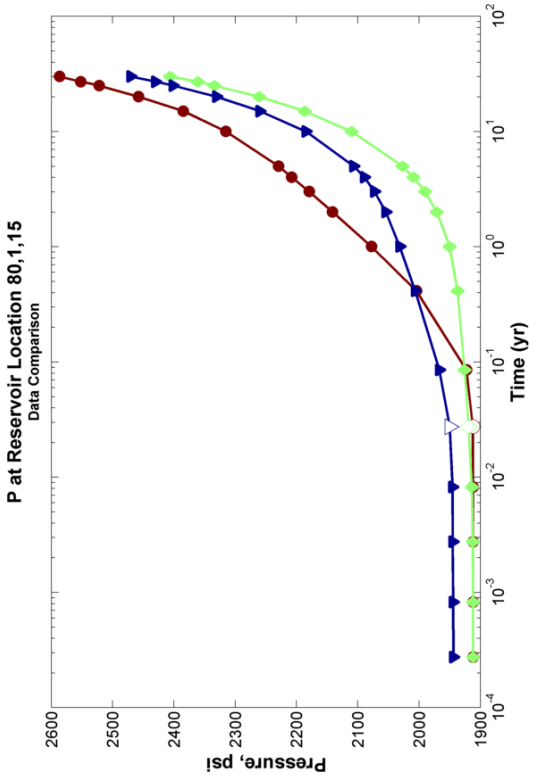
P at Reservoir Location 80,1,15
Data Comparison
Pressure, psi
Time (yr)

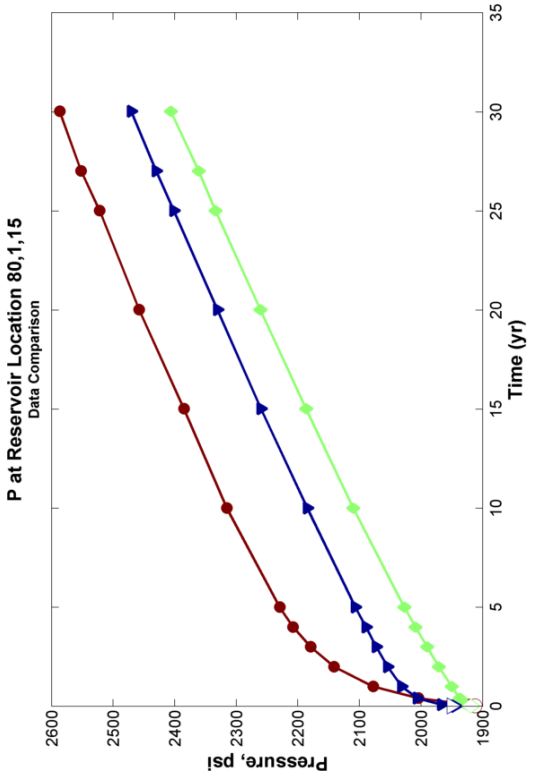
P at Reservoir Location 80,1,15
Data Comparison
Pressure, psi
Time (yr)

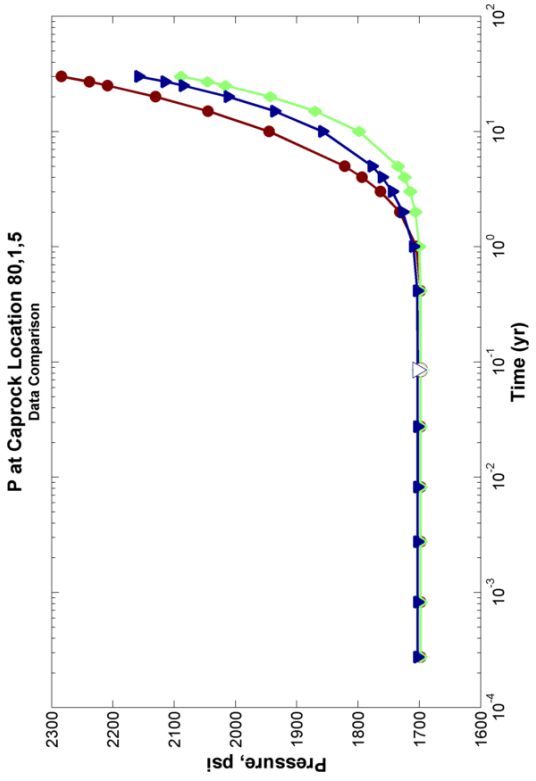
P at Caprock Location 80,1,5
Data Comparison
Pressure, psi
Time (yr)

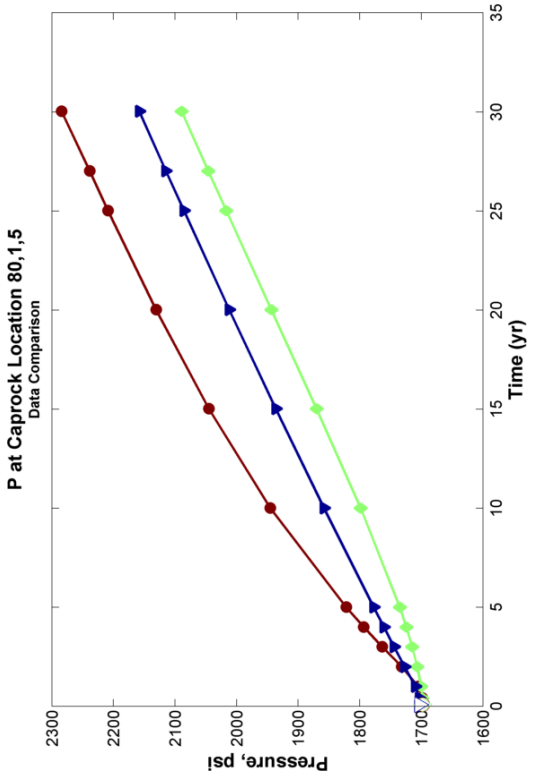
P at Caprock Location 80,1,5
Data Comparison
Pressure, psi
Time (yr)

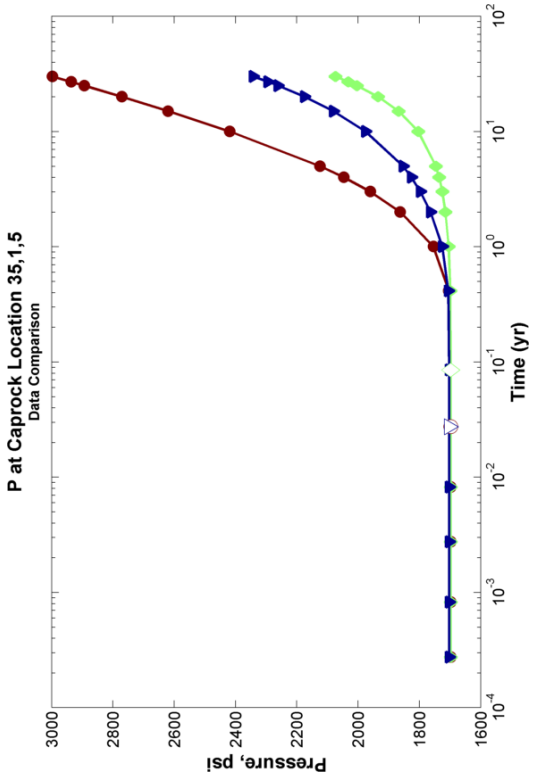
P at Caprock Location 35,1,5
Data Comparison
Pressure, psi
Time (yr)

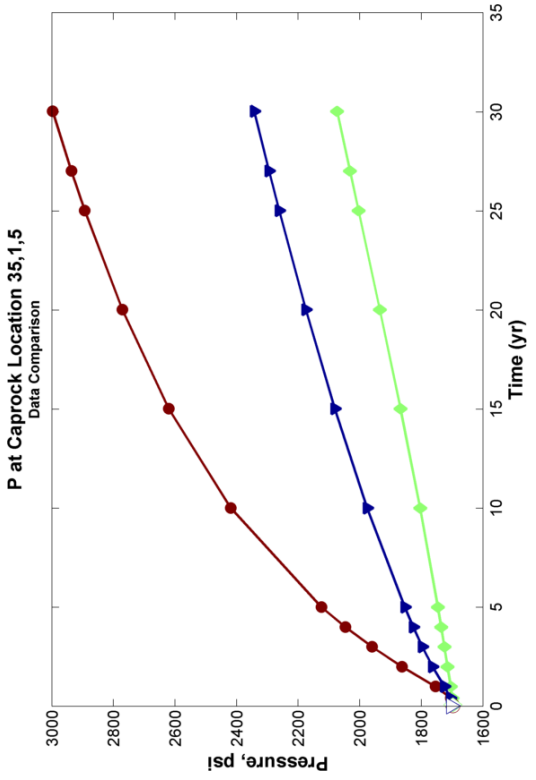
P at Caprock Location 35,1,5
Data Comparison
Pressure, psi
Time (yr)

REFERENCE RELATIVE PERMEABILITY CASE:
Parameter 5 Comparison
Cap Rock Permeability

	0.5 Slope Linear Fit x Value, psi (y =x*time^0.5)	
	Pressure Front	CO2Front
LOW Cap Rock Permeability = 0.002 mD	12528.39	359.68
Ref Cap Rock Permeability = 0.02 mD	16554.65	359.68
HIGH Cap Rock Permeability =0.2 mD	12018.72	359.68

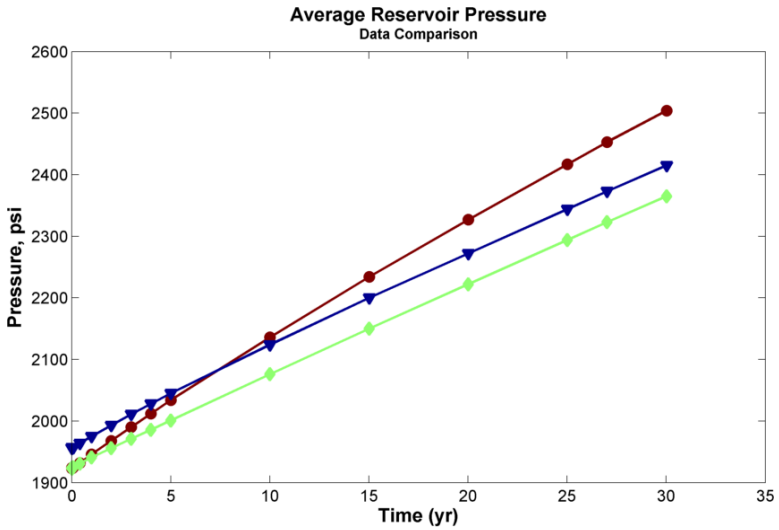

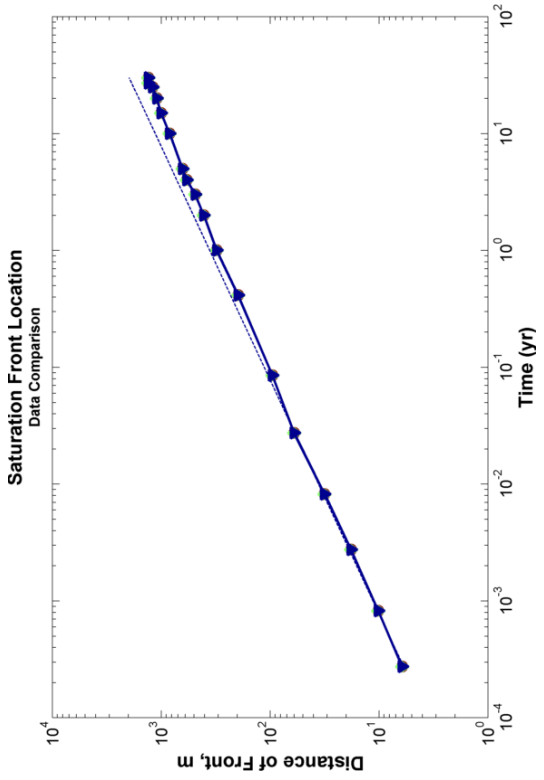
Saturation Front Location
Data Comparison
Distance of Front, m
Time (yr)

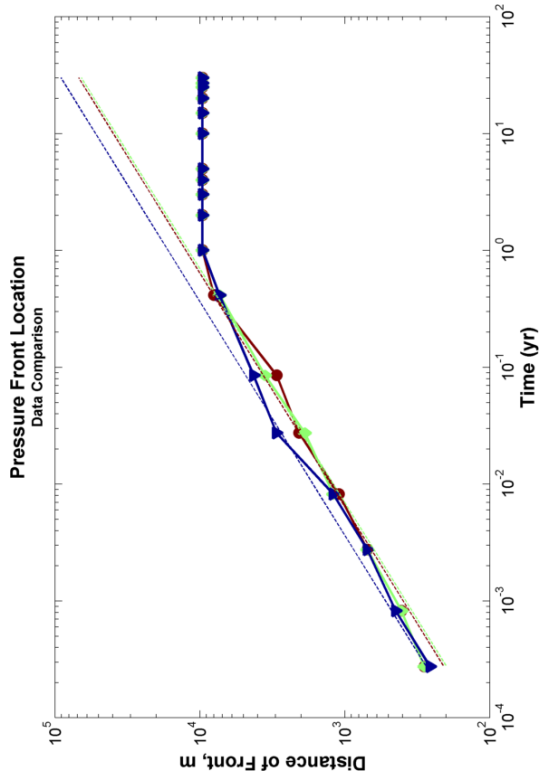
Pressure Front Location
Data Comparison
Distance of Front, m
Time (yr)

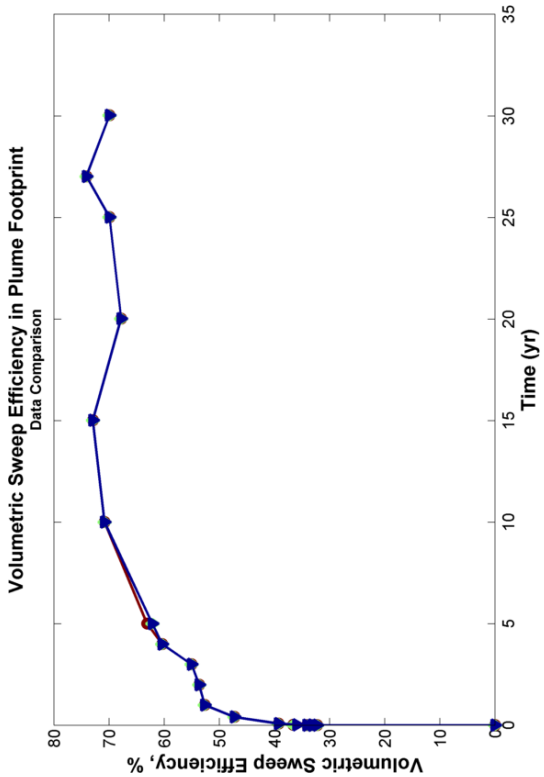
Volumetric Sweep Efficiency in Plume Footprint
Data Comparison
Volumetric Sweep Efficiency, %
Time (yr)

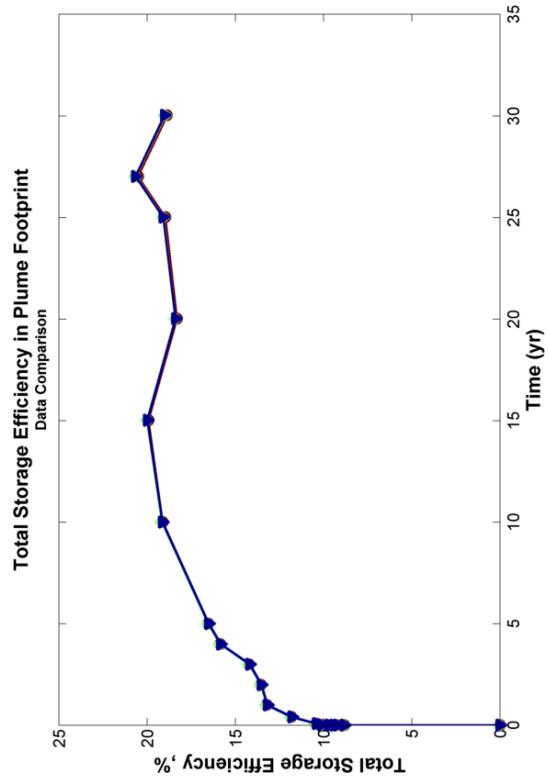
Total Storage Efficiency in Plume Footprint
Data Comparison
Total Storage Efficiency ,%
Time (yr)

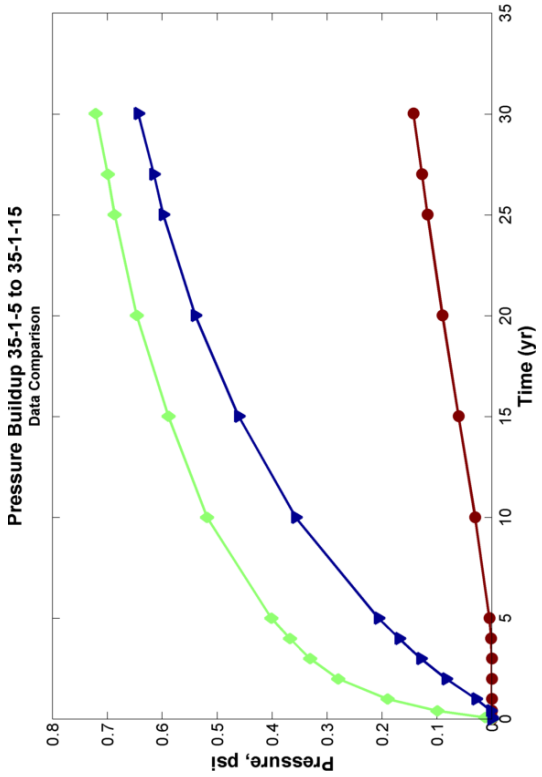
Pressure Buildup 35-1-5 to 35-1-15
Data Comparison
Pressure, psi
Time (yr)

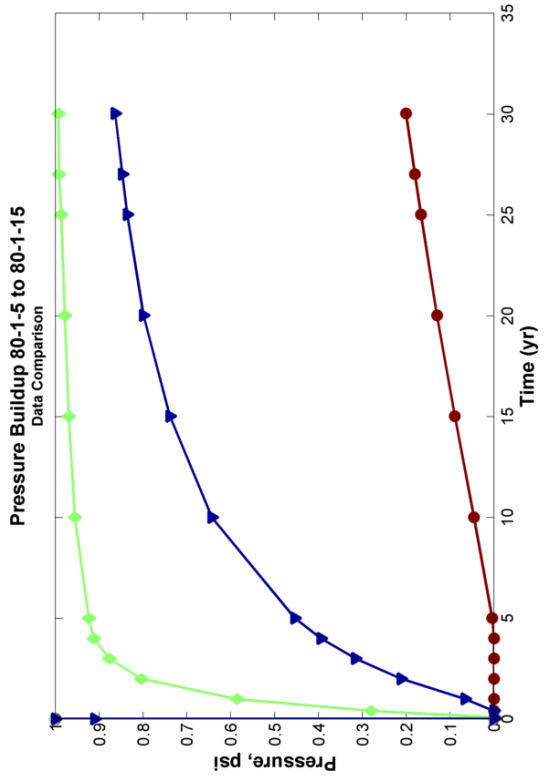
Pressure Buildup 80-1-5 to 80-1-15
Data Comparison
Pressure, psi
Time (yr)

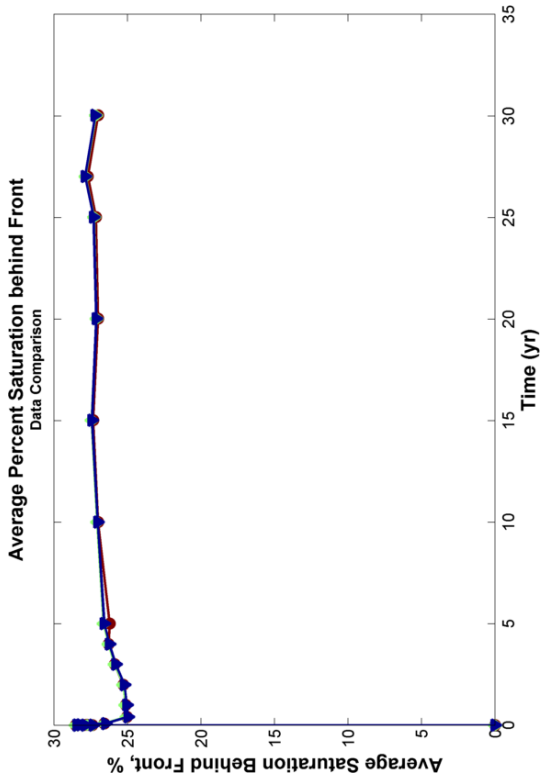
Average Percent Saturation behind Front
Data Comparison
Average Saturation Behind Front, %
Time (yr)

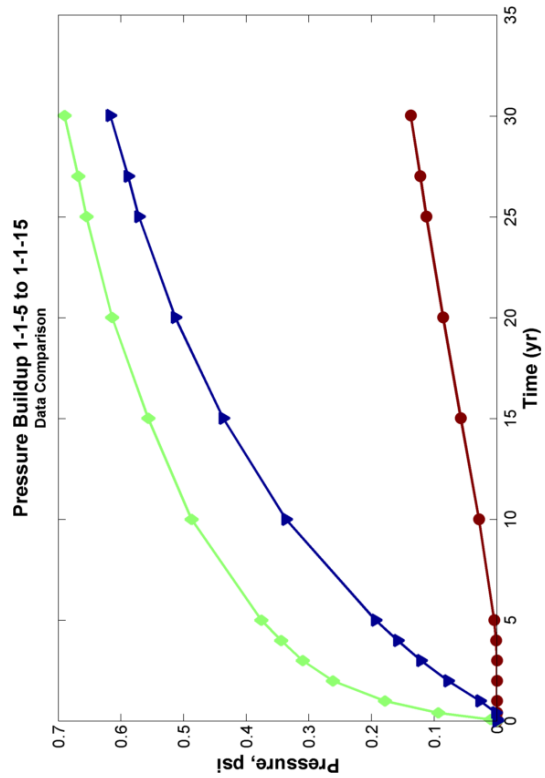
Pressure Buildup 1-1-5 to 1-1-15
Data Comparison
Pressure, psi
Time (yr)

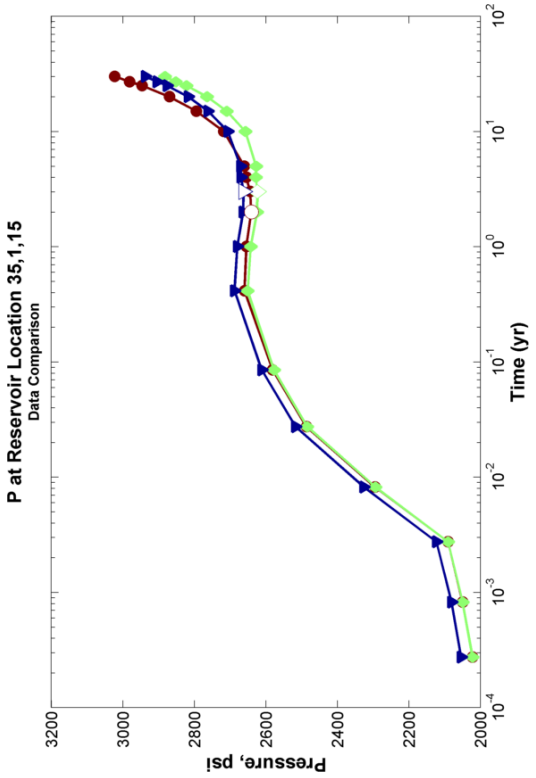
P at Reservoir Location 35,1,15
Data Comparison
Pressure, psi
Time (yr)

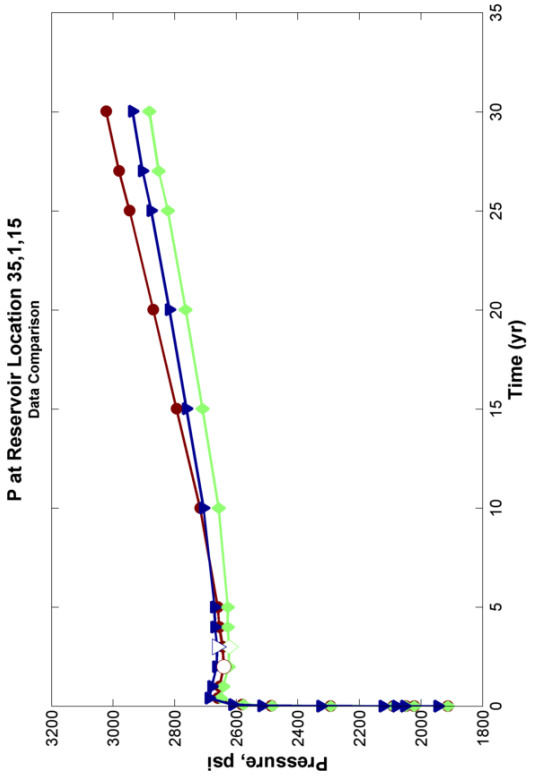
P at Reservoir Location 35,1,15
Data Comparison
Pressure, psi
Time (yr)

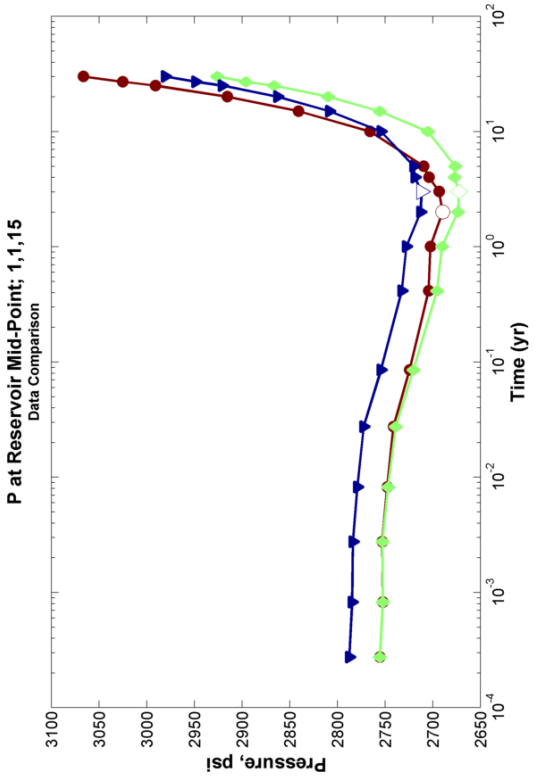
P at Reservoir Mid-Point; 1,1,15
Data Comparison
Pressure, psi
Time (yr)

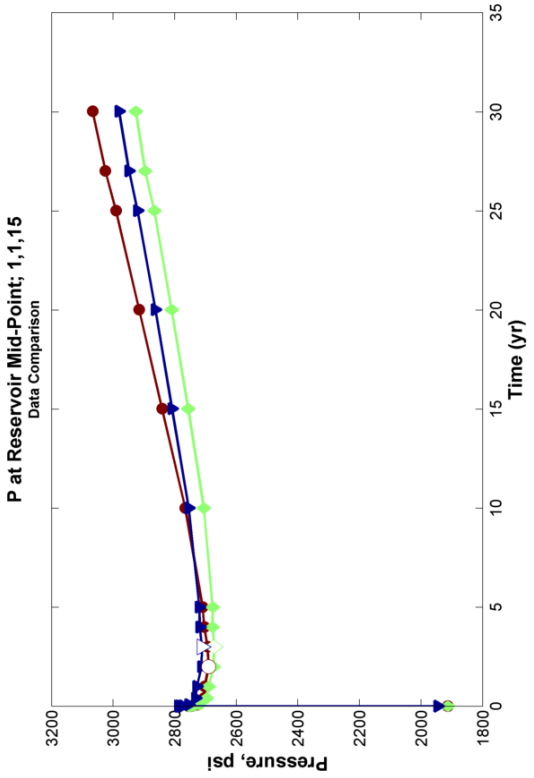
P at Reservoir Mid-Point; 1,1,15
Data Comparison
Pressure, psi
Time (yr)

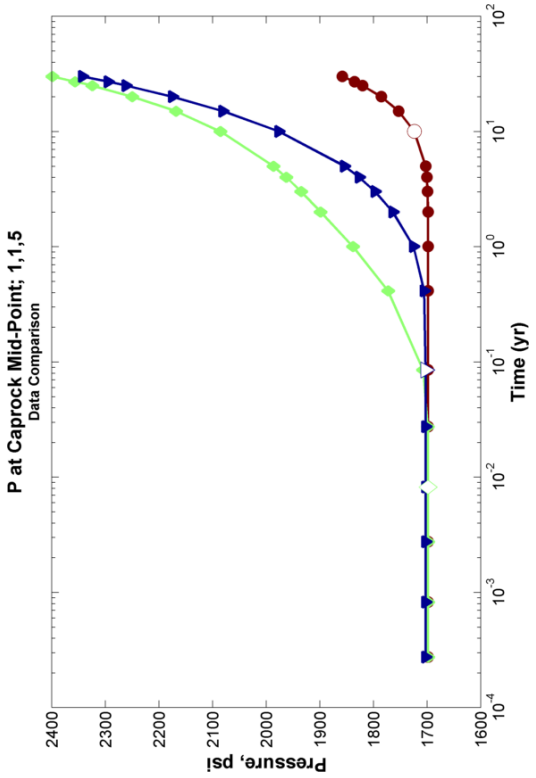
P at Caprock Mid-Point; 1,1,5
Data Comparison
Pressure, psi
Time (yr)

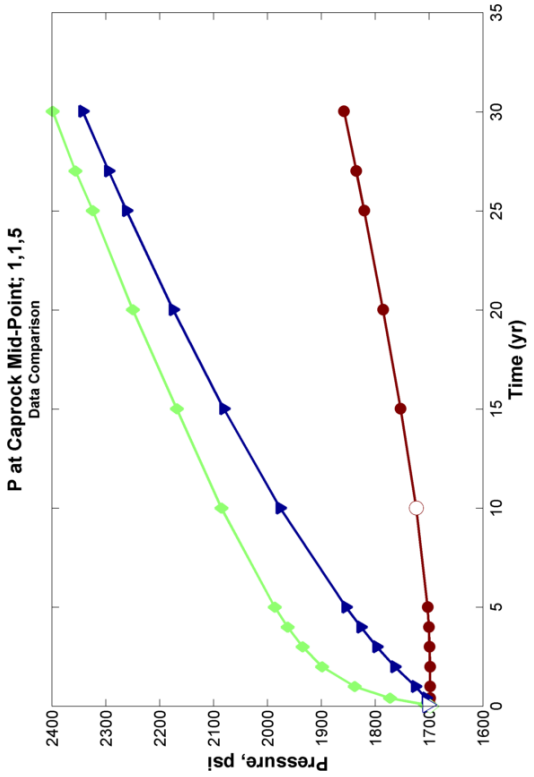
P at Caprock Mid-Point; 1,1,5
Data Comparison
Pressure, psi
Time (yr)

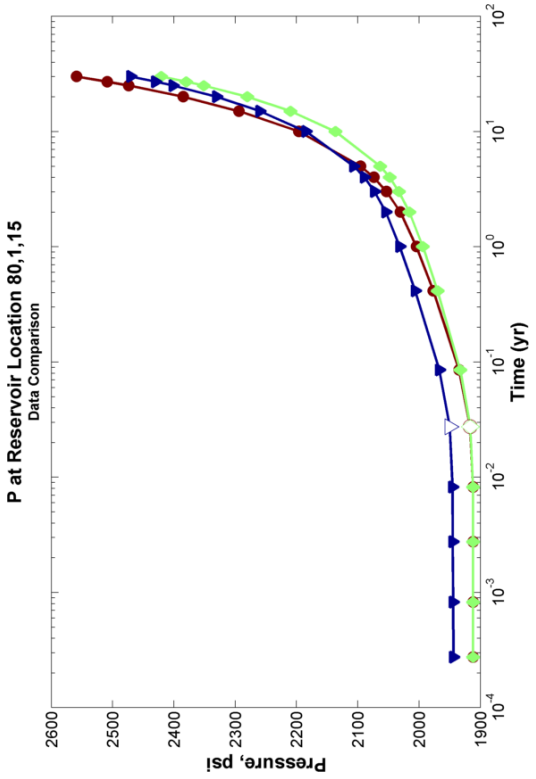
P at Reservoir Location 80,1,15
Data Comparison
Pressure, psi
Time (yr)

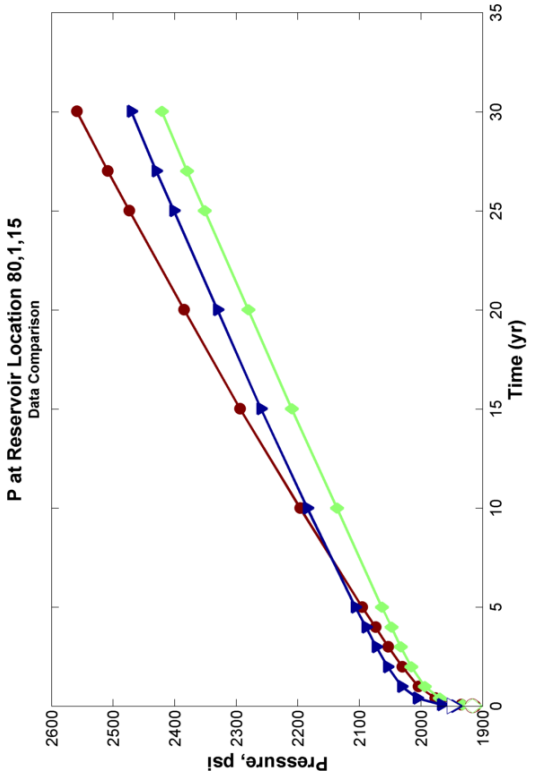
P at Reservoir Location 80,1,15
Data Comparison
Pressure, psi
Time (yr)

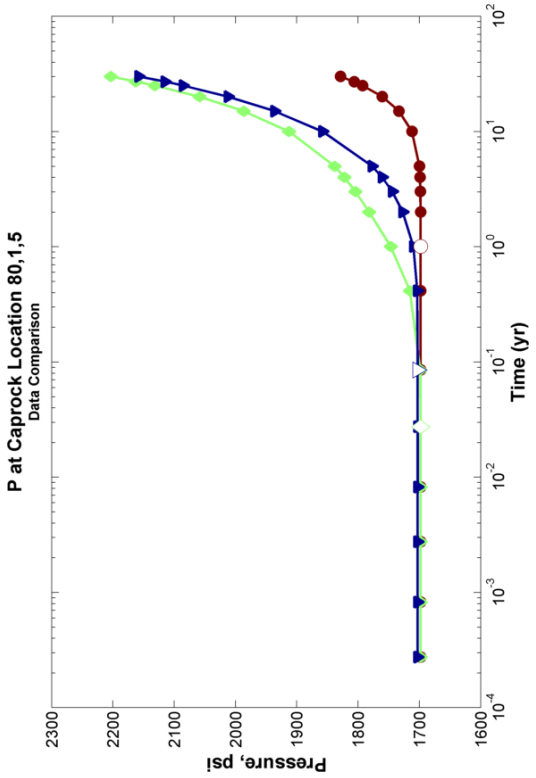
P at Caprock Location 80,1,5
Data Comparison
Pressure, psi
Time (yr)

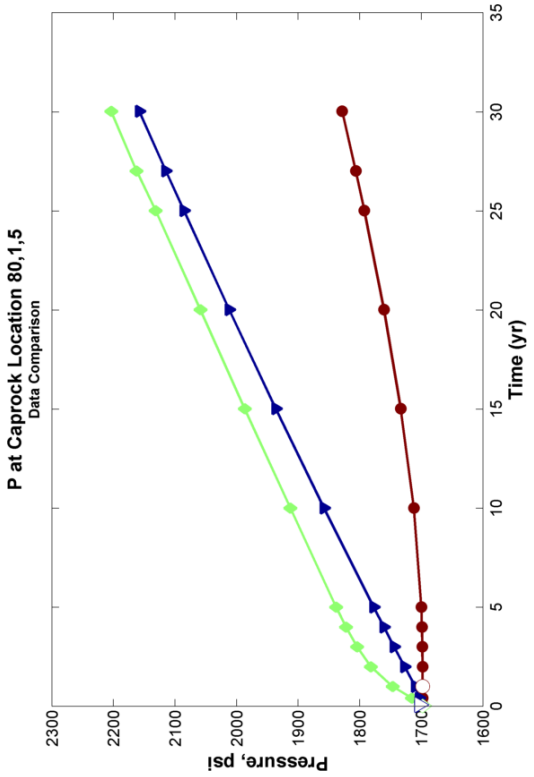
P at Caprock Location 80,1,5
Data Comparison
Pressure, psi
Time (yr)

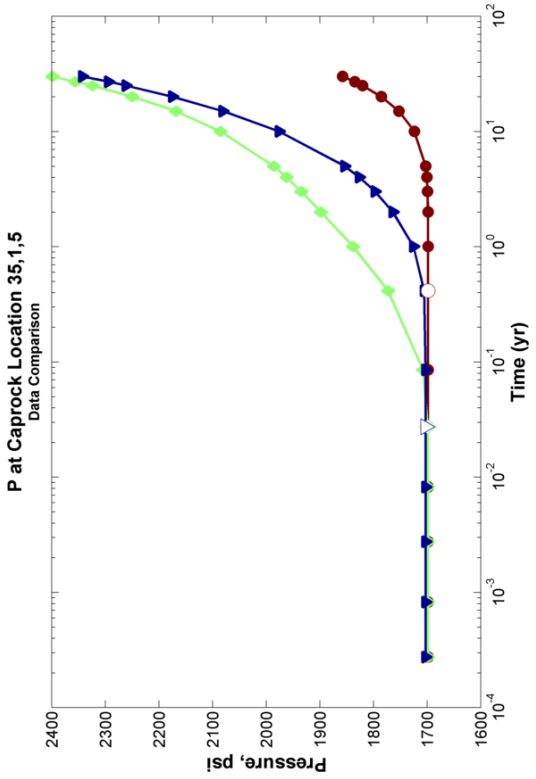
P at Caprock Location 35,1,5
Data Comparison
Pressure, psi
Time (yr)

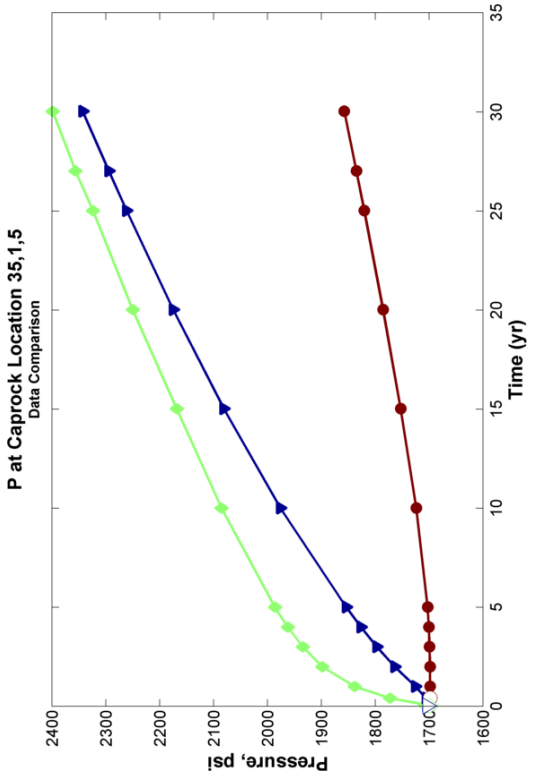
P at Caprock Location 35,1,5
Data Comparison
Pressure, psi
Time (yr)

REFERENCE RELATIVE PERMEABILITY CASE:
Parameter 6 Comparison
Reservoir Porosity

	0.5 Slope Linear Fit x Value, psi (y =x*time^0.5)	
	Pressure Front	CO2Front
LOW Reservoir Porosity = 0.08	15976.61	435.22
Ref Reservoir Porosity = 0.12	16554.65	359.68
HIGH Reservoir Porosity = 0.18	9856.92	298.99

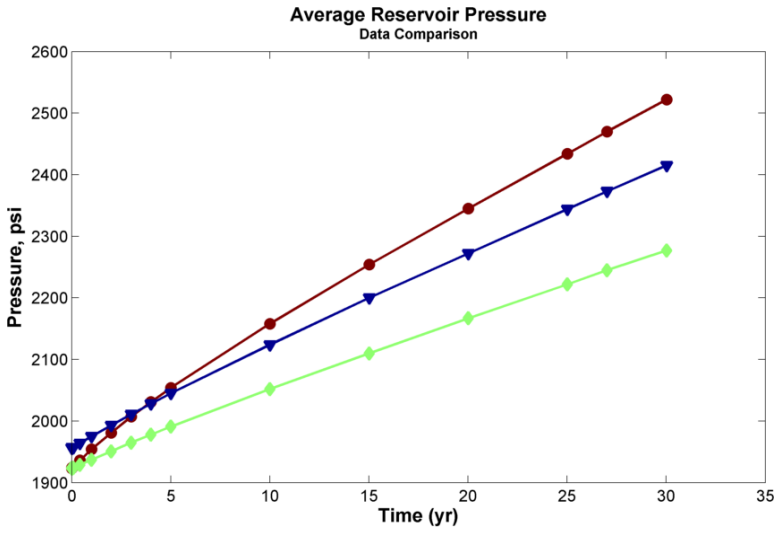

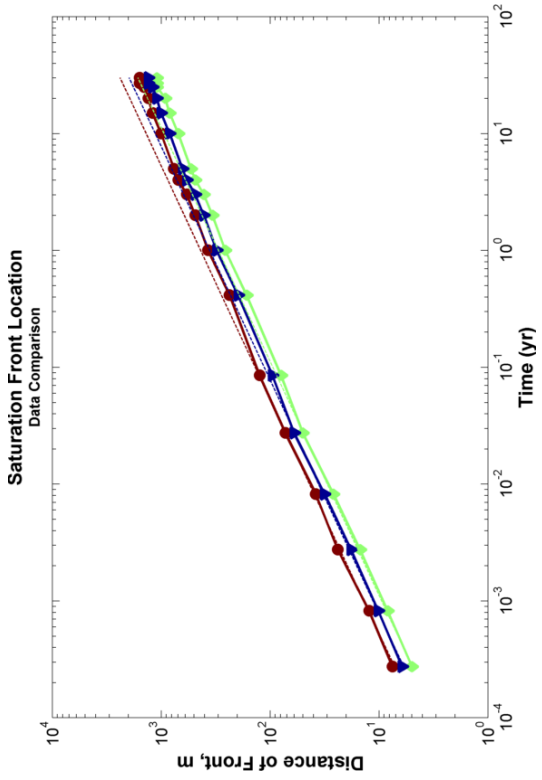
Saturation Front Location
Data Comparison
Distance of Front, m
Time (yr)

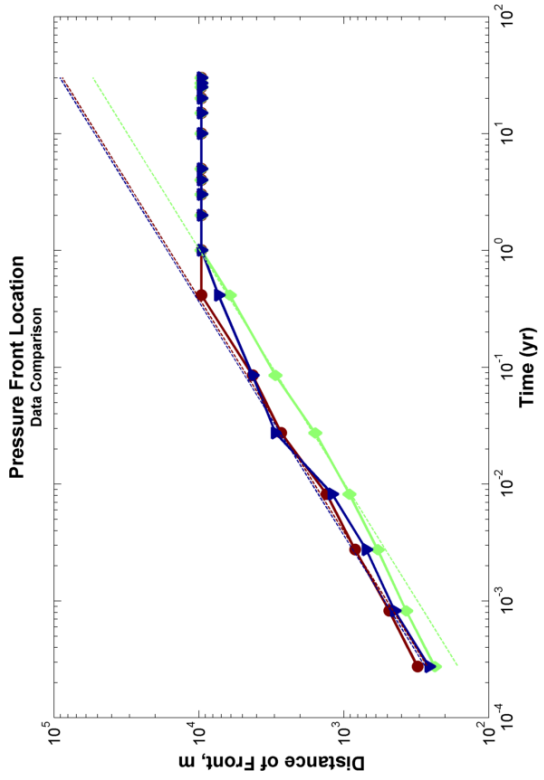
Pressure Front Location
Data Comparison
Distance of Front, m
Time (yr)

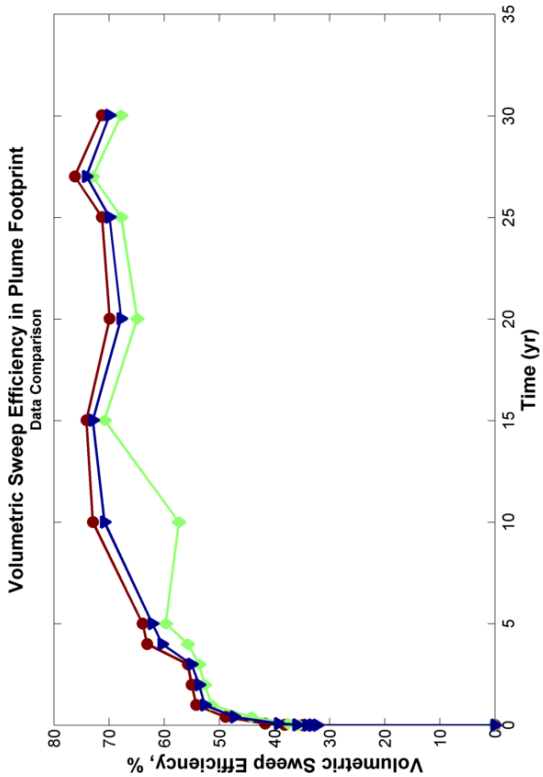
Volumetric Sweep Efficiency in Plume Footprint
Data Comparison
Volumetric Sweep Efficiency, %
Time (yr)

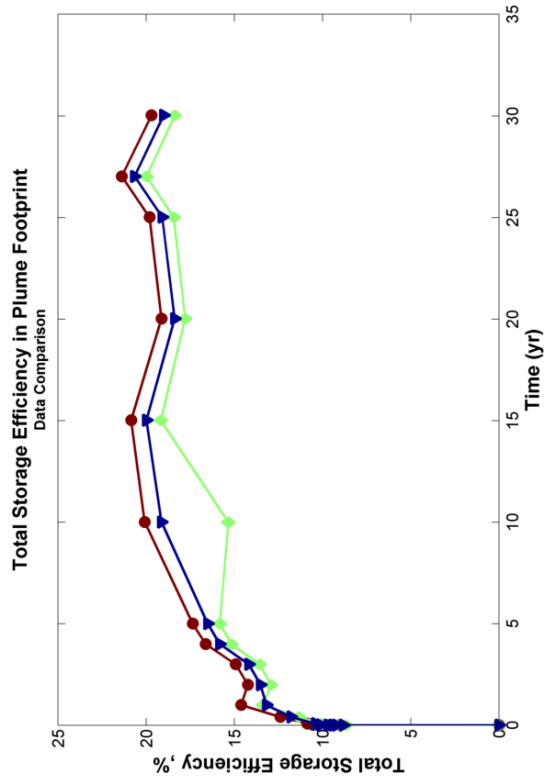
Total Storage Efficiency in Plume Footprint
Data Comparison
Total Storage Efficiency ,%
Time (yr)

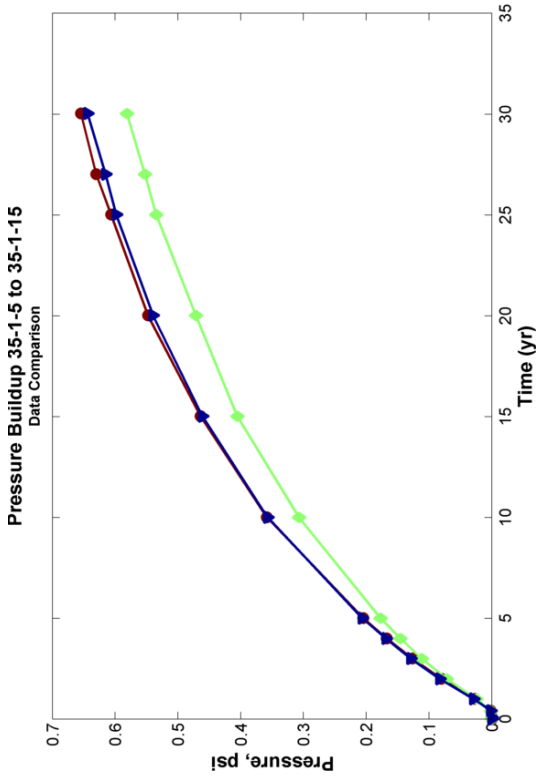
Pressure Buildup 35-1-5 to 35-1-15
Data Comparison
Pressure, psi
Time (yr)

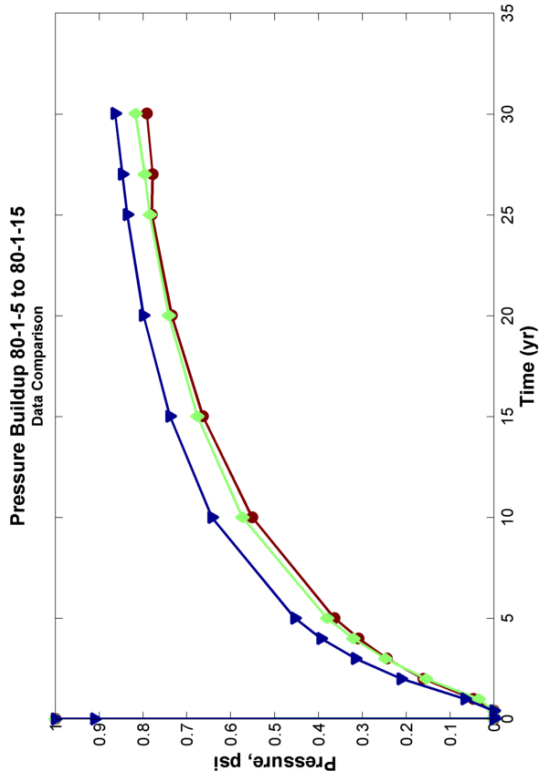
Pressure Buildup 80-1-5 to 80-1-15
Data Comparison
Pressure, psi
Time (yr)

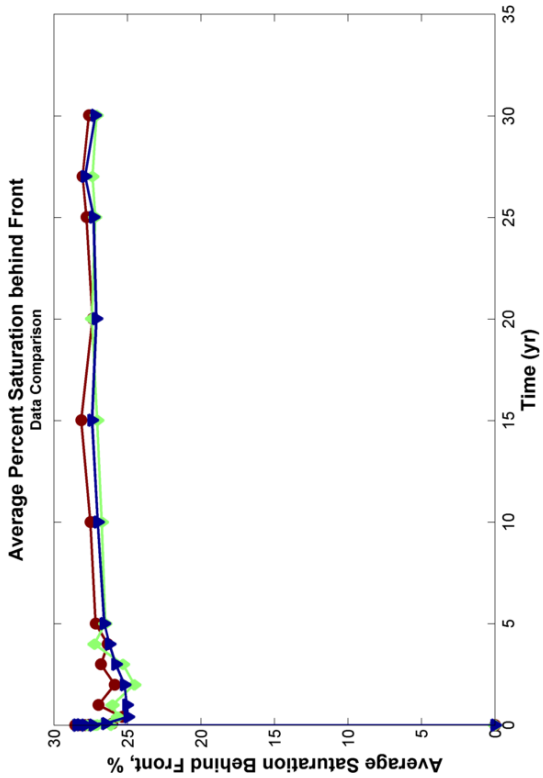
Average Percent Saturation behind Front
Data Comparison
Average Saturation Behind Front, %
Time (yr)

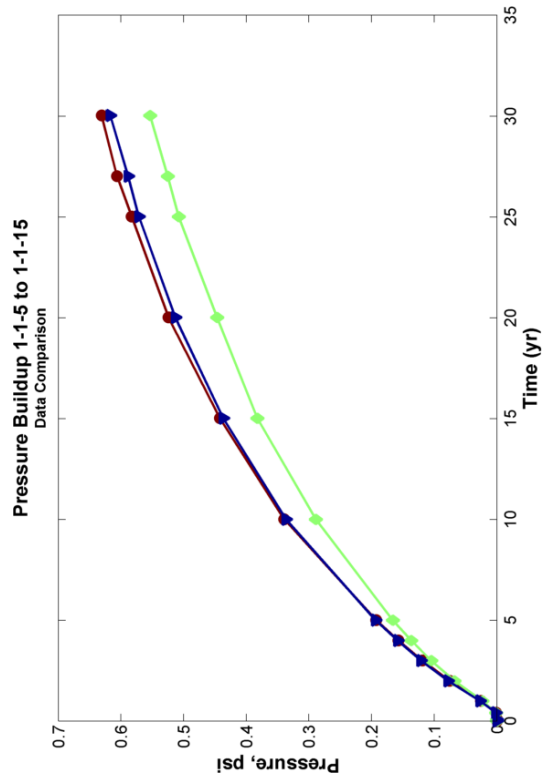
Pressure Buildup 1-1-5 to 1-1-15
Data Comparison
Pressure, psi
Time (yr)

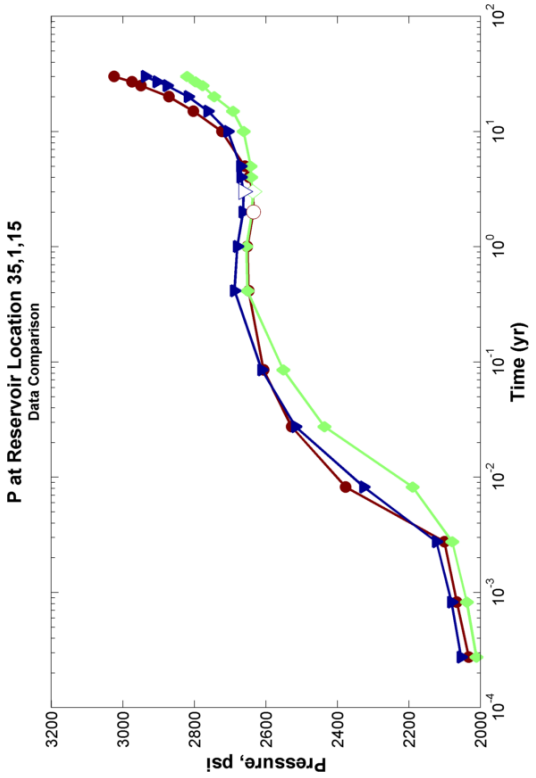
P at Reservoir Location 35,1,15
Data Comparison
Pressure, psi
Time (yr)

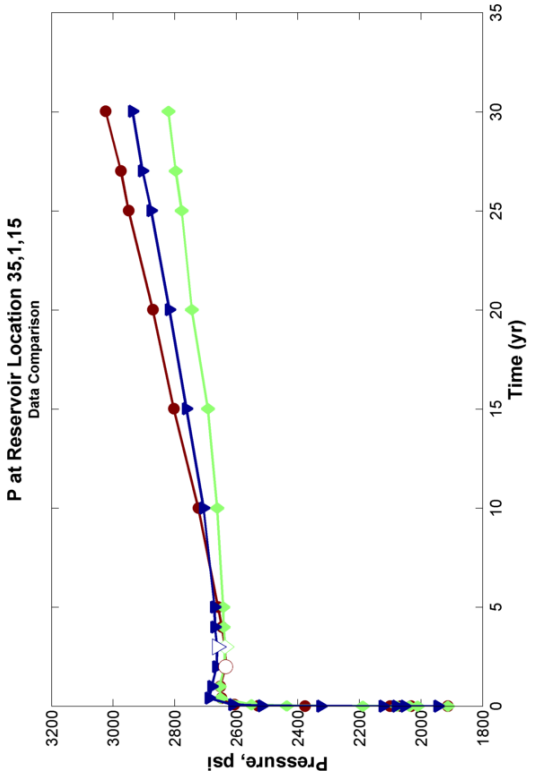
P at Reservoir Location 35,1,15
Data Comparison
Pressure, psi
Time (yr)

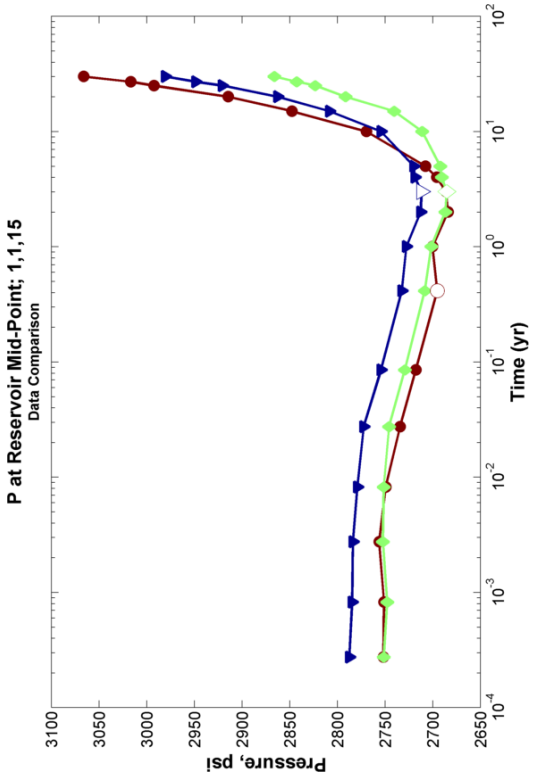
P at Reservoir Mid-Point; 1,1,15
Data Comparison
Pressure, psi
Time (yr)

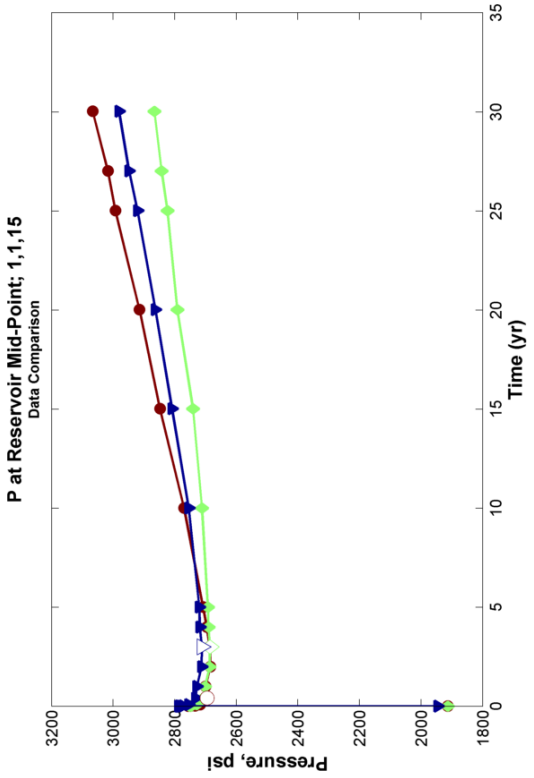
P at Reservoir Mid-Point; 1,1,15
Data Comparison
Pressure, psi
Time (yr)

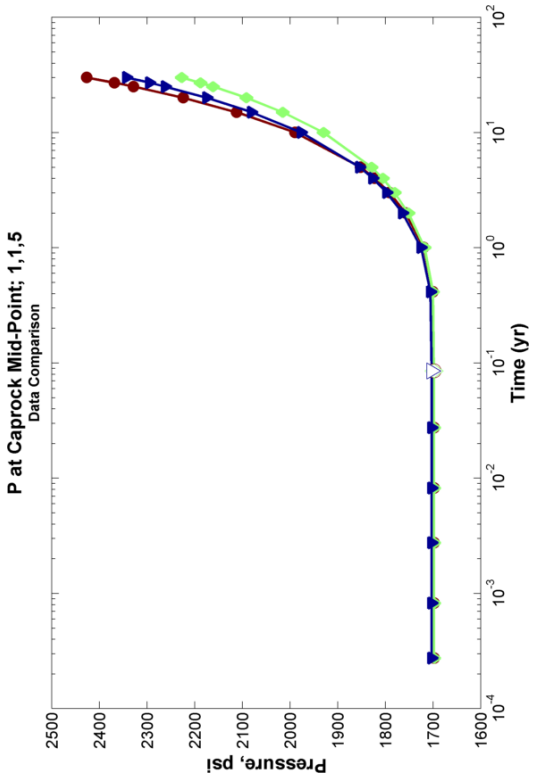
P at Caprock Mid-Point; 1,1,5
Data Comparison
Pressure, psi
Time (yr)

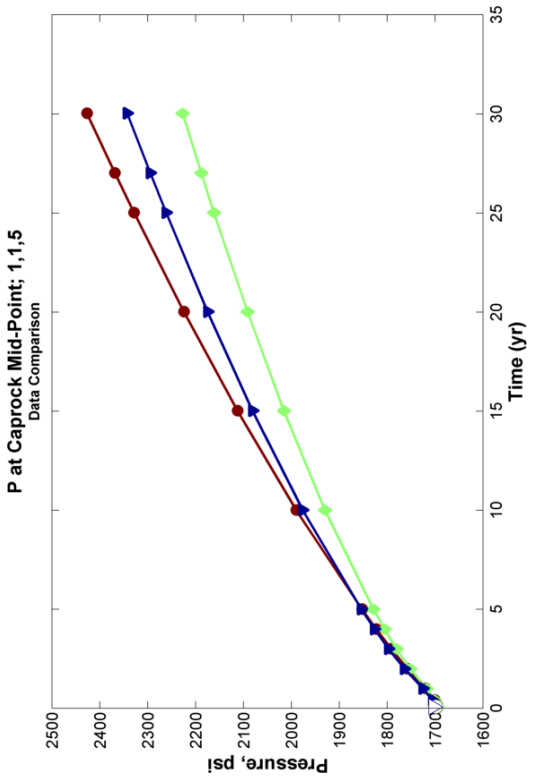
P at Caprock Mid-Point; 1,1,5
Data Comparison
Pressure, psi
Time (yr)

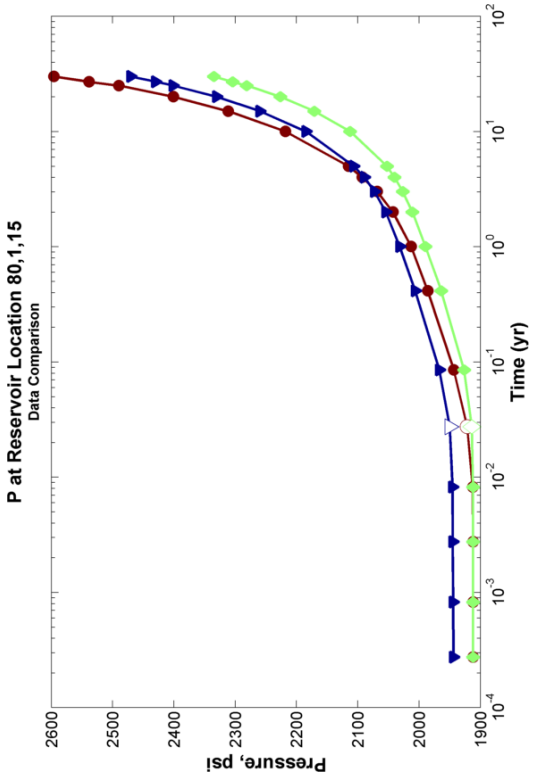
P at Reservoir Location 80,1,15
Data Comparison
Pressure, psi
Time (yr)

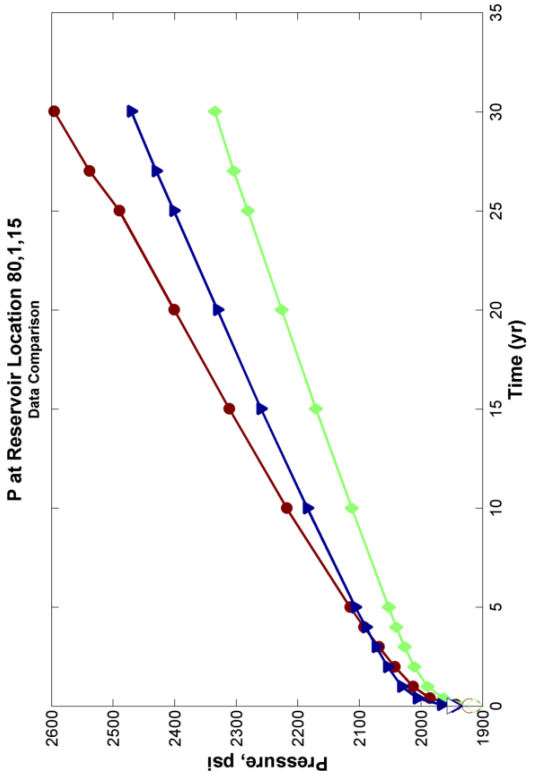
P at Reservoir Location 80,1,15
Data Comparison
Pressure, psi
Time (yr)

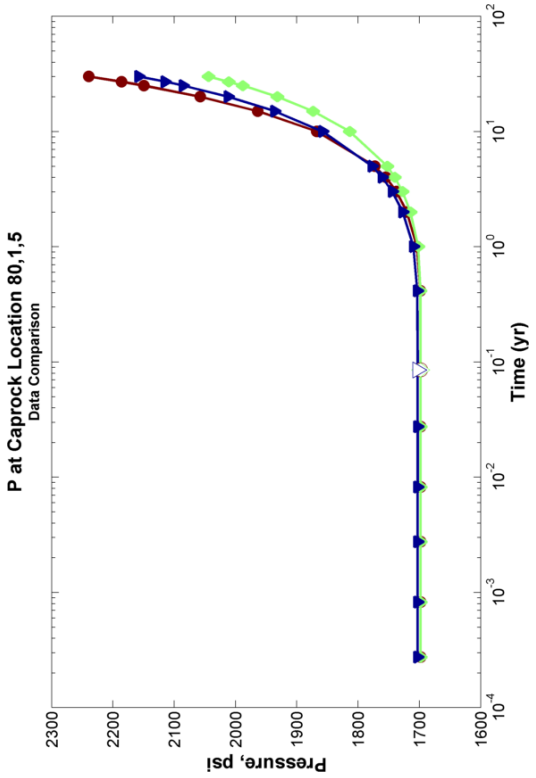
P at Caprock Location 80,1,5
Data Comparison
Pressure, psi
Time (yr)

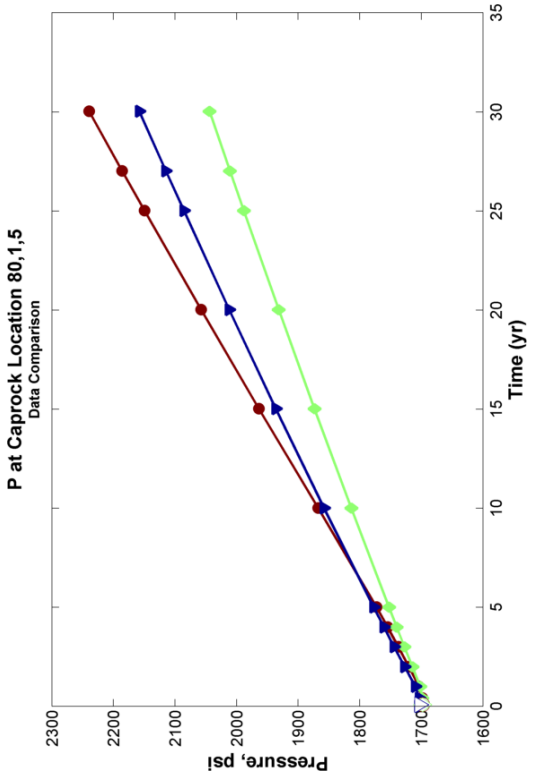
P at Caprock Location 80,1,5
Data Comparison
Pressure, psi
Time (yr)

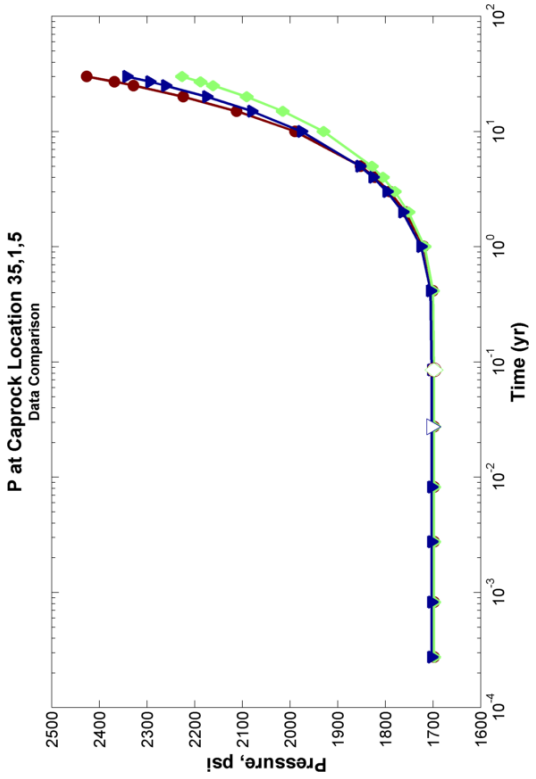
P at Caprock Location 35,1,5
Data Comparison
Pressure, psi
Time (yr)

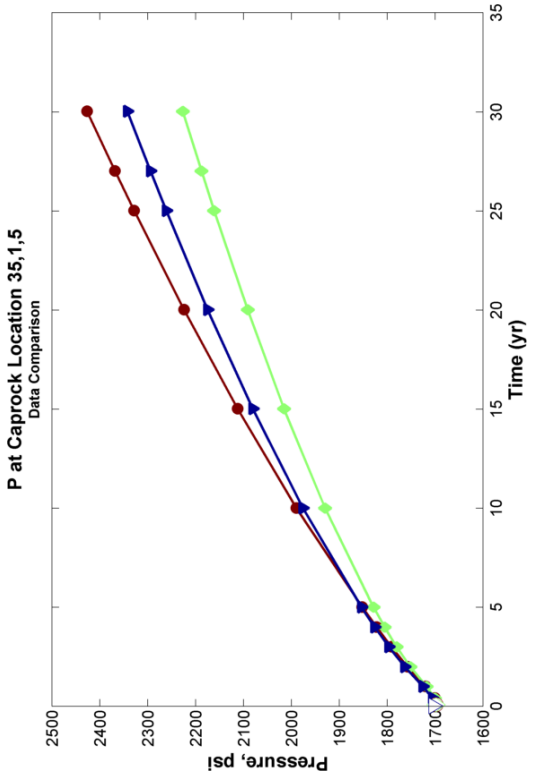
P at Caprock Location 35,1,5
Data Comparison
Pressure, psi
Time (yr)

REFERENCE RELATIVE PERMEABILITY CASE:
Parameter 7 Comparison
Cap Rock Porosity

	0.5 Slope Linear Fit x Value, psi (y =x*time^0.5)	
	Pressure Front	CO2Front
LOW Cap Rock Porosityy = 0.05	12528.39	359.68
Ref Cap Rock Porosity = 0.07	16554.65	359.68
HIGH Cap Rock Porosity = 0.1	12528.39	359.68

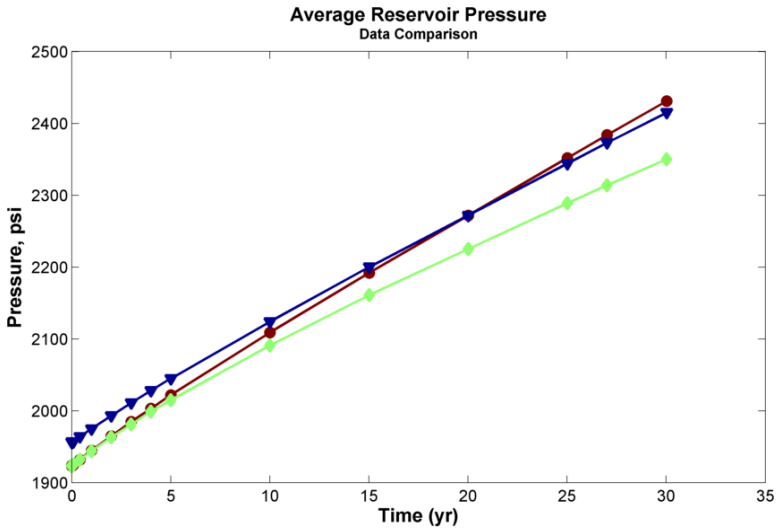

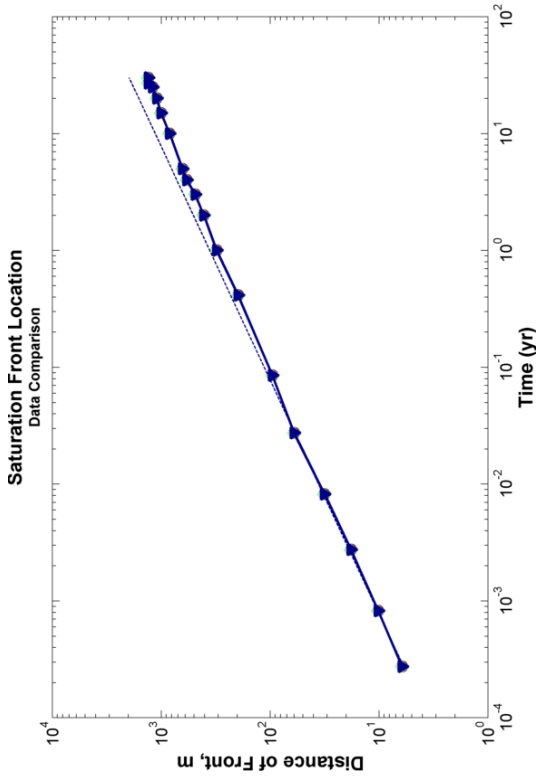
Saturation Front Location
Data Comparison
Distance of Front, m
Time (yr)

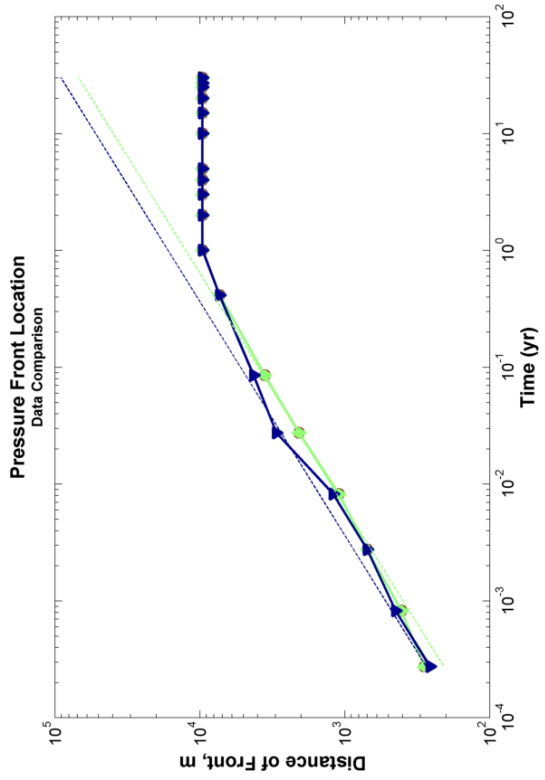
Pressure Front Location
Data Comparison
Distance of Front, m
Time (yr)

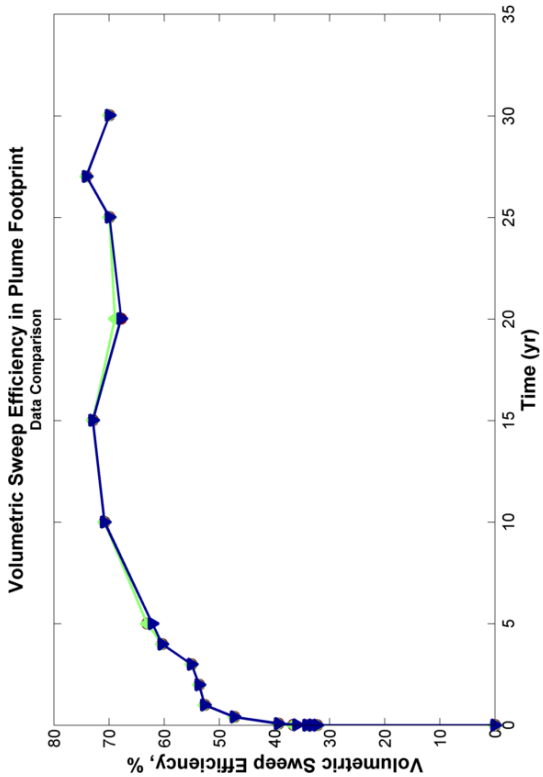
Volumetric Sweep Efficiency in Plume Footprint
Data Comparison
Volumetric Sweep Efficiency, %
Time (yr)

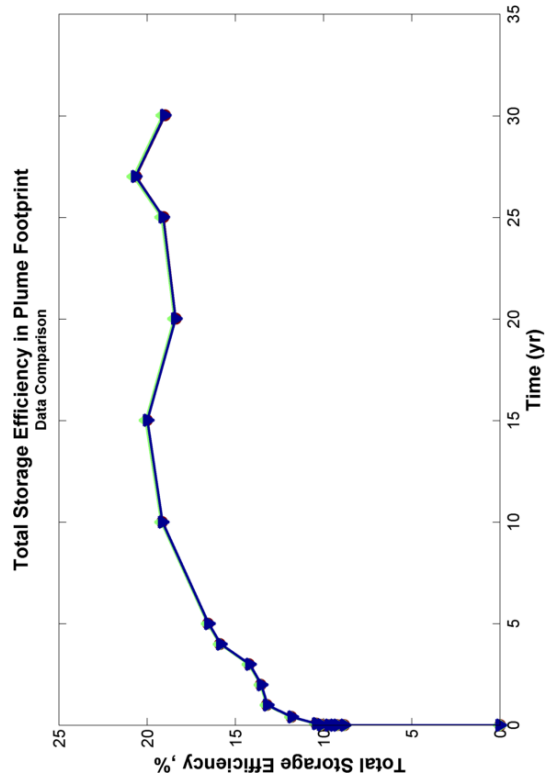
Total Storage Efficiency in Plume Footprint
Data Comparison
Total Storage Efficiency ,%
Time (yr)

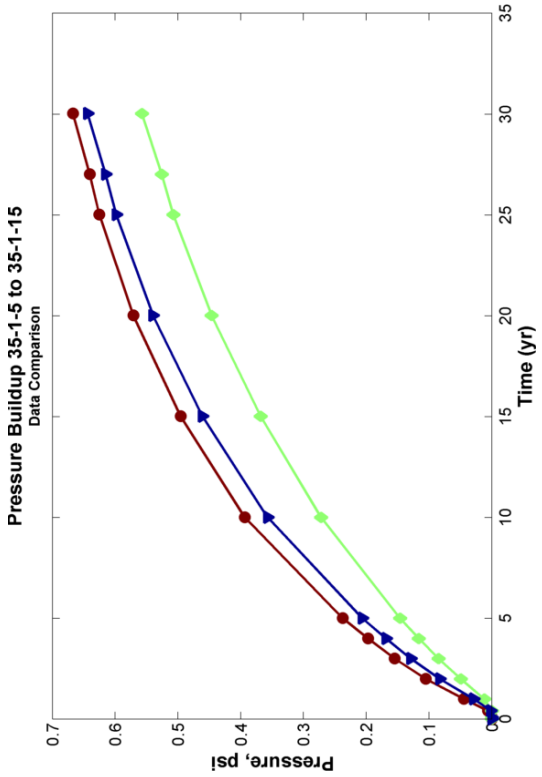
Pressure Buildup 35-1-5 to 35-1-15
Data Comparison
Pressure, psi
Time (yr)

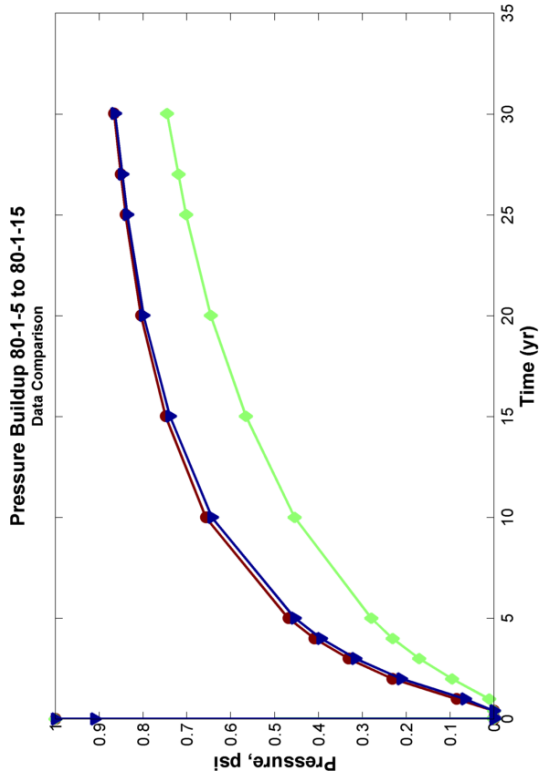
Pressure Buildup 80-1-5 to 80-1-15
Data Comparison
Pressure, psi
Time (yr)

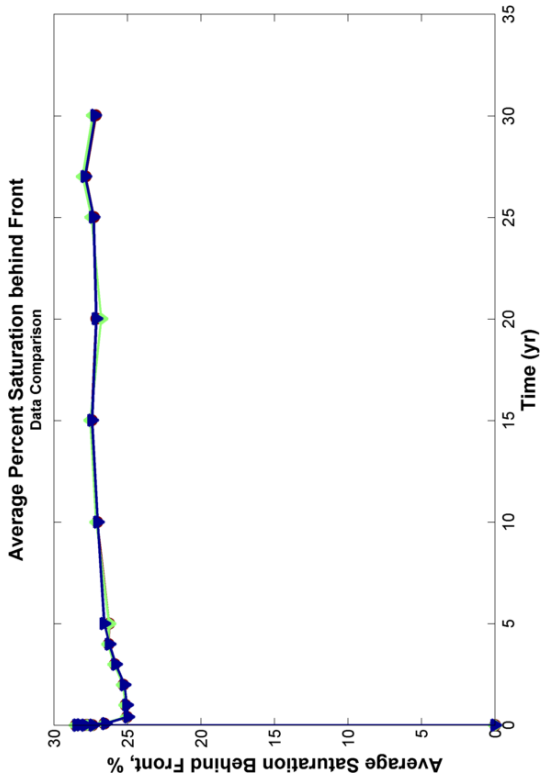
Average Percent Saturation behind Front
Data Comparison
Average Saturation Behind Front, %
Time (yr)

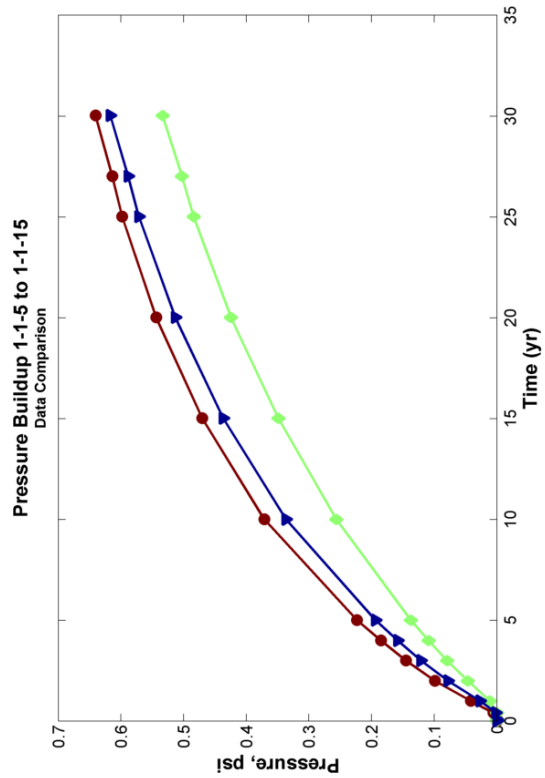
Pressure Buildup 1-1-5 to 1-1-15
Data Comparison
Pressure, psi
Time (yr)

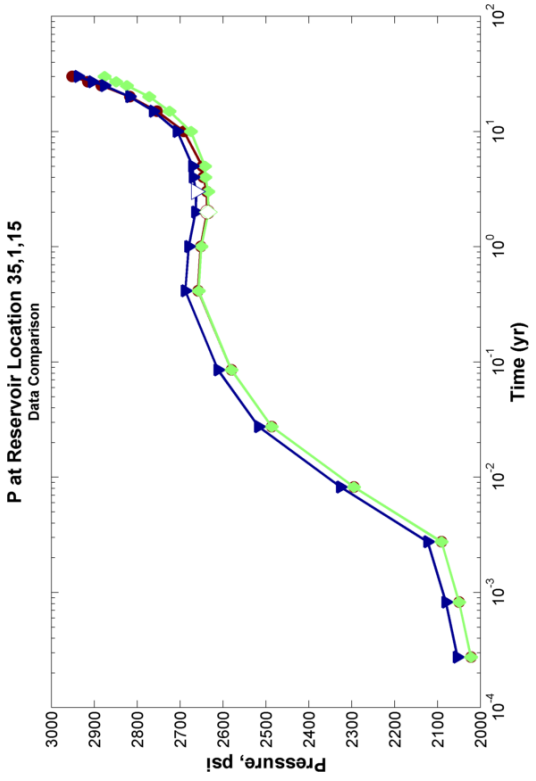
P at Reservoir Location 35,1,15
Data Comparison
Pressure, psi
Time (yr)

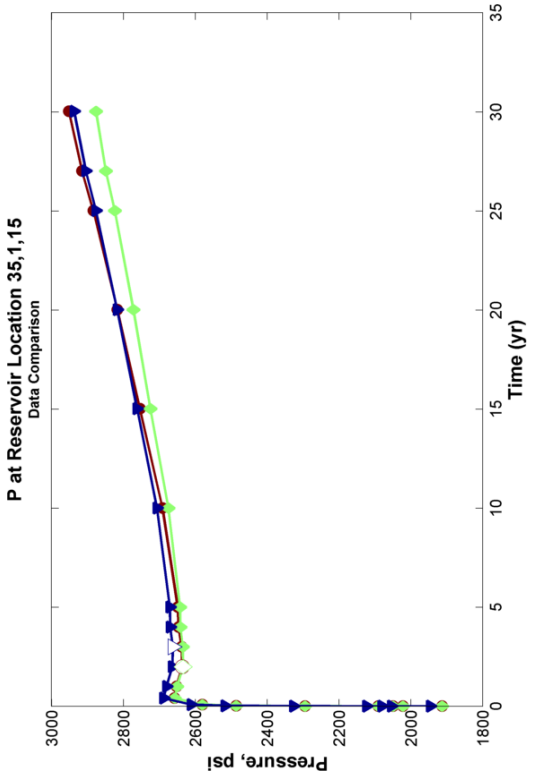
P at Reservoir Location 35,1,15
Data Comparison
Pressure, psi
Time (yr)

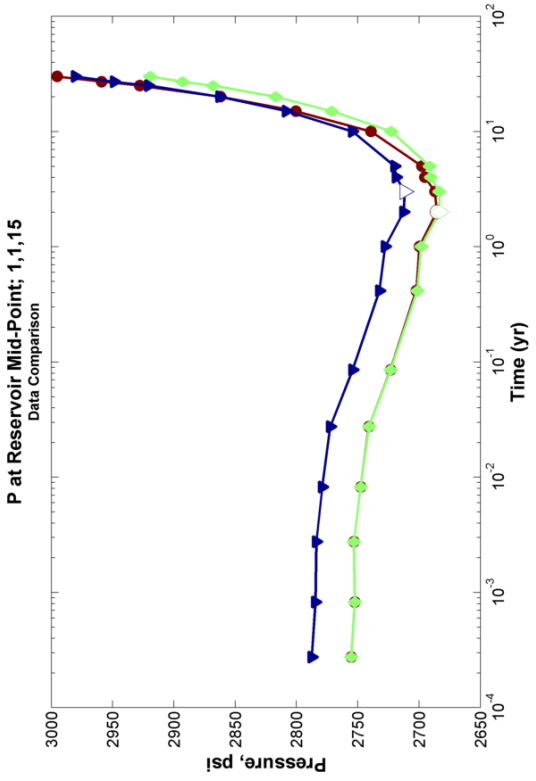
P at Reservoir Mid-Point; 1,1,15
Data Comparison
Pressure, psi
Time (yr)

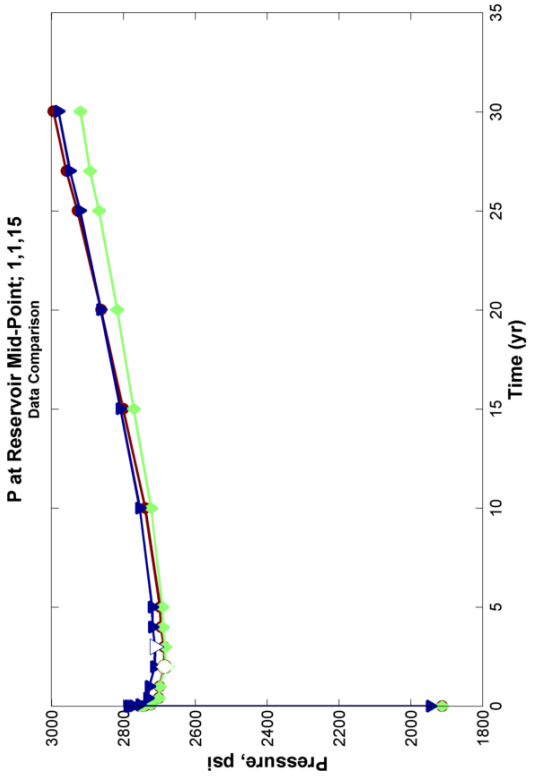
P at Reservoir Mid-Point; 1,1,15
Data Comparison
Pressure, psi
Time (yr)

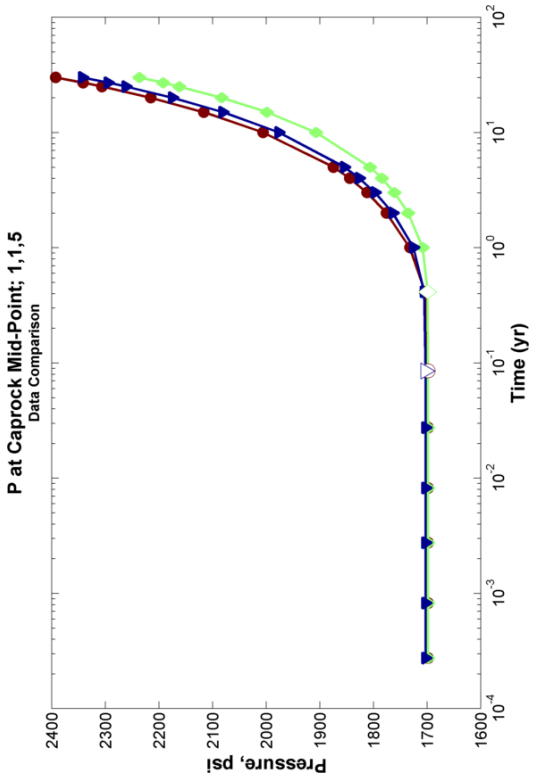
P at Caprock Mid-Point; 1,1,5
Data Comparison
Pressure, psi
Time (yr)

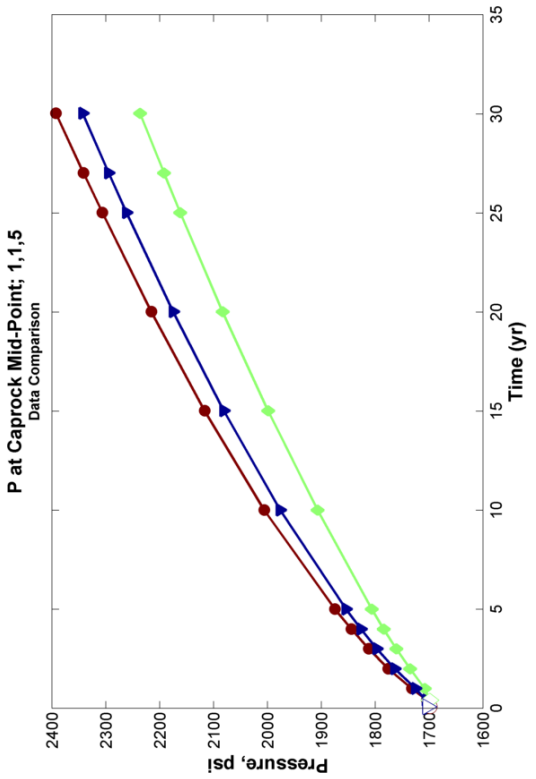
P at Caprock Mid-Point; 1,1,5
Data Comparison
Pressure, psi
Time (yr)

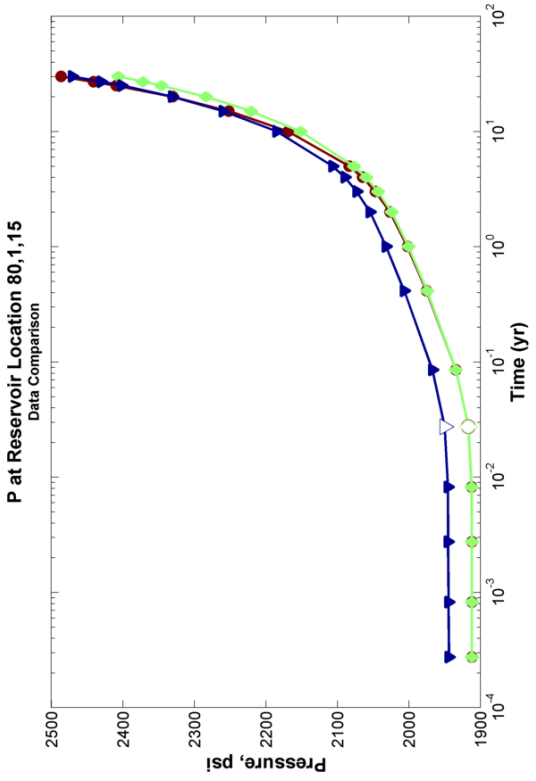
P at Reservoir Location 80,1,15
Data Comparison
Pressure, psi
Time (yr)

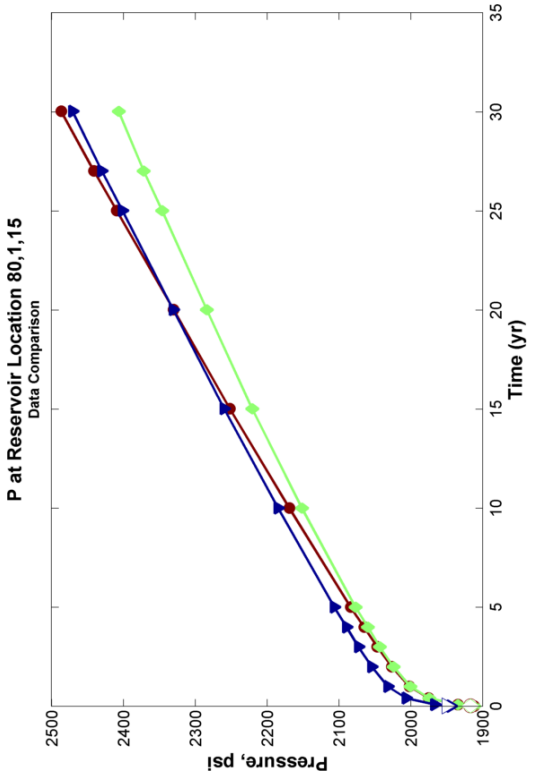
P at Reservoir Location 80,1,15
Data Comparison
Pressure, psi
Time (yr)

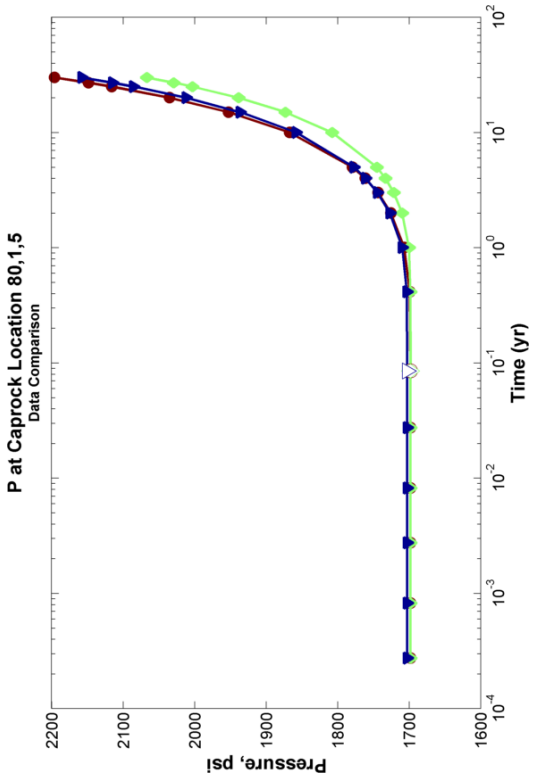
P at Caprock Location 80,1,5
Data Comparison
Pressure, psi
Time (yr)

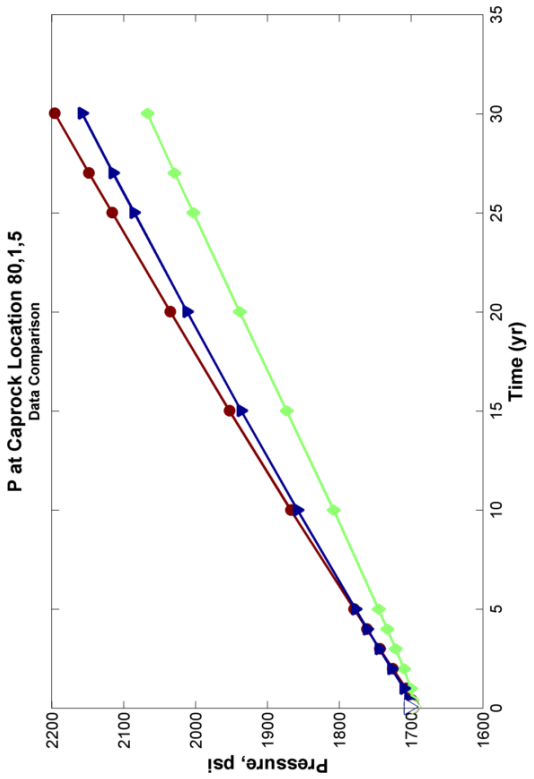
P at Caprock Location 80,1,5
Data Comparison
Pressure, psi
Time (yr)

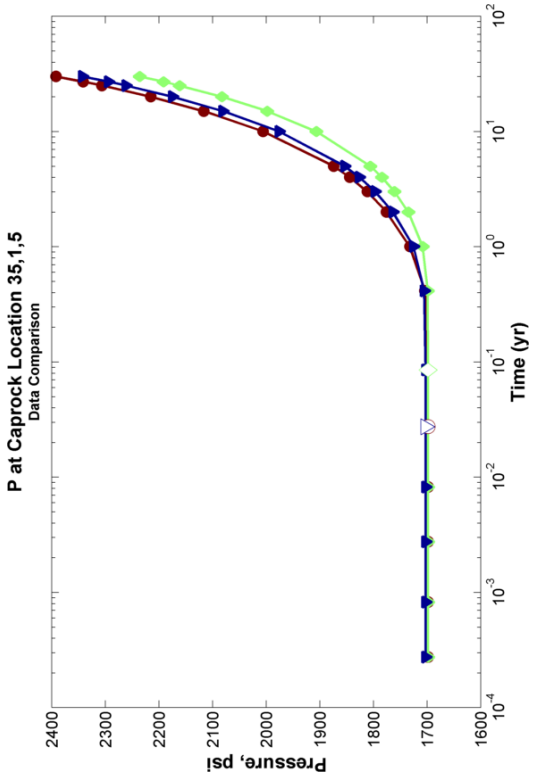
P at Caprock Location 35,1,5
Data Comparison
Pressure, psi
Time (yr)

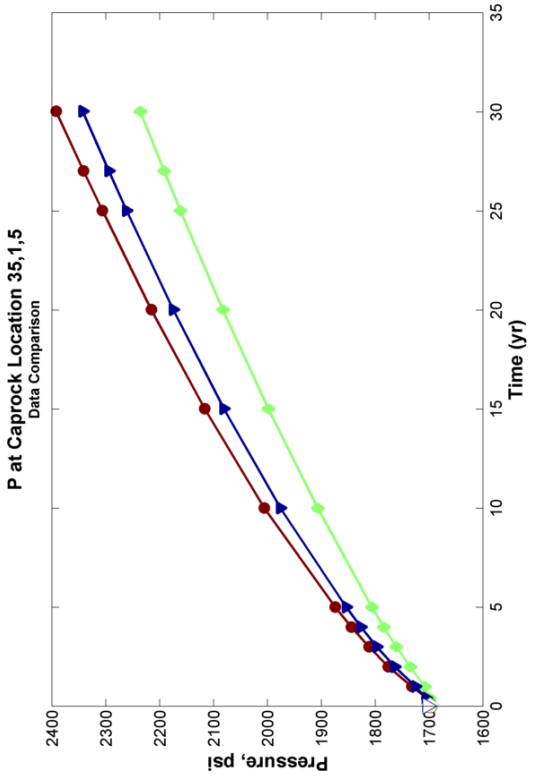
P at Caprock Location 35,1,5
Data Comparison
Pressure, psi
Time (yr)

REFERENCE RELATIVE PERMEABILITY CASE:
Parameter 8 Comparison
Injection Rate

	0.5 Slope Linear Fit x Value, psi (y =x*time^0.5)	
	Pressure Front	CO2Front
LOW Injection Rate = 0.33 MMT/yr	10443.42	233.06
REF Injection Rate = 0.83 MMT/yr	16554.65	359.68
HIGH Injection Rate = 1.33 MMT/yr	13183.27	428.53

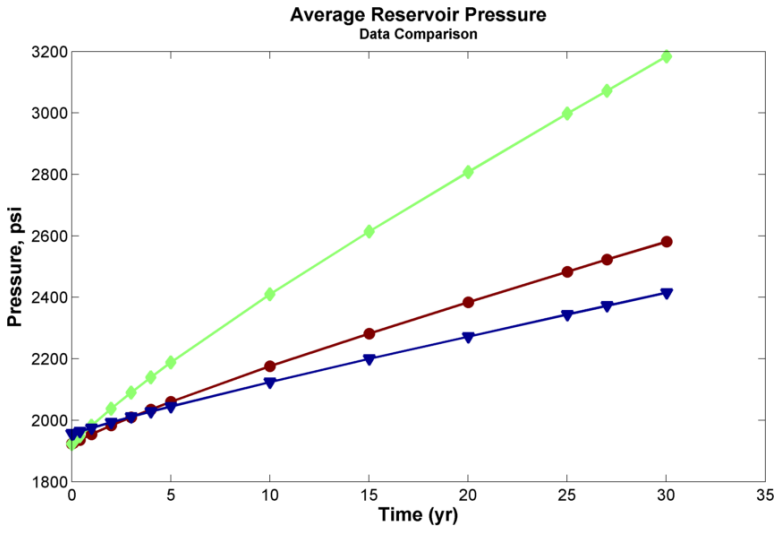

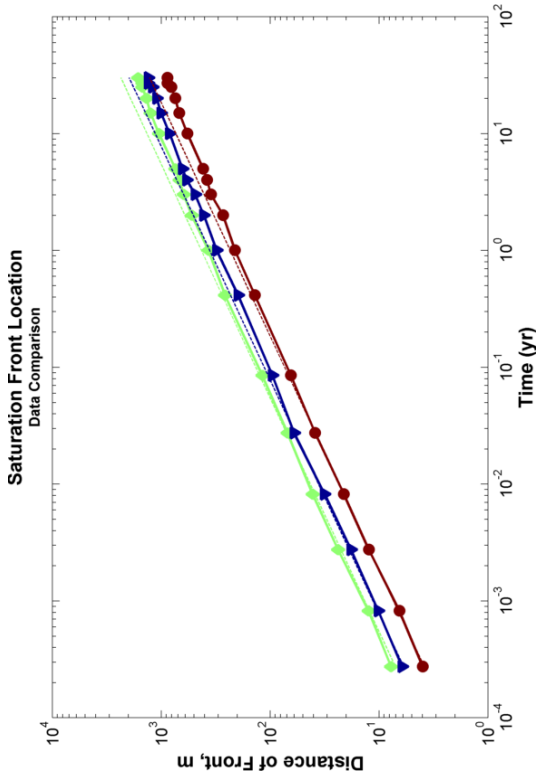

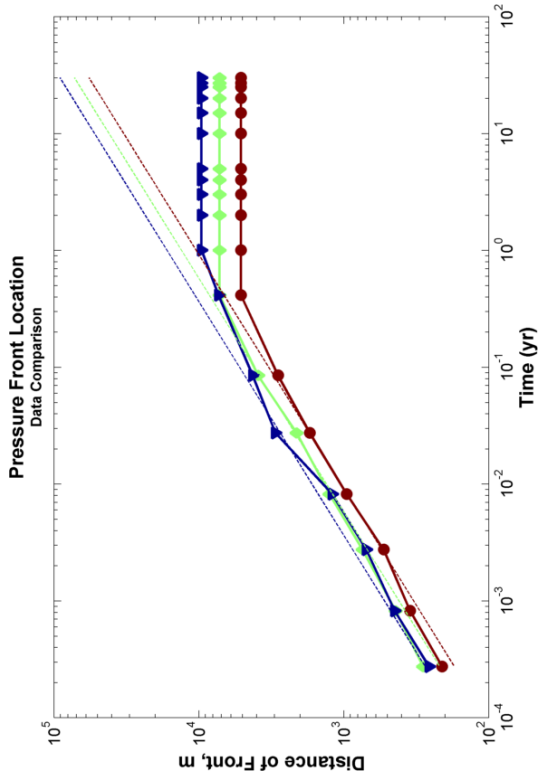

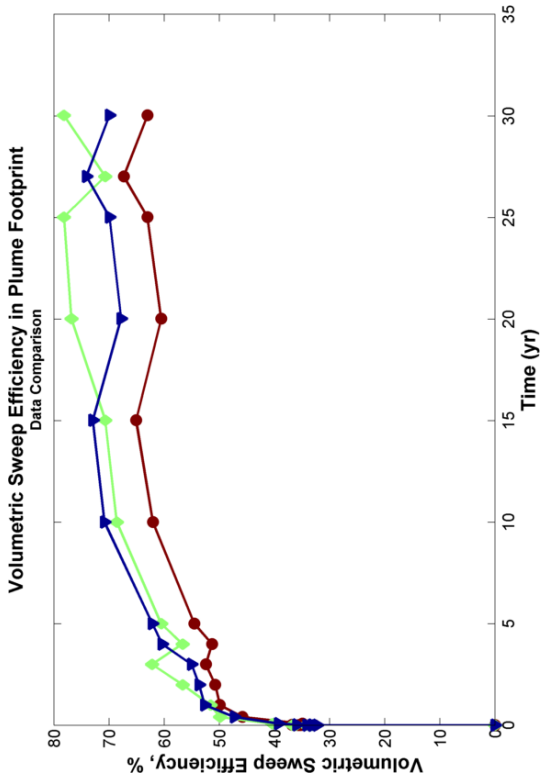

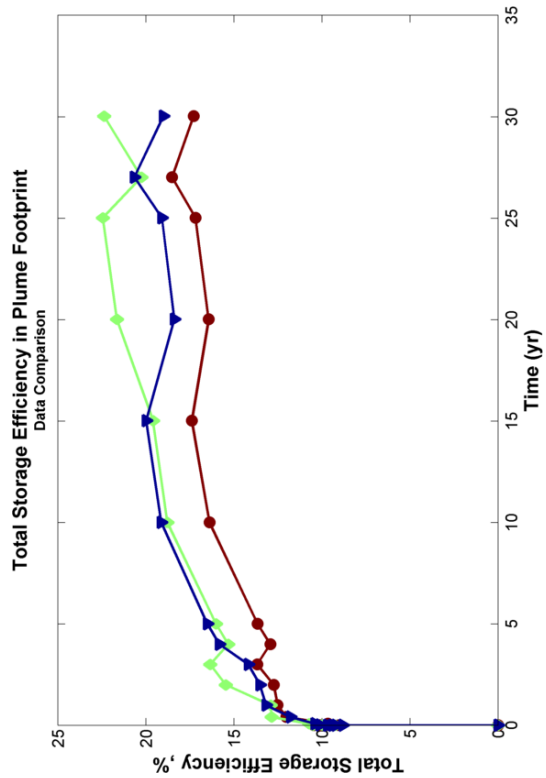

Parameter 8 Comparison (Injection rate) Ref0 -- Page 45 of 58

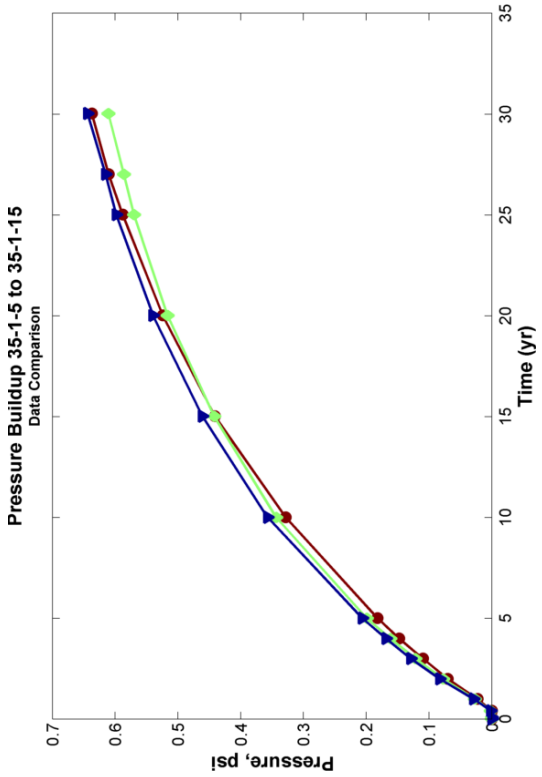

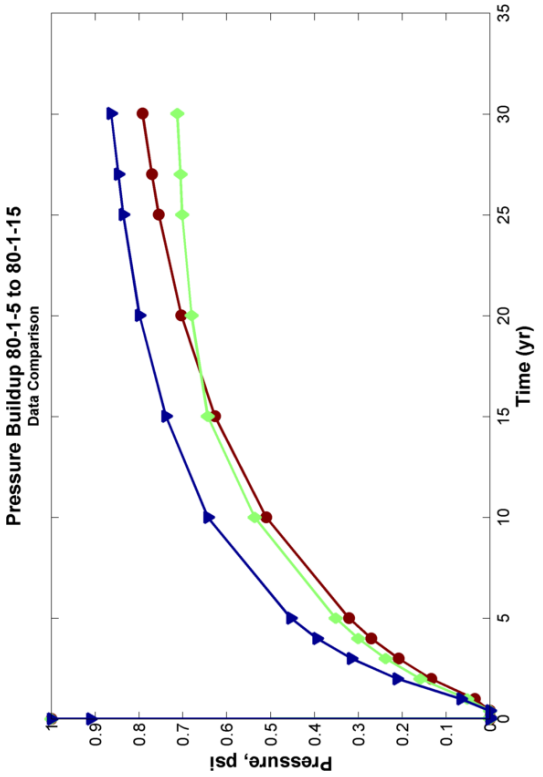

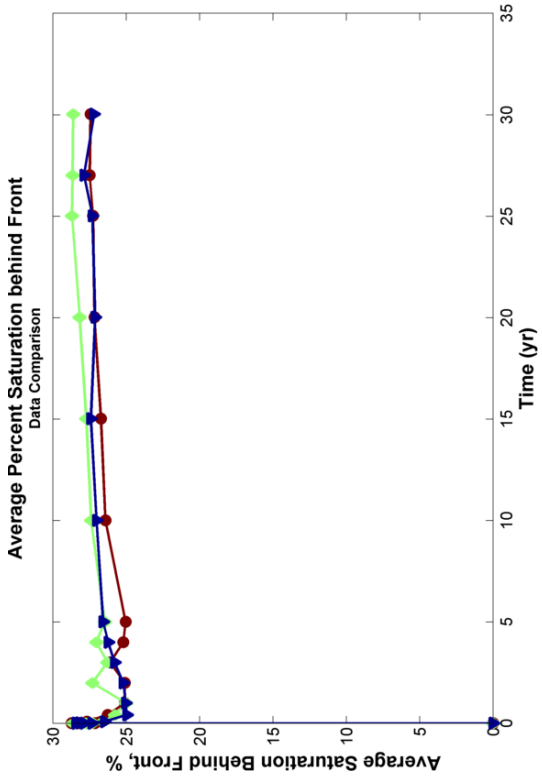

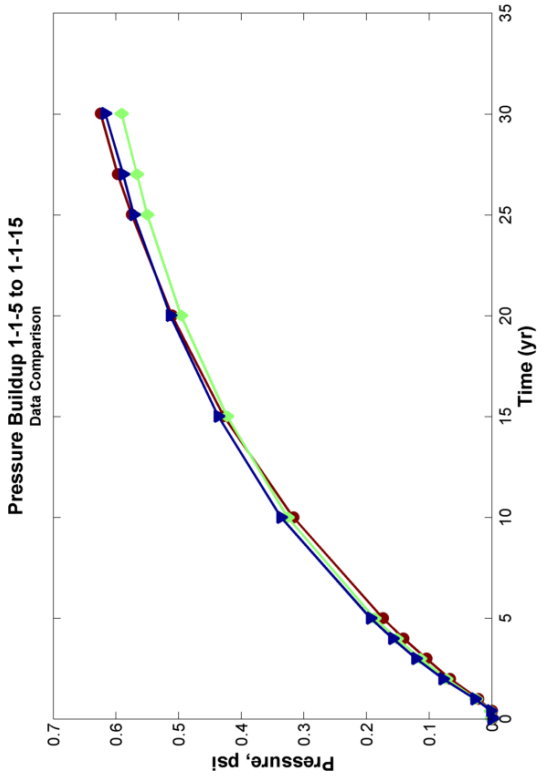

Parameter 8 Comparison (Injection rate) Ref0 -- Page 46 of 58

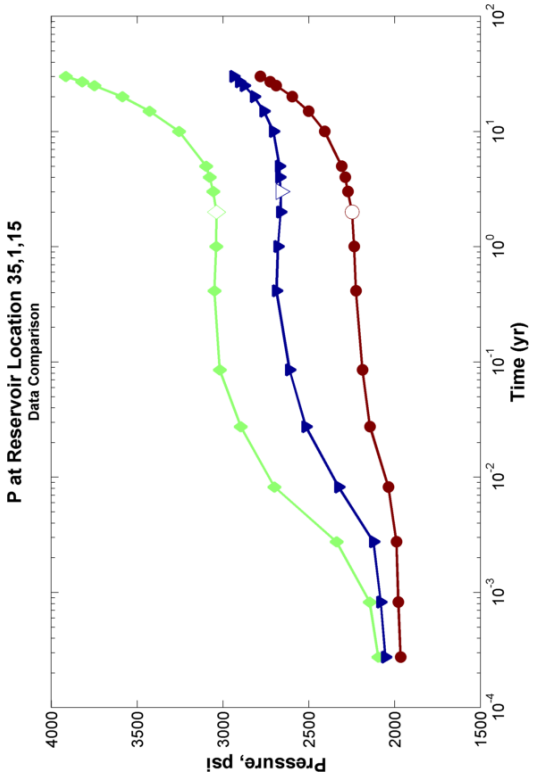
P at Reservoir Location 35,1,15
Data Comparison
Pressure, psi
Time (yr)

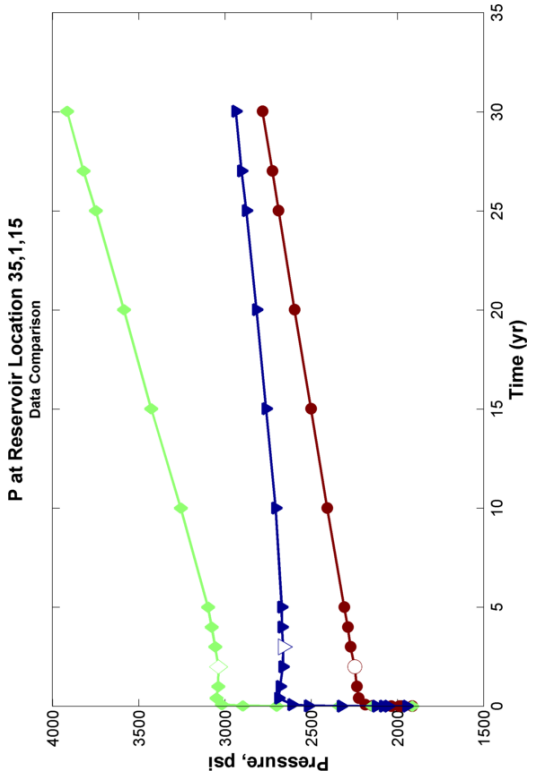
P at Reservoir Location 35,1,15
Data Comparison
Pressure, psi
Time (yr)

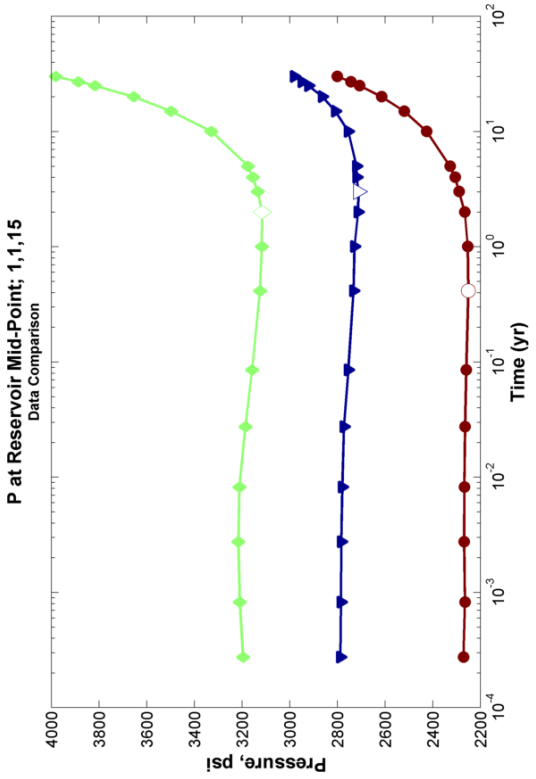
P at Reservoir Mid-Point; 1,1,15
Data Comparison
Pressure, psi
Time (yr)

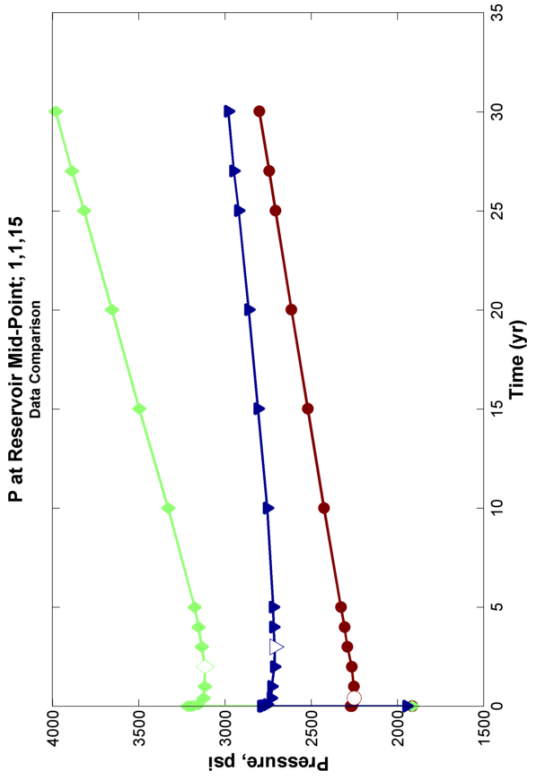
P at Reservoir Mid-Point; 1,1,15
Data Comparison
Pressure, psi
Time (yr)

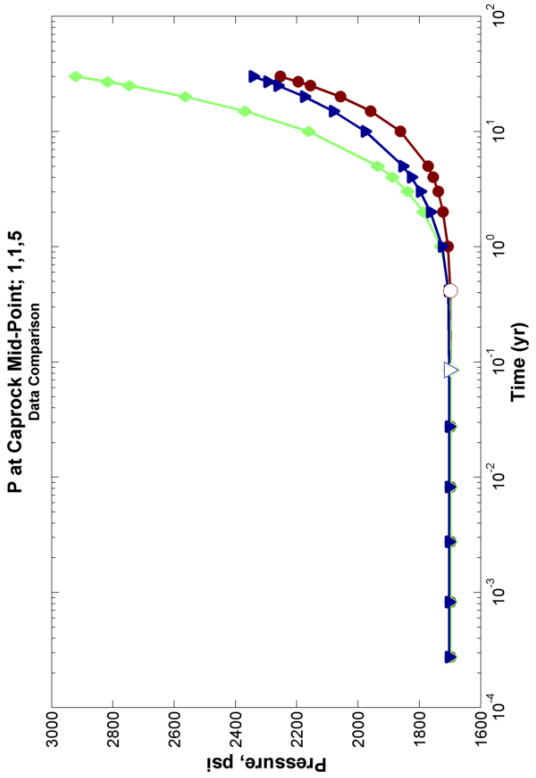
P at Caprock Mid-Point; 1,1,5
Data Comparison
Pressure, psi
Time (yr)

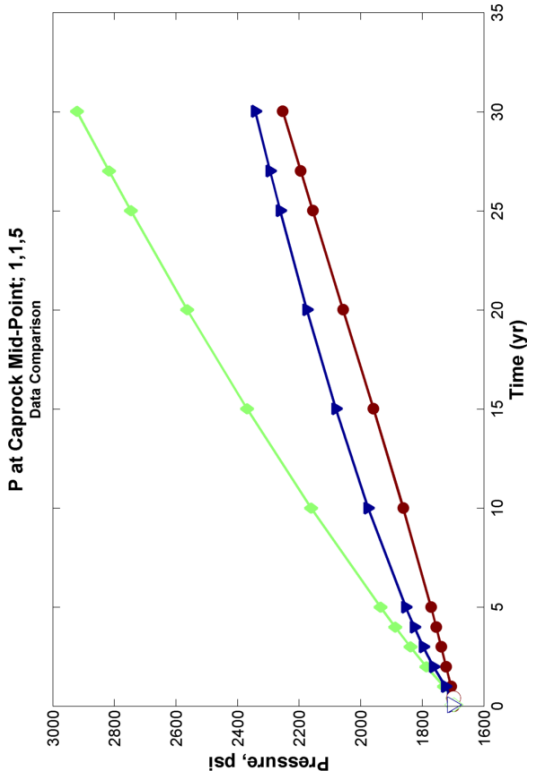
P at Caprock Mid-Point; 1,1,5
Data Comparison
Pressure, psi
Time (yr)

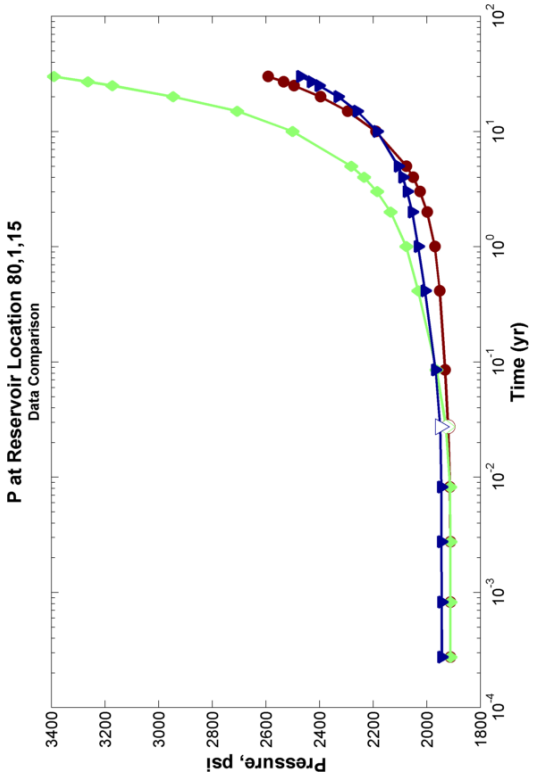
P at Reservoir Location 80,1,15
Data Comparison
Pressure, psi
Time (yr)

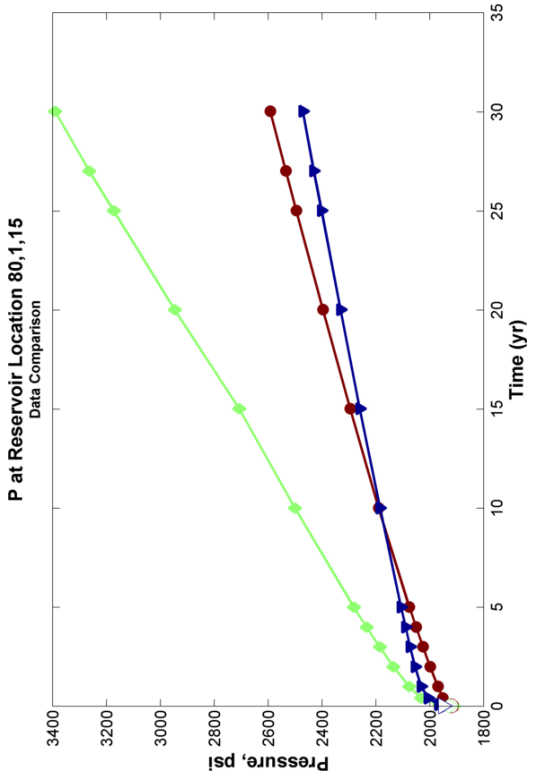
P at Reservoir Location 80,1,15
Data Comparison
Pressure, psi
Time (yr)

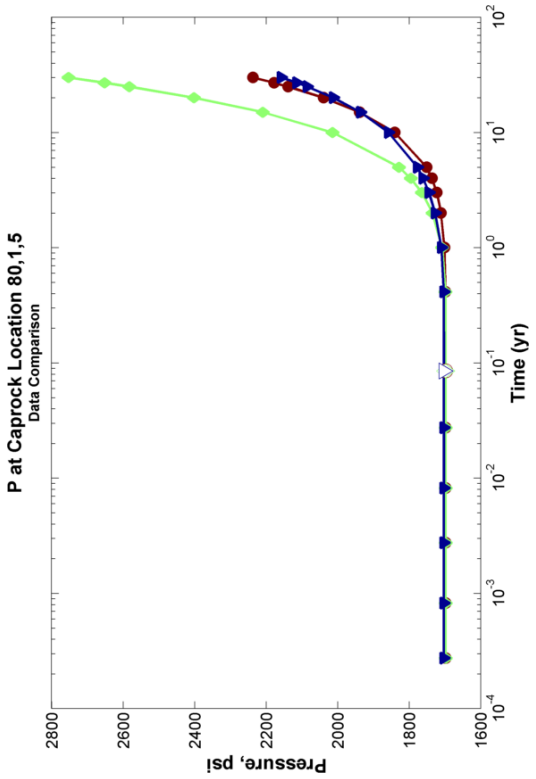
P at Caprock Location 80,1,5
Data Comparison
Pressure, psi
Time (yr)

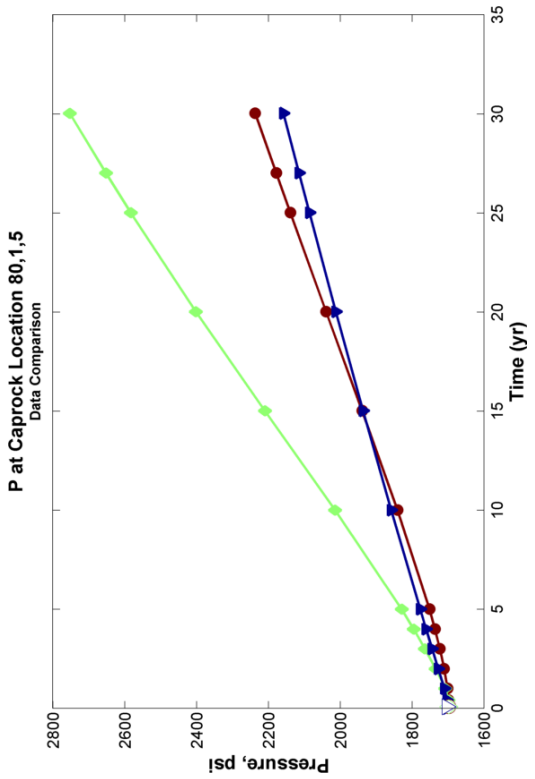
P at Caprock Location 80,1,5
Data Comparison
Pressure, psi
Time (yr)

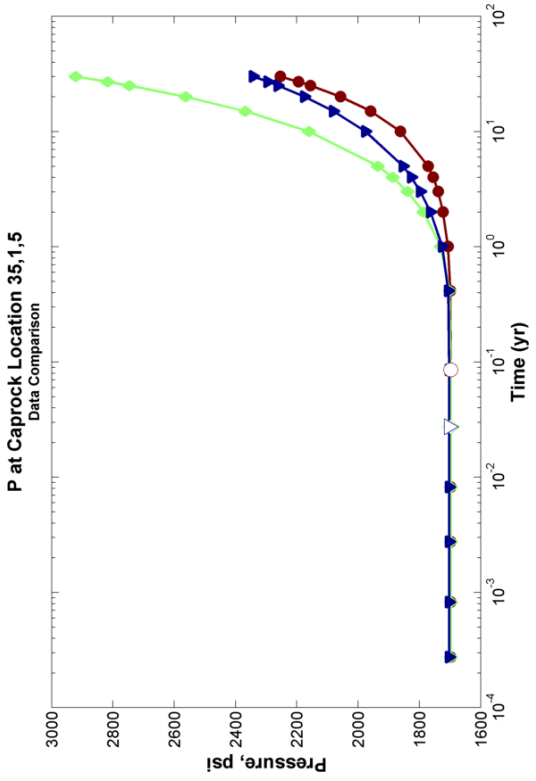
P at Caprock Location 35,1,5
Data Comparison
Pressure, psi
Time (yr)

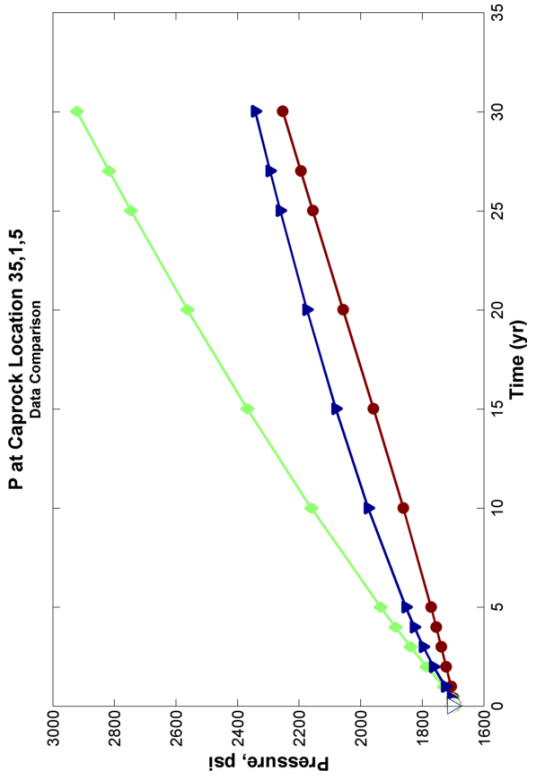
P at Caprock Location 35,1,5
Data Comparison
Pressure, psi
Time (yr)

REFERENCE RELATIVE PERMEABILITY CASE:
Parameter 9 Comparison
Anisotropy Ratio

	0.5 Slope Linear Fit x Value, psi (y =x*time^0.5)	
	Pressure Front	CO2Front
LOW Anisotropy Ratio = 0.01	13281.14	359.68
Ref Anistropy Ratio = 0.1	16554.65	359.68
HIGH Anisotropy Ratio = 1	11623.16	337.52

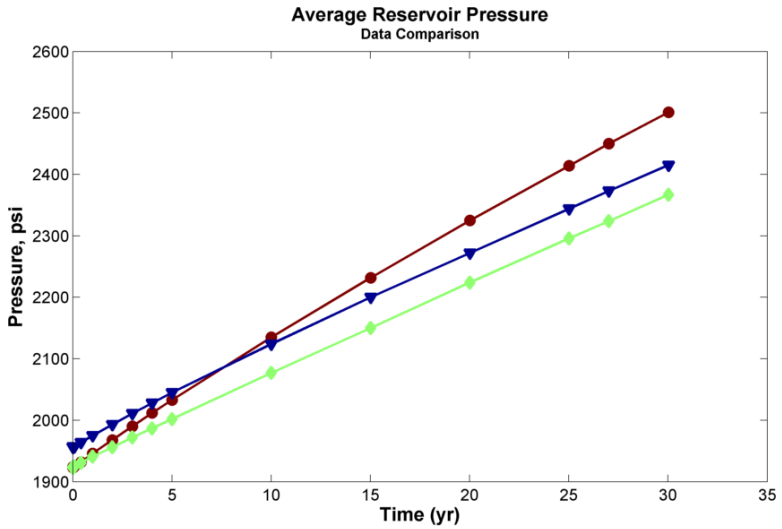

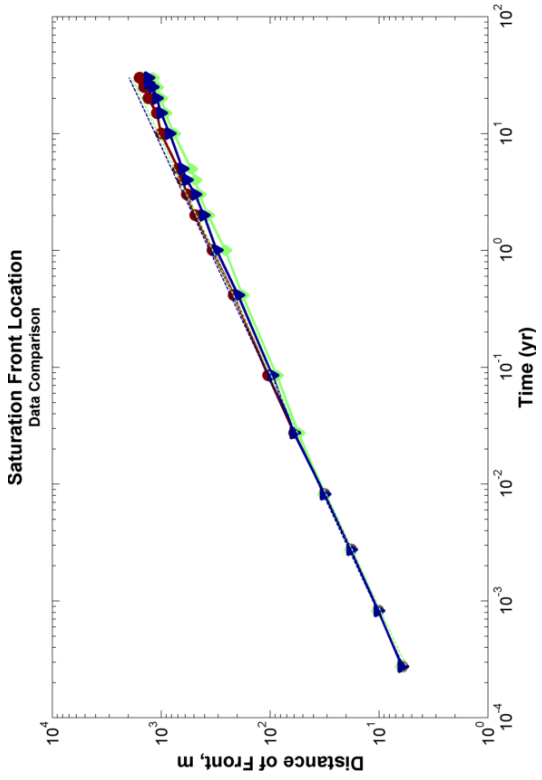
Saturation Front Location
Data Comparison
Distance of Front, m
Time (yr)

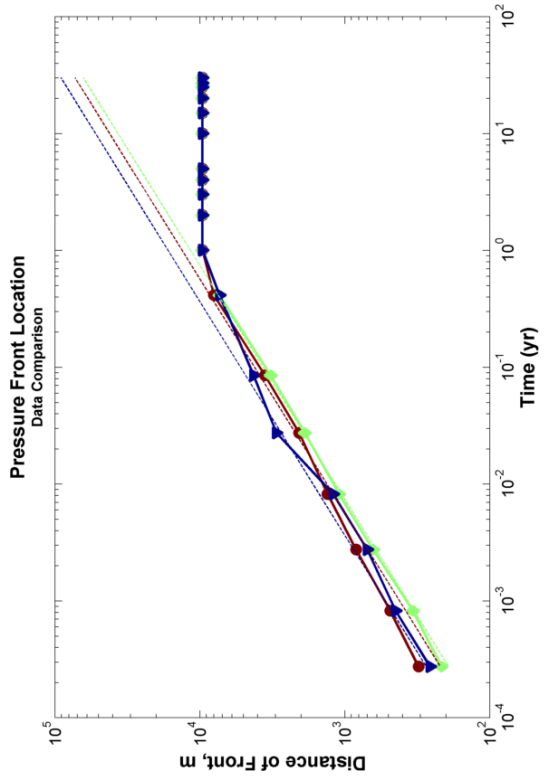
Pressure Front Location
Data Comparison
Distance of Front, m
Time (yr)

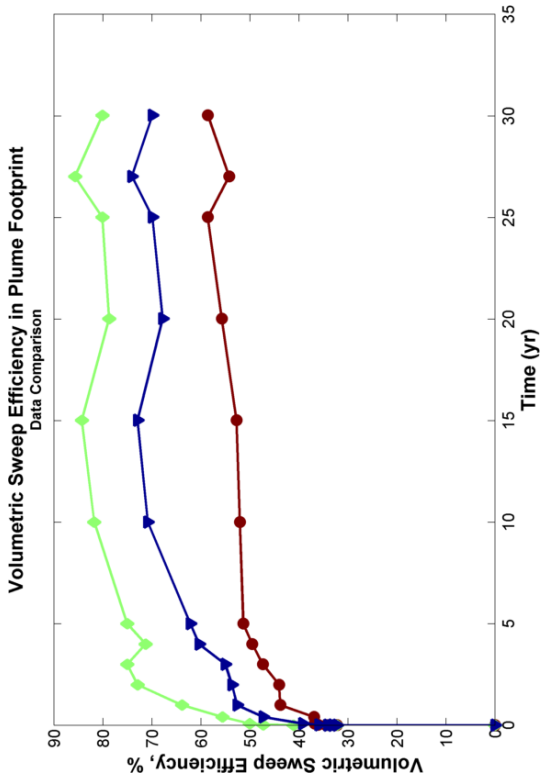
Volumetric Sweep Efficiency in Plume Footprint
Data Comparison
Volumetric Sweep Efficiency, %
Time (yr)

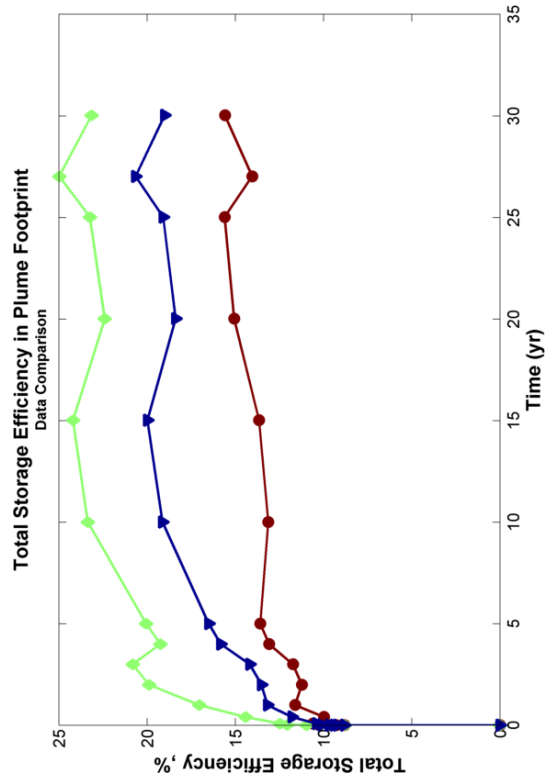
Total Storage Efficiency in Plume Footprint
Data Comparison
Total Storage Efficiency ,%
Time (yr)

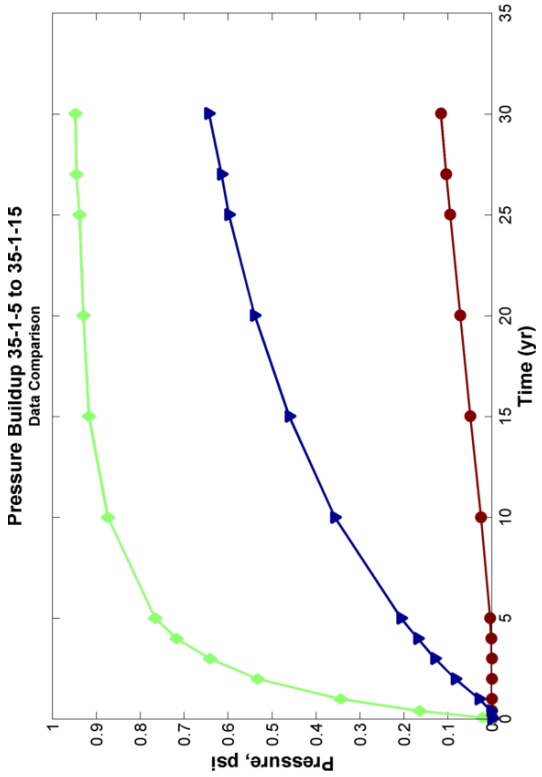
Pressure Buildup 35-1-5 to 35-1-15
Data Comparison
Pressure, psi
Time (yr)

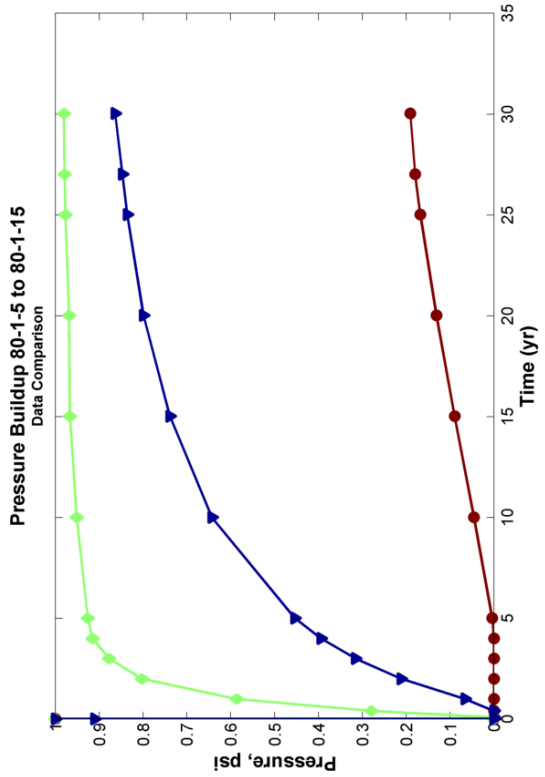
Pressure Buildup 80-1-5 to 80-1-15
Data Comparison
Pressure, psi
Time (yr)

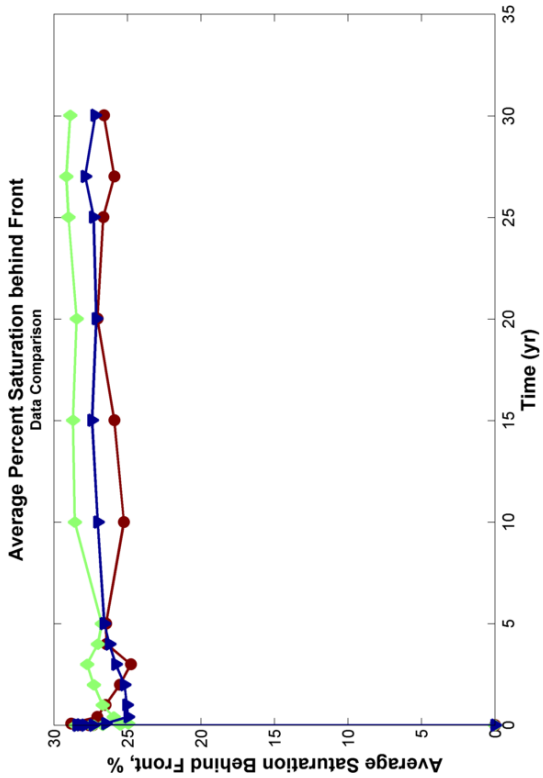
Average Percent Saturation behind Front
Data Comparison
Average Saturation Behind Front, %
Time (yr)

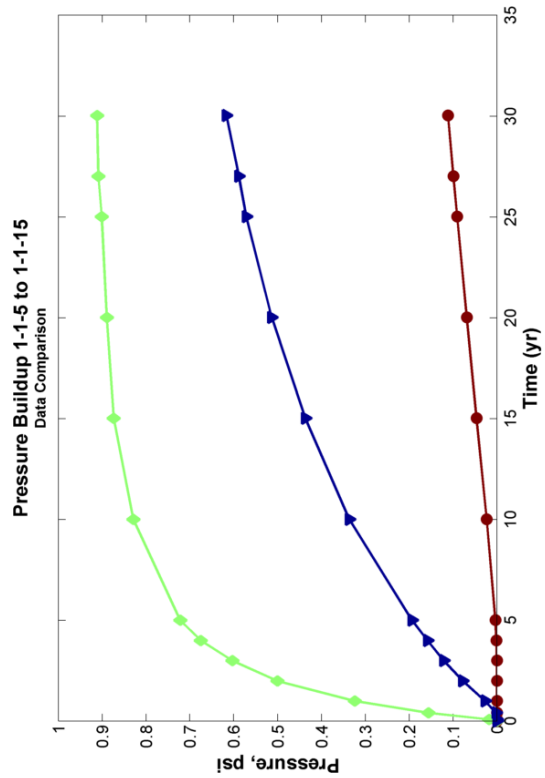
Pressure Buildup 1-1-5 to 1-1-15
Data Comparison
Pressure, psi
Time (yr)

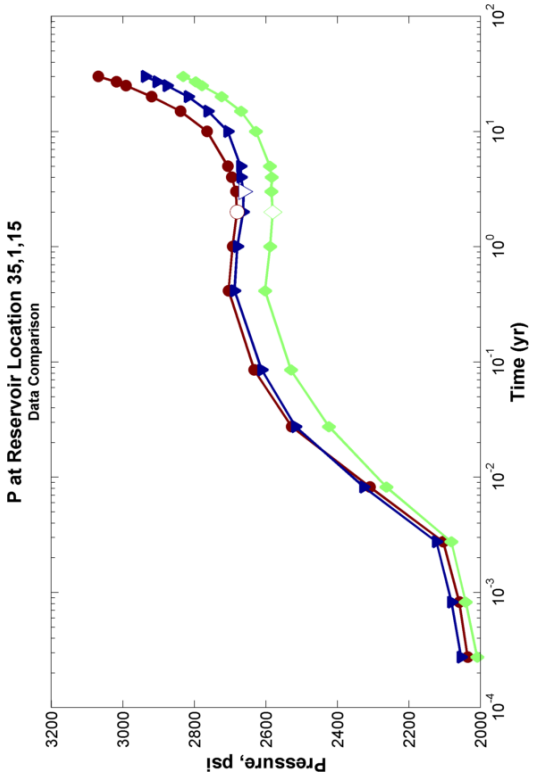
P at Reservoir Location 35,1,15
Data Comparison
Pressure, psi
Time (yr)

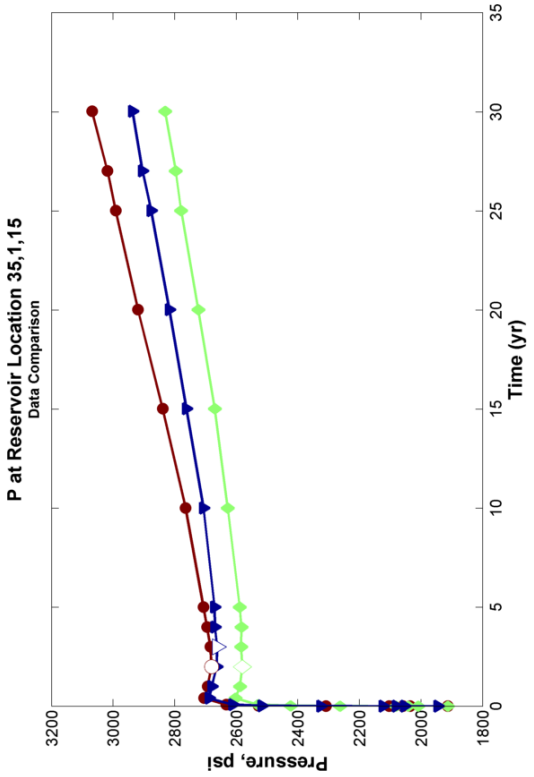
P at Reservoir Location 35,1,15
Data Comparison
Pressure, psi
Time (yr)

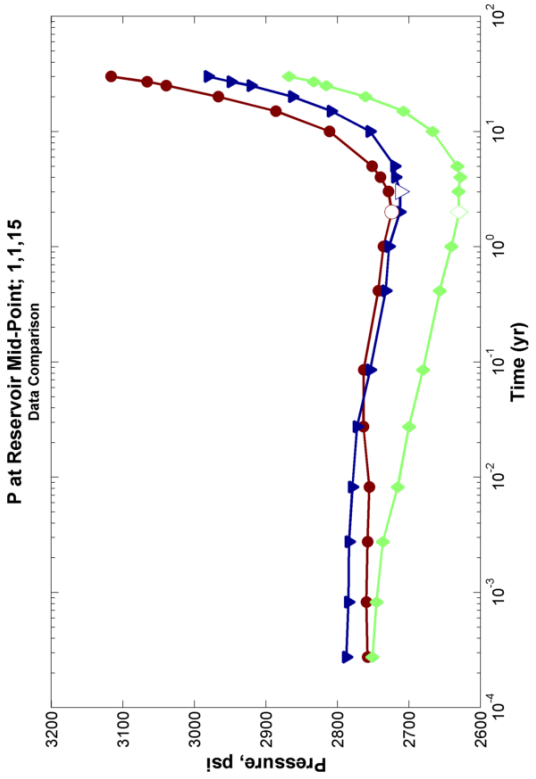
P at Reservoir Mid-Point; 1,1,15
Data Comparison
Pressure, psi
Time (yr)

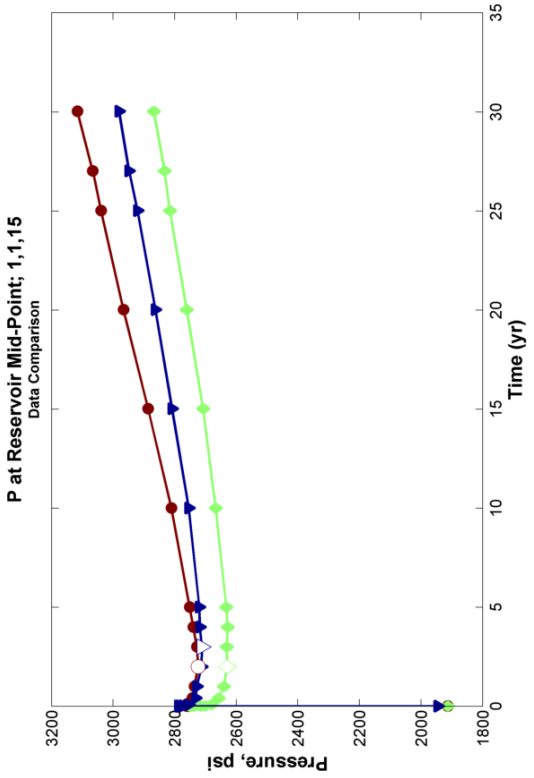
P at Reservoir Mid-Point; 1,1,15
Data Comparison
Pressure, psi
Time (yr)

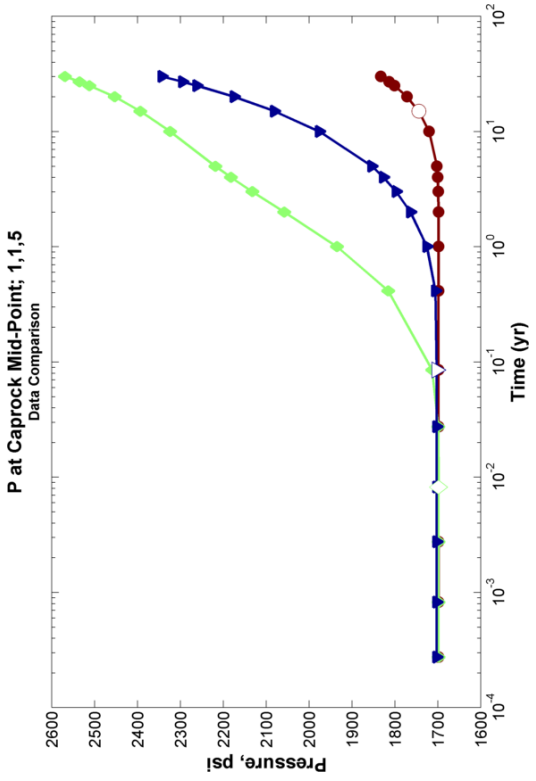
P at Caprock Mid-Point; 1,1,5
Data Comparison
Pressure, psi
Time (yr)

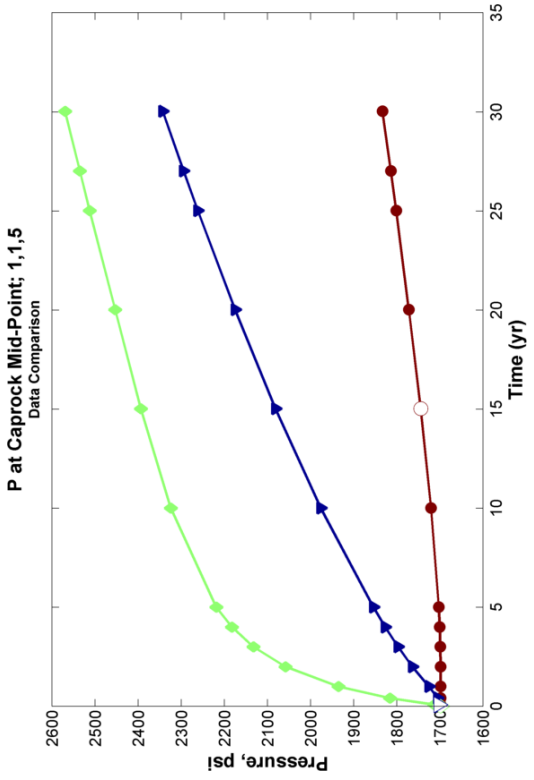
P at Caprock Mid-Point; 1,1,5
Data Comparison
Pressure, psi
Time (yr)

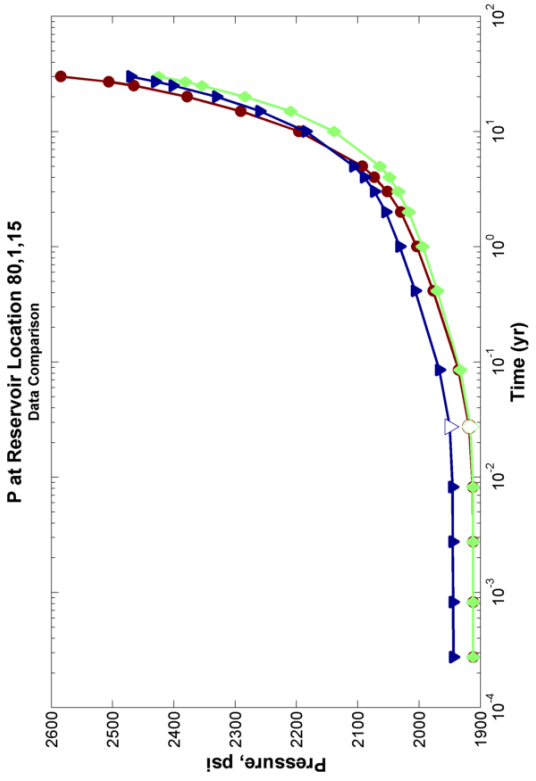
P at Reservoir Location 80,1,15
Data Comparison
Pressure, psi
Time (yr)

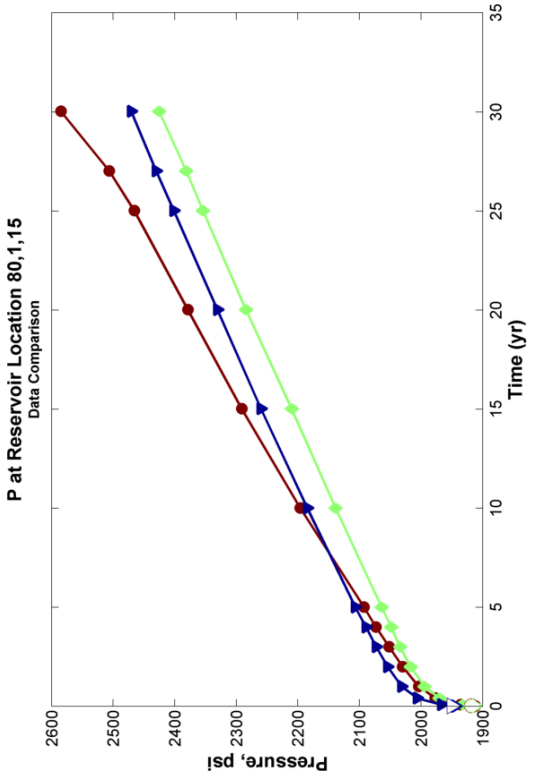
P at Reservoir Location 80,1,15
Data Comparison
Pressure, psi
Time (yr)

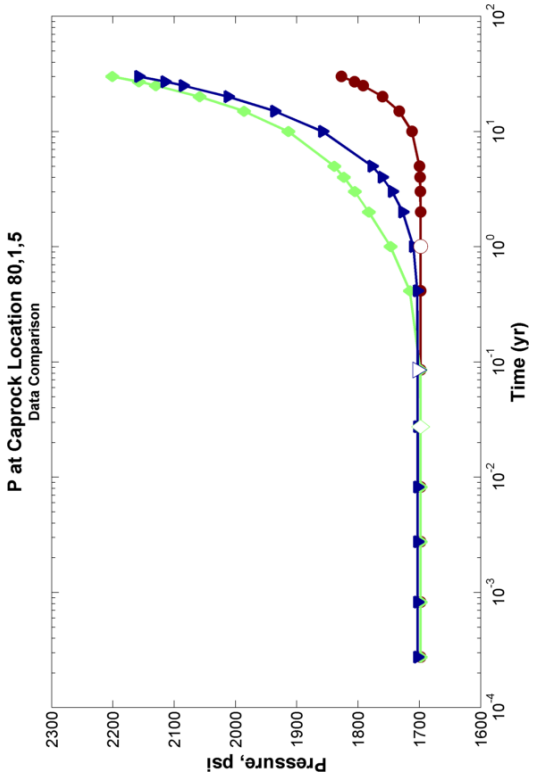
P at Caprock Location 80,1,5
Data Comparison
Pressure, psi
Time (yr)

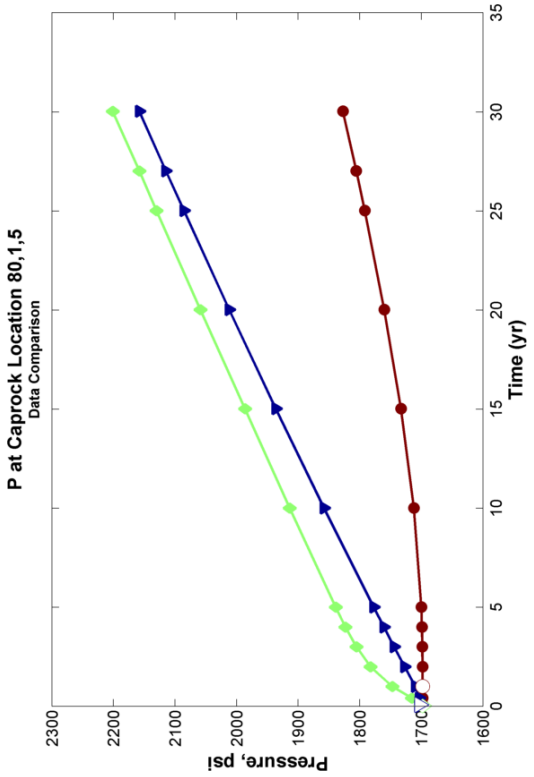
P at Caprock Location 80,1,5
Data Comparison
Pressure, psi
Time (yr)

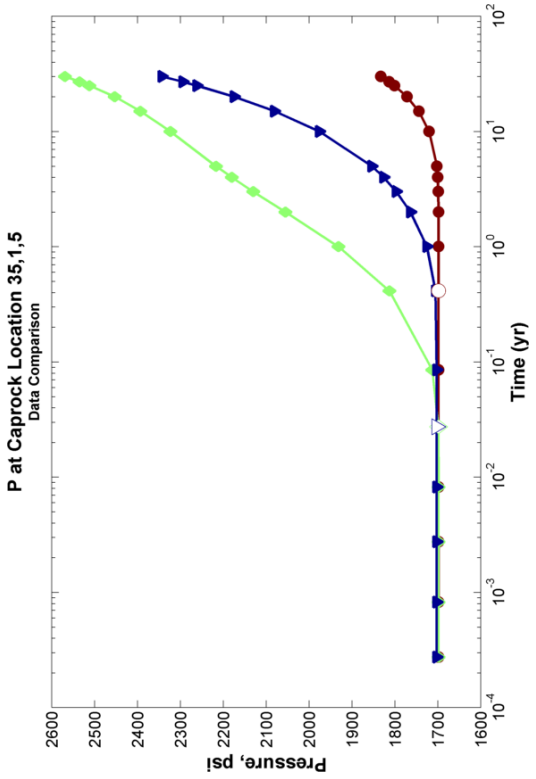
P at Caprock Location 35,1,5
Data Comparison
Pressure, psi
Time (yr)

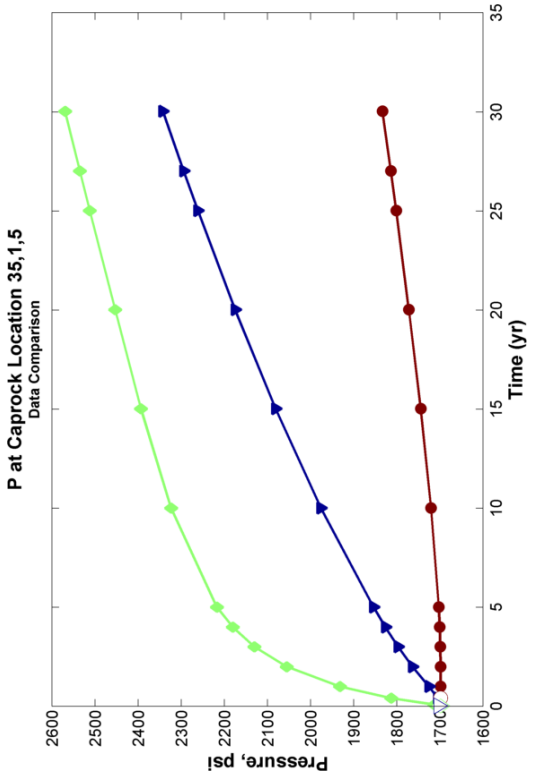
P at Caprock Location 35,1,5
Data Comparison
Pressure, psi
Time (yr)

Tables:

1. Table of values for effect of cap rock properties

Simulation case #	Case description	dfg/dSg	hCR, m	hR, m	htot, m	hCR/hR	<kR>, mD	<kCR>, mD	P @ t = 0, psi		P @ t = 30 yrs, psi		ΔP @ t = 30 yrs, psi		ΔPCR/ΔPR @ t = 30 yrs	
									R 1,1,15	CR 1,1,5	R 1,1,15	CR 1,1,5	R 1,1,15	CR 1,1,5	Simulation result	Predictive model
REF0																
12	No CR	1.74	0	150	150	0.0000	46	0.02	1913.2363	-	3286.6873	-	1373.4509			0.0348
0	Ref	1.74	150	150	300	1.0000	46	0.02	1945.1870	1704.0470	3104.8620	2361.6270	1159.6750	657.5800	0.5670	0.7185
2a	Thin CR	1.74	100	150	250	0.6667	46	0.02	1902.3010	1727.2830	2987.6558	2543.7566	1085.3548	816.4736	0.7523	0.7370
2b	Thick CR	1.74	200	150	350	1.3333	46	0.02	1926.3478	1674.3013	2950.6980	2140.1174	1024.3502	465.8162	0.4547	0.4535
5a	Low perm CR	1.74	150	150	300	1.0000	46	0.002	1913.2363	1699.4216	3066.4341	1857.8066	1153.1978	158.3850	0.1373	0.1351
5b	High perm CR	1.74	150	150	300	1.0000	46	0.2	1913.2363	1699.4216	2925.9597	2398.4756	1012.7234	699.0540	0.6903	0.6964
Case A																
12	No CR	6.24	0	150	150	0.0000	46	0.02	1913.2363	-	2795.7727	-	882.5364			0.0348
0	Ref	6.24	150	150	300	1.0000	46	0.02	1913.2363	1699.4216	2568.5088	2201.5105	655.2725	502.0889	0.7662	0.8458
2a	Thin CR	6.24	100	150	250	0.6667	46	0.02	1902.3005	1727.2834	2616.9709	2332.9189	714.6704	605.6355	0.8474	0.8219
2b	Thick CR	6.24	200	150	350	1.3333	46	0.02	1926.3478	1674.3013	2583.9932	2094.1731	657.6454	419.8718	0.6384	0.6233
5a	Low perm CR	6.24	150	150	300	1.0000	46	0.002	1913.2363	1699.4216	2697.8706	1871.8262	784.6343	172.4045	0.2197	0.2625
5b	High perm CR	6.24	150	150	300	1.0000	46	0.2	1913.2363	1699.4216	2563.1924	2252.8840	649.9561	553.4624	0.8515	0.8238
Case B																
12	No CR	4.64	0	150	150	0.0000	46	0.02	1913.2363	-	3021.0522	-	1107.8159			0.0348
0	Ref	4.64	150	150	300	1.0000	46	0.02	1913.2363	1699.4216	2688.5054	2266.4973	775.2690	567.0757	0.7315	0.8005
2a	Thin CR	4.64	100	150	250	0.6667	46	0.02	1902.3005	1727.2834	2841.9900	2486.5225	939.6895	759.2390	0.8080	0.7917
2b	Thick CR	4.64	200	150	350	1.3333	46	0.02	1926.3478	1674.3013	2805.6340	2144.7114	879.2863	470.4102	0.5350	0.5629
5a	Low perm CR	4.64	150	150	300	1.0000	46	0.002	1913.2363	1699.4216	2922.2708	1869.6001	1009.0344	170.1785	0.1687	0.2172
5b	High perm CR	4.64	150	150	300	1.0000	46	0.2	1913.2363	1699.4216	2782.9622	2370.5676	869.7258	671.1460	0.7717	0.7785

2. Table of values for P_D and E_S models

Run #	Run description	dfg/dSg	Lc	VDP	kR mD	Ng3	Total efficiency, % (mean)	(std. dev.)	Total efficiency, @ 30 yrs	PD (min)	PD (@ 0.3 days)	Simulation results RCO2, m	J = Q/ ΔP, bbl/day.psi	Regression model E_S, %	R_{CO2},m	P_D	J, bbl/day.psi
		X1	X2	X3_a	X3_b	X4_b	Y' = f{X}	σ	Y = f{X}	Z' = f{X}	Z = f{X}	R_sim	J_sim				
	Ref0																
0	REFERENCE	1.74	0.02	0.55	46	0.11	19.37	0.81	19.0085	10.7036	11.7203	1504.1801	22.6636	20.1053	1612.8026	10.6845	22.7040
1a	Low hR	1.74	0.02	0.55	46	0.00	24.14	1.72	25.8156	9.7652	11.8747	2158.5100	8.0860	21.2450	2584.2114	10.6845	7.3902
1b	High hR	1.74	0.02	0.55	46	0.68	16.07	1.29	16.8974	10.9706	11.5920	1255.6300	37.6484	16.3870	1421.9355	10.6845	38.6563
2a	Low hCR	1.74	0.02	0.55	46	0.11	19.20	0.79	18.8128	10.6623	11.6591	1504.1801	22.2331	20.0865	1605.2734	10.6845	22.1868
2b	High hCR	1.74	0.02	0.55	46	0.12	19.08	1.65	19.2462	10.8015	11.6935	1504.1801	22.9768	19.9572	1629.3429	10.6845	23.2282
4a	Low kRmean	1.74	-0.01	0.35	12	0.01	23.14	1.79	25.7407	11.1663	11.7281	1374.3101	5.6433	25.1910	1355.3751	11.1747	5.6391
4b	High kRmean	1.74	0.08	0.75	220	0.72	14.74	1.08	13.4599	10.4397	11.4019	1646.3300	111.2982	13.6818	2016.0474	9.4832	122.5245
5a	Low kCR	1.74	0.02	0.55	46	0.11	19.29	0.80	18.8757	10.8003	11.6732	1504.1801	22.4622	20.0815	1606.6133	10.6845	22.7056
5b	High kCR	1.74	0.02	0.55	46	0.12	19.37	0.81	18.9736	10.5610	11.6717	1504.1801	22.9712	19.9949	1621.9895	10.6845	22.7056
6a	Low phiR	1.74	0.02	0.55	46	0.11	20.15	0.82	19.6903	10.7185	11.6537	1801.9000	22.6337	20.0814	1606.6505	10.6845	22.7056
6b	High phiR	1.74	0.02	0.55	46	0.12	18.18	1.58	18.3711	10.7307	11.5995	1255.6300	22.6082	19.9561	1628.9682	10.6845	22.7058
7a	Low phiCR	1.74	0.02	0.55	46	0.11	19.37	0.81	18.9806	10.7417	11.6730	1504.1801	22.5847	20.0384	1614.2272	10.6845	22.7056
7b	High phiCR	1.74	0.02	0.55	46	0.12	19.47	0.82	19.1204	10.7102	11.6730	1504.1801	22.6512	19.9908	1622.7354	10.6845	22.7056
8a	Low Qinj/ Size	1.74	0.02	0.55	46	0.64	18.12	1.44	17.2927	10.5796	11.4447	994.4385	22.9555	16.5099	1133.5387	10.6845	22.7301
8b	High Qinj/ Size	1.74	0.02	0.55	46	0.06	19.80	1.80	22.3673	10.6770	11.7992	1699.9326	22.6986	20.6545	1932.3368	10.6845	22.6827
9a	Low kv/kh	1.74	0.02	0.55	46	1.07	14.51	1.05	15.5796	11.2839	11.7813	1646.3300	21.4992	16.2146	1783.4860	10.6845	22.7052
9b	High kv/kh	1.74	0.02	0.55	46	0.01	23.55	0.90	23.1438	9.9389	11.5645	1374.3101	24.4095	21.1292	1583.1402	10.6845	22.7059
3b	kR layering: inc from bottom	1.74	-0.39	0.55	46	0.12	16.31	0.65	16.0493	10.6445	11.7569	1646.3300	22.7908	15.4683	1844.8754	10.6845	22.7054
4a_3b		1.74	0.22	0.35	12	0.01	21.78	0.88	17.9365	11.2279	11.8254	1374.3101	5.6121	19.2826	1549.6797	11.1747	5.6388
4b_3b		1.74	0.59	0.75	220	0.74	9.22	0.55	7.9995	9.4819	10.5403	2158.5100	122.5456	7.1890	2784.2159	9.4832	122.5284
	Case A																
0	REFERENCE	6.24	0.02	0.55	46	0.14	6.46	0.64	7.5657	3.9183	3.9603	2362.4500	61.9875	8.2230	2585.9019	4.1026	59.2028
1a	Low hR	6.24	0.02	0.55	46	0.00	8.77	0.98	9.2974	3.8644	3.9283	3097.3000	20.4965	9.7061	3956.6817	4.1026	19.3067
1b	High hR	6.24	0.02	0.55	46	0.73	5.91	0.54	6.4893	4.3774	4.4516	1801.9000	94.3927	4.7277	2674.3792	4.1026	100.7170
2a	Low hCR	6.24	0.02	0.55	46	0.13	6.83	0.62	7.4880	4.1099	4.1099	2362.4500	57.7436	8.3187	2548.1289	4.1026	57.8470
2b	High hCR	6.24	0.02	0.55	46	0.15	7.05	0.65	7.7391	4.1253	4.1402	2362.4500	60.2316	8.1755	2605.7430	4.1026	60.5655
4a	Low kRmean	6.24	-0.01	0.35	12	0.03	7.29	0.59	8.1608	3.5417	3.5731	2158.5100	17.8639	9.4533	2332.5922	3.4857	18.1506
4b	High kRmean	6.24	0.08	0.75	220	0.75	6.46	0.72	6.8600	4.0273	4.1191	2362.4500	288.5905	6.1955	3011.8809	4.0082	289.9619
5a	Low kCR	6.24	0.02	0.55	46	0.13	6.89	0.62	7.5566	4.1184	4.1238	2362.4500	58.9736	8.3193	2548.8302	4.1026	59.2012
5b	High kCR	6.24	0.02	0.55	46	0.14	6.92	0.62	7.5810	4.1167	4.1225	2362.4500	58.9977	8.2189	2587.5291	4.1026	59.2012
6a	Low phiR	6.24	0.02	0.55	46	0.13	7.62	0.85	8.1036	4.1375	4.1730	2829.9399	58.7007	8.3235	2547.2686	4.1026	59.2007
6b	High phiR	6.24	0.02	0.55	46	0.15	6.15	0.57	7.1517	4.1142	4.1142	1972.1600	59.0334	8.1614	2610.2393	4.1026	59.2013
7a	Low phiCR	6.24	0.02	0.55	46	0.14	6.93	0.63	7.6023	4.1183	4.1237	2362.4500	58.9754	8.2679	2568.4665	4.1026	59.2012
7b	High phiCR	6.24	0.02	0.55	46	0.15	6.95	0.64	7.6453	4.1183	4.1237	2362.4500	58.9754	8.2085	2591.6059	4.1026	59.2012
8a	Low Qinj/ Size	6.24	0.02	0.55	46	0.70	6.51	0.70	7.2762	4.2621	4.3947	1512.9731	57.0080	4.7971	2126.1137	4.1026	59.2247
8b	High Qinj/ Size	6.24	0.02	0.55	46	0.07	6.94	0.59	7.5659	4.0713	4.1161	2871.4485	59.6323	8.9266	2998.0014	4.1026	59.1780
9a	Low kv/kh	6.24	0.02	0.55	46	1.34	4.65	0.40	4.7071	4.1811	4.2222	2585.6599	58.0884	5.7344	3070.9668	4.1026	59.2002
9b	High kv/kh	6.24	0.02	0.55	46	0.01	10.80	0.29	10.8525	4.0708	4.0708	1801.9000	59.6632	9.5820	2397.4374	4.1026	59.2017
3b	kR layering: inc from bottom	6.24	-0.39	0.55	46	0.15	3.58	0.30	4.0163	3.8236	3.9332	3389.9099	63.5229	3.1506	4179.9673	4.1026	59.2031
4a_3b		6.24	0.22	0.35	12	0.03	5.64	0.34	4.9836	3.5126	3.5902	2362.4500	18.0116	3.7373	3712.8499	3.4857	18.1505
4b_3b		6.24	0.59	0.75	220	0.76	2.43	0.04	2.0101	3.2432	3.2578	4060.6399	358.3687	0.3567	12555.9569	4.0082	289.9713

Run #	Run description	dfg/dSg	Lc	VDP	kR mD	Ng3	Total efficiency, % (mean)	(std. dev.)	Total efficiency, @ 30 yrs	PD (min)	PD (@ 0.3 days)	Simulation results RCO2, m	J = Q/ ΔP, bbl/day.psi	Regression model E_S, %	R_{CO2},m	P_D	J, bbl/day.psi
		X1	X2	X3_a	X3_b	X4_b	Y' = f{X}	σ	Y = f{X}	Z' = f{X}	Z = f{X}	R_sim	J_sim				
	Ref11c																
0	REFERENCE	4.64	0.02	0.55	46	0.13	12.51	0.50	12.3138	5.9181	5.9848	1801.9000	41.0276	15.6260	1860.8192	8.0297	30.2384
1a	Low hR	4.64	0.02	0.55	46	0.00	19.54	1.37	20.8735	7.5253	8.2978	2585.6599	10.5070	17.0308	2921.1845	8.0297	9.8470
1b	High hR	4.64	0.02	0.55	46	0.67	12.79	1.25	13.3481	8.2407	8.4864	1504.1801	50.1211	12.1948	1646.6535	8.0297	51.4382
2a	Low hCR	4.64	0.02	0.55	46	0.12	15.85	1.24	18.0087	8.0202	8.2942	1646.3300	29.5718	15.7871	1824.8045	8.0297	29.5366
2b	High hCR	4.64	0.02	0.55	46	0.13	15.55	0.45	15.4069	8.1078	8.3413	1646.3300	30.6258	15.6522	1855.5400	8.0297	30.9236
4a	Low kRmean	4.64	-0.01	0.35	12	0.02	15.77	1.21	17.0075	5.6110	5.7142	1646.3300	11.2631	18.2675	1645.8935	7.8065	8.0955
4b	High kRmean	4.64	0.08	0.75	220	0.74	8.16	0.60	8.7749	6.0227	6.1481	2362.4500	192.9594	12.0763	2154.6094	7.5418	154.0945
5a	Low kCR	4.64	0.02	0.55	46	0.12	15.94	1.23	18.0764	8.1075	8.3143	1646.3300	29.9375	15.7844	1825.9584	8.0297	30.2276
5b	High kCR	4.64	0.02	0.55	46	0.13	15.33	0.45	15.1707	7.9150	8.3131	1646.3300	30.6656	15.6923	1845.9802	8.0297	30.2276
6a	Low phiR	4.64	0.02	0.55	46	0.12	16.16	0.68	15.7927	8.0117	8.3470	1972.1600	30.2955	15.7864	1825.5827	8.0297	30.2274
6b	High phiR	4.64	0.02	0.55	46	0.13	14.80	0.89	14.6805	8.0223	8.3135	1504.1801	30.2555	15.6459	1856.2071	8.0297	30.2276
7a	Low phiCR	4.64	0.02	0.55	46	0.12	15.33	0.45	15.1707	8.0707	8.3142	1646.3300	30.0742	15.7376	1836.0715	8.0297	30.2276
7b	High phiCR	4.64	0.02	0.55	46	0.13	15.41	0.44	15.2852	8.0504	8.3142	1646.3300	30.1499	15.6854	1847.5086	8.0297	30.2276
8a	Low Qinj/ Size	4.64	0.02	0.55	46	0.66	14.31	0.88	13.9674	8.1528	8.3515	1081.5165	29.7946	12.2244	1322.7137	8.0297	30.2513
8b	High Qinj/ Size	4.64	0.02	0.55	46	0.06	16.81	1.26	18.0510	8.0366	8.3678	2024.5425	30.1791	16.3746	2185.0771	8.0297	30.2051
9a	Low kv/kh	4.64	0.02	0.55	46	1.17	11.61	0.83	12.4499	8.3079	8.4070	1972.1600	29.2150	12.2874	2067.0394	8.0297	30.2272
9b	High kv/kh	4.64	0.02	0.55	46	0.01	19.20	0.77	19.0014	7.6634	8.2446	1646.3300	31.6729	16.9092	1785.7651	8.0297	30.2279
3b	kR layering: inc from bottom	4.64	-0.39	0.55	46	0.14	8.69	0.43	8.8368	5.8539	6.0131	2362.4500	41.4778	10.6780	2256.7515	8.0297	30.2383
4a_3b		4.64	0.22	0.35	12	0.02	13.66	0.84	11.9672	5.5394	5.7378	1646.3300	11.4085	12.4811	1993.5484	7.8065	8.0954
4b_3b		4.64	0.59	0.75	220	0.75	4.19	0.24	3.7916	5.0547	5.2253	3097.3000	229.9234	6.0198	3051.9393	7.5418	154.0998

Similarity Solutions for Multiphase Flow in Inhomogeneous Layered Systems for CO_2 Sequestration

Michael J. Swickrath, Priya Ravi-Ganesh, Srikanta Mishra

Battelle Memorial Institute
505 King Avenue
Columbus, OH 43201

October 21, 2014

1 Introduction

According to recent estimates, carbon is released to the atmosphere, in the form of carbon dioxide (CO_2), at rates of 7 gigatons (Gt) per year (1 Gt = 1 billion metric tons of carbon equivalent) [1, 2]. Moreover, 85% of the world's energy comes in the form of fossil fuels [3] accounting for 30% of the generated carbon-equivalent [1]. With increased industrialization and a world population rising at an exponential rate, the demand for energy is growing rapidly. In fact, since the dawn of the industrial age, atmospheric CO_2 has surged by 40% (from 280 ppm to 360 ppm) [4].

The cumulative impact of carbon release is dire. Worldwide temperatures are estimated to rise by 0.3°C per decade. The increase in global temperature has a detrimental impact on plant life and agriculture [4]. Polar ice caps are also melting as a result, which in turn leads to rising sea levels. Moreover, carbon dioxide dissolves in oceans and freshwater forming carbonic acid which decreases the pH reducing the viability of aquatic life on a global scale.

Several CO_2 storage strategies have been advanced to minimize atmospheric carbon release. These include capture and storage in oil and gas reservoirs, deep saline aquifers, oceans, caverns, and coal seams [3]. Storage in fossil fuel reservoirs and saline aquifers is attractive because the approach is relatively mature having been established for decades as a technique for enhanced oil recovery.

Although reservoir and aquifer storage techniques are mature, they are not without technical and economic risks. To offset such risks, advanced physicochemical modeling is typically

performed to evaluate a site for CO_2 sequestration. Such modeling efforts rely on full-physics simulations of a formation using sets of coupled equations derived from first principles. These modeling efforts require significant resources both in site characterization to develop modeling parameters/coefficients and in computational time/hardware.

Recent efforts have focused on simplifying the full physics models enabling rapid screening and risk assessment through the capability to perform sensitivity and parametric analyses. The simplified modeling approach generally builds upon the seminal efforts of Woods and Comer [5] where pressure and saturation distributions are obtained for a radially extending gas front, a multiphase region of brine-gas, and a brine region undergoing displacement by the injected gas. The models can generally be classified as analytical versus numerical. One of the earliest applications of a numerical model to CO_2 sequestration involves the work of Saripalli and McGrail where a model was developed for radial injection of an immiscible CO_2 phase into a confined formation [6]. The semianalytic model was used to solve the axisymmetric flow equations around an injector which evolved into buoyancy-driven floating of the CO_2 phase. Noh et al. used a modified Buckley-Leverett approach to account for mutual solubility of CO_2 and brine to model gas saturation in the formation [7]. McMillan and colleagues developed a pressure solution for the Noh model for a constant pressure injection [8]. This was achieved by assuming constant pressure injection and by calculating the pressure gradients at any instant under the assumption of steady-state conditions for each value of the time-varying flow rate. Oruganti and Mishra evaluated the three-region model of McMillan et al. finding it accurately predicted the CO_2 saturation in the formation but that pressure-buildup was under predicted [9]. Oruganti and Mishra found that the agreement was improved when a representative two-phase mobility was calculated based on the actual mobility profile in the two-phase region. The analytical models are favorable from the stand point of ease of implementation and computational resources involved in calculating a solution. However, the analytical models also have a distinct disadvantage in that the derivation of a closed-form solution typically comes at the expense of decreased accuracy, by virtue of their inability to handle spatially varying aquifer properties.

Several analytical and numerical models, ranging in complexity, have been independently reviewed elsewhere [10]. Of particular interest to this work is the classification of analytical models applying an abrupt interface solution which implicitly assumes that the local-scale capillary forces are negligible such that the fluids become stratified with a sharp interface separating brine-gas with constant fluid saturation on either side of the interface. Nordbotten and colleagues developed a sharp interface model enforcing a volume balance and energy minimization under the assumption of gravity override [11–13]. Mathias, et al., extended the sharp interface model to evaluate an integral solution for pressure buildup and by accounting for fluid and rock compressibility [14]. A similar sharp interface model has been derived using the Dupuit approximation to account for buoyancy effects by Dentz and others [15, 16]. The practicality of such models is evidenced by their application toward probabilistic risk assessment to evaluate the suitability of an aquifer for CO_2 sequestration [17–20]. A simplified model is desirable for such applications since it enables the rapid evaluation, albeit with approximate physics, in which the set of good candidates can be dramatically reduced for further analysis with higher fidelity modeling techniques.

The sharp interface models are efficient from the standpoint of implementation. Agreement between the models, and full-physics simulation software, are decent although there has been much work to establish the conditions under which such solutions are applicable. Lu, et al., noted that the sharp interface solutions were unable to reliably calculate the outermost plume extent of CO_2 during injection [21] which elicited a response explaining the model assumptions and shortcomings [22] along with more comprehensive studies regarding there applicability [23]. In general, the initial sharp interface models were capable of accurately describing brine displacement by CO_2 under viscous flow conditions where properties are spatially constant [11–13]. Improvements to the model have been made by incorporating the ability to describe flow where gravitational forces outweigh viscous forces and for accounting for the effects of fluid compressibility [14, 16].

In the current report, we apply the sharp interface model against results collected from the GEM Compositional & Unconventional Reservoir Simulator. The simulator analyzed several aquifers in which the system was multilayered with variations in permeability. Several cases were analyzed in which the average brine saturation was based on simulator output or extracted from relative permeability curves. The results point to potential modifications that can be made to the sharp interface method leading to better agreement between the simplified model and commercial full-physics simulators.

2 Sharp Interface Model

2.1 Sharp Interface Model for Multiphase Flow

Multiphase flow, confined within a reservoir as illustrated in 1, under the assumption of negligible capillary pressure, is governed by the multiphase extension of Darcys law where the flow of phase α.

$$q_\alpha = -k\frac{k_{r,\alpha}}{\mu_\alpha}\nabla\left(p - gz\right) \tag{1}$$

In the above expression, q represents flux, μ is viscosity, k is permeability of the medium, and k_r is the relative permeability, p is fluid pressure, g is the acceleration due to gravity, and z is the vertical coordinate. Moreover, α indicates there phase where c and w denote the carbon dioxide and brine phases, respectively, while cw denotes the wet CO_2 region. Mass conservation of each phase is enforced with the additional relationships accounting for porosity ϕ, density ρ, and saturation S.

$$\frac{\partial}{\partial t}\left(\phi\rho_\alpha S_\alpha\right) + \nabla \cdot q_\alpha = 0 \tag{2}$$

Lastly, the system is closed by constraining that the pore space is completely filled, $S_c + S_{cw} + S_w = 1$.

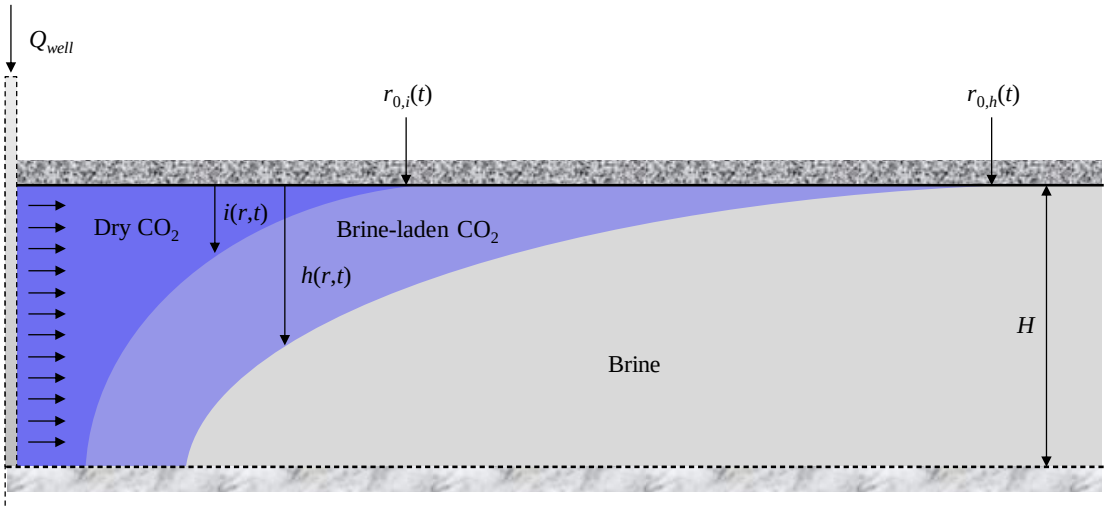

Figure 1: Conceptual illustration of the geometry under analysis with the sharp interface model.

Nordbotten, et al., derive the sharp interface model for multiphase transport during CO_2 injection with several important assumptions. Those include that the well is fully penetrating with rates and aquifer slope consistent such that the reservoir can be approximated as horizontal [12,24]. Furthermore, the brine-CO_2 interface is approximated as a sharp interface where saturation points of CO_2 in brine and brine in CO_2 (mass fractions β_1 and β_2), are held constant throughout the system. As will be demonstrated in this work, this assumption has relevant impacts on the model results.

Lastly, under the assumption that the horizontal length scale in the domain extends far beyond the vertical scale [11–13]. As a result, the vertical equilibrium assumption is invoked to generate a relationship for pressure variation in the horizontal direction is derived for three separate regions separated by the interfaces $i(r,t)$ for dry and wet CO_2 and $h(r,t)$ for wet CO_2 and brine.

$$\begin{aligned} p\left(r,t,0\right) = p\left(r,t,H\right) \quad &- \int_0^{i(r,t)} \left[\rho_c g + \frac{q_{c,z}(r,t,z)\mu_c}{k_z k_{r,c}}\right] dz \\ &- \int_{i(r,t)}^{h(r,t)} \left[\rho_{cw} g + \frac{q_{cw,z}(r,t,z)\mu_{cw}}{k_z k_{r,cw}}\right] dz \\ &- \int_{i(r,t)}^{H} \left[\rho_w g + \frac{q_{w,z}(r,t,z)\mu_w}{k_z k_{r,w}}\right] dz \end{aligned} \tag{3}$$

Equation (3) is an approximation which means mass conservation cannot be guaranteed at the local level. As a result, Nordbotten replaces equations (1) and (2) with their vertically integrated forms.

$$-2\pi r\phi\frac{\partial}{\partial t}\left(H-h\right)=\frac{\gamma_1}{1-S_{res}}\frac{\partial Q_w}{\partial r} \tag{4}$$

$$-2\pi r\phi\frac{\partial}{\partial t}i=\frac{\gamma_2}{1-S_{res}}\frac{\partial Q_c}{\partial r} \tag{5}$$

$$Q_c+Q_{cw}+Q_w=Q_{well} \tag{6}$$

In the above relationships, S_{res} is the residual saturation of the resident brine. Finally, the radially dependent vertically-integrated flow rates are defined assuming angular symmetry.

$$Q_c=-2\pi rik\frac{k_{r,c}}{\mu_c}\frac{\partial p_c}{r} \tag{7}$$

$$Q_{cw}=-2\pi r\left(h-i\right)k\frac{k_{r,cw}}{\mu_{cw}}\frac{\partial p_{cw}}{r} \tag{8}$$

$$Q_w=-2\pi r\left(H-h\right)k\frac{k_{r,w}}{\mu_w}\frac{\partial p_w}{r} \tag{9}$$

Parameters γ_1 and γ_2 are dimensionless phase transfer parameters.

$$\gamma_1=\left[1+\frac{\beta_1 S_{res}}{\left(1-S_{res}\right)\left(1-\beta_2\right)}\right]^{-1} \tag{10}$$

$$\gamma_2=\left[1+\frac{\left(1-\beta_1\right)S_{res}}{\left(1-S_{res}\right)\beta_2}\right]^{-1} \tag{11}$$

Having established the governing equations, the problem is now non-dimensionalized by combining equations (4–9) generating a self-similar set of second-order ordinary differential equations.

$$\frac{d}{d\chi}h'=\frac{4\Gamma\gamma_1}{\chi}\frac{d}{d\chi}\left[\left(1-h'\right)\chi\frac{d}{d\chi}p'\right] \tag{12}$$

$$\frac{d}{d\chi}i' = \frac{4\Gamma\gamma_2\lambda_1}{\chi}\frac{d}{d\chi}\left[i'\chi\frac{d}{d\chi}\left(p' + h' + \upsilon i'\right)\right] \tag{13}$$

$$\frac{d}{d\chi}p' = \frac{\frac{1}{2\chi\Gamma} + \left(\lambda_2 h' + \left(\lambda_1 - \lambda_2\right) i'\right)\frac{d}{d\chi}h' + \lambda_1 i'\upsilon\frac{d}{d\chi}i'}{\lambda_2\left(h' - i'\right) + \lambda_1 i' + \left(1 - h'\right)} \tag{14}$$

The nondimensional parameters are defined in Table 1 of this manuscript. The set of equations (12–14) is solved by Nordbotten, et al., using an appropriately devised numerical scheme [11]. However, for the case where gravity is negligible (i.e. gravity number $\Gamma \to 0$), equations (12–14) degenerate to a closed form analytical solution where $0 \leq i' \leq h' \leq 1$. These conditions exist when injection rates are high, permeability is low, and/or the aquifer is thin.

Table 1: Dimensionless numbers used in the current investigation.

Dimensionless Parameter	Dimensionless Formula
Dimensionless phase transfer parameter 1	$\gamma_1 = \left[1 + \frac{\beta_1 S_{res}}{(1-S_{res})(1-\beta_2)}\right]^{-1}$
Dimensionless phase transfer parameter 2	$\gamma_2 = \left[1 + \frac{(1-\beta_1)S_{res}}{(1-S_{res})\beta_2}\right]^{-1}$
Gravity number	$\Gamma = \frac{2\pi(\rho_w - \rho_{cw})gkH^2}{Q_{well}\mu_w}$
Temporal-spatial similarity variable	$\chi = \frac{2\pi H\phi(1-S_{res})r^2}{Q_{well}\mu_w}$
Dimensionless viscosity	$\lambda_1 = \frac{\mu_w}{\mu_c}$
Dimensionless relative permeability	$\lambda_2 = \frac{k_{r,cw}\mu_w}{\mu_{cw}}$
Dimensionless height - dry gas plume	$h' = \frac{h}{H}$
Dimensionless height - wet gas plume	$i' = \frac{i}{H}$
Dimensionless pressure	$p' = \frac{p}{(\rho_w - \rho_{cw})gH}$
Dimensionless density	$\upsilon = \frac{\rho_{cw} - \rho_c}{\rho_w - \rho_{cw}}$

$$h' = \frac{1}{\lambda_2 - 1}\left[\left(\frac{2\lambda_2\gamma_1}{\chi}\right)^{\frac{1}{2}} - 1\right] \tag{15}$$

$$i' = \frac{\sqrt{\chi} - \gamma_2\sqrt{2\lambda_2/\gamma_1}}{\sqrt{\chi}\left(\gamma_1 - \lambda_2\frac{\gamma_1}{\gamma_2}\right)} \tag{16}$$

Lastly, the non-dimensionalized outermost plume extent for the wet-CO_2 and drying front, $\chi_{0,i}$ and $\chi_{0,h}$, are calculable under the assumption of negligible gravitational forces.

$$\chi_{0,i} = \max\left(\frac{2\lambda_1^2\gamma_2^2}{\lambda_2\gamma_1}, \frac{2\lambda_1\gamma_2}{\lambda_2}\right) \tag{17}$$

$$\chi_{0,h} = 2\lambda_2\gamma_1 \tag{18}$$

Equations (15–16) can be readily transformed to dimensionalized quantities as demonstrated by equations (19–20), respectively.

$$h = H\left[1 - \left(\frac{\mu_c}{\mu_w - \mu_c}\right)\left(\sqrt{\frac{\mu_w\gamma_1 V}{\mu_c\phi\pi r H}} - 1\right)\right] \tag{19}$$

$$i = H\left[\left(\frac{1}{\frac{\mu_w}{\mu_c}\frac{\gamma_2}{\gamma_1} - \gamma_1}\right)\left(\gamma_2\sqrt{\frac{\mu_w V}{\gamma_1\mu_c\phi\pi r H}} - 1\right)\right] \tag{20}$$

Likewise, equations (17–18) can also be manipulated into a dimensional form.

$$r_{0,i} = \left(\frac{\gamma_1 k_{r,cw}\mu_w^2 Q_{well}}{\pi\phi\mu_{cw}H\left(1 - S_{res}\right)}\right)^{\frac{1}{2}} \tag{21}$$

$$r_{0,h} = \max\left[\left(\frac{\gamma_2^2\mu_{cw}\mu_w^2 Q_{well}}{\gamma_1 k_{r,cw}\mu_c^2\pi\phi H\left(1 - S_{res}\right)}\right)^{\frac{1}{2}}, \left(\frac{\gamma_2\mu_{cw}\mu_w Q_{well}}{k_{r,cw}\mu_c\pi\phi H\left(1 - S_{res}\right)}\right)^{\frac{1}{2}}\right] \tag{22}$$

The advantage of this approach is the estimates of the plume location can be rapidly calculated and re-dimensionalized. Consequently, parametric and sensitivity analyses become possible with the simplified model.

2.2 Barenblatt Solution to Front Location

Nordbotten, et al., also derive an analytical expression for the wet CO_2 front location as a function of height neglecting the multiphase region [11]. From this relationship, the outermost plume tip location can be calculated irrespective of gravity number so long as the assumptions used to derive the sharp interface model are appropriate. The derivation follows a similar analysis used to derive expressions (3)–(6). This analysis yields a differential equation in front height, *viz.*

$$\frac{\partial h}{\partial t} = \frac{\Delta\rho g k \lambda_w}{\phi\left(1-S_{res}\right) r}\frac{\partial}{\partial r}\left[\frac{\lambda_c h\left(H-h\right) r}{\lambda_c h + \lambda_w\left(H-h\right)}\frac{\partial h}{\partial r} + \frac{Q_{well}\left(H-h\right)}{2\pi\left(\lambda_c h + \lambda_w\left(H-h\right)\right)}\frac{1}{\Delta\rho g k}\right] \tag{23}$$

Equation (23) are similarly non-dimensionalized using definitions in Table 1.

$$\frac{\partial h'}{\partial \tau} = \frac{1}{\eta}\frac{\partial}{\partial \eta}\left[\frac{\Gamma\lambda h'\left(1-h'\right)\eta}{\lambda h' + \left(1-h'\right)}\frac{\partial h'}{\partial \eta} + \frac{1-h'}{\lambda h' + \left(1-h'\right)}\right] \tag{24}$$

A scaling variably is then introduced, $\chi = \eta^2/\tau$, converting the expression into a second–order differential equation.

$$\tau\frac{\partial h'}{\partial \tau} - \chi\frac{\partial h'}{\partial \chi} = 2\frac{\partial}{\partial \chi}\left[\frac{1-h'}{1+\left(\lambda-1\right)h'}\left(2\Gamma\lambda\chi h'\frac{\partial h'}{\partial \chi}+1\right)\right] \tag{25}$$

Equation (25) is expanded and divided by $\partial h'/\partial\chi$. Under the stationary limit, the resulting equation has a self-similar solution for the PDE which is calculated by satisfying a nonlinear second-order ordinary differential equation [25].

$$\begin{aligned} 0 = \quad & \chi \quad - \left[1+\Gamma\lambda\chi\tfrac{d\left(h'\right)^2}{d\chi}\right]\tfrac{2\lambda}{\left(1+\left(\lambda-1\right)h'\right)^2} \\ & + \quad 4\Gamma\lambda\tfrac{1-h'}{1+\left(\lambda-1\right)h'}\left[h' + \chi\tfrac{dh'}{d\chi} + h'\chi\tfrac{d^2h'}{d\chi^2}\left(\tfrac{dh'}{d\chi}\right)^{-1}\right] \end{aligned} \tag{26}$$

Equation (26) is solved by choosing a value of χ where $h' = 1$ denoted as $\chi_{0,h}$. The profile of h' is then calculated through integrating equation (26) from $\chi_{0,h}$ to the value of χ where $h' = 0$. The solution is not considered physical unless mass conservation is enforced. Per derivations included elsewhere [11], mass is conserved when the following condition is satisfied.

$$\int_0^{\chi_{0,h}} h'\left(\chi\right)d\chi = 2 \tag{27}$$

The solution satisfying (26) and (27) is regarded as the rigorous solution herein. After contacting Prof. Nordbotten of the Department of Mathematics at the University of Bergen, Prof. Nordbotten graciously supplied source code in the MATLAB® computing language to calculate a solution to equation (26). After minor modifications to the MATLAB® script, the results were re-dimensionalized and compared against solutions prepared through other techniques.

3 Simulation Test Cases

A multitude of simulation test cases were prepared for comparison of the sharp interface model to a commercial full-physics simulation code, CMG-GEM. These varied in complexity ranging from a one-dimensional homogeneous case to two-dimensional cases with heterogeneity and layering. A caprock layer was included in these cases. Eleven separate parameters were explored, although some were correlated, in which a minimum and maximum value were set and then the simulation was performed to track a variety of variables; most notably in this case, interface location and sweep efficiency. These test cases, and the variables under consideration, are summarized in Table 2 below.

Table 2: Summary of variable parameter ranges explored with the CMG-GEM software and the sharp interface model.

No.	Parameter	Description	Units	Reference Value	Low Value	High Value
1	h_R	Reservoir thickness	m	150	50	250
2	h_{CR}	Caprock thickness	m	150	100	200
3	$k_{avg,R}$	Average reservoir permeability	mD	46	12	220
	V_{DP}	Dykstra-Parson's coefficient*	—	0.55	0.35	0.75
4	$k_{avg,CR}$	Average caprock permeability	mD	0.02	0.002	0.2
5	k_V/k_H	Anisotropy ratio	—	0.1	0.01	1.0
6	q	CO_2 injection rate	MMT/yr	0.83	0.33	1.33
	L	Outer radius of reservoir§	km	10	5	7
7	f_R	Porosity of reservoir	—	0.12	0.08	0.18
8	f_{CR}	Porosity of caprock	—	0.07	0.05	0.1
9	l_v	Indicator for permeability layering	—	Random	Increasing from top	Increasing from bottom

∗ – Correlated with $k_{avg,R}$

§ – Correlated with q

In addition to the parameterization in Table 2, three separate relationships for relative permeability were explored as illustrated in Figure 2. The capillary pressure-saturation relationship for the aquifers are described with the van-Genuchten formulation and have been analyzed in a former analysis for a reference case [9] which will also be referred to as case (A). Two additional cases were also analyzed. In one case, the relative permeability was set such the value at full gas saturation, $S_c = 1$, is equivalent to that of the reference case and linear in between, referred to as case (B). Lastly, a case with an amplified permeability was also assessed as the high permeability case, referred to as (C). The three separate curves

provide a range of permeability characteristics from which the sharp interface model can be benchmarked against a full-physics model.

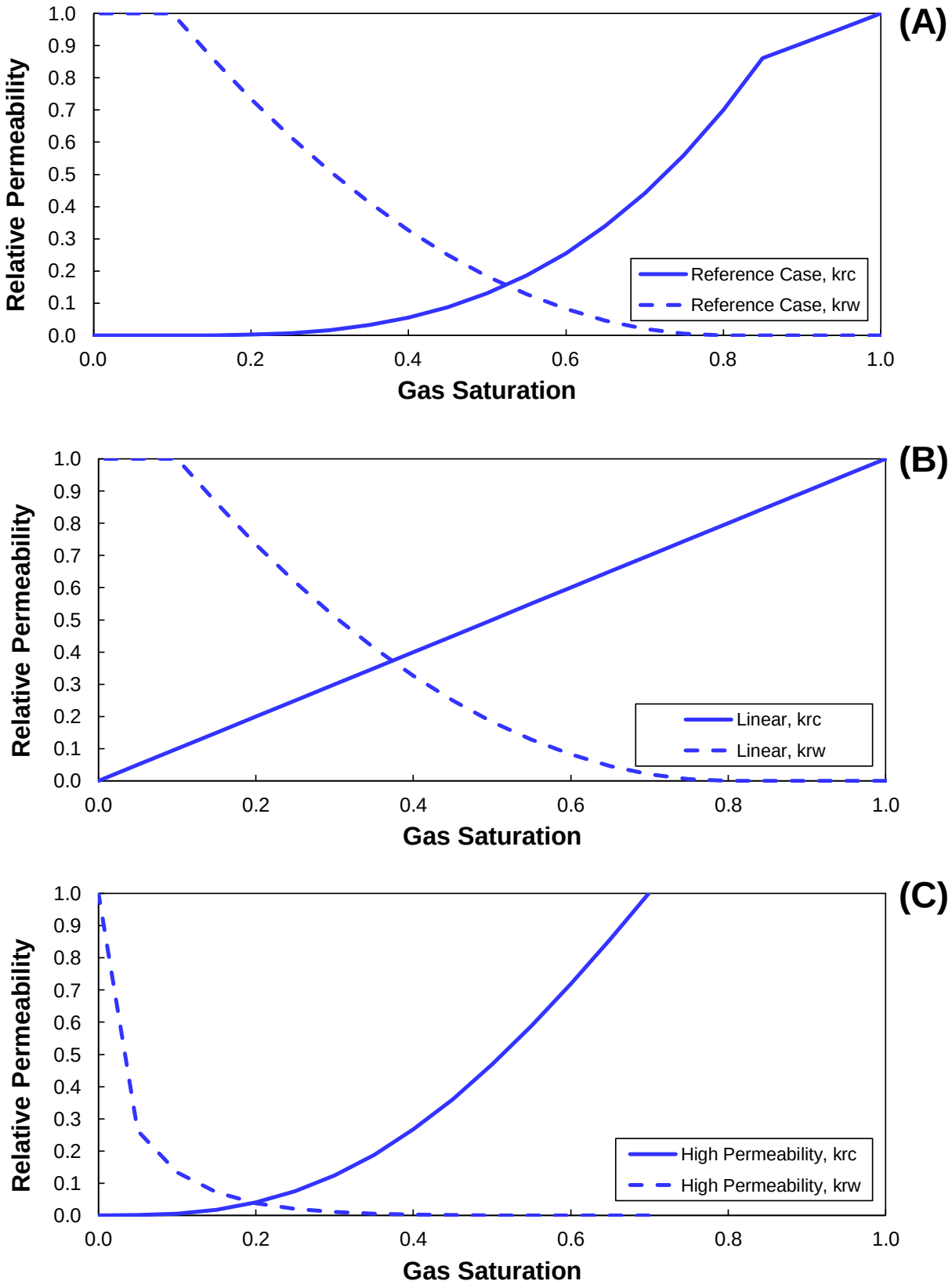

Figure 2: Relative permeability relationships considered in this analysis. (A) Reference case, (B) linear permeability, and (C) high permeability.

4 Model Verification for Varying Gravity Number

The sharp interface model has been derived herein according to the pioneering efforts of a variety of researchers studying multiphase flow in porous media [11–13,15,17,26]. To evaluate their accuracy and reliability in forecasting, the model has been calculated in parallel to results generate with the CMG-GEM full physics reservoir simulator software. In particular, equations (15–16) can be used to solve for the front profile. In this case, we compare our results to the model and numerical routine derived by Nordbotten, et al. in a previous study [13]. These results are demonstrated by Figure 3.

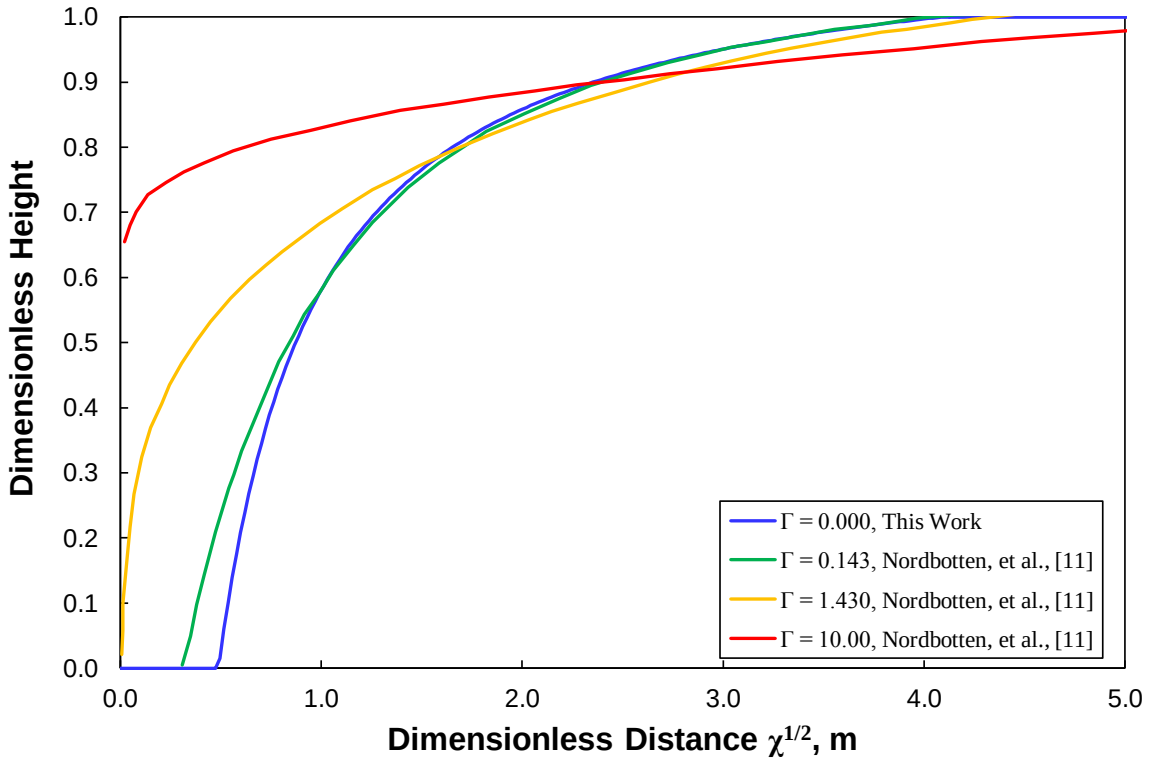

Figure 3: Comparison of simplified sharp interface model to Nordbotten et al. [13] with various gravity numbers, Γ.

As shown in Figure 3, equation (15) was solved and compared against the results for a variety of gravity numbers using the numerical solution to equations (17–18) presented elsewhere [13]. As indicated by these results, the agreement between the closed form analytical solution and the numerical model are good when gravity number is small. Nordbotten and Bachu suggest a criterion of $\Gamma \leq 0.5$ as the range of applicability [11–13, 27]. Even after the gravity number exceeds unity, the agreement in front location at h'=1 is still decent. As the gravity number grows beyond that, the deviation becomes substantial. The numerical model

results in Figure 3 showed favorable comparison to the Schlumberger ECLIPSE software. Consequently, this analysis provides further confidence the sharp interface model has merit as a predictive tool and that our implementation of the model appears sound.

5 Comparison of Simulator and Sharp Interface Model

Having established the analytical sharp interface model (equations 15–18), rather than the semi-analytic numerical implementation (equations 12–14), it is now possible to extend the model against the test cases explained by Table 2 and Figure 2. These results are summarized in a series of figures.

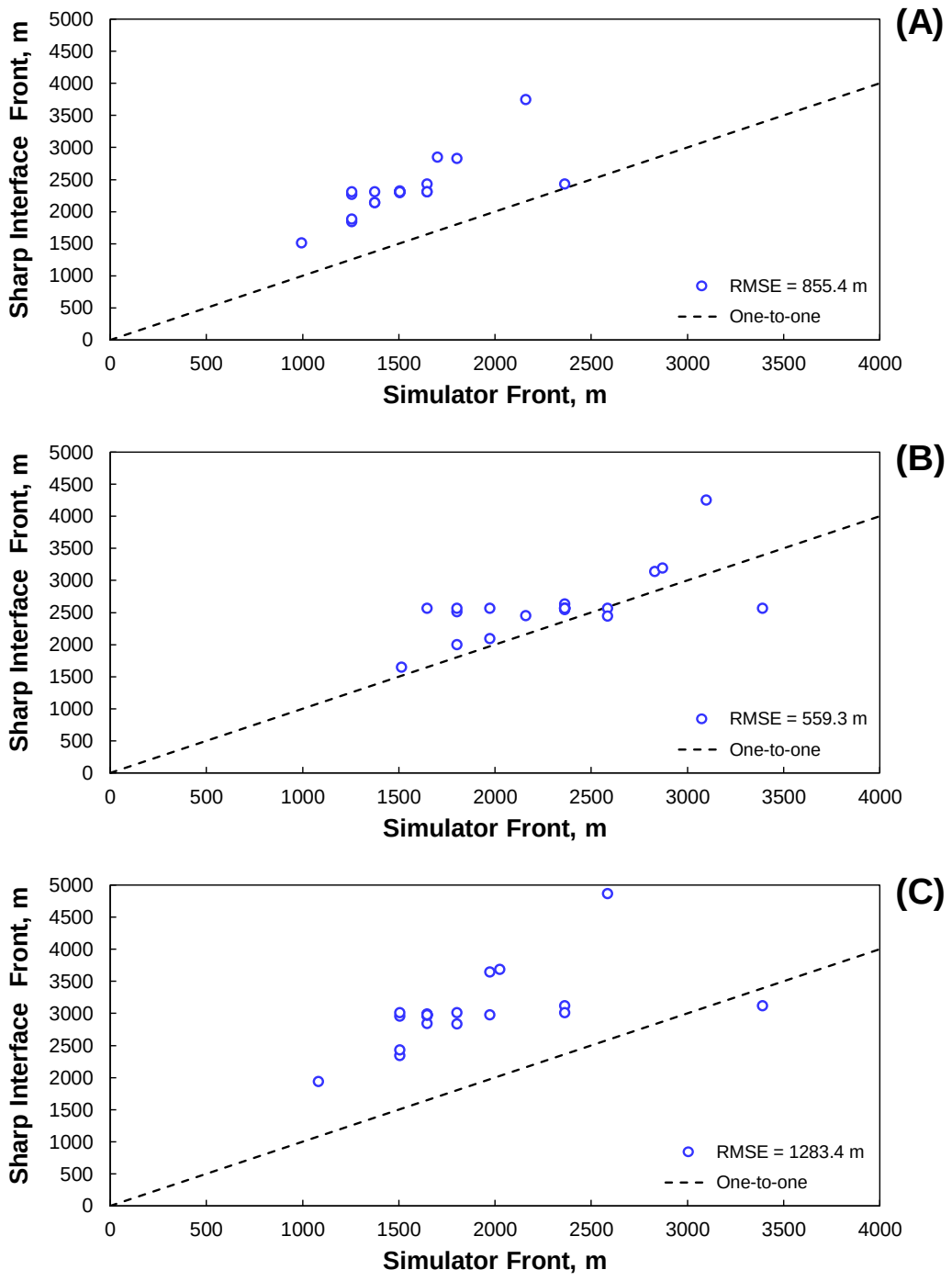

Figure 4: Comparison of sharp interface model predictions against the CMG-GEM simulator when the end-point relative permeability is used. (A) Reference case permeability, (B) linear relative permeability, and (C) high relative permeability. RMSE = root-mean-square error.

5.1 Sharp Interface Model

Figure 4 (A), (B), and (C) show the results when the relative permeability is set according to the end point relative permeability. Specifically, the end point relative permeability is determined by finding the brine saturation (i.e. $(1 - S_g)$) at which $k_{r,w} \rightarrow 0$ and then determining the gas relative permeability at that point, $k_{r,c}$. For (A), (B), and (C), the values of S_{res} are then 0.2, 0.2, and 0.3, respectively, leading to $k_{r,cw}$ values of 0.7, 0.8, and 1.0. Note the implicit assumption here that the interface is sharp, and hence, the permeability of the multiphase zone is approximately the relative permeability of the CO_2. With this assumption, the sharp interface model generally over predicts the outer most plume location as compared to the simulator.

Disagreement between the sharp interface model and commercial simulators has been noted elsewhere [21]. Hence, this disagreement was not entirely unexpected. Moreover, in some cases, the gravity number under analysis exceeded unity although it was always less than 10. The implications of an increasing gravity number are demonstrated in Figure 3 which prompted Nordbotten, et al., to suggest a threshold value of 0.5 for applicability [11–13, 27]. In turn, responses to discrepancies with more detailed analysis have been publicly released [22, 23]. These results suggested a sensitivity investigation of the model to which it became immediately apparent that the mobility of the multiphase zone, $k_{r,cw}/\mu_{cw}$ which is captured by the dimensionless parameter λ_2, most significantly influences the front location.

5.2 Sharp Interface Model with Relative Permeability Calculated at Average Gas Saturation

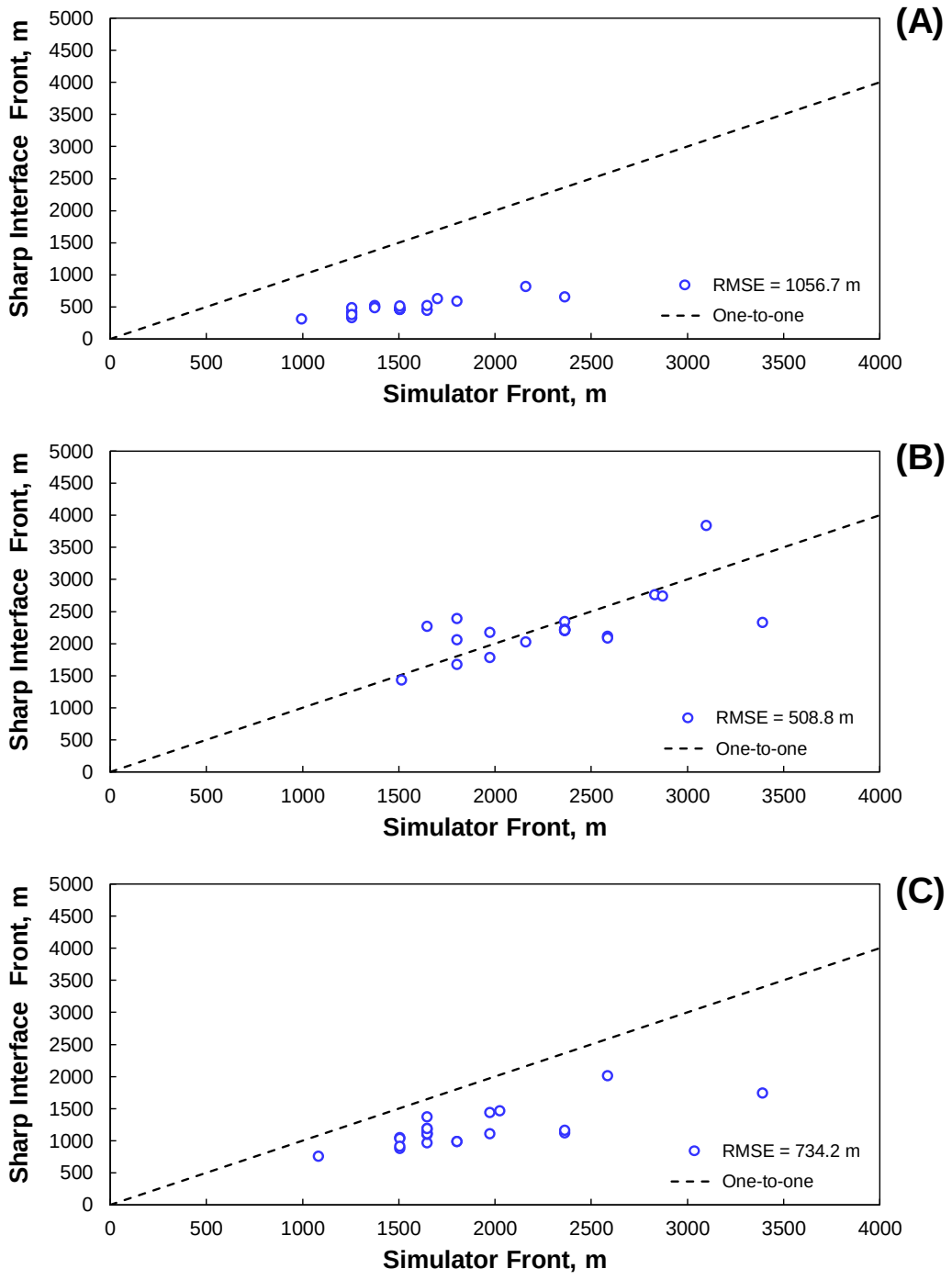

Figure 5: Comparison of sharp interface model predictions against the CMG-GEM simulator when the relative permeability is calculated based on the average gas saturation in the two-phase region. (A) Reference case permeability, (B) linear relative permeability, and (C) high relative permeability. RMSE = root-mean-square error.

Noting the discrepancy is associated with phase mobility, the first hypothesis tested was that the endpoint relative permeability provides an incorrect value for the model. To evaluate this hypothesis, instead the relative permeability was interpolated from the relationships in Figure 2 using the average gas saturation in the multiphase zone. This adaptation seems reasonable since the average gas saturation in the multiphase zone according to the simulator was much different than one minus the residual brine saturation in the sharp interface model (i.e., $1-\langle S_g \rangle \neq S_{Res}$). These results are indicated by Figure 5. In this case, the sharp interface model appears to under predict the location of the front in comparison to the commercial simulator with the exception of case (E) where the results are scattered about the one-to-one line. This approach did not satisfactorily improve the sharp interface prediction overall.

5.3 Sharp Interface Model with Modified Multiphase Mobility

Based on previous findings indicating the importance for accounting for the two-phase mobility [9], an attempt was made to determine the correct mobility at which the sharp interface model and numerical simulator were in precise agreement to lend insight into what mobility resolves the discrepancy. The rationale is that with simulated injection pressures ranging from 1870-2050 psia, at reservoir temperatures of around 100 °F, the carbon dioxide is supercritical (critical temperature 84.8 °F and pressure of 1071.3 psia). Under such conditions, water solubility in the carbon dioxide phase is greatly increased. Consequently, it may be necessary to adapt the mixture viscosity to account for dissolved water in the multiphase region. Moreover, the method to best adapt the viscosity is unknown necessitating the optimization study.

The optimization study was implemented by first calculating γ_2 from the simulator. This was achieved by using the simulator-predicted plume location, and then by calculating $\chi_{0,h}$ (see Table 1), and finally calculating γ_2 via equation (18). Then the viscosity of the multiphase mixture, μ_{cw}, was manipulated using, the bisection method, until a match was achieved. As a result, the sharp interface model could be corrected to precisely match the simulator.

The corrected viscosity was then used to explore applicability of different mixing rules to CO_2 sequestration. A variety of mixing rules have been collected and summarized in Table 3 based on previous work analyzing mixing rule applicability in petroleum blends [28]. The sharp interface model was then solved with the mixing law calculation for μ_{cw}. The mixing laws were applied with both the end point relative permeability and the permeability at brine gas saturation. In the latter case, the mixing laws tended to produce viscosity values larger than viscosity of water. Consequently, those results were deemed nonphysical and instead we infer it is more appropriate to use the end point relative permeability for the sharp interface model. The cases in which pure CO_2 viscosity was applied is essentially the control group where the sharp interface model remains unmodified.

Table 3: Viscosity mixing rules considered in the current investigation.

Mixing Law	Mixing Law Relationship
Pure CO_2	$\mu_{cw} = \mu_c$
Linear	$\mu_{cw} = S_c\mu_c + S_w\mu_w$
Logarithmic	$\ln \mu_{cw} = S_c \ln \mu_c + S_w \ln \mu_w$
Bingham	$\frac{1}{\mu_{cw}} = \frac{S_c}{\mu_c} + \frac{S_w}{\mu_w}$
Reid	$\mu_{cw} = \frac{(S_c+S_w)\mu_c\mu_w}{S_c\mu_c+S_w\mu_w}$
Arrhenius	$\mu_{cw} = \mu_c^{S_c}\mu_w^{S_w}$
Power-law	$\mu_{cw}^n = S_c\mu_c^n + S_w\mu_w^n$
Kendall-Monroe	$(\mu_{cw})^{1/3} = S_c\,(\mu_c)^{1/3} + S_w\,(\mu_w)^{1/3}$
Bingham-Reid Avg.	$\mu_{cw} = \frac{1}{2}\left[\left(\frac{S_c}{\mu_c} + \frac{S_w}{\mu_w}\right)^{-1} + \frac{(S_c+S_w)\mu_c\mu_w}{S_c\mu_c+S_w\mu_w}\right]$

The problem of accurately estimating mixture viscosity remains one of the most challenging amongst the field of physical property calculations. Arrhenius was one of the first to propose a mixing rule in 1887 as a basis for subsequent study [29]. Bingham published some of the first comprehensive theoretical and experimental studies indicating mixture viscosity is not an additive property [30]. Kendall & Monroe proposed an exponent based method which showed good agreement with experimental data [31]. Today, a multitude of empirical viscosity mixing rules exist to choose from with a detailed discussion presented elsewhere [28]. Figure 6 illustrates the influence of each viscosity mixing rule on the calculated viscosity as compared to the viscosity required to match the mobilities between the sharp interface model and the simulator data. A linear mixing law (i.e. additive viscosity assumption) tended to dramatically over-predict the viscosity with the Kendall-Monroe, logarithmic, and power law relationships providing only slight improvement. However, none of these mixing laws appeared to perform as well as simply using the dry CO_2 viscosity. In contrast, the Bingham and Reid models generally bounded the optimized viscosity in the cases where the relative permeability relationship was non-linear (cases (A) and (C)). Agreement was further improved when an average of the Bingham and Reid models was applied.

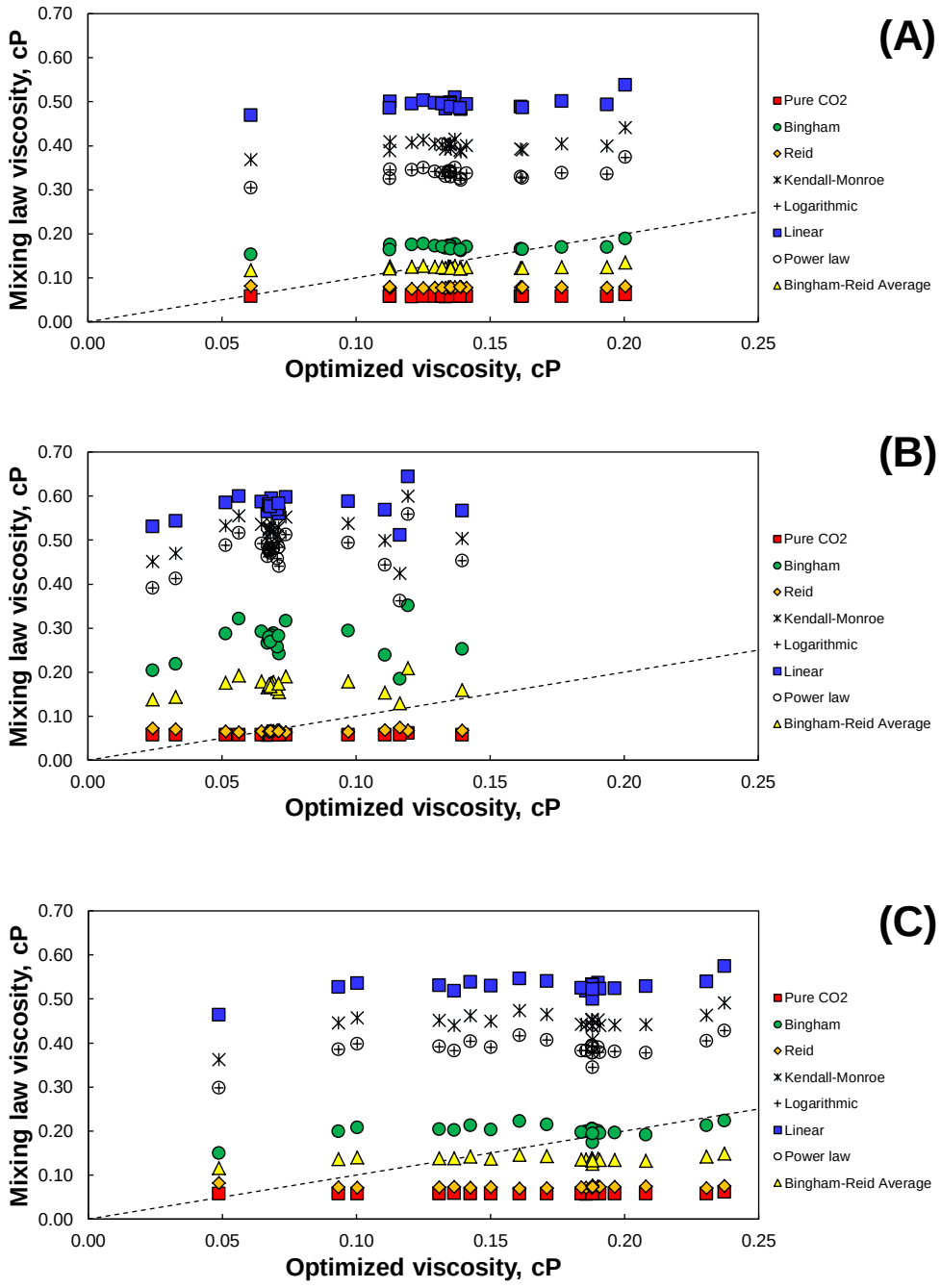

Figure 6: Mixing rule viscosity plotted against the optimized viscosity resulting in agreement between the sharp interface model and the GEM full-physics simulator. (A) Reference case permeability, (B) linear relative permeability, and (C) high relative permeability.

It is worth noting that a few specific cases tended to be problematic for the sharp interface model, even with a modified viscosity. Those cases involved layering increasing from the bottom and high reservoir permeability. The points are depicted in Figure 7 toward the

right of the charts where the simulator predicts a large distance for the outermost plume while the sharp interface model dramatically under predicts the location in comparison.

The previous analysis suggests the application of non-additive mixing laws can produce a CO_2-brine phase mobility that improves agreement between the sharp interface model. These results were confirmed in Figure 7. As illustrated in the plots, the agreement is much improved for the cases were the relative permeability relationship is non-linear as in (A) and (C). Table 4 summarizes the root-mean-square error for the cases investigated herein.

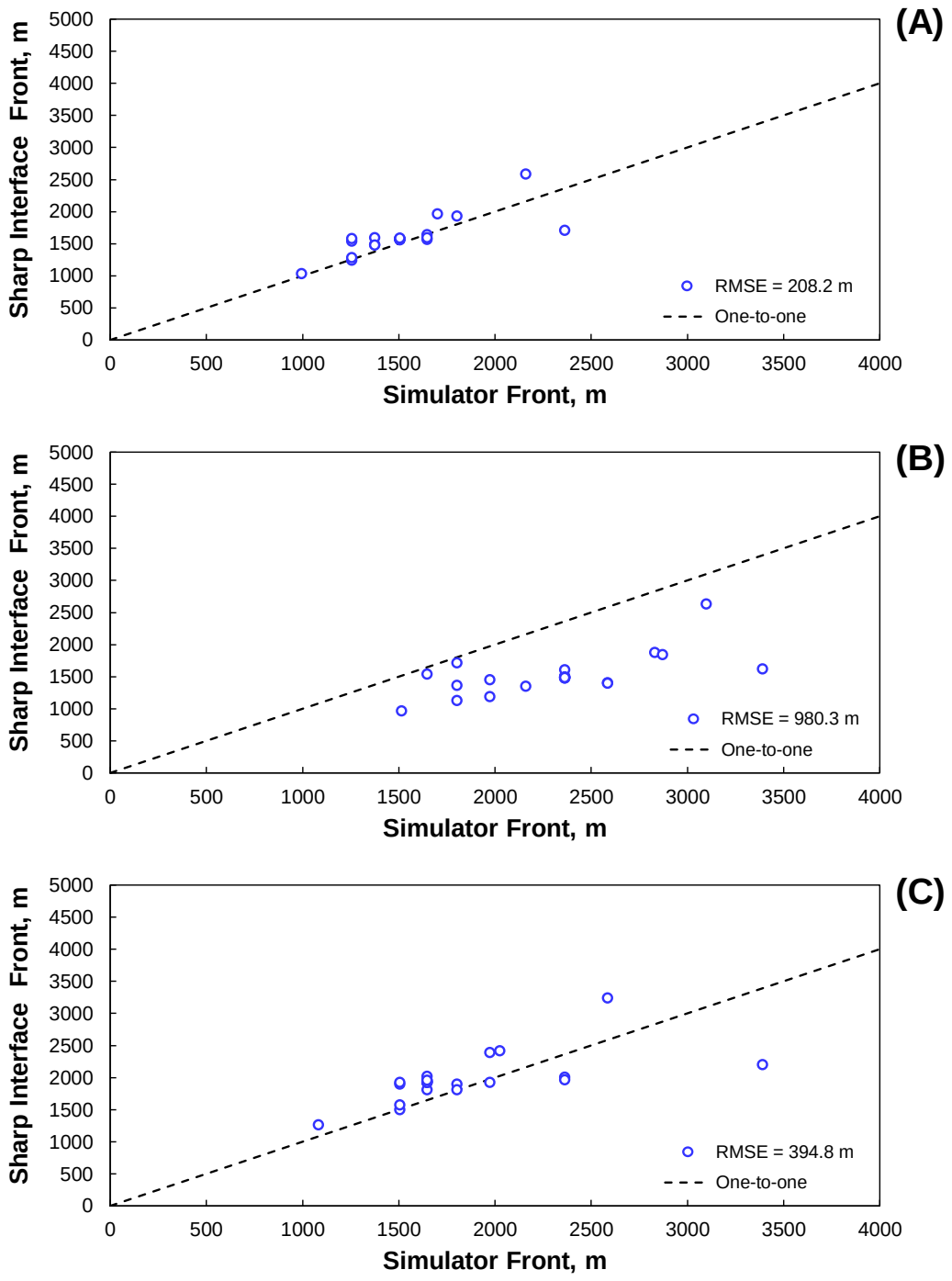

Figure 7: Comparison of sharp interface model predictions against the CMG-GEM simulator when the Bingham-Reid mixing law is used to calculate CO_2-brine viscosity. (A) Reference case permeability, (B) linear relative permeability, and (C) high relative permeability. RMSE = root-mean-square error.

Lastly, an analysis was performed where both the Bingham-Reid mixing rule and relative permeability at average gas saturation was performed as shown in Figure fig:SIM4. This effectively increases the viscosity applied within the model while also reducing the value of the relative permeability. The two factors in aggregate represent a significant increase in resistance in the horizontal direction within the model. As a result, the model represented by equation (18) typically under predicts the front location.

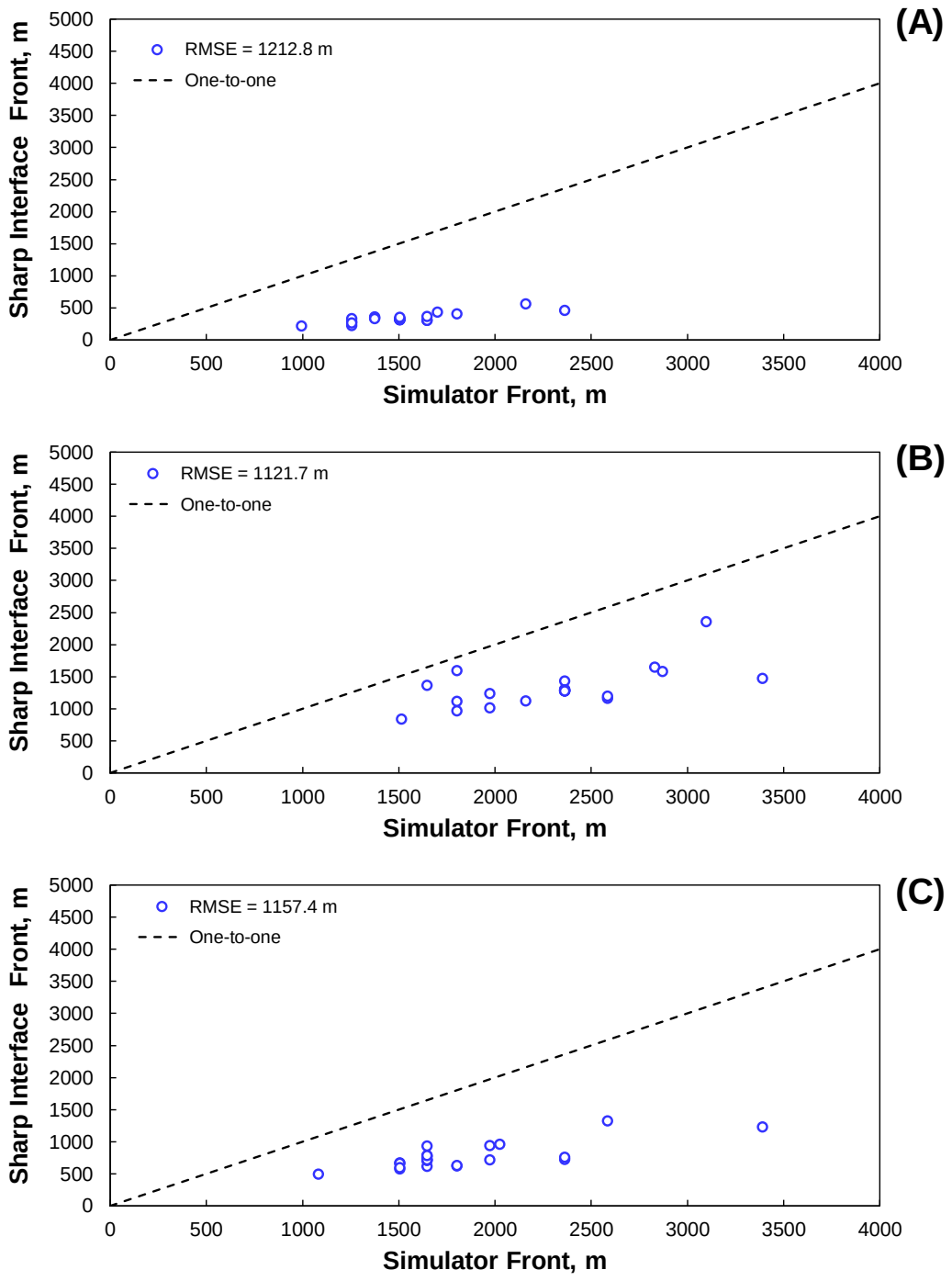

Figure 8: Comparison of sharp interface model predictions against the CMG-GEM simulator when the Bingham-Reid mixing law is used to calculate CO_2-brine viscosity. (A) Reference case permeability, (B) linear relative permeability, and (C) high relative permeability. RMSE = root-mean-square error.

Table 4: Summary of root-mean-square error (RMSE) for sharp interface model with and without multiphase viscosity correction. (A) Reference case permeability, (B) linear relative permeability, and (C) high relative permeability.

Root-mean-square error, m	(A)	(B)	(C)
End-point relative permeability	855.4	559.3	1283.4
Rel. permeability at average gas saturation	1056.7	508.3	734.2
End-point relative permeability with mixture viscosity	208.2	980.3	394.8
Avg. sat. relative permeability with mixture viscosity	1212.8	1121.7	1157.4

5.4 Error as a Function of Gravity Number, Γ

A significant amount of deviation is observed between the data produced by a full-physics simulator and both the analytic profile (equations 15–16) and analytic plume tip (equations 17–18) from the sharp interface model. It was believed that the deviation was attributed to applying the sharp interface solution to situations characterized by a high gravity number. Consequently, plots were prepared in which the error was analyzed as a function of gravity number as indicated in Figure 9. As suggested in the literature for the sharp interface model, as gravity number increases beyond 0.5, the model should start diverging from the simulator. This trend was not observed. In addition, a regression model was applied to the error between simulator and sharp interface model for the three separate relative permeability cases. Coefficients were considered for up to a cubic polynomial although only the linear fits are shown in Figure 9. Regression p-values indicated that in most cases, there was no apparent correlation between error and gravity number. In many cases, the linear coefficient was actually negative indicating error decreases as the gravity number increases. While it is clear from Figure 3 that gravity number dramatically influences the shape of the plume, this analysis suggests that there are other factors that serve to complicate the analysis.

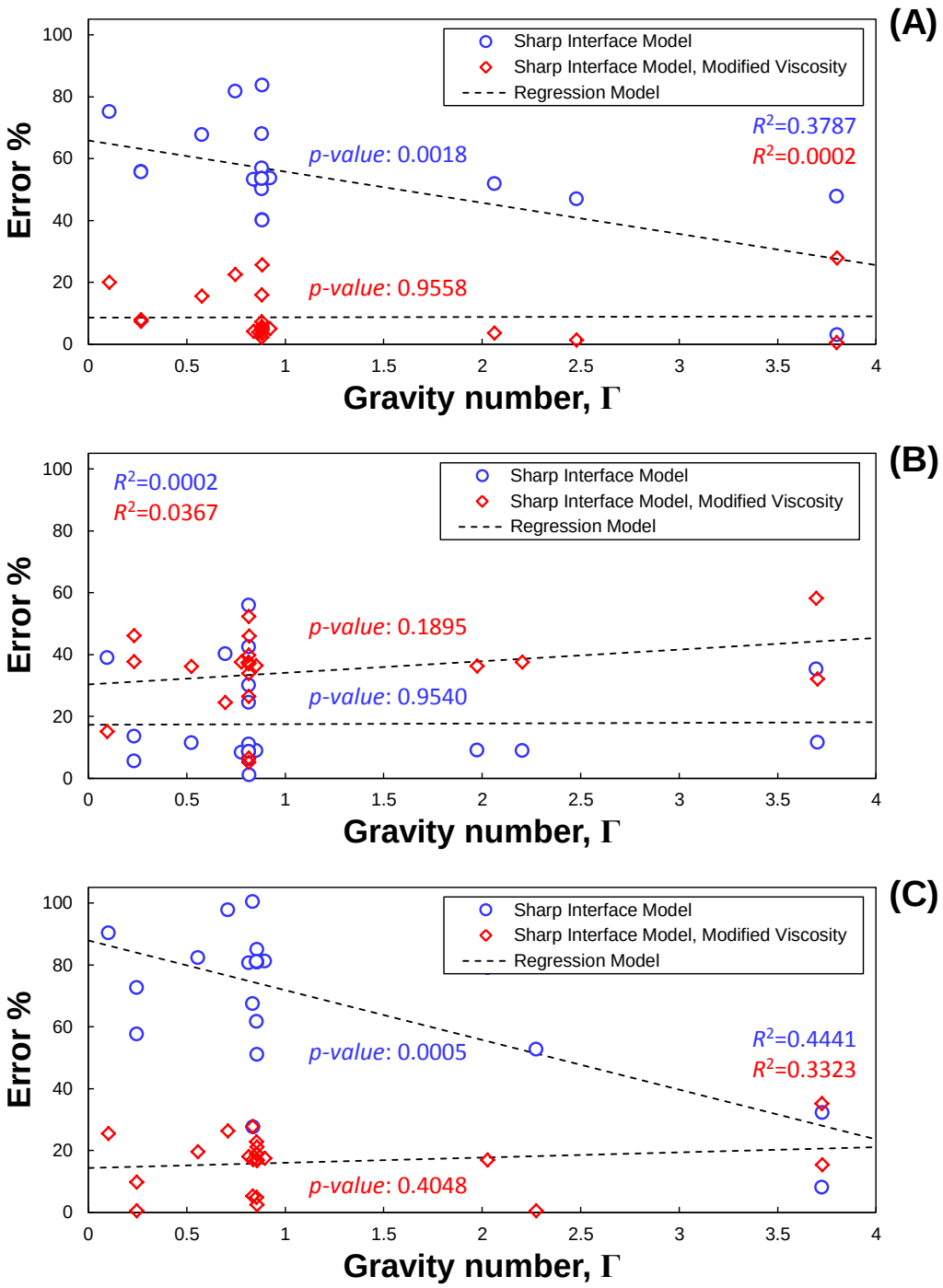

Figure 9: Error in plume front location as a function of gravity number. (A) Reference case permeability, (B) linear relative permeability, and (C) high relative permeability.

The results in Figure 9 proved inconclusive with respect to understanding the influence of gravity number on the accuracy of the analytic and semi-analytic sharp interface solutions. In

addition, Figure 9 does seem to indicate the importance the gravity number on the resulting interface profile. These observations suggest that the rigorous solution (equations 26–27) is necessary to accurately predict front location.

5.5 Rigorous Numerical versus Semi-analytic Solutions

Based on the variability in predicted values by the modified analytic relationships, the investigation was expanded to consider the rigorous solution to the sharp interface model with modified viscosity. In aggregate, all of the cases in Table 2 with the relative permeability relationships in Figure 2, were analyzed using viscosity mixing rules in Table 3. For the analysis, the relative permeability was calculated using either the end-point saturation value at the wet-gas/brine interface or by using the average saturation in the wet-gas region. The expanded analysis is summarized in Figure 10. In total, 1244 versions of the sharp interface model were compared against results generated from the commercial code.

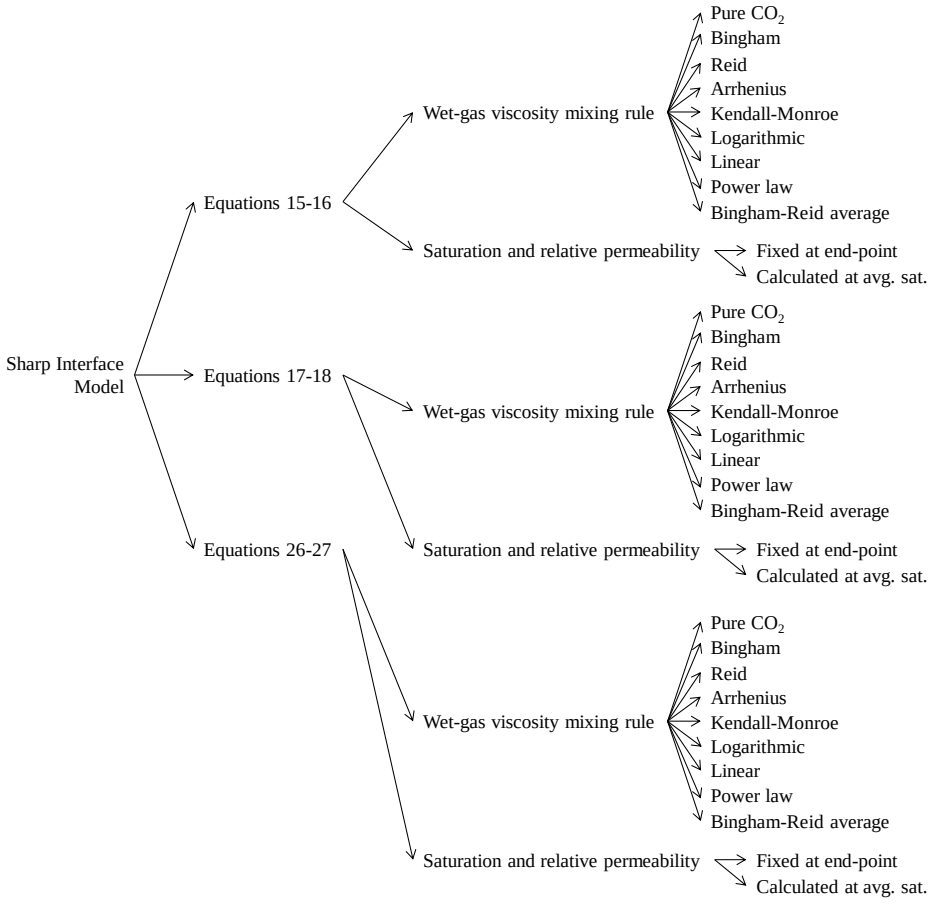

Figure 10: Factors evaluated in the expanded analysis of the sharp interface model.

The root-mean error-squared (RMSE) between the commercial simulator and the sharp interface model were calculated as the metric to assess the accuracy of the model. While it is understood that the commercial simulator may have error intrinsic to its prediction arising from a number of assumptions used to derive the set of equations and with the numerics involved in computing the solution, the level of fidelity involved in calculating the solution is much higher than the comparable reduced order model. Therefore, the simulator results are regarded as the accurate solution for this analysis.

The rigorous solution, as compared to the simulator and the analytical solutions, are presented in Figure 11. In this comparison, the end-point saturation is used to calculate relative permeability and the wet-gas is presumed to have the density and viscosity of pure CO_2 (*i.e.* this is the implementation of the sharp interface model applied in [11,11]). As demonstrated, the sharp interface typically over-predicts the location of the plume tip in comparison to the simulator. It is also apparent that the rigorous solution does produce a difference in comparison to the analytical solutions which consider the gravity as negligible. When gravity was considered, the error between the simulator and sharp interface model actually increases.

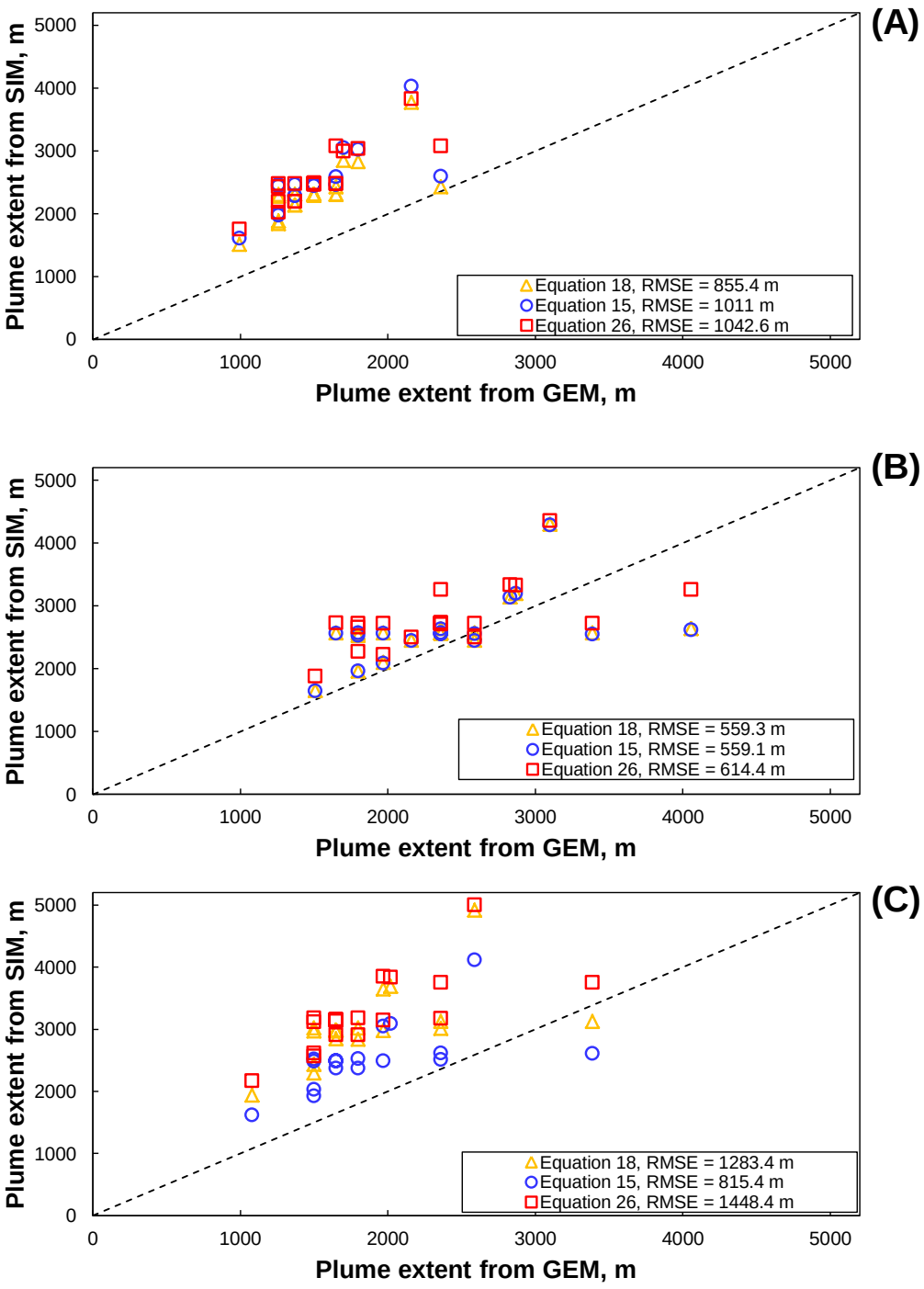

Figure 11: Comparison of plume tip location predictions for the commercial simulator versus the sharp interface model for the analytical profile (Eq. 15), analytical tip (Eq. 18), and the rigorous profile (Eq. 26). (A) Reference case permeability, (B) linear relative permeability, and (C) high relative permeability. RMSE = root-mean-square error.

As the error with the rigorous model is still significant, and since viscosity mixing rules seemed to improve the predictive capability of the analytical models, a mixing rule has also been applied to the rigorous solution. Results using the Bingham-Reid mixing rule are shown in Figure 12. As demonstrated in Figure 12, the agreement is significantly improved over the earlier implementation of the sharp interface model when the relative permeability relationship is non-linear as in (A) and (C). In the case of linear relative permeability, case (B), the agreement is still unsatisfactory.

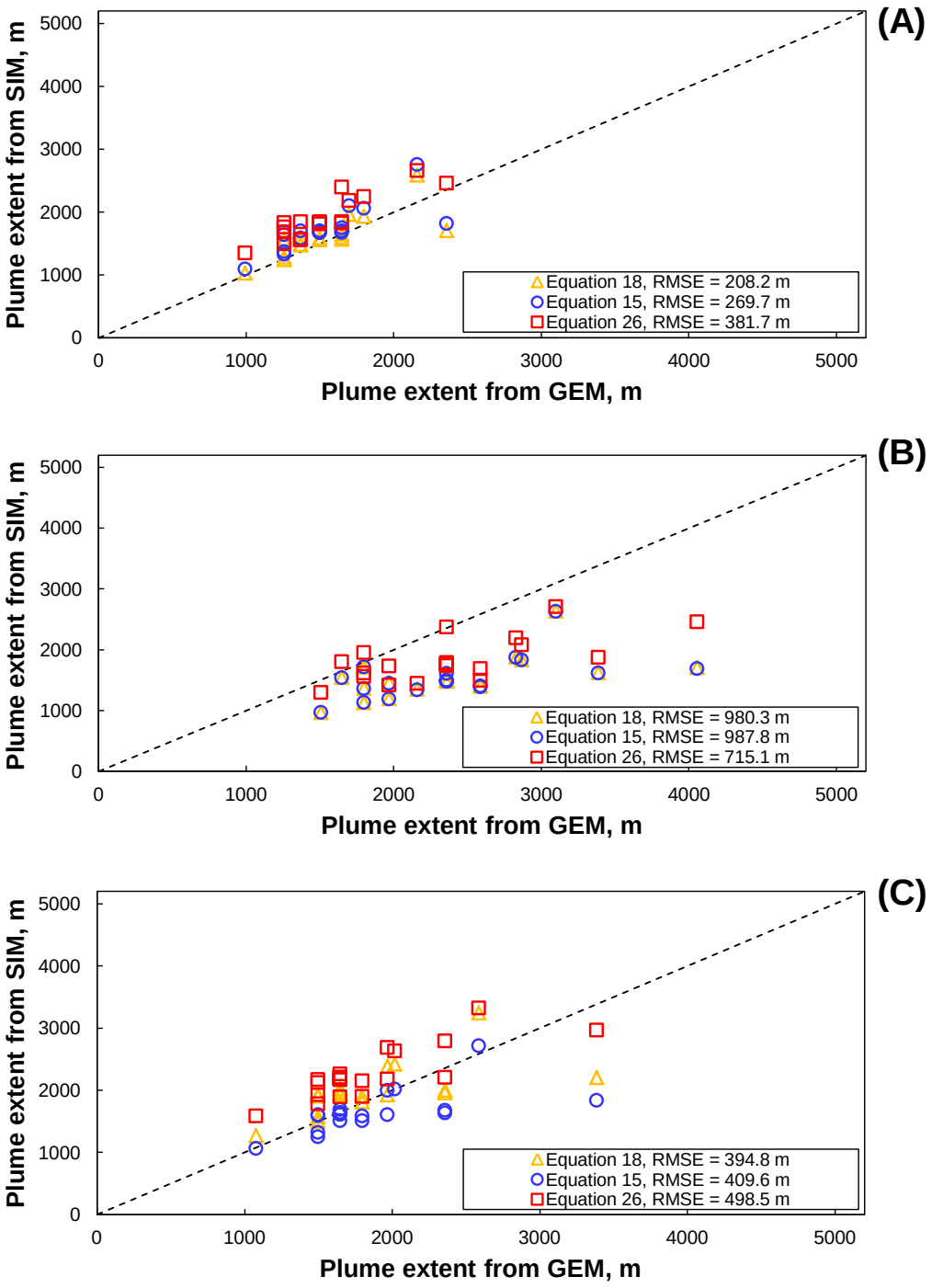

Figure 12: Comparison of plume tip location predictions for the commercial simulator versus the sharp interface model using a Bingham-Reid mixing law for the analytical profile (Eq. 15), analytical tip (Eq. 18), and the rigorous profile (Eq. 26). (A) Reference case permeability, (B) linear relative permeability, and (C) high relative permeability. RMSE = root-mean-square error.

It was postulated that error could be attributed to the application of an end-point saturation for the entire wet-gas region. In reality, the average wet-gas saturation can vary significantly from the end-point value. Therefore, a relative permeability calculated at the wet-gas average saturation may be more applicable for the sharp interface model. Figure 13, demonstrates the model results using the average gas saturation. For the reference permeability (A), the agreement between the rigorous solution and the simulator is very good. Moreover, the agreement between the high permeability case is also very good. Conversely, the error for the linear relative permeability in case (B) has increased leading to over-prediction of plume tip location.

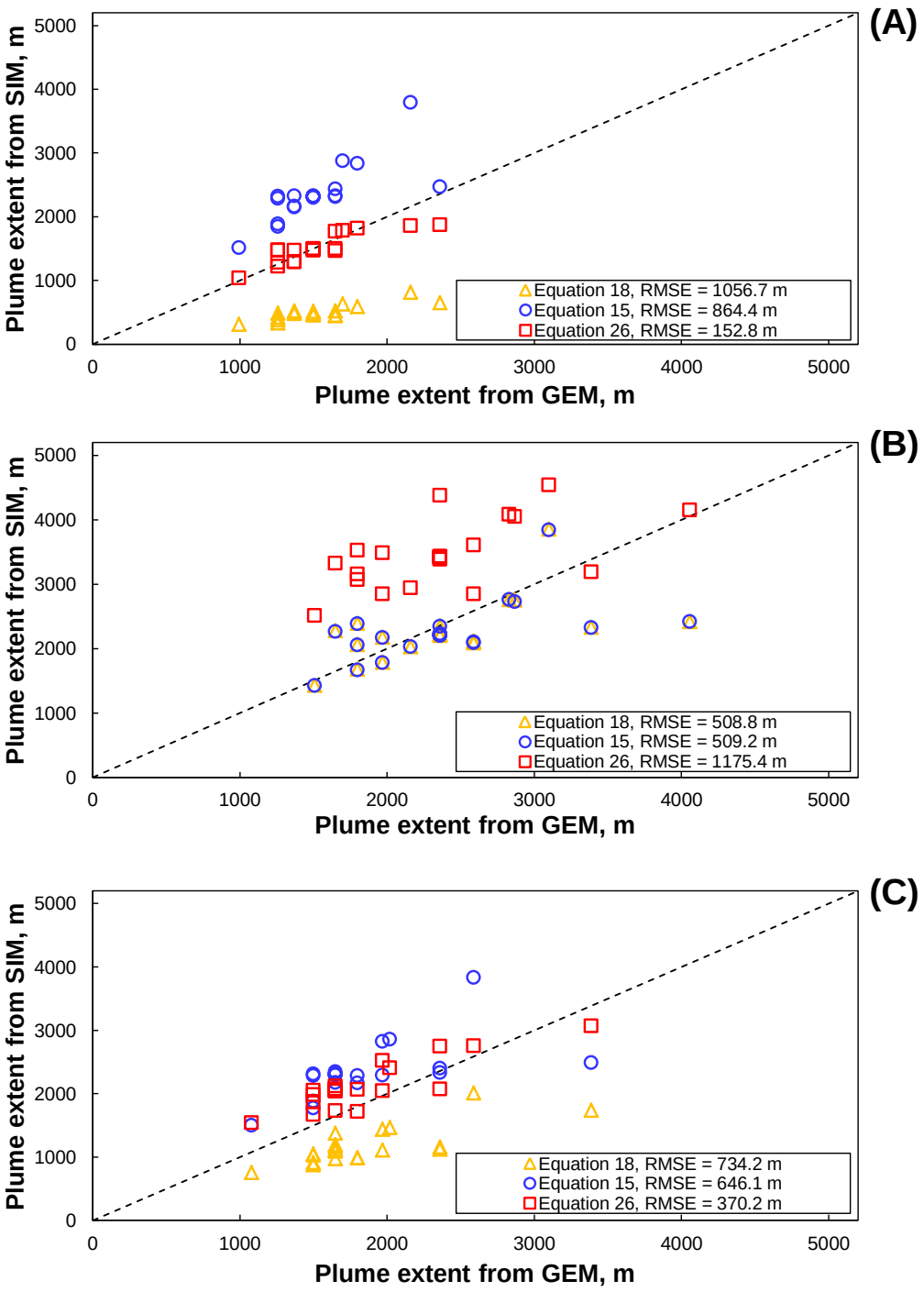

Figure 13: Comparison of plume tip location predictions for the commercial simulator versus the sharp interface model using the relative permeability at the wet-gas average saturation value for the analytical profile (Eq. 15), analytical tip (Eq. 18), and the rigorous profile (Eq. 26). (A) Reference case permeability, (B) linear relative permeability, and (C) high relative permeability. RMSE = root-mean-square error.

Lastly, the rigorous solution was solved using average gas saturation to calculate relative permeability and through applying a Bingham-Reid mixing law. These data are illustrated in Figure 14. Through this technique, the error for the reference case (A) marginally increases while the error for the linear (B) and high relative permeability (C) relationships decrease dramatically.

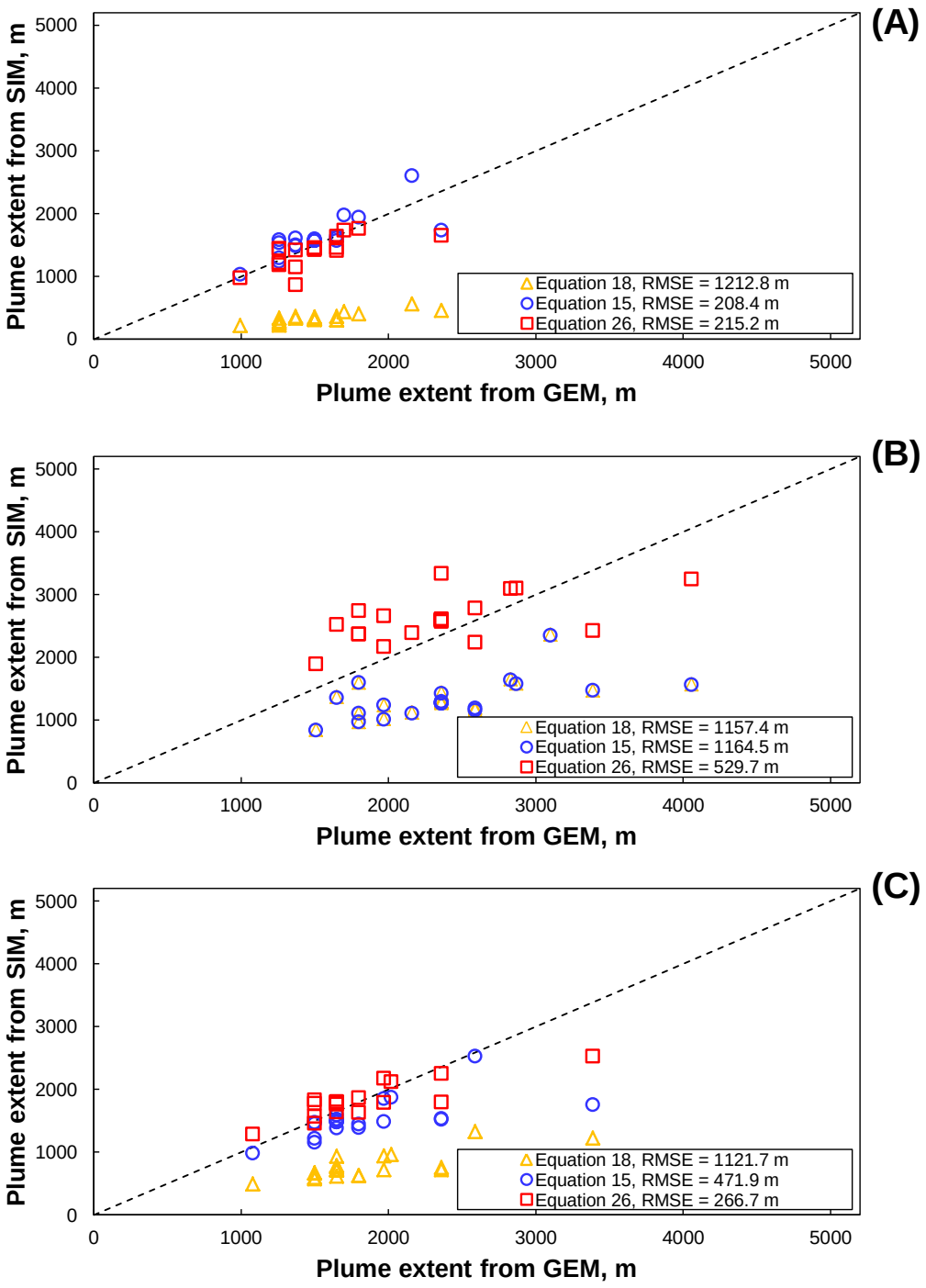

Figure 14: Comparison of plume tip location predictions for the commercial simulator versus the sharp interface model using the relative permeability at the wet-gas average saturation value with a Bingham-Reid mixing rule for the analytical profile (Eq. 15), analytical tip (Eq. 18), and the rigorous profile (Eq. 26). (A) Reference case permeability, (B) linear relative permeability, and (C) high relative permeability. RMSE = root-mean-square error.

As demonstrated herein, some relative simple modifications to the sharp interface model presented elsewhere [11,12] significantly improved the agreement between the sharp interface model and a commercial full-physics simulator. The Bingham-Reid mixing law produced the best agreement when the relative permeability is calculated using the wet-gas region average permeability.

6 Conclusions

Simplified models, eliminating the complication of the full-physics models while retaining the essence of the physical process, are attractive for CO_2 sequestration since they eliminate the time requirement involved in comprehensive modeling and enable parametric analyses. This report focuses on the abrupt interface solution for multiphase transport of CO_2 and brine in an aquifer. Three separate relative permeability relationships were evaluated while systematically manipulating aquifer properties.

In general, the sharp interface model did not appear to have great reliability in comparison with a commercial code simulating the full physics of the process. It was later found that the sharp interface model was most sensitive to the mobility of the multiphase brine-CO_2 zone. This effect presumably arises due to the simplification in the sharp interface model that approximates the properties in the multiphase region as constant and similar to pure CO_2.

The root of this sensitivity was further explored by manipulating the relative permeability and viscosity in the multiphase region. First, the relative permeability in the sharp interface model was set to the relative permeability of the multiphase region as predicted by the simulator. This technique slightly improved the performance of the sharp interface model. Next, the viscosity was manipulated until the model and simulator were in agreement providing insight into the magnitude of correction for mobility necessary to bring the two models in alignment.

Subsequently, viscosity mixing laws were used to evaluate the results under the assumption that fluid mixing at the interface may lead to a non-constant viscosity in the multiphase region. This investigation showed the use of dry CO_2 viscosity led to poor predictive capability and that a mixing law was necessary. The study further confirmed viscosity additivity is not appropriate. For the cases where the relative permeability was non-linear as in (A) and (C), a Bingham-Reid average mixing law dramatically improved performance of the sharp interface model. For the linear relative permeability in case (B), agreement was only modestly improved.

Finally, the rigorous solution to the sharp interface model was calculated as reported elsewhere [11, 12]. Agreement between the high fidelity simulator and simplified model were relatively poor. After adding a viscosity mixing rule, agreement was improved in some cases.

Similarly, accounting for the average gas saturation, rather than an end-point value, also improved the predictions in some cases. Lastly, when a mixing rule and average saturation are used in tandem, the agreement between the rigorous solution to the sharp interface model and the commercial simulator were significantly improved.

The results of this investigation indicate that with a few relatively simple modifications to the sharp interface model, the results match those produced by a rigorous full-physics simulator across a wide variety of reservoir conditions. This result is encouraging as it suggests simple forecasting tools, capable of rapid parametric analysis, can be reliably used to predict CO_2 sequestration processes. Future work will involve comparisons to reservoir data.

References

[1] Aaron Douglas and Costas Tsouris. Separation of CO_2 from flue gas: a review. *Separation Science and Technology*, 40(1-3):321–348, 2005.

[2] Howard J Herzog. Peer reviewed: What future for carbon capture and sequestration? *Environmental science & technology*, 35(7):148A–153A, 2001.

[3] Danae A Voormeij and George J Simandl. Geological, ocean, and mineral CO_2 sequestration options: A technical review. *Geoscience Canada*, 31(1), 2004.

[4] Parissa Mirjafari, Koorosh Asghari, and Nader Mahinpey. Investigating the application of enzyme carbonic anhydrase for CO_2 sequestration purposes. *Industrial engineering chemistry research*, 46(3):921–926, 2007.

[5] EG Woods and AG Comer. Saturation distribution and injection pressure for a radial gas-storage reservoir. *Journal of Petroleum Technology*, 14(12):1,389–1,393, 1962.

[6] Prasad Saripalli and Peter McGrail. Semi-analytical approaches to modeling deep well injection of CO_2 for geological sequestration. *Energy Conversion and Management*, 43(2):185–198, 2002.

[7] Myeong Hwan Noh, Larry Wayne Lake, Steven Lawrence Bryant, and Aura N Araque-Martinez. Implications of coupling fractional flow and geochemistry for CO_2 injection in aquifers. *SPE Reservoir Evaluation Engineering*, 10(04):406–414, 2007.

[8] Burton McMillan, Navanit Kumar, and Steven Lawrence Bryant. Time-dependent injectivity during CO_2 storage in aquifers. In *SPE Symposium on Improved Oil Recovery*. Society of Petroleum Engineers.

[9] Yagna Deepika Oruganti and Srikanta Mishra. An improved simplified analytical model for CO_2 plume movement and pressure buildup in deep saline formations. *International Journal of Greenhouse Gas Control*, 14:49–59, 2013.

[10] Xinwo Huang, Karl W Bandilla, Michael A Celia, and Stefan Bachu. Basin-scale modeling of CO_2 storage using models of varying complexity. *International Journal of Greenhouse Gas Control*, 20:73–86, 2014.

[11] Jan M Nordbotten and Michael A Celia. Similarity solutions for fluid injection into confined aquifers. *Journal of Fluid Mechanics*, 561:307–327, 2006.

[12] Jan M Nordbotten and Michael A Celia. Analysis of plume extent using analytical solutions for CO_2 storage. In *Proceedings of the 16th conference on Computational Methods in Water Resources*.

[13] Jan Martin Nordbotten, Michael A Celia, and Stefan Bachu. Injection and storage of CO_2 in deep saline aquifers: Analytical solution for CO_2 plume evolution during injection. *Transport in Porous media*, 58(3):339–360, 2005.

[14] Bernd Wiese and Simon A Mathias. Semi-analytical solution for constant pressure injection of CO_2 in saline aquifers. 2010.

[15] Marco Dentz and Daniel M Tartakovsky. Abrupt-interface solution for carbon dioxide injection into porous media. *Transport in Porous media*, 79(1):15–27, 2009.

[16] Victor Vilarrasa, Diogo Bolster, Marco Dentz, Sebastia Olivella, and Jesus Carrera. Effects of CO_2 compressibility on CO_2 storage in deep saline aquifers. *Transport in Porous media*, 85(2):619–639, 2010.

[17] Michael A Celia, Jan M Nordbotten, Benjamin Court, Mark Dobossy, and Stefan Bachu. Field-scale application of a semi-analytical model for estimation of CO_2 and brine leakage along old wells. *International Journal of Greenhouse Gas Control*, 5(2):257–269, 2011.

[18] Alv-Arne Grimstad, Sorin Georgescu, Erik Lindeberg, and Jean-Francois Vuillaume. Modelling and simulation of mechanisms for leakage of CO_2 from geological storage. *Energy Procedia*, 1(1):2511–2518, 2009.

[19] Rajesh J Pawar, Theresa L Watson, and Carl W Gable. Numerical simulation of CO_2 leakage through abandoned wells: Model for an abandoned site with observed gas migration in alberta, canada. *Energy Procedia*, 1(1):3625–3632, 2009.

[20] Philip H Stauffer, Hari S Viswanathan, Rajesh J Pawar, and George D Guthrie. A system model for geologic sequestration of carbon dioxide. *Environmental science technology*, 43(3):565–570, 2008.

[21] Chuan Lu, Si-Yong Lee, Weon Shik Han, Brain J McPherson, and Peter C Lichtner. Comments on abrupt-interface solution for carbon dioxide injection into porous media by m. dentz and d. tartakovsky. *Transport in Porous media*, 79(1):29–37, 2009.

[22] Marco Dentz and Daniel M Tartakovsky. Response to comments on abrupt-interface solution for carbon dioxide injection into porous media by dentz and tartakovsky (2008) by lu et al. *Transport in Porous media*, 79(1):39–41, 2009.

[23] Benjamin Court, Karl W Bandilla, Michael A Celia, Adam Janzen, Mark Dobossy, and Jan M Nordbotten. Applicability of vertical-equilibrium and sharp-interface assumptions in CO_2 sequestration modeling. *International Journal of Greenhouse Gas Control*, 10:134–147, 2012.

[24] SE Gasda, MA Celia, and JM Nordbotten. Significance of dipping angle on CO_2 plume migration in deep saline aquifers. In *Proceedings of the XVI International Conference on Computational Methods in Water Resources*.

[25] Grigory Isaakovich Barenblatt. *Scaling, self-similarity, and intermediate asymptotics: dimensional analysis and intermediate asymptotics*, volume 14. Cambridge University Press, 1996.

[26] Simon A Mathias, Paul E Hardisty, Mark R Trudell, and Robert W Zimmerman. Approximate solutions for pressure buildup during CO_2 injection in brine aquifers. *Transport in Porous media*, 79(2):265–284, 2009.

[27] Stefan Bachu, Jan M Nordbotten, and Michael A Celia. Evaluation of the spread of acid gas plumes injected in deep saline aquifers in western canada as an analogue to CO_2 injection in continental sedimentary basins. In *Proceedings of 7th International Conference on Greenhouse Gas Control Technologies*, volume 1.

[28] Guillermo Centeno, Gabriela Snchez-Reyna, Jorge Ancheyta, Jos AD Muoz, and Nayeli Cardona. Testing various mixing rules for calculation of viscosity of petroleum blends. *Fuel*, 90(12):3561–3570, 2011.

[29] Svante Arrhenius. *Über die Dissociation der in Wasser gelösten Stoffe*. Verlag von Wilhelm Engelmann, 1887.

[30] Eugene C Bingham. The viscosity of binary mixtures. *The Journal of Physical Chemistry*, 18(2):157–165, 1914.

[31] James Kendall and Kenneth Potter Monroe. The viscosity of liquids. ii. the viscosity-composition curve for ideal liquid mixtures. *Journal of the American Chemical Society*, 39(9):1787–1802, 1917.